The Philosophical Magazine

UNIVERSITY OF HAWAII
LIBRARY
MAR 15 '61

FIRST PUBLISHED IN 1798

A Journal of Theoretical Experimental and Applied Physics

Vol. 6 January 1961 No. 61
Eighth Series

25s. 0d., plus postage
Annual Subscription £13 10s. 0d., payable in advance

ALERE FLAMMAM

Printed and Published by
TAYLOR & FRANCIS LTD
RED LION COURT, FLEET STREET, LONDON, E.C.4

THE PHILOSOPHICAL MAGAZINE

Editor

Professor N. F. Mott, M.A., D.Sc., F.R.S.

Editorial Board

Sir Lawrence Bragg, O.B.E., M.C., M.A., D.Sc., F.R.S.
Sir George Thomson, M.A., D.Sc., F.R.S.
Professor A. M. Tyndall, C.B.E., D.Sc., F.R.S.

Authors wishing to submit papers for publication in the Journal should send manuscripts directly to the Publishers.

Manuscripts should be typed in *double* spacing on one side of quarto (8 × 10 in.) paper, and authors are urged to aim at absolute clarity of meaning and an attractive presentation of their texts.

References should be listed at the end in alphabetical order of authors and should be cited in the text in terms of author's name and date. Diagrams should normally be in Indian ink on white card, with lettering in soft pencil, the captions being typed on a separate sheet.

A leaflet giving detailed instructions to authors on the preparation of papers is available on request from the Publishers.

Authors are entitled to receive 25 offprints of a paper in the Journal free of charge, and additional offprints can be obtained from the Publishers.

The *Philosophical Magazine* and its companion journal, *Advances in Physics*, will accept papers for publication in experimental and theoretical physics. The *Philosophical Magazine* publishes contributions describing new results, letters to the editor and book reviews. *Advances in Physics* publishes articles surveying the present state of knowledge in any branch of the science in which recent progress has been made. The editors welcome contributions from overseas as well as from the United Kingdom, and papers may be published in English, French and German.

The Scientific Papers of Sir Geoffrey Ingram Taylor, II

EDITED BY G. K. BATCHELOR

The second volume of the *Scientific Papers*, edited by DR G. K. BATCHELOR, is the first of three to be devoted to work mainly on the mechanics of fluids. It contains papers on meteorology, oceanography and turbulent flow.

75*s. net*

Confluent Hypergeometric Functions

L. J. SLATER

A discussion of the main properties of the confluent hypergeometric functions and the Whittaker functions, with an outline of the functional analysis needed in the development of asymptotic expansions. Tables of the function ${}_1F_1(a;\ b;\ x)$ over those ranges most useful to the computer are also given.

65*s. net*

From Dualism to Unity in Quantum Mechanics

A. LANDÉ

Professor Landé aims to give quantum mechanics a new and sound theoretical basis. He sets out to reduce the quantum phenomena to more elementary general principles, such as symmetry, invariance and continuity, and he develops the current Born–Heisenberg account into a unitary theory. A significant contribution to both physics and the philosophy of science.

18*s.* 6*d. net*

Classical Electricity & Magnetism

E. S. SHIRE

A textbook bridging the gap between the elementary account of electricity and magnetism taught in schools and a mathematical treatment based on Maxwell's equations. The book covers the subject to the standard of a general degree course in physics or engineering and can be used with 'rationalised' or 'unrationalised' M.K.S. and c.g.s. systems.

45*s. net*

CAMBRIDGE UNIVERSITY PRESS

REVISED CHEAPER EDITION FOR LIBRARIES AND SCHOOLS

A History of Mathematics

From antiquity to the early nineteenth century

By J. F. SCOTT, B.A., D.Sc., Ph.D.
Vice-Principal of St. Mary's College, Strawberry Hill, Twickenham, Middlesex
Author of *The Scientific Work of René Descartes* (1596–1650),
Mathematical Work of John Wallis, D.D., F.R.S. (1616–1703), and other works

CONTENTS: Mathematics in Antiquity—Greek Mathematics—The Invention of Trigonometry—Decline of Alexandrian Science and the Revival in Europe—Mathematics in the Orient—Progress of Mathematics during the Renaissance—New Methods in Geometry—The Rise of Mechanics—The Invention of Decimal Fractions and of Logarithms—Newton and the Calculus—Taylor and Maclaurin, the Bernoullis and Euler, Related Advances—The Calculus of Variations, Probability, Projective Geometry, Non-Euclidean Geometry—Theory of Numbers—Lagrange, Legendre, Laplace, Gauss. This volume is intended primarily to help students who desire to have a knowledge of the development of the subject but who have too little leisure to consult works and documents. The author has availed himself of the facilities afforded by the Royal Society and other learned Societies to reproduce extracts from manuscripts and many scarce works.

Size $9\frac{3}{4}'' \times 6\frac{3}{4}''$. 266 pp. **Price 27s. 6d.** plus postage and packing 2*s*. 0*d*.

Some Reviews of the First Edition

" The invention of trigonometry, decimal fractions, logarithms and the calculus are each discussed clearly and concisely. The book is easy to read for anybody who knows the elements of mathematics and, although not free from minor errors, can be strongly recommended."—*British Book News*, April 1958.

" Physicists will find that the development in applied mathematics are clearly set out, from ancient times, through that of Archimedes, to the mechanics of the sixteenth century when interest was revived. Significant advances made by Stevin, Galileo, Descartes, Huygens and others are stressed, and help the reader to appreciate what Newton achieved. There are useful appendices giving brief biographical notes on mathematical topics and terminology, followed by a bibliography."—*Proceedings of The Physical Society*, September 1958.

" . . . it has been written with clarity and balance, and the excellent printing helps to make it a pleasure to read."—*The Times Educational Supplement*, 21 March 1958.

" . . . his (Dr. Scott's) wide knowledge of the material, his careful description of methods combine to provide an account which at times gives a sense of the excitement of discovery."—*Nature*, 26 July 1958.

" The printers and publishers are to be congratulated upon having produced such an attractive volume, ... We feel sure the book will be received with delight by all those interested in mathematical histories."—*BEAMA Journal*, August 1958.

" The work comes to life mainly because of his admirable use of the writings of mathematicians themselves, which vividly illustrates the great difficulties under which many of them laboured. This is not a book for the layman but both the student and anyone to whom figures are a fascination, will find the subject clearly and pleasantly presented."—*Technical Bookguide*, March 1958.

Printed and Published by

TAYLOR & FRANCIS LTD
RED LION COURT, FLEET STREET, LONDON, E.C.4

THE

PHILOSOPHICAL MAGAZINE

A JOURNAL OF THEORETICAL, EXPERIMENTAL
AND APPLIED PHYSICS

First Published in 1798

[EIGHTH SERIES—VOL. 6]

Observations on an Electrical Effect obtained during Deformation of Sodium Chloride Crystals†

By G. REMAUT and J. VENNIK
Laboratorium voor Kristallografie en Studie van Vaste Stoffen Rozier, 6, Gent, Belgium

[Received June 7, 1960]

ABSTRACT

An electrical signal obtained during the plastic deformation of sodium chloride crystals is described. This effect is attributed to the movement of charged dislocations. During a first series of experiments the specimens were submitted to a cyclic deformation. The magnitude of the electrical effect was measured in function of the amplitude of deformation. The influence of annealing was also investigated. In a second series of experiments the crystals were deformed by a series of stress pulses. A tentative explanation for the shape of the obtained signal is given.

§ 1. INTRODUCTION

By extending Lehovec's theory (Lehovec 1953) of a space-charge layer at the surface of an ionic crystal to a dislocation, Eshelby *et al.* (1958) concluded that dislocations in an ionic crystal should be electrostatically charged. To test this assumption, they suggested that plastic deformation of an ionic crystal would probably give some kind of an electrical effect.

In two previous notes (Amelinckx *et al.* 1959, Remaut *et al.* 1960) it was shown that an electrical effect is produced when a NaCl crystal is submitted to a cyclic stress. We then suggested that this effect was probably due to the motion of charged dislocations during the plastic deformation. In order to verify this hypothesis, a series of experiments was performed of which some results have already been described in the previous notes. We are now able to give some more results which support this hypothesis.

---

† Communicated by Professor Dr. W. Dekeyser.

§ 2. EXPERIMENTAL

2.1. *Deformation by Cyclic Bending*

In a first series of experiments practically the same apparatus was used as described before. The NaCl specimens were rectangular slabs of about 7 mm × 3 mm × 45 mm cut from crystals grown in our laboratory. The specimens were then bent to introduce an excess of dislocations of the same mechanical sign. By varying the radius of curvature we could change the dislocation density. One end of the bent specimen was rigidly mounted, the other was fastened to the moving part of the vibrator (fig. 1). The amplitude of vibration was measured by a vibrating capacitor mounted on the crystal. The calibration of the capacitor was performed by measuring the amplitude directly with a microscope.

Fig. 1

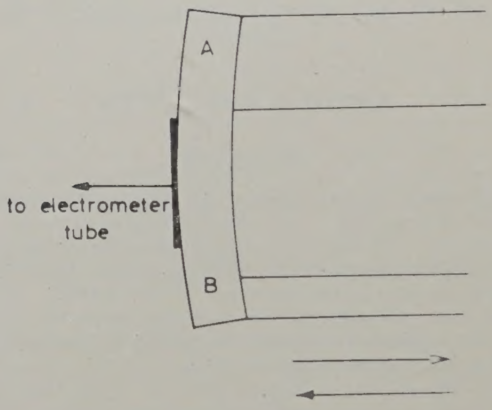

Bent specimen AB with end A rigidly mounted and end B fastened to the vibrator.

The electrical effect was detected by evaporating a gold electrode on the crystal and connecting it by means of a gold wire (0·005 mm diameter) to an electrometer with a very high input impedance and further to one of the channels of a dual-trace oscilloscope. By connecting the vibrating capacitor to the second channel of the oscilloscope it was possible to compare the signal coming from the specimen with its deformation.

A photo of the electrical effect obtained during cyclic bending is given in fig. 2†. The shape of this signal, except for the relative length of the horizontal step, stayed practically the same in the whole frequency range considered (10–3000 c/s). In fig. 3 the signal coming from the NaCl crystal is compared with that of the capacitor. Here, one can clearly see the shift of the two curves with respect to a common time axis. This shift is independent of the frequency in the range considered.

---

† Figures 2, 3, 7 and 10 are shown as plates.

Fig. 4

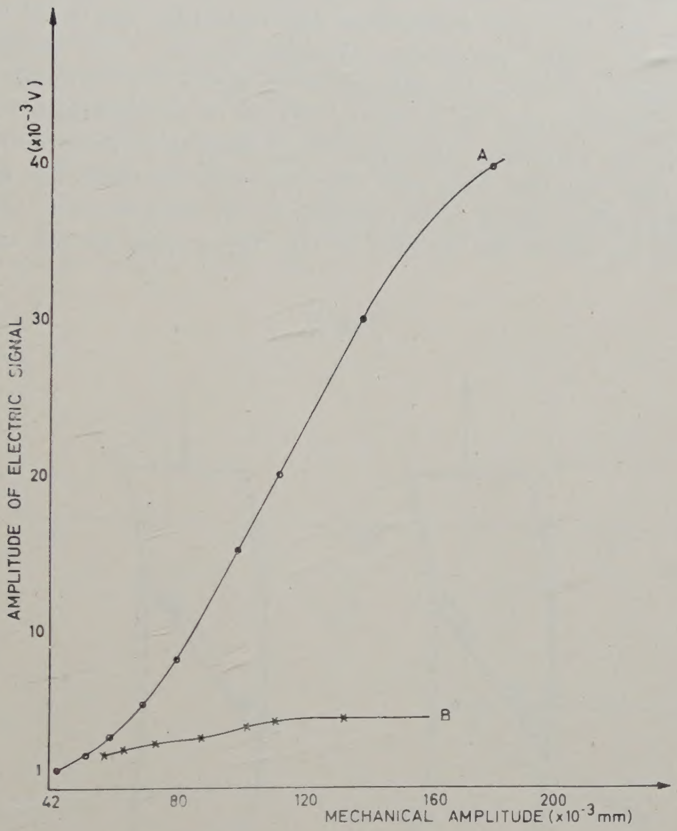

Relationship between the amplitude of the electrical signal and the amplitude of vibration.

Fig. 5

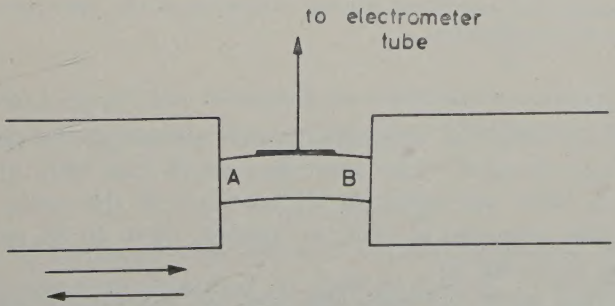

Bent specimen AB rigidly mounted at the end B and fastened to the vibrator at the end A.

In fig. 4, curve A gives the relationship for a particular specimen between the amplitude of the electrical signal and that of the vibration. Specimens with the same dimensions and curvature, cut from the same mother crystal, gave practically identical curves. For specimens of different origin, the value of amplitude of the signal, for a same mechanical amplitude, depends very much on the history of the specimen.

Curve B of fig. 4 gives an analogous relationship to curve A but now for a specimen that was first bent and then annealed at 600°c for 48 hours. The electrical effect during cyclic stressing is now much smaller. A possible explanation for this is the pinning of the dislocations during annealing.

Fig. 6

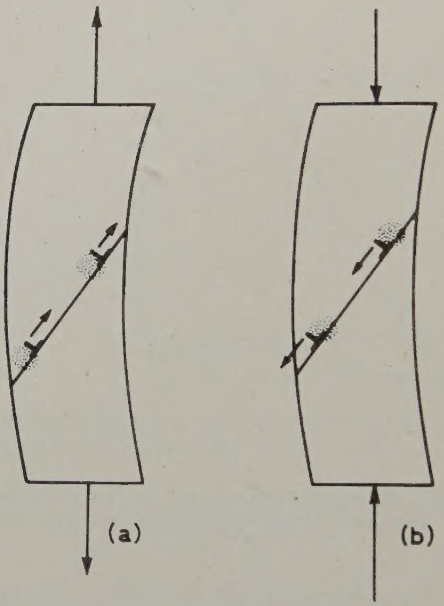

Movement of dislocations during an extension and compression cycle: (*a*) represents the movement during extension of the specimen; (*b*) corresponds to compression.

2.2. *Specimen Submitted to an Extension and Compression Cycle*

In a second series of experiments the procedure for stressing the specimens was changed. The specimens which had been given a small curvature to have an excess of dislocations of the same mechanical sign, were now mounted in order to subject them to an extension and compression cycle (fig. 5).

The electrical signal obtained this way had exactly the same shape as that obtained during the first series of experiments. The displacement between the electrical and mechanical signal was also the same. But, contrary to what we found during cyclic bending, the signals coming from opposite faces of the specimen were now in opposition. This is to be expected, because when the specimen is compressed or extended, dislocations will always leave one face of the specimen while at the same time others will arrive at the opposite face. This is visualized in fig. 6.

With this experimental procedure it was also possible to determine the shear stress at which the electrical signal begins, i.e. the shear stress at which the dislocations begin to move in great numbers. The measured value for different specimens lay in the vicinity of 75 g/mm^2 which is very close to the value given by Schmid and Boas (1950) for the yield stress of NaCl. We can thus conclude that the electrical effect begins at the moment we get plastic deformation.

Fig. 8

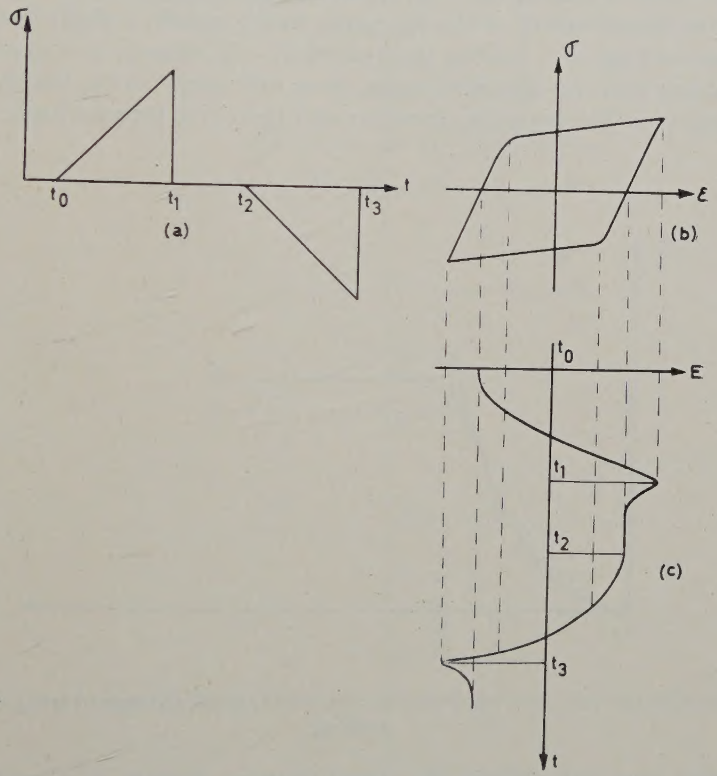

A possible explanation for the shape of the signal corresponding to alternating pulses.

2.3. *Pulse Stressing*

In order to investigate the effect of a stress increasing linearly, with time, specimens were deformed by feeding a series of sawtooth current pulses to the vibrator on which the crystal was mounted. The circuit was arranged in such a way that successive pulses could have the same or the opposite direction. In the latter case the specimen was alternately extended and compressed while in the former the specimen was successively compressed. This type of experiments gave some interesting results.

The electrical signal corresponding to alternated pulses is seen in fig. 7. A possible explanation for the shape of the signal obtained is the following. During the period $(t_0 - t_1)$ [fig. 8 (*a*)], the stress rises linearly from zero to a maximum value. It then drops instantaneously to zero and stays so until t_2, where it starts increasing linearly again, but now in the reversed direction. This continues till t_3, where it drops back to zero again. The specimens hysteresis loop which should correspond to this cycle of deformation is shown in [fig. 8 (*b*)]. From this, one can deduce the form of the electrical signal [fig. 8 (*c*)]. At t_0 the specimen starts to deform but the signal stays zero till a critical stress is reached where we then obtain a rapid increase of the signal. At t_1, the stress drops abruptly to zero, and we get an elastic recoil of the specimen which causes a slight decrease of the observed signal. During the period $(t_1 - t_2)$ there is no movement of dislocations and the electrical signal does not vary. At t_2 the saw-tooth pulse starts in the opposite direction and the cycle repeats itself.

Fig. 9

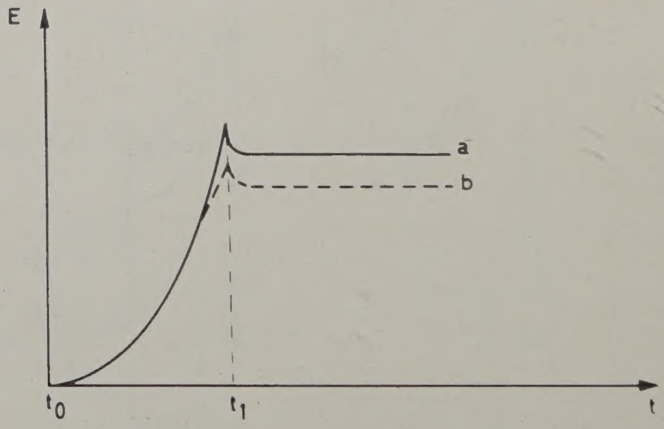

A schematic picture showing how the electrical signal changes during continued pulsing.

During sawtooth cycling the signal changes slightly in amplitude and in form. In fig. 9 the full line represents the signal corresponding to the first pulses; the dotted curve represents the signal after equilibrium has been reached. As can be seen the signal decreases. We suppose that this results from the damage done in the glide-plane during continued deformation; probably the rate of deformation will also have a big influence. This should be further investigated.

The result of imposing on the specimen a series of pulses of the same polarity, can be seen in fig. 10. As was to be expected during the first pulse (t_0, t_1) [fig. 11 (*c*)] the signal changed from zero to a maximum value. At t_1 where the stress dropped to zero, the electrical effect decreased slightly as a result of the elastic recoil, but it then stayed constant till t_2. At t_2 a new pulse started and a slight increase in the signal was obtained owing to the small elastic and plastic deformation which accompanied this pulse. This continued for some time till the signal reached a certain

Fig. 11

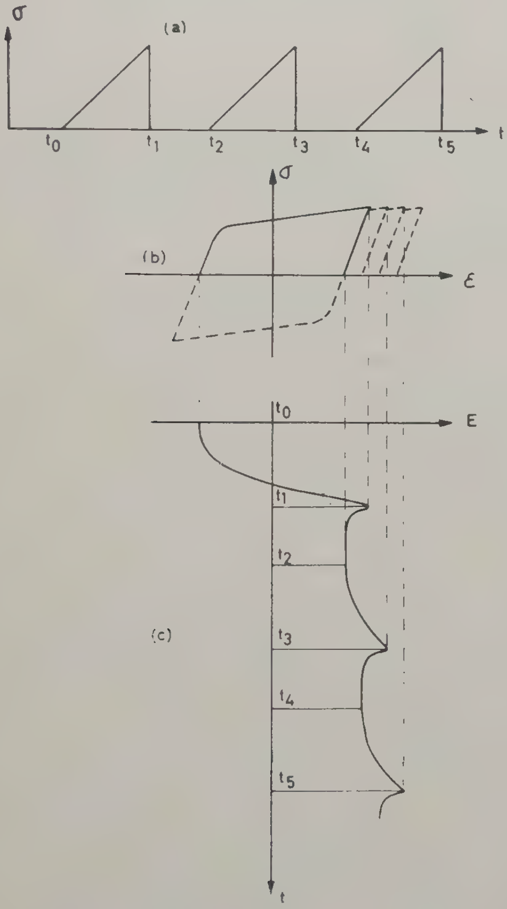

Relationship between the stress (σ) applied to the specimen, the elongation (ϵ), the electrical signal (E) and the time (t).

maximum value where it then stayed constant probably as the result of the piling up of dislocations. By slightly raising the stress the dislocations were made to break through these barriers and a sudden increase in signal was observed. If this was repeated several times one remarked that the increase in signal which accompanied the increase in stress, diminished.

One finally arrived at the situation where an increase in stress had practically no influence any more on the electrical effect. At this moment a slight increase in stress usually resulted in the fracture of the specimen.

§ 3. CONCLUSION

From these experiments one can conclude that the electrical effect studied is closely related to the movement of dislocations. As a result of this, this method of investigation should be a promising tool for the study of such phenomenon as plastic flow, work-hardening, Peierls-Nabarro forces and fatigue of ionic crystals.

ACKNOWLEDGMENT

This work is part of a research scheme supported by the Institut pour l'Encouragement de la Recherche Scientifique dans l'Industrie et l'Agriculture (C.E.S.). We wish to thank Professor Dr. W. Dekeyser for his continuous interest.

REFERENCES

AMELINCKX, S., VENNIK, J., and REMAUT, G., 1959, *J. Phys. Chem. Solids*, **11,** 170.

ESHELBY, J. D., NEWEY, C. W. A., PRATT, P. L., and LIDIARD, A. B., 1958, *Phil. Mag.*, **3,** 76.

LEHOVEC, K., 1953, *J. chem. Phys.*, **21,** 1123.

REMAUT, G., VENNIK, J., and AMELINCKX, S., 1960, *J. Phys. Chem. Solids* (to be published).

SCHMID, E., and BOAS, W., 1950, *Plasticity of Crystals* (London: F. A. Hughes & Co. Ltd.).

Effect of Slip Distribution on the Fracture Behaviour of Magnesium Oxide Single Crystals†

By R. J. Stokes, T. L. Johnston, and C. H. Li
Honeywell Research Center, Hopkins, Minnesota, U.S.A.

[Received June 23, 1960]

Abstract

The tensile deformation of chemically polished magnesium oxide crystals has been correlated with the distribution of slip at the *onset* of plastic flow. If two slip bands, generated on orthogonal {110} planes, happen to intersect to nucleate a crack before other slip bands develop nearby, then the crack so formed is unstable and the crystal completely brittle. If, however, there is a higher density of slip sources cracks can become stabilized by adjacent slip bands and the crystals continue to deform. Sometimes slip is confined to a single slip band which expands laterally to fill the entire gauge length, these crystals are extremely ductile. The fracture behaviour of a given crystal depends critically upon the relative orientation, number, thickness and spacing between slip bands.

The density of slip may be increased artificially when dislocation sources are injected into the crystal surface by sprinkling with carborundum before loading. Such crystals are *always ductile* in tension. A similar treatment for crystals to be bent leads to a profound change in their fracture behaviour.

§ 1. Introduction

When the mechanical properties of different magnesium oxide crystals are compared with one another there is an alarming lack of reproducibility both in their yield strength and ductility. Studies of variation in the yield strength have led to the general conclusion that a form of precipitation hardening is involved (Kronberg *et al.* 1960, Thompson and Roberts 1960, Gorum *et al.* 1960) so that the rate of cooling from an annealing temperature (1000°c and above) is particularly critical. Indeed it is possible to halve the yield strength, by quenching rather than slowly cooling the crystals. In the present work we have equalized the yield strength of a number of crystals with a standard annealing treatment and then studied some of the factors controlling their ductility.

In some cases the variation in ductility may be attributed to the preparation of the specimen surface since cleavage and subsequent handling are now known to introduce surface defects which can propagate to cause premature failure under stress (Stokes *et al.* 1960, Clarke and Sambell 1960). However, when the precaution is taken to eliminate defects by chemically polishing and carefully handling the crystals the scatter in ductility still persists. It will be shown below that this *innate scatter* may be interpreted in terms of the dependence of the fracture behaviour upon certain slip parameters.

---

† Communicated by the Authors.

An earlier paper (Stokes *et al.* 1959 a) has described the relationship between slip and the cleavage fracture of polished magnesium oxide crystals deformed at a slow strain rate under bending. For the sake of continuity and the need for reference the details of this fracture mechanism will be briefly reviewed at this point. It was concluded from the previous observations that a cleavage crack nucleated at the end of a $(\bar{1}10)$ slip plane by the coalescence of edge dislocations which became held up against an obstacle provided by dislocations concentrated in an orthogonal intersecting (110) slip band. The crack nucleus lay parallel to the (110) plane of the orthogonal slip band and propagated by cleavage over this plane until halted by another (110) slip band parallel and adjacent to the original $(\bar{1}10)$ slip band. Although the crack was prevented from propagating further in the [110] direction by the slip band, it remained free to develop parallel to the [001] line of intersection. In this way a stable internal (110) [001] slit was formed along the channel between the two slip bands. For complete fracture of the specimen the slit switched out of the (110) plane into the (100) plane normal to the applied stress. All crystals fracturing by this mechanism contained a characteristic (110) [001] step across their fracture surface, referred to descriptively as the 'line' source.

There are two factors which are most important in this fracture mechanism. First, slip must be activated on two orthogonal planes which intersect each other before the crack can nucleate. Second, the effectiveness of the adjacent band in halting and then stabilizing the growing crack nucleus depends on its thickness and its distance from the [001] line of nucleation. The distance from the line of nucleation (or slip band separation) is particularly critical since it determines (*a*) the velocity attained by the accelerating crack front before it hits the slip band and (*b*) the stabilized crack length, which in turn determines its associated stress concentration. An additional factor which could be important is that the slip bands must be sufficiently thick to act as an obstacle to an edge dislocation avalanche for crack nucleation.

With this mechanism it is possible to appreciate how different slip band configurations can modify the fracture process and thereby the ductility of magnesium oxide crystals. For example, there is the situation where a crystal contains just two orthogonal slip bands which happen to intersect each other to nucleate a crack before any other slip bands develop. Under these conditions crack propagation is uninhibited and the crystal extremely brittle. However, if there is a higher density of intersecting slip bands the cracks that form become stabilized and a certain amount of ductility is to be expected. In addition, there is the configuration where slip is confined to a single plane only, in which case no intersections occur, no pile-ups form and the conditions for crack nucleation by the above mechanism do not exist within the crystal. Such crystals would be expected to be extremely ductile. The fracture behaviour of a given crystal, therefore, depends critically upon the relative orientation, number, thickness and spacing between slip bands operative from the *onset* of plastic flow.

In § 3 of this paper it will be shown that the innate scatter in the ductility of chemically polished magnesium oxide crystals when tested in tension may be correlated with their slip behaviour in the above manner. In §§ 4 and 5 experiments are described in which the slip distribution at the onset of plastic flow was controlled artificially, a procedure which made it possible to increase the ductility reproducibly and in some instances to modify the fracture behaviour quite profoundly.

§ 2. EXPERIMENTAL PROCEDURE

As emphasized elsewhere (Stokes *et al.* 1960) a detailed study of the mechanical properties of rock-salt type ionic solids is possible only if exceptional care is taken in the surface preparation and handling of the crystals. In all of the work reported here magnesium oxide crystals were initially chemically polished and then untouched within their gauge length (apart from the special procedures of §§ 4 and 5) so that the observations refer to their innate mechanical behaviour.

The specimens to be tested in tension were first cleaved from bulk crystals (supplied by Norton Co.) to dimensions approximately 0·1 in. square and $\frac{3}{4}$ in. in length. They were next given a standardized annealing treatment in which the temperature was raised to 2000°C in 15 min, held there for 20 min and then slowly cooled to room temperature over a period of 30 min. As a consequence all of the crystals yielded at approximately the same resolved shear stress, 5000 p.s.i. After polishing in hot orthophosphoric acid they were carefully mounted in split tensile grips with an epoxy resin cement to leave an approximate $\frac{3}{8}$ in. gauge length. The tests were conducted in a hard tensile machine at a low strain rate of $1{\cdot}5 \times 10^{-5}\,\mathrm{sec}^{-1}$. The alignment of each crystal was checked visually in the early stage of the tension test with a polarized light technique. Any non-uniform stress distribution was revealed by a colour gradient across the specimen in which case the specimen was unloaded and re-aligned. In general the stress distribution throughout the specimen was fairly uniform although constraints in the vicinity of the grips (the specimens were not machined or polished to give a reduced gauge section) gave rise to local stress concentrations.

Some of the experimental observations described in this paper were recorded on motion-picture film. The crystals used for these experiments were illuminated with polarized light and the pictures taken through an analyser crossed with the polarizer for extinction under zero stress. Because of the high stresses involved in plastic flow and the thickness of the crystal the birefringent pattern produced was highly coloured. To record this colour 16 mm Kodachrome film was used. The photographs reproduced in this paper are direct, and therefore negative, enlargements from the film.

To change the distribution of slip bands, artificial slip sources were introduced into the specimen in two days, first by cleavage and second by sprinkling with silicon carbide powder. Dislocations produced along cleavage tear lines may be expanded under an applied tensile stress (Stokes *et al.* 1959 b, Gilman 1959). Accordingly, crystals were prepared whose dimensions were such that successive division into two equal parts yielded a specimen of the appropriate, 0·1 in. × 0·1 in. cross section. The large crystals were first chemically polished. Special precautions were then taken to avoid the introduction of undesirable surface microcracks during the act of cleavage. To do this the crystals were cleaved while standing upright on a piece of filter paper and were given a sharp tap with the chisel to propagate a fast crack. In this way specimens were prepared which had either one surface or two opposite surfaces in the as-cleaved condition.

A more uniform distribution of slip sources was obtained by sprinkling chemically polished and mounted tensile specimens liberally on either one, two opposite, or all four $\{100\}$ surfaces with fine particles of 200 mesh silicon carbide powder from a height of 3 in. The impact produced by these particles was just sufficient to inject dislocation half loops into the surface of the crystals, yet insufficient to form microcracks (Stokes *et al.* 1959 b). In a few instances, however, sprinkled specimens did fracture prematurely due to a surface defect introduced by sprinkling; such tests were omitted from the present discussion.

Crystal beams to be tested in bending were cleaved to a $\frac{1}{4}$ in. × $\frac{1}{8}$ in. cross section and 1 in. length, chemically polished and then when desired thoroughly sprinkled on all four surfaces with 200 mesh silicon carbide. After being loaded in air to the stress level at which yielding could just be detected, the crystal was removed from the machine and repolished. The purpose of the second polish was to remove any surface flaws which may have been introduced in sprinkling, a procedure which obviously had to wait until the dislocation loops had been expanded deep enough into the crystal or they too would have been eliminated. (A similar repolishing procedure was not possible with the tensile specimens because they were mounted in grips.) The deformation was then continued to fracture.

A number of specimens which had been sprinkled and pre-strained slightly by bending to introduce dense slip were further deformed by impact. A small Charpy-type impact machine was used with a capacity of 10 in./lb and a hammer velocity such that the outer fibre was strained at a rate of 40 $\sec^{-1}$, an increase of 10^6 over the low strain rate tests. The direction of impact was in the same direction as the pre-strain.

§ 3. INTRINSIC SLIP SOURCES

The plastic behaviour of polished magnesium oxide crystals under tension may be broadly classified into three categories, each of which will be shown to be characterized by a certain distribution of slip. As can be seen from fig. 1, the deformation before fracture increased from category I to II to III, even though the yield stress remained consistently in the range 4000 to 5000 p.s.i. For category I the crystals deformed less than 0·2% strain; in some instances plastic deformation was hardly detectable and macroscopically the specimens appeared completely brittle. All crystals of category I fractured within the gauge length (as indicated by the vertical arrow). Crystals of category II were more ductile and fractured within the gauge length after approximately 5% strain. For category III there was a distinct change in the yielding behaviour in that the stress–strain curves were initially flat, exhibiting in somes cases a yield point. Such crystals were extremely ductile and never fractured within the gauge length (indicated by the horizontal arrow), they either pulled loose from or fractured at the grips.

Fig. 1

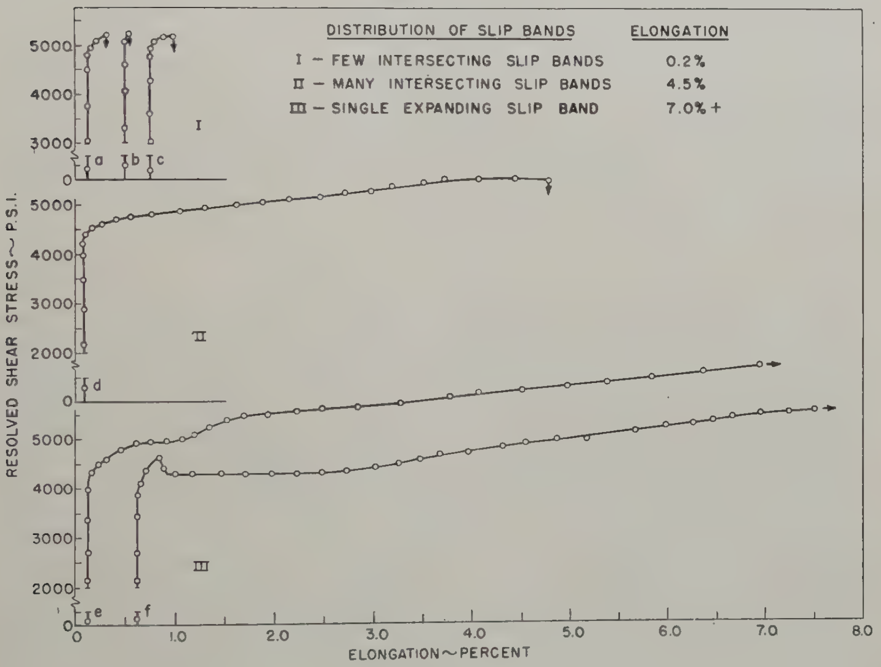

Tensile stress–strain curves for chemically polished magnesium oxide crystals tested at room temperature.

We will now discuss in turn the details of the slip band distribution and fracture for each of these three situations.

3.1. *Category I*

Figure 2† shows the slip band distribution, as revealed by etch pits, for the specimen represented by curve (*a*) in fig. 1. It can be seen that along the whole gauge length there were no more than ten individual bands of slip, and, most important, two of these bands intersected along a line coincident with the fracture surface. The appearance of the fracture surface for this particular specimen is reproduced in fig. 3 and shows the characteristic (110) [001] line source.

Figure 4 is a composite photomicrograph taken on the two fractured halves of the specimen represented by curve (*b*) in fig. 1. The individual pieces were cleaved down their middle after fracture to expose surfaces suitable for etching, hence the cleavage lines in the photographs. On the basis of the stress–strain curve this crystal appeared completely brittle but after etching was found to contain *just two* slip bands within the gauge length, the two illustrated in the figure. Again, cleavage fracture originated from the (110) [001] slit formed along their line of intersection.

In summary, it was concluded that crystals of category I were brittle because cleavage cracks nucleated at slip band intersections before other slip bands had developed which could have stabilized them.

3.2. *Category II*

Crystals of this category had a slip distribution essentially the same as category I except that there was now a sufficient density of slip sources operating from the onset of flow to stabilize the cracks as they formed. Thus, although the crystals contained cracks at relatively small strains they were able to continue deforming under tension.

Interesting direct observations of the development of slip and the formation of stabilized cracks in a crystal of this category have been recorded on motion film. Figure 5 reproduces selected frames from the sequence. There were two regions of interest. The first was the group of slip bands represented by A on the right-hand side of the figure. Between frames (*g*) and (*h*), which were approximately 1/16 second apart, a stable (110) microcrack could be seen to have formed which was bound at each end by a slip band. The crack grew in steps represented by frames (*i*), (*j*), and (*k*), being arrested as it crossed each (110) slip band in its path. In the frame next after (*k*) the crystal had completely fractured.

The other region of interest was that associated with the slip band B. In frames (*a*) to (*e*) the stress concentration associated with this band increased in intensity, while in (*f*) it decreased and in (*g*) had disappeared altogether. At the same time at the lower right extremity of the band a tiny crack formed, as in (*f*) (just above arrow) and subsequent frames. This crack was completely stable and did not increase its dimensions throughout the rest of the deformation.

---

† Figures 2–6, 9 and 10, 12–15 are shown as plates.

There can be no doubt from these observations that slip bands have the ability to halt and stabilize cleavage crack nuclei and that this is an important parameter in the ductility of magnesium oxide crystals.

3.3. *Category III*

It was possible in some crystals of magnesium oxide for a *single* slip band to grow uninterrupted in width until it had covered the gauge length from end to end. In general, these slip bands were observed to originate at the stress concentration near one of the grips and spread from one end to the other. However, examples were seen where a single slip band nucleated at the centre of the gauge length and spread in both directions towards the grips, also where a number of slip bands active on the same plane merged together to form a single band.

The slip bands could be seen to expand through a low-power microscope while the crystal was being deformed. The tilt in the crystal surface where each edge of the slip band emerged (drawn on an exaggerated scale for band Y in fig. 16 (*c*)) appeared as a fine line which moved along the specimen. This was analogous to the appearance of moving low-angle boundaries as observed in zinc by Li *et al.* (1953). If the orientation of the slip band was such that a step was not produced on the surface under examination (i.e. when viewed in a direction perpendicular to the Burgers vector) then the profile of the slip band could be detected with polarized illumination. The stress concentration at the edge of the band then produced a marked stress birefringence. Records of expanding slip bands in magnesium oxide for both orientations have been obtained on motion-picture film. The distribution of slip in a specimen which had started to deform in this way but which parted prematurely from the grips is shown in fig. 6. The density of etch pits within the band on the right-hand side of the photograph was so high that the surface appeared to be uniformly stained. On the left-hand side, however, a low-angle boundary and isolated dislocation etch pits could be distinguished in the region which had not yet deformed.

As indicated in fig. 1, crystals of category III deformed by the greatest amount. Unfortunately, in all instances they parted from the grips when the gauge length was filled by the slip band. It was possible that the stress concentration in the grips or the surface tilt to accommodate the slip caused the epoxy resin to relax. It would be interesting to know just how much these crystals would elongate and by what mechanism they would continue to deform and fracture within the gauge section. The reason for the increased ductility may be understood in terms of the fracture mechanism outlined in § 1. When slip was confined to a single plane no intersections developed and one of the conditions for crack nucleation by this mechanism did not exist within the gauge length.

The reason why the number of intrinsic slip sources operative from the onset of plastic flow should be different for crystals of the different categories is not understood. It is possibly related to the impurity amount and distribution, i.e. whether in solid solution or precipitate, although no correlation between impurity content and characteristic behaviour has been found. In general it was true that specimens originally prepared from the same bulk crystal fell into the same category and by far the greatest number behaved as in category I.

§ 4. Slip Sources Introduced by Cleavage

We have compared the mechanical behaviour of crystals having carefully cleaved surfaces with the behaviour of companion crystals having chemically polished surfaces. Tensile stress–strain curves for the cleaved crystals are reproduced in fig. 7; their innate mechanical behaviour fell in the category indicated. Since the slip sources introduced by cleavage were limited in number by the distribution and nature of the tear lines, this treatment essentially put all crystals, irrespective of their origin, into category II. In this respect, the most interesting change in behaviour was shown by the crystal of curve 1. Its ductility should have been approximately zero (category I) but this has now been increased to 6%.

Optical examination of cleaved specimens after fracture revealed that many stable (110) [100] slits had formed during deformation and that one of these had propagated for fracture to give the characteristic line source of fig. 3.

Fig. 7

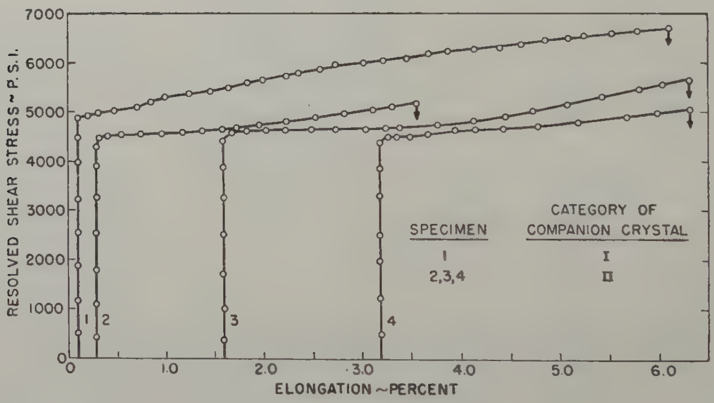

Tensile stress strain curves for magnesium oxide crystals having carefully cleaved faces.

Crystal 1; companion of crystal of category I, fig. 1. Cleaved on one face only.

Crystal 2, 3, 4; companion of crystal of category II, fig. 1. Cleaved on two opposite faces.

§ 5. Slip Sources Introduced by Sprinkling

The observations of §§ 3 and 4 suggested that if the number of slip sources could be increased many-fold by sprinkling the surface uniformly with fine silicon carbide powder, then the distribution of slip bands would be made so dense as to fill the whole crystal and suppress the formation of cracks by the conventional mechanism described in § 1 altogether. This was found to be the case for crystals deformed in bending, but in tension the same procedure led to rather unexpected results. For continuity the tension tests will be presented first.

5.1. *Tension Tests*

Crystals which had been sprinkled were found to be consistently ductile in tension irrespective of their origin. Figure 8 reproduces the stress–strain curves for a number of specimens and shows how the enhancement of ductility was approximately the same whether one surface, two opposing or all four surfaces were impacted.

Fig. 8

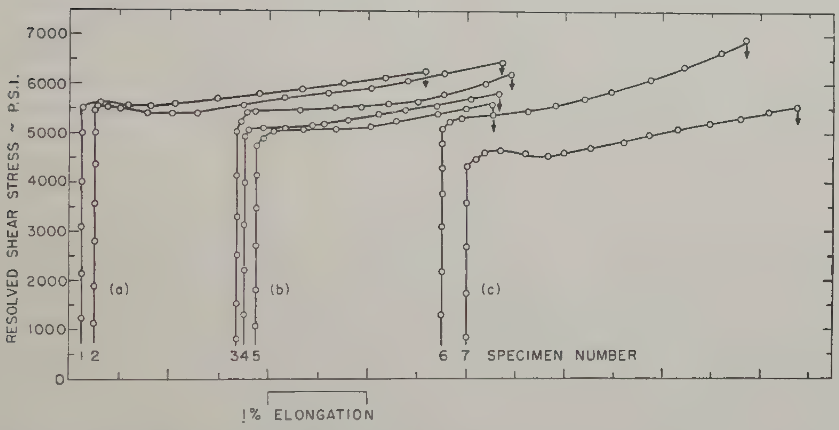

Tensile stress–strain curves for magnesium oxide crystals which have been sprinkled with silicon carbide on (*a*) one surface, (*b*) two opposite surfaces, and (*c*) all four surfaces.

Crystal 1, 2 ; companion of category III, fig. 1.
Crystal 3, 4, 5, 6 ; companion of category I, fig. 1.
Crystal 7; companion of category II, fig. 1.

The rather surprising feature of the deformation was the manner in which the slip was distributed along the crystal. The gauge length became sub-divided into a number of blocks within which slip was very dense and confined to a single slip plane. In the individual blocks slip could take place on one of the four {110} planes available, although it was generally found along the gauge length that slip alternated between the two orthogonal planes of a conjugate pair. At the boundary between the blocks (across which the slip plane changed) the slip was less dense and the two systems were able to interpenetrate one another. This is illustrated for the two blocks in fig. 9 (*b*) and (*c*). Only a few isolated bands were able to penetrate completely across the boundary into the region of dense slip on the orthogonal system on the other side. Significantly, slits were only to be found in those regions of less dense interpenetrating orthogonal slip located at the block boundaries as shown in fig. 9 (*c*).

While a few specimens fractured within the gauge length by the propagation of a slit formed in a block boundary, more typically fracture occurred in the vicinity of the grips where stress inhomogeneities did not favour the activation of dense single slip. As may be expected, the ductility and microscopic aspects of slip varied somewhat for different crystals, depending upon the number of blocks developed and the relative orientation of slip on either side of a block boundary. The number of blocks formed was independent of the number of surfaces sprinkled so that one can readily appreciate why sprinkling one surface was just as effective as sprinkling all four in promoting ductility (fig. 8).

Block formation is a well-known phenomenon in sodium chloride single crystals when compressed (Taylor and Pratt 1958) or deformed in tension (Webb 1960). It is not properly understood why a crystal which contains many sources for slip on all four equally stressed planes should prefer to confine slip to one plane within a given block, although this could be the consequence of a non-uniform stress distribution due to mis-alignment or variation in cross section along the gauge length.

5.2. *Bend Tests*

In contrast to the spectrum of mechanical properties observed in tension (§ 3), polished magnesium oxide crystals behaved more consistently when deformed by bending. Such crystals always slipped on the two {110} planes having the bending axis as their zone axis. They were fairly ductile, formed stable slits and fractured cleanly in two from a 'line' source (Stokes *et al.* 1959 a). Sprinkling these specimens to increase the density of slip resulted in a three to five-fold improvement in ductility but in addition, and more significant, there was a profound change in the fracture behaviour.

In the first place, sprinkling did not result in the formation of slip blocks as was the case under tension. Instead slip on the two intersecting {110} planes was made very dense in the deformed zone at the centre of the specimen as shown in fig. 10. Second, stable (110) [001] slits were never found, at least with the resolution of the optical microscope, either in the crystals during deformation or in the fractured pieces. Finally, when the crystals fractured they shattered to leave a very rough and complicated fracture surface.

In order to understand this fracture behaviour we should consider the change in shape which occurs when a crystalline beam is severely bent. In a truly elastic body the tension surface becomes curved about an axis parallel to the length of the beam as shown in fig. 11 (*a*). This curvature is due to the lateral contraction of the beam. It is termed anticlastic curvature (Timoshenko 1934) and is proportional to Poisson's ratio. In plastic crystalline solids, at least those of the rock-salt structure, this curvature is accommodated by a kinking mechanism, which will be referred to as *anticlastic kinking*. This is illustrated diagrammatically in fig. 11 (*b*). The kinks produced in silver chloride, sodium chloride and lithium fluoride bent at room temperature and above are so pronounced they can be seen with the naked eye and felt with the finger. Their formation will be described elsewhere.

In magnesium oxide anticlastic kinking at room temperature was a more difficult process and by resisting lateral contraction the transverse stress at the tension surface was not relaxed. Consequently when cracks nucleated in the severely bent sprinkled crystals (by a mechanism not yet understood) they propagated *parallel* with the length of the crystal. Figure 12 is a photomacrograph of the tension surface of a specimen which bent to the point where anticlastic kinking could in fact just be detected in certain regions along the edge of the specimen (fig. 13). It will be noticed that the edges of this specimen have for the most part shattered instead of kinking and that longitudinal cracks have formed towards the centre of the specimen.

Fig. 11

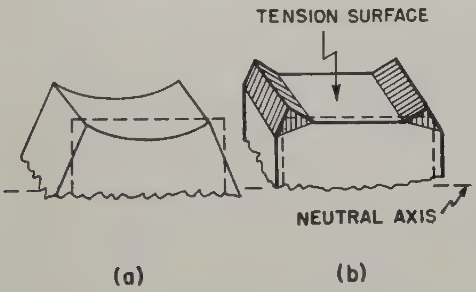

(*a*) Anticlastic curvature in an elastic solid.
(*b*) Anticlastic kinking in a plastic crystalline solid.

More typically longitudinal cracks developed before any anticlastic kinking occurred whatsoever. Figure 14 shows a longitudinal crack at a high magnification. The crack surface was very complex; it contained many forked offshoot cracks which themselves were likewise branched many-fold. Focusing into the crystal beneath the tension surface it was found that the offshoot cracks visible on the surface did not penetrate very deep but were replaced by other branched offshoots from the main crack surface. The longitudinal crack surface was neither flat nor characterized by any readily identifiable crystallographic planes, although the branched offshoot fingers tended to point in either [100] or [110] directions. Attempts were made to observe the formation of a longitudinal crack directly, by loading sprinkled crystals in a bending jig adapted for the specimen stage of the metallograph. It proved impossible, however, to detect them at any stage of development before fracture and it was presumed that they formed more or less instantaneously. Slip traces parallel to the tension direction were detected in some cases, indicative of the existence of the transverse stress component. Examples may be seen in the region of the crack in fig. 14.

It will be noted that there was a step at the point where the longitudinal crack of fig. 14 intersected the specimen fracture surface. Examination of the fracture surface, fig. 15, confirmed that the step did in fact correspond with the origin of fracture. In other words these observations taken together indicated that the longitudinal crack was formed first in the crystal parallel to the tension direction, that it generated offshoot cracks which lay in some cases perpendicular to the tension direction and that one of these offshoot cracks was eventually able to propagate through the crystal for fracture. The appearance of the fracture surface which was very rough, and the high number of offshoot cracks which did not propagate for fracture, strongly suggest that crack propagation through the densely slipped material was a very difficult process.

§ 6. BEHAVIOUR UNDER IMPACT

It was of interest to determine whether densification of slip would produce a similar enhancement of mechanical properties in a test conducted at a higher strain rate, especially in view of the strong strain rate sensitivity of ionic solids. Consequently, a comparison was made between the energy absorbed in impact by chemically polished crystals and crystals which had been sprinkled, pre-strained a slight amount, and repolished. It was necessary to preload the crystals at four different points along the beam to ensure that the whole volume to be loaded under impact was prestrained uniformly. In fact, fig. 10 was taken on a specimen prestrained for use in the impact study. The table includes a comparison of the energy absorbed for these two states. It can be seen that dense slip generally increased the energy absorbed in fracture under impact. Indeed, one of the specimens tested actually bent further without fracture and was, therefore, able to absorb all of the impact energy (10 in. lb) without fracture. This was very surprising for it has been shown that polished specimens normally have to be heated to 1900°C to bend under impact (Johnston *et al.* 1959).

Effect of dense slip on energy absorbed in impact

Energy absorbed (in. lb)	
As polished	Polished–sprinkled Preloaded–repolished
	0·31
0·42	0·78
0·60	0·81
0·61	3·88
	5·26
	~10·0 bent without fracture

§ 7. THE USE OF STRESS BIREFRINGENCE TO DETERMINE SLIP DISTRIBUTION IN MAGNESIUM OXIDE

At this point it is appropriate to comment upon the interpretation of stress birefringence patterns with respect to the distribution of slip in magnesium oxide. It was found that stress birefringence was produced only by the stress concentration at the *edge* of a slip band. Thus, in crystals of category III (§ 3) where slip was confined to a single wide band, the birefringence pattern delineated the two edges of the band only, within the band extinction was practically complete. Similarly, in fig. 9 (*a*) stress birefringence was most pronounced at the block boundary where narrow slip bands intersected one another and along the isolated bands (indicated by arrows) which penetrated across the block boundary. In the region on the left-hand side of fig. 9 (*a*) where slip was most dense but confined to a single plane there was no stress birefringence pattern. When the slip was dense and on intersecting planes, as in fig. 10, then the stress birefringence pattern gave a reasonable indication of the slip distribution.

Thus the generally accepted correlation between the birefringent pattern and the lines of dislocation etch pits established by Kear and Pratt (1958) for lithium fluoride and by Shaskol'skaya and Tui-fang (1960) for sodium chloride did not apply for magnesium oxide unless the slip bands were sufficiently narrow. Indeed in certain instances, fig. 9 (*a*) for example, stress birefringence gave almost the inverse pattern to that expected, being strongest in the regions which had deformed the least. It is probable that the reason for the lack of stress birefringence within a slip band is due to the cancellation of the stresses of the positive and negative edge dislocations retained there.

§ 8. DISCUSSION

While the location and orientation of slits described in §§ 3, 4 and 5.1 of the present work are consistent with results of the previous paper (Stokes *et al.* 1959 a), there are certain additional observations which cannot be accounted for in detail by the fracture mechanism as proposed there and outlined in §1. It will be remembered that there are two stages in slit formation, first the nucleation and second the growth and stabilization stage. With regard to stabilization, it is considered that the original interpretation is correct. The new evidence supports the original contention that a crack is held up by a slip band, probably because of the sudden increase in surface energy when it encounters the high density of screw dislocations retained in the band. The details of the nucleation mechanism, however, are not so clear and the following additional observations must be accounted for by the model.

There are frequent occasions where a slip band bursts across the crystal to be held up by an intersecting band within the gauge length. An example is indicated by the arrow in fig. 5 (*d*). Even though this event is equivalent to a sudden avalanche of edge dislocations piling into an obstacle a crack does not form. Instead the slip band eventually breaks through the intersection, fig. 5 (*e*), and crosses the crystal. Indeed cracks are only to be found at intersections where two slip bands have *completely cut through* one another, and are generally associated with slip bands formed in the very early stages of plastic flow (fig. 5). The reason why only these slip band intersections nucleate a crack remains a topic for more detailed investigation.

The situation of the slit in fig. 4 warrants further discussion. It may be interpreted with the aid of fig. 16. Consider two independent slip bands as in fig. 16 (*a*), growing in width to meet and intersect one another. From the sign and direction of motion of the edge dislocations it can be deduced that a crack can nucleate at A (fig. 16 (*c*)) by the piling up of dislocations moving in band Y against the barrier provided by band X. It will be noted that this line of intersection does not exist (fig. 16 (*b*)) until the edge of band Y has cut completely through X. Once the crack has nucleated it can propagate along the edge of (in the [110] direction) and across (in the [100] direction) slip band X, but at the same time slip band Y continues to grow in width until it is finally cut off by the fracture path. This leaves the distribution of slip shown in fig. 16 (*d*) which corresponds with the distribution of etch pits shown in fig. 4. This mechanism explains why the line source of fracture is so close to the edge for crystals in this category (fig. 3). However, there is a weakness in the interpretation in the necessary

Fig. 16

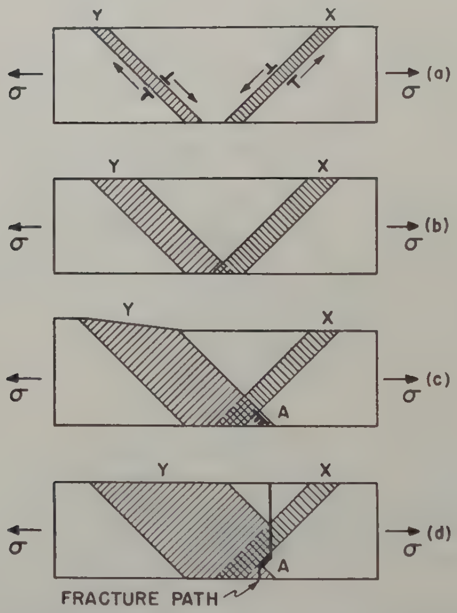

The formation of a crack at the intersection of two expanding slip bands to give the distribution of slip shown in fig. 4.

assumption that dislocations moving at the edge of slip band Y pile up against slip band X. These dislocations move only a short distance to the intersection at A, and slip band X, the barrier, is the narrower slip band of the two.

The complete suppression of slit formation in bent crystals for which intersecting slip has been densified (§ 5.2) may be influenced by two factors. First, it is possible that the change in behaviour is a consequence of the stabilization mechanism. If the spacing between slip bands is reduced below microscopic dimensions by sprinkling, then the slits, even though they may form, will not be visible and, being so small, will not exceed the critical size for catastrophic propagation across the crystal under the applied tensile stress. As fig. 14 and the behaviour under impact (§ 6) indicate, the propagation of a crack through a uniformly strained crystal is a difficult process.

Second, it is possible that the crack nucleation process is upset when intersecting slip occurs on a very fine scale. Dislocation sources introduced by sprinkling are able to expand and multiply to form short slip line segments *uniformly* throughout the crystal at quite low stresses compared to the macroscopic yield point (Stokes *et al.* 1959 *b*). As plastic deformation proceeds the slip bands develop gradually until slip more or less saturates the crystal. For polished crystals, on the other hand, the number of intrinsic sources is limited and most of the plastic strain at any instant is confined to the *edge* of a few isolated slip bands. The stress concentration in this region is more conducive to the dislocation avalanche which may be involved in crack nucleation. The effect of sprinkling then is to change the manner in which slip bands develop in the crystal. We may regard the high number of slip sources as effectively homogenizing the strain and, therefore, the stress through the crystal.

The observations of this paper indicate an additional factor which should be considered in discussion of the apparent difference in ductility between crystals strained in bending and in tension. It is frequently possible with a polished (unsprinkled) crystal to obtain as much as 10% surface strain under bending while an equivalent strain has never been produced in tension. This difference might be connected with the distribution of slip in the two instances. Under tension there is a large volume of material under stress and the chances of a crack forming at an intersection before sufficient stabilizing slip has been introduced are greater than under three point bending where the highest stress is confined to the surface of a narrow region at the centre of the crystal. It is then possible for slip from many sources on orthogonal systems to develop, so that when cracks form they are immediately stabilized and the crystal continues to bend.

An important aspect of the dislocation theory of fracture is concerned with understanding how much plastic deformation precedes brittle cleavage fracture and whether it is the nucleation or the propagation of fracture which is the critical stage. On the basis of these observations on magnesium oxide it is obvious that the amount of plastic deformation preceding cleavage fracture depends primarily upon the density and distribution of slip sources at the onset of plastic flow. It depends also upon the chance that a particular slip band intersection will nucleate a crack, which, until more is understood of the nucleation mechanism, should be regarded as statistical in nature. Whether crack nucleation or propagation is the more critical stage depends again upon the density of slip sources and when the crack forms. If it nucleates before other slip is present to stabilize it then obviously nucleation is the critical stage. Whereas if a crack is formed and stabilized then it is the propagation through the surrounding slip bands which is the critical stage of fracture.

ACKNOWLEDGMENTS

The authors wish to acknowledge the assistance of Mr. K. H. Olsen and Mr. D. J. Sauve in performing the experiments described in this paper. They are also grateful to Dr. J. J. Harwood of the O.N.R. and Dr. F. J. Larsen, Director of Research, for their interest and permission to publish. This work was supported in part by the Office of Naval Research.

REFERENCES

CLARKE, F. J. P., and SAMBELL, R. A. J., 1960, *Phil. Mag.*, **5,** 697.
GILMAN, J. J., 1959, *J. appl. Phys.*, **30,** 1584.
GORUM, A. E., LUHMANN, W., and PASK, J. A., 1960, *J. Amer. ceram. Soc.*, **43,** 241.
JOHNSTON, T. L., STOKES, R. J., and LI, C. H., 1959, *Phil. Mag.*, **4,** 1361.
KEAR, B. H., and PRATT, P. L., 1958, *Acta Met.*, **6,** 457.
KRONBERG, M. L., and MAY, J. E., 1960, *J. Amer. ceram. Soc.*, **43,** 525.
LI, C. H., EDWARDS, E. H., WASHBURN, J., and PARKER, E. R., 1953, *Acta Met.*, **1,** 223.
SHASKOL'SKAYA, M. P., and SUN TUI-FANG, 1960, *Soviet Physics-Crystallography*, **4,** 74.
STOKES, R. J., JOHNSTON, T. L., and LI, C. H., 1959 a, *Phil. Mag.*, **4,** 920; 1959 b, *Trans. Amer. Inst. min. (metall.) Engrs*, **215,** 437; 1960, *Ibid.*, **218,** 655.
TAYLOR, A., and PRATT, P. L., 1958, *Phil. Mag.*, **3,** 1051.
THOMPSON, D. S., and ROBERTS, J. P., 1960, *J. appl. Phys.*, **31,** 433.
TIMOSHENKO, S., 1934, *Theory of Elasticity* (McGraw-Hill), p. 221.
WEBB, W. W., 1960, *J. appl. Phys.*, **31,** 194.

Grain Boundary Luminescence in an Alkali Halide Phosphor†

By R. Illingworth
Department of Electron Physics, The University of Birmingham,
Edgbaston, Birmingham

[Received July 13, 1960]

Segregation of impurities to grain boundaries has been described for a number of crystalline solids of different structures (Amelinckx and Dekyser 1959). Etching, autoradiography, ' decoration ' and electron microscopy are examples of methods used in the investigation of such segregations. In a phosphor, if segregation of an activating impurity occurs, it should be visible under the microscope, the impurity acting, in effect, as an optical tracer. Segregation of silver ions to dislocation walls in a strained silver-activated rocksalt crystal has been demonstrated in this way (Van der Vorst and Dekyser 1956), luminescence photographs showing diffuse lines corresponding to the dislocations. This note describes segregation of impurity to grain boundaries of tin-activated potassium bromide during growth from the melt.

The impurity absorption band for this phosphor has its maximum intensity at 2650 Å with the corresponding emission band lying completely in the visible region. Polycrystalline specimens were grown from a melt of potassium bromide doped with 1% by weight of stannous bromide and held in a quartz beaker. A conventional tube furnace was used, growth being in air at atmospheric pressure. A brass rod, held in a water-cooled brass chuck, was lowered into the melt which was at a temperature only just above its freezing point. The furnace temperature was then allowed to drop to below the melting point. As the furnace cooled, the surface of the melt cooling faster than the bulk of the melt, growth suddenly proceeded outwards from the brass rod along the melt surface. This ' skin ' was lifted off just before it reached the sides of the beaker, total growth times being less than one minute. Grain dimensions were about 0·5 mm in width with thicknesses from 0·5 mm up to 2 mm, each grain extending through the whole thickness of the polycrystalline sheet. Quite regular hexagonal networks were often formed, the grains usually having a (100) direction close to the horizontal plane.

Figure 1‡ is a luminescence photograph of a fragment of polycrystalline sheet grown as described above and immediately cooled to room temperature. Unfiltered radiation from a mercury low-pressure discharge tube stimulates visible emission. Figure 2 is shown for comparison purposes, the ultra-violet radiations of the lamp being removed by placing a glass plate between lamp and specimen. Figure 2 shows no sign of the slightly diffuse luminescent network of fig. 1. Exposure times were 5 min using H.P.S. roll film, exposure and development times being the same for the two photographs. Figure 3 shows the surface structure revealed by transmitted light, the grain boundaries forming two similar networks where they meet the two surfaces of the specimen. Because of the small magnification and large depth of focus, both surfaces are well defined in fig. 3. Comparison of fig. 1 with fig. 3 shows that the luminescent network corresponds to where grain boundaries cut the top surface of the specimen as it was when removed from the furnace. The good contrast of fig. 1 indicates that the light emitted from near grain boundaries cannot be due to preferential scattering of light emitted from the bulk of the grains, but is, in fact, due to a non-uniform distribution of activating impurity. Annealing at temperature greater than 300°c followed either by quenching or slow cooling to room temperature caused the luminescent network to disperse.

---

† Communicated by Professor J. Sayers.

‡ Figures 1, 2 and 3 are shown as a plate.

These specimens were prepared while work was being carried out on the growth of single crystals of tin-activated potassium bromide from the melt. In the latter case the segregation coefficient of tin in potassium bromide was found to be too small for it to be possible to grow mixed crystals containing any significant quantities of tin. It is, therefore, probable that as a polycrystalline sheet grew quickly over the melt surface, impurities rejected by the advancing growth surface formed a concentration gradient into the melt at the solid–liquid interface. Right at the surface of the melt where the degree of super-cooling was greatest, impurities at the growth surface, while not accepted by the bulk crystal, could enter the solid phase at disordered regions near the boundaries. Conditions for the occurrence of the segregation described in this note were found to be very critical, only a few of the examined specimens showing luminescence associated with the boundaries. Closer control of the growth conditions will be necessary before the precise mechanisms of solidification and luminescence can be understood and reproducible specimens prepared for study.

REFERENCES

AMELINCKX, S., and DEKYSER, W., 1959, *Solid State Physics*, **8,** 325.
VAN DER VORST, W., and DEKYSER, W., 1956, *Phil. Mag.*, **1,** 882.

Effective Ionic Charge in Relation to Lattice Vibrations†

By J. R. Hardy
J. J. Thomson Physical Laboratory, Whiteknights Park, University of Reading

[Received July 8, 1960]

Abstract

A discussion is given of the assumptions involved in recent theories of the dielectric constants of the alkali halide crystals with particular reference to the contributions arising from short-range polarization effects. A theory is developed on a semi-empirical basis which makes it possible to divide this effect unambiguously between the positive and negative ions. This theory is consistent with the experimental data and should provide a means of including this effect in calculations on the lattice dynamics of these crystals.

§ 1. Introduction

In two papers on the dielectric properties of ionic crystals Szigeti (1949, 1950) deduced, from a study of long-wave optical vibrations in these crystals, the following pair of equations:

$$M\omega_0^2(\epsilon_0+2)/(\epsilon_\infty+2)=6R_0/K, \quad . \quad . \quad . \quad . \quad (1)$$

$$\epsilon_0-\epsilon_\infty=(\epsilon_\infty+2)^2 4\pi Ne^2/9\bar{M}\omega_0^2. \quad . \quad . \quad . \quad . \quad . \quad (2)$$

These relate the empirical static and optical frequency dielectric constants, ϵ_0 and ϵ_∞ respectively, to the corresponding compressibilities and restrahlen frequencies K and ω_0. The other parameters are R_0 the equilibrium nearest-neighbour separation, $\bar{M}$ the reduced ionic mass and e the effective ionic charge.

The derivation of (1) and (2) (Born and Huang 1954, denoted by A hereafter) leads one to expect that $|e|=1$ electronic charge. In the table (after Szigeti) the values of K and $|e|$ (K^* and e^*) calculated from eqns. (1) and (2) are compared with the actual values. It is at once clear that the first relation is obeyed rather better than the second, particularly by the lighter salts. Furthermore there appears to be little correlation between violations of the two relations. This suggests very strongly that at least two distinct effects are present and that any theory should allow for this fact. However, the data used in calculating the results in the table are all room-temperature data, while the various theories of these effects are strictly only true for crystals at absolute zero. It is thus a matter of some importance for measurements of the relevant data to be made at low temperatures. This applies particularly to the restrahlen frequencies ω_0 and the static dielectric constants ϵ. (There are two sets of the latter available (A, p. 85, Haussühl 1957), both measured at room temperature but which differ by as much as 10%.) Thus the data do not make it possible to test any theory very rigorously. What is certain however is that the theory which led to eqns. (1) and (2) must be modified in some way. Such a modification will affect not only the long-wavelength lattice vibrations, but the whole spectrum, and the problem which faces us is that of attempting to predict this effect. We want to do this, if possible, in such a way that the results are not too strongly dependent on the detailed mechanisms responsible for the failure of the Szigeti relations. In this way we may hope that the results of the analysis will remain valid as more exact theories are developed.

---

† Communicated by the Author.

Salt	K^*/K	$\lvert e^*/e \rvert$
LiF	1·0	0·87
NaF	0·83	0·93
NaCl	0·99	0·74
NaBr	1·13	0·69
NaI	1·05	0·71
KCl	0·96	0·80
KBr	0·95	0·76
KI	0·99	0·69
RbCl	0·89	0·84
RbBr	0·83	0·82
RbI	0·66	0·89

§ 2. Basic Assumptions

The analysis (A, p. 100) which leads to the two Szigeti relations is based on the following assumptions:

In the case of the first relation:

(*a*) That the effective field acting on an ion in a uniformly polarized crystal of polarization P and in a field E is

$$E+\tfrac{4}{3}\pi P.$$

(This only applies to crystals with cubic or tetrahedral symmetry.)

(*b*) That the repulsive interactions due to ionic overlap act only between nearest neighbours and depend only on the absolute magnitude of their separation.

(*c*) That there are no non-central interactions.

The second relation requires only (*a*) to be valid, but involves one further assumption:

(*d*) That the dipole moment at an ion site when the ion in question is displaced by a small distance ξ is $\pm e\xi$ (apart from the electronic polarization). The failure of the second relation implies that either (*a*) or (*d*) is invalid. Tessman *et al.* (1953) have carried out an analysis of the optical frequency refractive indices of these crystals and have shown that it is possible to derive a set of polarizabilities for all the ions such that the value for a given ion does not depend on its environment. This work was also based on assumption (*a*), and they found, when they tested this by varying the Lorentz factor $4\pi/3$, that any other value produced a less consistent set of results. It thus seems fairly certain that assumption (*d*) is false. It is therefore necessary to explain this breakdown, if possible, in a way which does not imply any violation of (*b*) or (*c*). Szigeti (1950) himself suggested that the mechanism in question is a distortion of the ions associated with the overlap repulsion. Born and Huang (A, p. 112) have extended this idea and shown that if each nearest-neighbour bond has associated with it a dipole moment depending only on the absolute separation of the two ions then the effective charge

$$e^* = |e| + 2m'(R_0) + 4m(R_0)/R_0 \quad . \quad . \quad . \quad . \quad . \quad . \quad . \quad (3)$$

where $m(r)$ is the 'deformation' dipole associated with each nearest-neighbour bond of length r, $m'(r) = [dm(r)/dr]_r$ and R_0 is the equilibrium separation of the ions. This derivation is quite general and independent of the details of the mechanism involved. Furthermore, it does not automatically imply the failure of any of the other assumptions.

However, before one can set up a complete phenomenological theory, based on the empirical data, one needs to know both $m(r)$ and $m'(r)$ separately and where the dipoles should be located within the unit cell. The theory leading to relations (1) and (2) gives us neither piece of information; it only determines e^* and, for the homogeneous polarizations involved, the exact location of the dipoles is unimportant. It is thus necessary to have a more specific understanding of the effect.

§ 3. THEORY OF THE DIELECTRIC CONSTANTS

There have recently been two treatments of this problem (Dick and Overhauser 1958, denoted by B hereafter, and Hanlon and Lawson 1959) which have proposed detailed models with 'short-range' polarization mechanisms incorporated into them. Of these the first treatment is the more complete and will be our main concern here, and this paper follows their notation. However, both treatments are open to the same objection; they both employ a 'shell' model in which the ions are regarded as massive cores isotropically coupled to rigid massless shells consisting of the valence electrons. Ionic polarization then appears as a relative movement of core and shell and, in antiphase motion, the positive and negative ions, by virtue of the overlap repulsion between shells, induce dipoles on each other which do not in general cancel and are the main cause (in the Hanlon–Lawson theory the only cause) of the deformation dipole moment. This feature implies that assumption (*b*) of the Szigeti theory is invalid since the repulsive potential between two ions depends not only on the internuclear distance but also on the relative core-shell displacements. This leads one to expect not only the failure of the first Szigeti relation, but also that K^*/K will always be *greater* than unity by an amount which should depend almost linearly on the sum of the positive and negative ion polarizabilities. Both these results are obviously not true of the data in the table. It is rather surprising that K^*/K is generally <1 since one would expect short-range interactions due to overlap between other than nearest neighbours, which are the most obvious cause of deviations from unity, to be repulsive, in which case K^*/K would be >1. The fact that this is not so seems to imply that the Van der Waals attraction between nearest like neighbours is the more important term.

The theory of Dick and Overhauser does, however, include another short range polarization mechanism; the 'exchange charge' polarization. This effect arises naturally when the charge density in the crystal is derived using a Slater determinant of free ion orbitals. These are non-orthogonal in the crystal and this fact is responsible for an additional term in the charge density; an 'exchange' term:

$$=2|e|\sum_{ij} S_{ij} U_i(\mathbf{r}) U_j(\mathbf{r})$$

where U_i and U_j denote orbitals centred on nearest neighbour ions and

$$S_{ij}=\int U_i(\mathbf{r}) U_j(\mathbf{r}) dr.$$

The total localized charge q_{ex} is exactly compensated by a spherically symmetric increase in the free ion charge densities whose total magnitude is $-q_{ex}/2$ for each ion. In a uniformly polarized crystal there is a redistribution of exchange charge which gives rise to a net dipole moment. Furthermore, in the unpolarized crystal, this charge distribution has cubic, rather than spherical, symmetry about each ion. Dick and Overhauser have estimated the contribution of the exchange charge polarization to the value of $|e^*/e|$. A lower limit to $|e^*/e|$ is given by assuming this charge to lie at the centre of the positive ion, but, even when this is done, most of the calculated values are still about 10% too large and about half the calculated deviation from unity is due to the relative motion of cores and shells. If this last effect is ignored, in view of the way in which the observed data satisfy the first Szigeti relation, then $(1-|e^*/e|)$ is probably $<10\%$ for most of the alkali halides. (An earlier, but possibly more exact, calculation by Lundqvist (1955) gave $(1-|e^*/e|)=8\%$ for NaCl.)

§ 4. CONTRIBUTION OF IONIC DEFORMATION TO THE EFFECTIVE CHARGE

There is one possibility which is not included in the Dick and Overhauser treatment; this is a redistribution of charge *within* an ion owing to a marked difference between the outermost parts of free ion and crystal wave functions.

There are two pieces of evidence for this view:

(*a*) The fairly large differences between the polarizabilities of free ions, as calculated by Pauling (1927) and the T.K.S. crystal polarizabilities. Dick and Overhauser have attempted to account for these in terms of the exchange charge, but the predicted values are too small by about a factor of five.

(*b*) The contour maps of electron density as measured by Witte and Wolfel (1955) for LiF and NaCl. These show a pronounced cubic symmetry, but a theoretical calculation by Howland (1957) for KCl using free ion functions fails to reproduce the distinct 'bulges' of electron density along the $\langle 110 \rangle$ directions which occur in the experimental data for NaCl. He explains these as dynamical effects arising from ionic thermal motion along preferred directions. However, in LiF the 'bulges' lie along $\langle 100 \rangle$ directions and it seems more likely that they result from a genuine distortion of the ions, which is not represented by this theory, owing to the change in the outer parts of the wave functions.

These facts provide support for the deformation hypothesis. If this hypothesis is true it would seem that most of the deviation of $|e^*/e|$ from unity is due to this effect, which does not imply any violation of the first Szigeti relation.

§ 5. IONIC DEFORMATION AND LATTICE VIBRATIONS

In the theory of lattice vibrations one has to be able to deal with lattice distortions which change markedly over a few interionic distances. This was first done for an ionic lattice by Kellermann (1940) for NaCl. He deduced a lattice vibration frequency spectrum allowing for the long-range Coulomb interactions, but regarding the ions as rigid point charges. This work has recently been repeated and extended to other alkali halides by Karo (1959, 1960) and the agreement with experimental heat capacity data (e.g. Berg and Morrison 1957) is very good. However, in another recent paper (Hardy 1959) it was shown that the effect of ionic polarization, when it is included in the NaCl theory, is to destroy this agreement. If deformation dipole effects are included, the agreement can be restored even though the resulting frequency spectrum is very different from that predicted by the simple theory.

In this particular case the entire deformation dipole effect was assumed to be localized on the Cl^- ion owing to its large 'size' relative to that of the Na^+ ion. However, in order to construct a general theory, applicable whenever the first Szigeti relation holds, it is necessary to split up the deformation dipole moment $m(r)$ associated with each nearest-neighbour bond into two parts: $m_+(r)$ at the centre of the positive ion and $m_-(r)$ at the centre of the negative ion, each moment directed *outwards* from the centre of the ion in question. This division is implicit in the Dick–Overhauser theory, which has been used by Cochran (1959) to calculate frequency-wave number dispersion curves for lattice waves propagating along $\langle 100 \rangle$ directions. The results are in good agreement with those obtained during the previous work (Hardy and Karo 1960) but this might not be so if the positive ion were larger.

In § 3 we referred to the exchange charge q_{ex} defined by Dick and Overhauser. To estimate the strength of the dipole associated with each nearest-neighbour bond they assumed that the total exchange charge between each ion pair is concentrated at the point of tangency of spheres centred on each ion, and having the appropriate crystal radii r_+ and r_- defined by Zachariasen (see Kittel 1953, p. 40). Thus

$$m_\pm = \frac{q_{ex} r_\pm}{2} = |e| \sum_{ij} S_{ij}{}^2 r_\pm . \qquad (4)$$

One would certainly expect the maximum exchange charge density to lie in this region and to be fairly strongly localized there.

In the absence of a set of true crystal wave functions it would seem reasonable to assume that the change in charge density, due to ionic distortion, is *proportional* to that predicted from the overlap of the free ion functions. However, in B it is shown that:

$$\sum_{ij} S_{ij}{}^2 \propto \lambda R_0 \exp(-R_0/\rho)$$

where $R_0 = r_+ + r_-$ is the equilibrium nearest-neighbour distance and ρ and λ are the constants in the overlap repulsion.

Thus we may write, quite generally, that

$$m_\pm = d_\pm r_\pm R_0 \lambda \exp(-R_0/\rho) \qquad (5)$$

where $d_\pm$ are disposable parameters. Hence, from eqns. (3) and (5)

$$1 - |e^*/e| = 2R_0\lambda\left[\frac{1}{\rho} - \frac{2}{R_0}\right][d_- r_- - d_+ r_+]\exp(-R_0/\rho)$$

or

$$1 - |e^*/e| = 2\lambda d_-\left[r_-{}^2 - r_+{}^2 - \frac{(d_+ - d_-)}{d_-} r_+ R_0\right]\left[\frac{1}{\rho} - \frac{2}{R_0}\right]\exp(-R_0/\rho). \qquad (6)$$

If our initial assumption regarding the proportionality of the total displaced charge and the exchange charge is correct, then in a given compound $d_+ = d_-$. Let us now make the further assumption that $d = d_-$ is the same for all these salts, then from eqn. (6) we have

$$1 - |e^*/e| \propto \lambda (r_-{}^2 - r_+{}^2)\left(\frac{1}{\rho} - \frac{2}{R_0}\right)\exp(-R_0/\rho).$$

In the figure the resulting points are those without*. The K^+ and Rb^+ halides (except RbI) lie on a straight line through the origin of slope $d_+ = d_- = 23{\cdot}5 \times 10^{18}$ (erg cm)$^{-1}$. Thus the two initial assumptions provide us with a self-consistent theory of these salts. There remain the problems presented by LiF, RbI and the Na salts. The first presents no real difficulty since we assumed, following B, that $\sum_{ij} S_{ij}{}^2$ is proportional to the overlap repulsion, but we should reduce the constant of proportionality in the ratio 3 : 1 for LiF to remain consistent with B. When we do this the resultant point, LiF** lies close to the K^+Rb^+ line. RbI seems to be anomalous and probably cannot be treated on the same basis as the rest of these salts†. Thus, the sodium salts present the only real problem. NaF, NaCl and NaBr lie on a straight line, but it no longer runs through

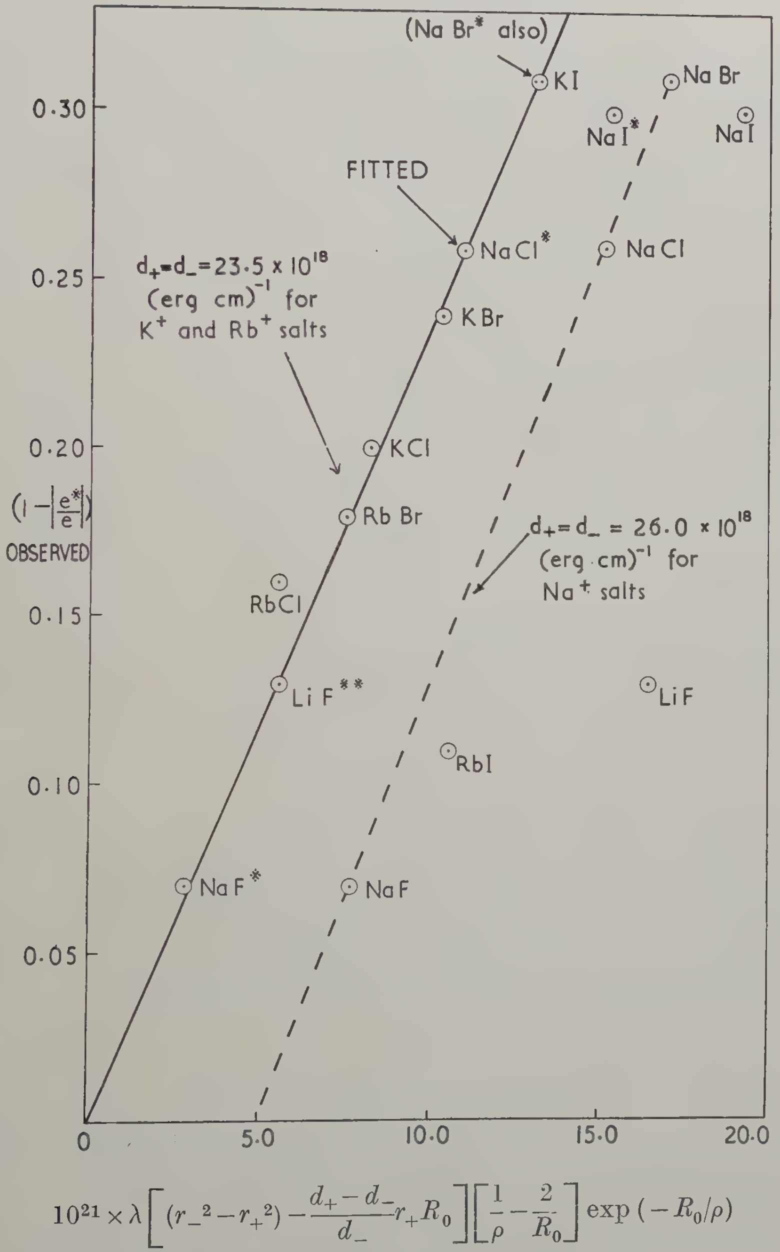

---

† Recently Havinga (1960, *Phys. Rev.*, **119**, 1193) has pointed out errors in Szigeti's (1950) values of $(1-|e^*/e|)$ for LiF and RbI. The new values are 0·17 and 0·21 respectively. If one uses these the LiF data agree less well with the present theory, but most of the large RbI anomaly disappears.

the origin. If we now assume that the effective centre of the displaced charge lies at a distance $r_+ + \delta r$ from the positive ion, then we have

$$m_\pm(r) = d(r_\pm \pm \delta r)R_0\lambda \exp(-R_0/\rho),$$

d here is assumed to have the same value as for the K^+ and Rb^+ salts. Then

$$\left(1-|e^*/e|\right) = 2d\lambda\left[\frac{1}{\rho}-\frac{2}{R_0}\right][r_-^2 - r_+^2 - 2R_0\delta r]\exp(-R_0/\rho),$$

which is exactly equivalent to eqn. (6) if

$$d = d_- \quad \text{and} \quad \frac{d_+ - d_-}{d_-} = \frac{2\delta r}{r_+}, \quad \text{i.e.} \quad d_+ = d_-\left(1+2\frac{\delta r}{r_+}\right).$$

If we assume that δr is the same for all the Na^+ salts, and then choose $\delta r/r_+ = 0{\cdot}114$ to fit the resulting point NaCl* to the K^+, Rb^+ line in accordance with the initial assumption that $d = d_- = 23{\cdot}5 \times 10^{18}$ (erg cm)$^{-1}$. The NaF and NaBr points then lie very close to this line. NaI is still anomalous; but to accord with this theory $(1-|e^*/e|)$ would have to be $\sim 0{\cdot}35$ for this salt, and as the theory probably breaks down when $(1-|e^*/e|)$ becomes large, the discrepancy seems to indicate that NaI is a case in this region. Values for the heavier Li^+ halides would be of interest in order to test this hypothesis.

We have now found a self-consistent phenomenological theory of effective charge in the alkali halides which involves only two disposable parameters ($d_- = d$, and δr) and describes at least nine of these salts well. This fact would seem to support the basic assumptions fairly strongly.

The next stage of this work is to incorporate the values of $d_\pm$ which we have deduced into calculations on the lattice dynamics of those alkali halides which have large positive ions. The important result of this work is that we have now obtained a means of dividing the 'deformation' polarization unambiguously between the two types of ion, and one may hope, as more exact inelastic neutron scattering data become available, to test the theory by comparing the predicted and observed phonon dispersion curves, particularly in the short wave-length region.

ACKNOWLEDGMENTS

I should like to express my thanks to Dr. A. B. Lidiard for helpful discussion and to A. E. I. for the Research Fellowship during the tenure of which this work was carried out.

REFERENCES

BERG, W. T., and MORRISON, J. A., 1957, *Proc. roy. Soc.* A, **242,** 478.
BORN, M., and HUANG, K., 1954, *Dynamical Theory of Crystal Lattices* (Oxford: Clarendon Press).
COCHRAN, W., 1959, *Phil. Mag.*, **4,** 1082.

Dick, B. J., and Overhauser, A. W., 1958, *Phys. Rev.*, **112,** 90.
Hanlon, J. E., and Lawson, A. W., 1959, *Phys. Rev.*, **113,** 472.
Hardy, J. R., 1959, *Phil. Mag.*, **4,** 1278.
Hardy, J. R., and Karo, A. M., 1960, *Phil. Mag.*, **5,** 859.
Haussühl, S., 1957, *Z. Naturf.* A, **12,** 445.
Howland, L. P., 1957, *Quart. Rep., M.I.T.*, Solid State Gp., **25,** 15.
Karo, A. M., 1959, *J. chem. Phys.*, **31,** 1489; 1960, *Ibid.* (in the press).
Kellermann, E. W., 1940, *Phil. Trans.* A, **238,** 513.
Kittel, C., 1953, *Introduction to Solid State Physics*, 1st edition (New York : Wiley).
Lundqvist, S. O., 1955, *Ark. Fys.*, **9,** 425.
Pauling, L., 1927, *Proc. roy. Soc.* A, **114,** 181.
Szigeti, B., 1949, *Trans. Faraday Soc.*, **45,** 155; 1950, *Proc. roy. Soc.* A, **204,** 51.
Tessman, Kahn, and Shockley, 1953, *Phys. Rev.*, **92,** 890.
Witte, H., and Wölfel, E., 1955, *Z. Phys. Chimie*, **3,** 296.

The Relation Between the Plastic Deformation of Aluminium Single Crystals and Polycrystals†

By S. Howe and C. Elbaum
Physics Department, Metals Research Laboratory, Brown University, Providence, Rhode Island

[Received July 16, 1960]

Abstract

Single crystals of ⟨100⟩, ⟨111⟩ and ⟨110⟩ axial orientation, and polycrystals, both of 99·99% pure aluminium, were deformed in tension at temperatures of 27°c, 200°c, 400°c and 600°c. The experiments on single crystals reveal that as the temperature is increased, the shear stress–shear strain curves for the three orientations become more and more similar until at 600°c they are identical. On the other hand, the surface appearance of the crystals strained at 600°c indicates that the mode of deformation depends drastically on orientation.

Taylor's criterion for the comparison of the stress–strain curves of single and polycrystals was found to be valid at 27°c. As the temperature is raised, however, the criterion ceases to be applicable.

From the results of these experiments it is proposed that at the lower temperatures in both single crystals and polycrystals the principal hardening mechanism is the formation of Lomer–Cottrell barriers that act as obstacles against which glide dislocations can pile up. As the temperature is raised these barriers become ineffective as obstacles to slip, whereas grain boundaries in polycrystals continue to be effective in causing dislocation pile-ups.

§ 1. Introduction

1.1. *Relation Between the Deformation of Single and of Polycrystals*

Metals with the face-centred cubic structure deform plastically by slip on one or more of twelve geometrically equivalent slip systems. Each system consists of one of the three ⟨110⟩ directions in each of the four {111} planes.

In a single crystal the number of acting slip systems depends on the magnitude of the resolved shear stresses in the various slip systems. If the resolved shear stress is initially greatest in one slip system, slip will start in that system. If the resolved shear stresses are equal on more than one slip system then slip occurs on some or all of these slip systems. In all cases the shear stresses τ and shear strains γ are related to the uniaxial tensile stress σ and the tensile strain ϵ by the familiar expressions $\tau=\sigma/M$ and $\gamma=M\epsilon$ where M is the 'resolving' factor‡.

---

† Communicated by the Authors. This work was sponsored by the Office of Naval Research under Contract No. Nonr 562 (12).

‡ $M=1/\cos\lambda\cos\phi$, λ = angle between slip direction and tensile axis; ϕ = angle between normal to slip plane and tensile axis.

The situation in a polycrystal is somewhat different. A grain of a polycrystal is not free to deform by single slip, for it is subject to constraints imposed by the surrounding grains. In order to maintain continuity across the boundary, a grain must deform in a particular way. Since an arbitrary strain is described by the six independent components of the strain tensor, in the most general case six independent conditions are necessary to produce such a strain. If one assumes that the volume remains constant during deformation, then slip on five independent systems will satisfy the remaining five conditions necessary for the grains to undergo any arbitrary deformation. These considerations must be taken into account in deriving the factor M which relates the applied tensile stress and the resolved shear stresses in various slip systems of an inividual grain in the polycrystal.

Among many attempts to compute M for a polycrystal, the work of Taylor (1938) is most noteworthy. Taylor's method is based on the principle of virtual work, and can be summarized as follows.

Consider a set of n shears that satisfy the continuity conditions at the grain boundary. The energy expended in producing the n shears is $\sum_{s=1}^{n} \tau_S d\gamma_S$ where $d\gamma_S$ is an element of shear strain in the glide system s and τ_S is the shear stress to activate it. This energy must equal the work done by the external uniaxial tensile stress in producing an elongation $d\epsilon$. Thus

$$\sigma d\epsilon = \sum_{s=1}^{n} \tau_S d\gamma_S. \qquad (1)$$

In the restricted case where τ_S has the same value in every slip system,

$$\sigma d\epsilon = \tau \sum_{s=1}^{n} |d\gamma_S|. \qquad (2)$$

This may be rewritten as

$$\frac{\sigma}{\tau} = \frac{\sum_{s=1}^{n} |d\gamma_S|}{d\epsilon}. \qquad (3)$$

In analogy with the single crystal, M is defined by $M = \sigma/\tau$.

Taylor argued that M can be computed by finding the combination of slips which produces the imposed external strain and gives the minimum value of $\sum|d\gamma|$. All other combinations of slips which satisfy the conditions of continuity at the grain boundaries would require a higher value of σ than $(\tau/d\epsilon)$ times the minimum value of $\sum|d\gamma|$ to produce the required deformation.

If one assumes that at any stage of deformation the hardening value is the same throughout the polycrstal, the problem reduces to finding the numerical value of M. For this purpose Taylor assumed that the strain in each grain is the same as that of the whole specimen. He further postulated that exactly five slip systems will operate in each grain and that this set of systems will be the one out of 96 irreducible sets in a face-centred cubic crystal† which gives the lowest value of

$$M = \frac{\sum |d\gamma|}{d\epsilon}.$$

Taylor calculated these minimum values of M for 44 orientations of the tensile axis with respect to the crystal orientation. Averaging these values for a quasi-isotropic, face-centred cubic polycrystal in tension gave $M = 3{\cdot}06$‡.

Taylor first tried to compare the stress–strain behaviour of a polycrystal with a single crystal of 'average' orientation (whose axis was situated inside the stereographic triangle). Unfortunately such a comparison may not be meaningful, since a single crystal so oriented will deform predominately by slip on one slip system, whereas an average grain in a polycrystal will slip on more than one slip system. Kocks (1958) pointed out that one should compare a polycrystal with a polyslip orientation single crystal (one having five or more slip systems with equal resolved shear stresses), for such a single crystal is found to deform (by slip line examination) in a manner similar to that of a grain in a polycrystal. The $\langle 100 \rangle$ and $\langle 111 \rangle$ axial orientation single crystals satisfy this requirement. For reasons to be discussed later, the $\langle 111 \rangle$ orientation with six slip systems having equal resolved shear stresses is most suitable for this purpose. The comparison is carried out between the actual tensile stress–tensile strain curve obtained for a polycrystal and a fictitious tensile stress–tensile strain curve for a polycrystal, obtained from the stress–strain curve of the single crystal; this curve is derived by converting the true shear stress–shear strain curve of the single crystal into a tensile stress–tensile strain curve using the resolving factor $M = \sigma/\tau = 3{\cdot}06$.

§ 2. EXPERIMENTAL PROCEDURE

Single crystals for this investigation were grown from the melt by a modified Bridgman technique developed by Chalmers (1953), permitting one to obtain specimens of any desired orientation. The material used was aluminium 99·99% pure. Specimens of $\langle 111 \rangle$, $\langle 100 \rangle$ and $\langle 110 \rangle$ axial orientation, three millimetres in diameter and about ten inches long, were produced by the above method. They were subsequently cut into two-inch long pieces with an oxy-acetylene torch to prevent deformation; small spheres of aluminium were melted on the ends of the samples to provide a method of gripping the crystals in special slotted holders in the tensile machine. This method prevents slipping in the grips and premature deformation. The polycrystals studied were prepared from hard drawn aluminium wire (99·99% pure) three millimetres in diameter, by annealing for five minutes at 620°C. This treatment produced grains about 0·3–0·4 mm in diameter, corresponding to about 50 grains in the cross section. Subsequently these specimens were prepared in the same way as the single crystals. An X-ray examination of these polycrystals, using the Laue transmission method, showed complete recrystallization with no evidence of preferred orientation.

---

† In his original work Taylor took into account only 24 systems; for the correction see Taylor (1955).

‡ More recent work on this subject by Bishop and Hill (1951), who used more elaborate assumptions, gave the same result as Taylor's calculations, in the case of uniaxial stress.

After the single crystals were grown and cut into individual tensile specimens they were annealed for twenty-four hours at 625°C. All specimens were deformed in a 'hard' type (Instron) tensile machine. The various test temperatures above room temperature were achieved by means of a low-temperature gradient furnace mounted on the tensile machine. The temperature for any test was held constant to within ±1°.

The single and polycrystals were deformed at room temperature, 200°C, 400°C and 600°C at an elongation rate of $4 \times 10^{-5}\,\mathrm{sec}^{-1}$. In addition, single crystals of the $\langle 111 \rangle$ axial orinetation at 600°C, and polycrystals at all the above indicated temperatures were also extended at a rate of $4 \times 10^{-3}\,\mathrm{sec}^{-1}$. To determine the reproducibility of the curves, two single crystals of the same orientation were extended at each temperature; only several percent variation was noted between two such specimens. The stress–strain curves were obtained from continuous recordings of load versus elongation, which were replotted to show resolved shear stress–shear strain diagrams.

§ 3. Experimental Results

3.1. *Deformation of* $\langle 100 \rangle$, $\langle 110 \rangle$ *and* $\langle 111 \rangle$ *Single Crystals*

At room temperature (figs. 1, 2 and 3) all curves show a steeply rising initial portion of the shear stress–shear strain curve. In the $\langle 100 \rangle$ crystal this is followed by a sharp bend, the stress then rising only slightly. Kocks (1958) observed a similar phenomenon; in both investigations the bend occurred at about 900 g/mm². The slope of the curve for $\langle 111 \rangle$ crystals tested at room temperature gradually decreases after the steep rise to a much higher level of stress; the same is observed for $\langle 110 \rangle$ crystals, but the decrease of slope begins at a lower stress level.

At 200°C the $\langle 100 \rangle$ curve still bends over rather sharply and then becomes practically linear with a small slope. The $\langle 110 \rangle$ curve rises from the start with a gradually decreasing slope. The $\langle 111 \rangle$ curve becomes almost horizontal in contrast to the curve at room temperature.

At the higher temperatures the curves for the three orientations become horizontal after about 10% shear strain; at 600°C the levels of stress become almost identical for all three orientations. The rate of work hardening decreases markedly above room temperature in all three cases, becoming essentially zero at 400°C and above.

Surface examination of the three types of crystals strained at the higher temperatures reveals interesting features of the deformation pattern. At 400°C, the markings (figs. 4, 5 and 6, Pl. 9) on all three crystals are

Fig. 1

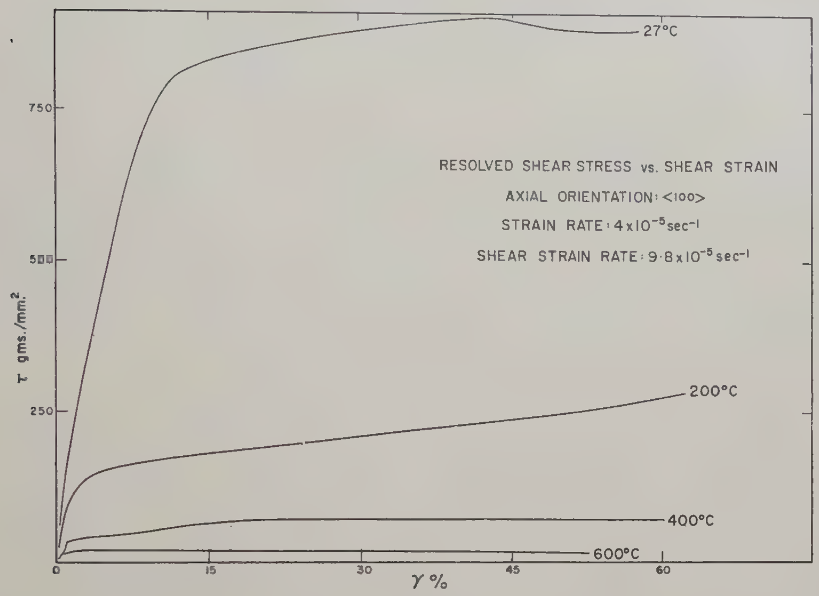
27°C
750
RESOLVED SHEAR STRESS vs. SHEAR STRAIN
AXIAL ORIENTATION: <100>
STRAIN RATE: 4x10⁻⁵sec⁻¹
SHEAR STRAIN RATE: 9·8x10⁻⁵sec⁻¹
500
τ gms./mm.²
250
200°C
400°C
600°C
0
15
30
45
60
γ %

Fig. 2

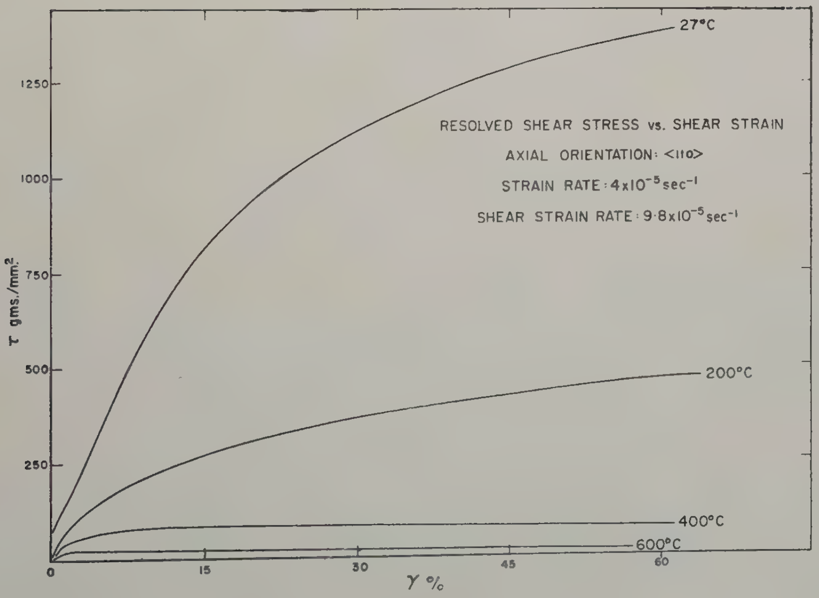
27°C
1250
RESOLVED SHEAR STRESS vs. SHEAR STRAIN
AXIAL ORIENTATION: <110>
STRAIN RATE: 4x10⁻⁵sec⁻¹
SHEAR STRAIN RATE: 9·8x10⁻⁵sec⁻¹
1000
750
τ gms./mm.²
500
200°C
250
400°C
600°C
0
15
30
45
60
γ %

similar, showing evidence of multiple slip; the slip lines are closely spaced. At 600°c (figs. 7, 8 and 9, Pl. 9) the surfaces are strikingly different. The ⟨110⟩ crystal shows widely spaced, sharp-edged slip bands, similar to the bands that occur on centre orientation crystals deformed at 600°c; this is strong evidence of single slip. The cross section of the crystal was elliptical after deformation.

The ⟨100⟩ crystal also shows widely spaced slip bands with these differences: the edges of the bands are rounded, and in different regions of the crystal, deformation took place on different {111} planes. In any one region of the crystal the cross section is elliptical. The rounded edges are probably due to a combination of slip on many adjacent planes in the neighbourhood of the slip band, and to cross slip.

Fig. 3

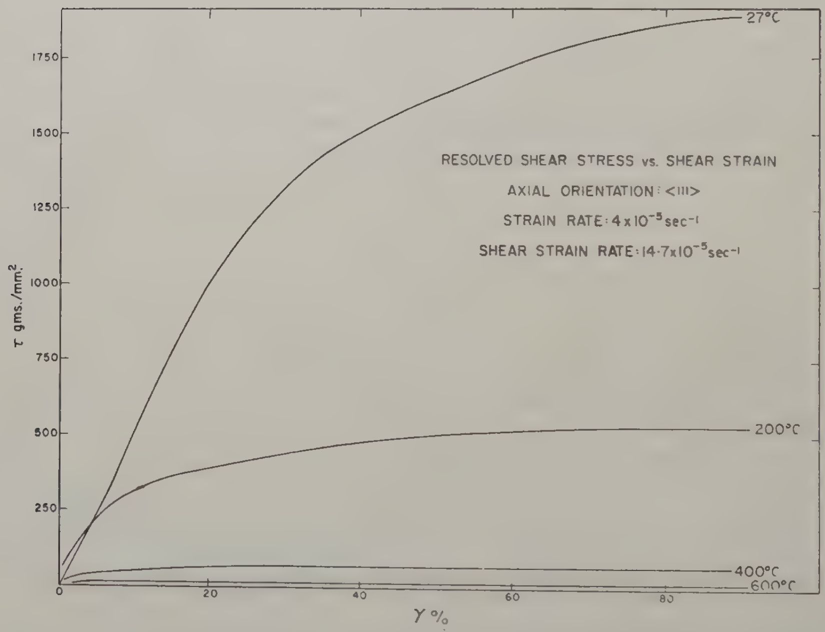

The ⟨111⟩ crystal remained circular in cross section after deformation at all temperatures. The surface displayed many short, intersecting slip lines and deformation appeared to occur fairly homogeneously over the entire length of the crystal.

3.2. *Comparison of ⟨111⟩ Crystal and Polycrystal*

A comparison between the tensile stress–tensile strain curves of the actual polycrystal and the one derived from the deformation of the ⟨111⟩ single crystal was made using Taylor's criterion (see Introduction). Figures 10, 11, 12 and 13 show the results of this comparison. A measure

Fig. 10

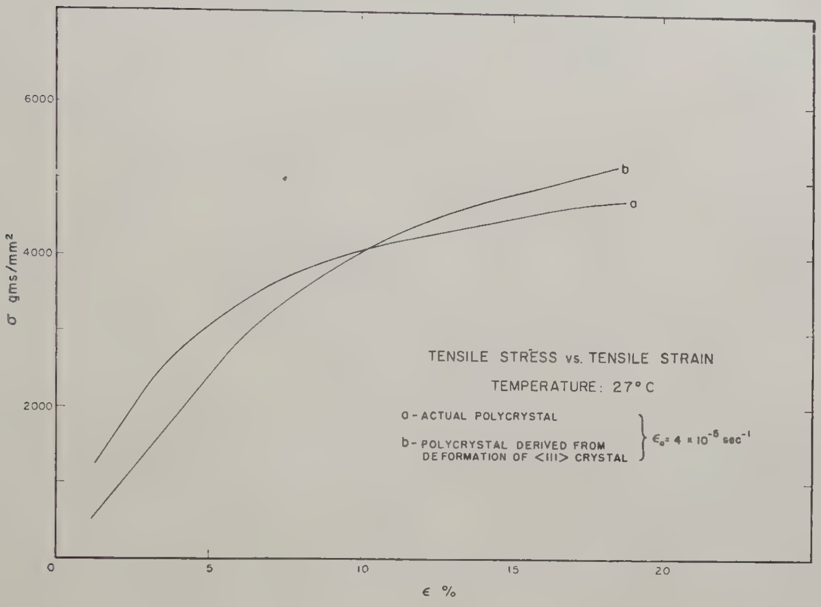
6000
4000
2000
0
5
10
15
20
σ gms/mm²
ε %
b
a
TENSILE STRESS vs. TENSILE STRAIN
TEMPERATURE: 27°C
a - ACTUAL POLYCRYSTAL
b - POLYCRYSTAL DERIVED FROM DEFORMATION OF <111> CRYSTAL
$\dot{\epsilon}_0 = 4 \times 10^{-5}\ \mathrm{sec}^{-1}$

Fig. 11

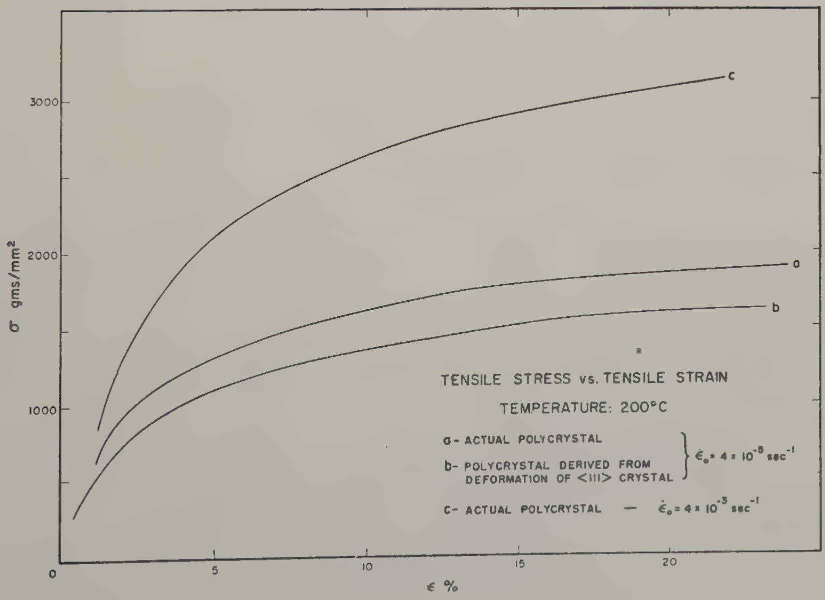
3000
2000
1000
0
5
10
15
20
σ gms/mm²
ε %
c
a
b
TENSILE STRESS vs. TENSILE STRAIN
TEMPERATURE: 200°C
a - ACTUAL POLYCRYSTAL
b - POLYCRYSTAL DERIVED FROM DEFORMATION OF <111> CRYSTAL
$\dot{\epsilon}_0 = 4 \times 10^{-5}\ \mathrm{sec}^{-1}$
c - ACTUAL POLYCRYSTAL — $\dot{\epsilon}_0 = 4 \times 10^{-3}\ \mathrm{sec}^{-1}$

Fig. 12

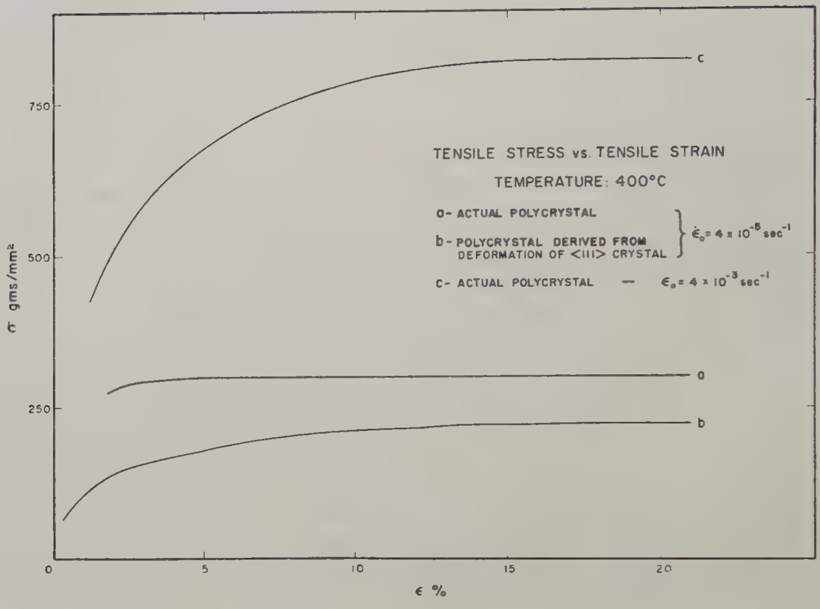
TENSILE STRESS vs. TENSILE STRAIN
TEMPERATURE: 400°C
a- ACTUAL POLYCRYSTAL
b- POLYCRYSTAL DERIVED FROM DEFORMATION OF <111> CRYSTAL
$\dot{\epsilon}_o = 4 \times 10^{-5}$ sec^{-1}
c- ACTUAL POLYCRYSTAL — $\epsilon_o = 4 \times 10^{-3}$ sec^{-1}
c
a
b
σ gms/mm²
750
500
250
0
5
10
15
20
ε %

Fig. 13

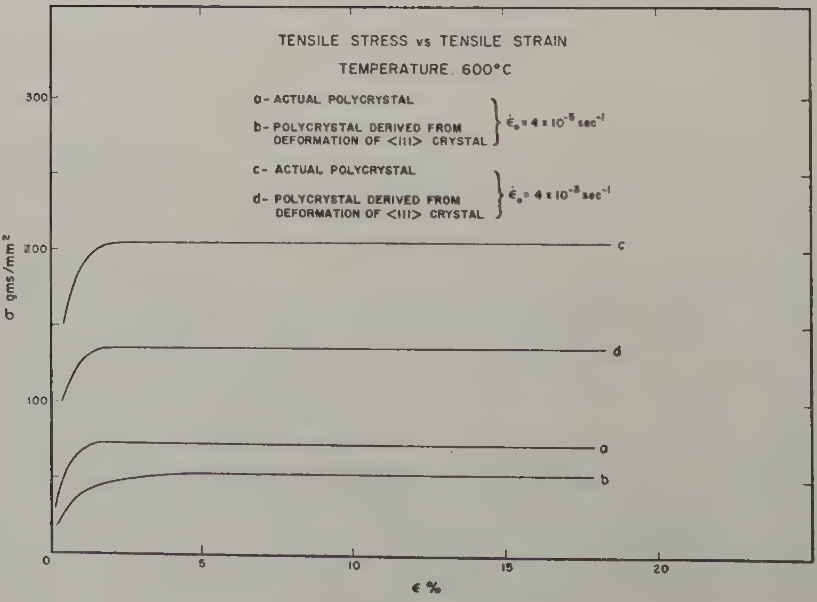
TENSILE STRESS vs TENSILE STRAIN
TEMPERATURE. 600°C
a- ACTUAL POLYCRYSTAL
b- POLYCRYSTAL DERIVED FROM DEFORMATION OF <111> CRYSTAL
$\dot{\epsilon}_o = 4 \times 10^{-5}$ sec^{-1}
c- ACTUAL POLYCRYSTAL
d- POLYCRYSTAL DERIVED FROM DEFORMATION OF <111> CRYSTAL
$\dot{\epsilon}_o = 4 \times 10^{-3}$ sec^{-1}
c
d
a
b
σ gms/mm²
300
200
100
0
5
10
15
20
ε %

of the similarity, that is, the ratio of the stresses at a given strain, $\sigma_{\text{poly}}/\sigma_{\langle 111\rangle}$, is given in the table. The strain rate is $4\times10^{-5}\,\text{sec}^{-1}$. Also included in the figures are stress–strain curves of polycrystals deformed at a strain rate of $4\times10^{-3}\,\text{sec}^{-1}$. The ratio $(\sigma_{\text{fast}}/\sigma_{\text{slow}})$ for polycrystals at 15% strain is also given in the table.

Temperature	27°c	200°c	400°c	600°c
$\sigma_{\text{poly}}/\sigma_{\langle 111\rangle}$	1·00 ($\epsilon=11\%$)	1·16	1·46	1·38
$(\sigma_{\text{fast}}/\sigma_{\text{slow}})$† poly	1·11	1·63	2·70	2·83

† σ_{fast}—at 4×10^{-3} per sec. σ_{slow}—at 4×10^{-5} per sec.

§ 4. Discussion

4.1. *Orientation Dependence of Single Crystal Deformation*

If a uniaxial stress is applied along a ⟨100⟩ or ⟨111⟩ direction (‘polyslip’† orientations) or along a ⟨110⟩ direction (‘multislip’† orientation) of a f.c.c. single crystal, the resolved shear stresses are equal on eight, six and four slip systems respectively, and are nil on the rest of the twelve available systems. In these cases plastic deformation occurs, from the onset, by slip on at least several of the equally stressed systems. Furthermore, if slip occurred on all the equally stressed systems, in the ⟨111⟩ orientation three sets of Lomer–Cottrell dislocations would form along stressed ⟨110⟩ directions, in the ⟨100⟩ orientation two such sets would form along unstressed ⟨110⟩ directions and in the ⟨110⟩ orientation only one set would form along an unstressed ⟨110⟩ direction.

The differences in the stress–strain relationships for these three orientations, found at room temperaure, can be rationalized in terms of the above differences in the numbers and distribution of Lomer–Cottrell dislocations (Hosford *et al.* 1960).

The results of the present experiments show that as the temperature of testing is increased, the shear–stress shear strain curves for the three axial orientations (⟨111⟩, ⟨100⟩ and ⟨110⟩) become more and more similar, until at 600°c they are identical. On the other hand, the surface appearance of the crystals strained at 600°c indicates that the mode of deformation depends drastically on orientation. It should also be pointed out that for deformation at 600°c, the shear stress–shear strain curves of crystals oriented for single slip (‘centre’ orientations) are the same as for the three ‘corner’ orientations discussed above. One is thus led to conclude from the similarity of the shear stress–shear strain curves for all these cases, that the mechanism of strain hardening at high temperature is the same regardless of orientation. This happens in spite of the fact that the numbers of Lomer–Cottrell dislocation sets expected for form are not the same for each orientation, and that the number of both active and equally favoured slip systems is also different in each case. It is apparent, therefore, that in aluminium at 600°C Lomer–Cottrell barriers become ineffective as obstacles to slip.

---

† We are defining these terms as follows: polyslip orientation—one having five or more slip systems with equal resolved shear stresses; multislip orientation—one having more than one but less than five slip systems with equal resolved shear stresses.

4.2. *The Relation Between Single Crystal and Polycrystal Deformation*

To satisfy continuity conditions at the grain boundaries, a grain in a polycrystal deforms plastically by slip on several slip systems (five systems in the most general case). Hardening by the formation of Lomer–Cottrell barriers will also take place within a grain of a polycrystal, the only difference between the single crystal and the polycrystal being the presence of grain boundaries in the latter. In the case of aluminium deformed at room temperature, it was shown by work on multicrystals (Elbaum 1960) that the only effect of the grain boundaries is to force additional slip systems into operation in order to satisfy the continuity conditions; the boundary contributes no intrinsic strength of its own to the polycrystal.

The results of the present study on polycrystal deformation show that, at room temperature, the stress–strain curve of a polycrystal can be derived from the deformation of a $\langle 111 \rangle$ single crystal using Taylor's criterion. Equally good agreement is obtained in the case of $\langle 100 \rangle$ crystals for the first few percent of plastic strain. For higher strains the $\langle 100 \rangle$ crystals undergo a characteristic change from deformation by slip on 'many' slip systems to deformation consistent with slip on two systems only. This difference between the two orientations is thought to originate in an inherent instability of the $\langle 100 \rangle$ orientation. In particular, in the $\langle 100 \rangle$ case, it can be shown (Hauser and Jackson 1960, Kocks 1959) that if deformation occurs to any great extent on a particular slip plane, it will continue on that plane with a resulting gradual change in orientation. For the specific purpose of the present discussion it remains significant that good agreement is found between the behaviour of polycrystals and of $\langle 111 \rangle$ or $\langle 100 \rangle$ single crystals, as long as the latter deform by slip on several systems. These results suggest that the energies consumed in the deformation of a polycrystal, or of a single crystal oriented for polyslip, consist in both cases of the energy for polyslip and are essentially the same. More specifically, these results indicate that at room temperature the work hardening mechanisms in polycrystals and in single crystals oriented for polyslip are also the same. It will be assumed that work hardening is due to the formation of dislocation pile-ups caused by Lomer–Cottrell barriers. This mechanism is not sensitive to the presence of grain boundaries in a polycrystal because the spacing between effective barriers to slip in each grain is small compared to the size of the grain.

At elevated temperatures the stress–strain curves for polycrystals, derived from the deformation of $\langle 111 \rangle$ single crystals, no longer coincide with the actual curves for polycrystals. It should also be pointed out that at 600°C, after the initial deformation of 2 or 3%, no work hardening is detected in either single crystals or polycrystals (deformation takes place under a constant stress). This implies that a steady state is reached, where the dislocation configuration remains the same in the crystal during deformation. In particular, the number of annihilated active dislocations is equal to the number created; however, the steady state is reached at different stress values in the single crystal than in the polycrystals. Also, both single crystals and polycrystals are strain rate sensitive, but at 600°C the strain rate sensitivity is higher for polycrystals than for single crystals. These observations indicate that the predominant relief mechanisms are different in single crystals and in polycrystals, although both mechanisms lead to a steady state dislocation distribution. Of the two mechanisms, at least one, or both, must depend on the nature of the obstacles to slip. If both mechanisms were independent of the type of obstacle, or if the obstacles were the same in the two cases, one would not expect to find any difference between single crystal and polycrystal deformation. (This happens at room temperature where Lomer–Cottrell dislocations are thought to be responsible for work-hardening in both cases.) Since no orientation dependence was found in the stress–strain relationship of single crystals deformed at 600°C, it was postulated that Lomer–Cottrell dislocations become ineffective as obstacles to slip at this temperature. The only likely obstacles to slip that remain in a polycrystal and which are not present in a single crystal are grain boundaries. It is therefore suggested that at 600°C in single crystals and in the interior of a grain in a polycrystal, break-up of Lomer–Cottrell dislocations occurs, whereas a grain boundary in a polycrystal is capable of supporting larger dislocation pile-ups. Relief from these pile-ups at a grain boundary may occur through climb, cross slip, or escape of dislocations into the grain boundary. No clear distinction can be made between these relief mechanisms on the basis of the available results.

It should be pointed out that grain boundary sliding is not important at 600°C even at the slowest strain rates used in these experiments. If grain boundary sliding required a lower stress than slip within the grains, the stress–strain curve for a polycrystal would be expected to lie below the stress–strain curve derived from ⟨111⟩ single crystal deformation, whereas the opposite is found to occur.

4.3. *The Validity of the Taylor Criterion*

Using Taylor's criterion

$$M = \frac{\sigma}{\tau} = \frac{\sum_{s=1}^{n} |d\gamma|}{d\epsilon},$$

the stress–strain curve for a polycrystal can be derived from the stress–strain curve of a single crystal only when the microscopic deformation mechanisms, and particularly the work hardening mechanisms, are similar in both cases. This condition is satisfied at room temperature, if the comparison is carried out between polycrystals and single crystals deforming by polyslip. Here work hardening is in both cases due to obstacles to slip (Lomer–Cottrell dislocations) formed by similar dislocation interactions within the single crystals or within the grains of a polycrystal. This mechanism is not sensitive to the presence of grain boundaries, because the spacing between effective barriers to slip in each grain is small compared to the size of the grain (or spacing between grain boundaries).

At elevated temperatures, where grain boundaries become more effective barriers to slip than Lomer–Cottrell dislocations, polyslip deformation in single crystals and in polycrystals is not the same. In this case the stress–strain curve for a polycrystal can no longer be derived from the stress–strain curve of a single crystal, using Taylor's criterion.

§ 5. Conclusions

It may be concluded from the experiments described above that: (1) Taylor's criterion for deducing the stress–strain behaviour of a polycrystal from that of a single crystal ceases to be valid (in the case of aluminium) as the temperature rises much above room temperature, and (2) the principal work hardening mechanism that operates at lower temperatures (namely, the formation of Lomer–Cottrell dislocations that become obstacles against which other dislocations can pile up) ceases to function at elevated temperatures. That is, the Lomer–Cottrell locks are no longer effective obstacles to slip at higher temperatures in both single crystals and polycrystals. The only barriers that remain effective are grain boundaries present in polycrystals.

The experiments dealt with in this investigation and in previous studies of room temperature plastic deformation of multicrystals (Hosford *et al.* 1960) were carried out on aluminium only. It is, therefore, not possible to extend all the conclusions of these investigations to other metals with the f.c.c. structure. Similar investigations in this area, on other metals, particularly on f.c.c. metals that are characterized by a low stacking-fault energy (for example copper), are necessary for a more complete understanding of the relations between single and polycrystal deformation.

References

Bishop, J. F. W., and Hill, R., 1951, *Phil. Mag.*, **42,** 414, 1298.
Chalmers, B., 1953, *Canad. J. Phys.*, **31,** 132.
Elbaum, C., 1960, *Trans. Amer. Inst. min. (metall.) Engrs*, **218,** 444.
Hauser, J., and Jackson, K. A., 1961, *Acta Met.* (to be published).
Hosford, W., Fleischer, R. L., and Backofen, W. A., 1960, *Acta Met.*, **8,** 187.
Kocks, U. F., 1958, *Acta Met.*, **6,** 85; 1959, *Ph.D. Thesis*, Harvard University.
Taylor, G. I., 1938, *J. Inst. Met.*, **62,** 307; 1955, *IUTAM Colloquium*, Madrid, p. 7.

Possible Dislocation Gating Mechanisms for Fatigue Extrusion†

By A. J. KENNEDY
The College of Aeronautics, Cranfield

[Received July 20, 1960]

ABSTRACT

Cross-slip now appears to be an important factor in the initiation of fatigue cracks, and this lends support to the Mott screw-cycling model. The reason for progressive unidirectional cycling of the required kind under alternating stress is, however, not easily understandable. Two possible gating mechanisms are here proposed to account for this effect, both of which involve interactions with Lomer–Cottrell barriers. One of these mechanisms can provide an explanation for the very rapid appearance of extrusions in a few cycles of stress, and does not require any initial internal void to exist, as does Mott's original model.

§ 1. INTRODUCTION

OF the mechanisms proposed to account for the phenomenon of fatigue-induced intrusion and extrusion in slip bands, that which involves the cross-slip of screw dislocations (Mott 1958) appears to accord most satisfactorily with the experimental observations. The double-slip system of Cottrell and Hull (1957) and the mechanism of Thompson (1959) are both open to certain objections; the former in requiring intrusions and extrusions to be necessarily associated, and to occur in different slip bands, and the latter in its limitation to the case of extrusions only. The experiments of McEvily and Machlin (1959) on certain single crystals (LiF, AgCl, NaCl) were designed specifically to test some of the features of the different theories, and the general outcome was that extrusions and intrusions, and susceptibility to fatigue failure, are strongly associated with ease and predominance of cross-slip. McEvily and Machlin go on to examine possible dislocation configurations which could lead to the occurrence of intrusion and extrusion in the same slip band under an alternating stress.

One of the difficulties of the cross-slip hypothesis is that systematic unidirectional cycling of screw dislocations is required, of such a type that when the stress is reversed the screw dislocations do not simply retrace their forward paths; in other words, the dislocation movement is not reversible. May (1960) takes the view that no specific mechanism need be invoked to account for the observations, which could arise as the consequence of a kind of random cross-slipping of dislocations from one slip plane to another. This model is developed statistically by May, who assumes that as the surface roughens, the valleys so created become preferred regions for slip, and that these deepen until a crack may be considered to exist. With certain assumptions, for example that groups of about 20 dislocations are the operative elements, the model leads to values for N (cycles to failure) of the right order of magnitude. The model does not attempt to examine how the random cross-slipping might be initiated, nor can it explain how relatively large extrusions, up to $\sim 5\,\mu$ in length, can develop in a relatively few cycles.

---

† Communicated by the Author.

In view of the support that the cross-slip hypothesis of Mott has received from recent experiment it appears worthwhile to attempt some closer examination of the possible gating mechanisms which might lead to progressive cycling of the required type.

Fig. 1

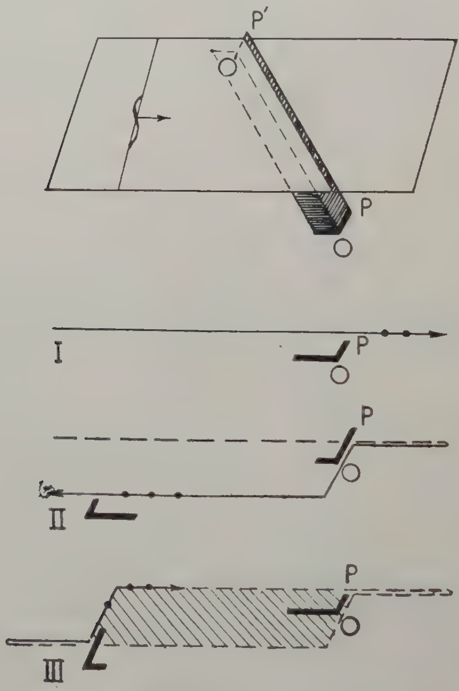

The impeding action of stacking faults associated with Lomer–Cottrell dislocations, showing in the sequence I, II, III the operations required for the extrusion or intrusion of the shaded area.

§ 2. Gating by Stacking Faults associated with Lomer–Cottrell Dislocations

Consider the situation depicted in fig. 1. Screw dislocations approaching the Lomer–Cottrell (L–C) dislocation could be impeded by the stacking fault OPP′O′. If the sign of the partial PP′ is such that it moves towards the sessile dislocation OO′ during this stress cycle, then the screw dislocations could pass freely over the stacking fault. On the negative half cycle, OPP′O′ extends, and the returning dislocations are held up by the stacking fault. Cross-slip is thus initiated, the screw dislocations slipping onto some other parallel plane, as shown. If during their slip on this plane they negotiate an L–C barrier in the open state, then the elements exist for some kind of cycling, because in the next positive half cycle the dislocations traverse the path indicated in fig. 1. It is not essential for such an ideal two-barrier unit to form in order to introduce a bias into the behaviour of dislocations. The principle could be applied to a random distribution of such barriers, each operating as a directional device. In such a case, the barriers might well constitute the physical elements required by May's statistical theory. One weakness of such a model is that the barrier offered by a single stacking fault would appear to be too slight to promote extensive cross-slip: this difficulty might be resolved by considering the gating elements as closely spaced groups of

Fig. 2

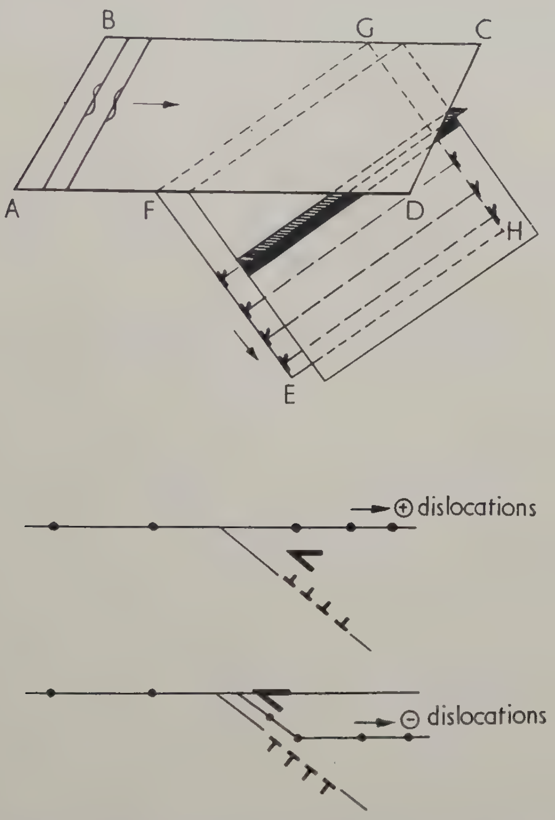

Dislocation system required to promote cross-slip by the cyclic blocking of screw dislocations by L–C barriers.

similar L–C barriers. However, it does seem more reasonable to seek a mechanism which utilizes the blocking action of the L–C barrier itself, and this leads to the next model.

§ 3. Gating by Lomer–Cottrell Dislocations

Consider the situation shown in fig. 2. The stressing system is such that screw dislocations are generated on ABCD and edge dislocations generated on EFGH. In the positive half cycle screw dislocations (say positive) traverse the plane ABCD from left to right. Edge dislocations traverse the EFGH plane and shift the L–C barrier away from ABCD. In the negative half cycle of stress, edge dislocations of opposite signs are generated the L–C barrier is translated into the ABCD plane, and thus screw dislocations (negative) are held up, and are forced to cross-slip as shown. The essential elements for progressive extrusion or intrusion now exist. Similar events at other points on these slip planes could result in segments of extrusion and intrusion occurring in the same slip band. Very rapid development of these features can occur: in fact in a single stress cycle, hundreds or thousands of screw dislocations could be generated and large extrusions/intrusions result. It is thus not essential for a given group of dislocations to be taken around a closed path (although this could indeed occur by such a mechanism) but merely necessary that there should exist

Fig. 3

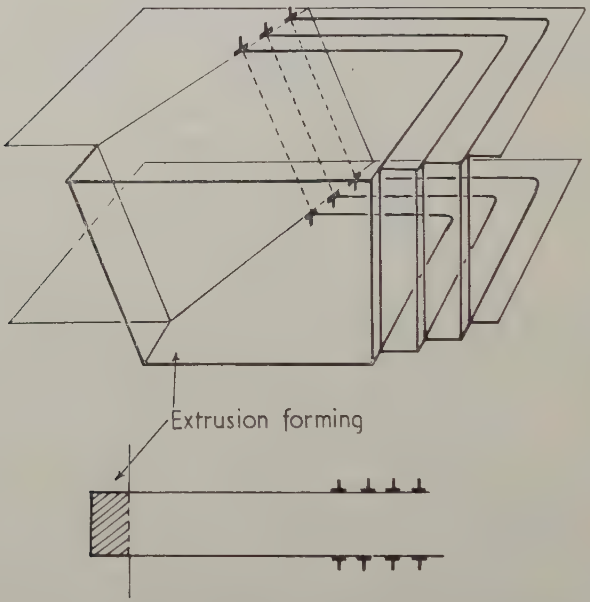

The consequence of the operation of the system indicated in fig. 2.

a path discrimination between positive and negative dislocations in the way indicated. Such a model suggests that finite extrusions might well be seen after a very few cycles.

The model does not require any initial internal voids, as does the unmodified Mott model, nor does extrusion imply that such voids must be formed. The passage of the screw dislocations will leave a concentration of positive and negative edge dislocations (see fig. 3) and this is a sufficient consequence of extrusion or intrusion. However, high dislocation concentrations could lead to an actual void forming, in precisely the manner which Mott (1958) envisaged. This modified model therefore accounts for both of Mott's original features by a single basic mechanism.

REFERENCES

COTTRELL, A. H., and HULL, D., 1957, *Proc. roy. Soc.* A, **242,** 211.

McEVILY, A. J., JR., and MACHLIN, E. S., 1959, *Proceedings of an International Conference on the Atomic Mechanisms of Fracture* (Technology Press and Wiley, 1959), p. 450.

MAY, A. N., 1960, *Nature, Lond.*, **185,** 303.

MOTT, N. F., 1958, *Acta Met.*, **6,** 195.

THOMPSON, N., 1959, *Proceedings of an International Conference on the Atomic Mechanisms of Fracture* (Technology Press and Wiley, 1959), p. 354.

On the Theory of Solid Solutions in Copper, Silver and Gold†

By W. Hume-Rothery
Department of Metallurgy, Oxford
and D. J. Roaf
Cavendish Laboratory, Cambridge

[Received July 15, 1960]

Abstract

It is proposed that the change in crystal structure on alloying the noble metals with elements of the B sub-groups (e.g. copper–zinc) is due to the Fermi surface touching the cube faces of the Brillouin zone of the face-centered cubic structure rather than the octahedral faces which are already touched in the pure metals. A reasonable band structure for copper is consistant with this suggestion.

It has been established empirically (Hume-Rothery *et al.* 1934) that, when the atomic size factors are favourable, the maximum solid solubility of many B sub-group elements in copper and silver occurs at an electron concentration of approximately 1·4. The explanation of this advanced by Jones (1936) was that, in so far as electronic energy is concerned, if the density of states or N(E) curve is of the general form of fig. 1, there will be a tendency for a phase to become unstable in the range A–B. For, if all other possible crystal structures are considered, there will probably be one or more of them for which the N(E) curve continues to rise after the electron concentration of A, and which will, therefore, accommodate the electrons with a lower energy.

Fig. 1

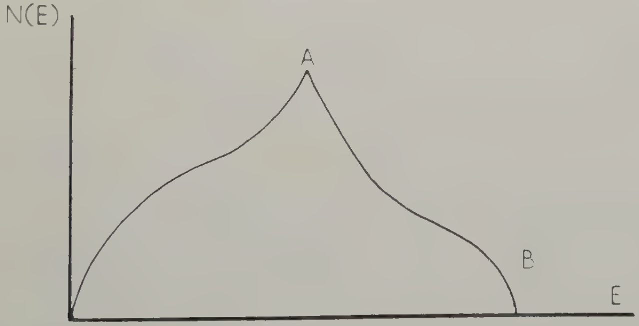

For the face-centred cubic structure, the first Brillouin zone is the well-known truncated octahedron. If the Fermi surface is assumed to be spherical, it touches the octahedral faces of the zone at an electron

---

† Communicated by the Authors.

concentration of 1·36, in remarkable agreement with the observed values of the maximum solubilities. In later work Jones (1937) calculated the N(E) curve for the face-centred cubic structure more accurately by assuming the energy gap across the octahedral faces of the zone to be that indicated by the optical properties of copper. The peak at A then corresponded to an electron concentration of about 1·0, and thus indicated a marked distortion of the Fermi surface. This was later confirmed by the work of Pippard (1957) on the anomalous skin effect in copper which indicated that the Fermi surface has just touched the octahedral face of the zone, and is in agreement with more recent work by Shoenberg (1960) on the de Haas–van Alphen effect which shows that the zone face is touched by the Fermi surface in copper, silver and gold.

In the calculations of Jones referred to above it was assumed that the same energy gap would exist across the dodecahedral faces of the Brillouin zone for the body-centred cubic structure. Marked distortion of the Fermi surface was again found, and the energy relations were such that in the equilibrium of the α/β brass type (between face-centred and body-centred cubic structures), the α-solubility limit was again in general agreement with experiment.

The calculations of Jones were thus satisfactory in predicting the marked distortion of the Fermi surface, and in indicating the approximate position of the $\alpha/\alpha+\beta$ solubility limits, but their acceptance meant the dropping of the correspondence between the position of a peak on an N(E) curve, and the electron concentration at the limit of a solid solution, which had been such a remarkable feature of the early theory. Cohen and Heine (1958) pointed out that with solutes such as zinc, the *s* valency levels were lower than the *p* valency levels by an amount which was considerably greater than for copper, and for this metal they concluded that, at the centre of the octahedral face, states inside the zone would be purely *p*-like, and those outside purely *s*-like. They, therefore, argued that the solution of zinc in copper would tend to lower *s* states relatively to *p* states, and would thus decrease the energy gap at the zone face, and make the Fermi surface more spherical, so that with increasing zinc-content the surface would at first shrink away from the zone-face, and then swell out again in a more spherical form and so satisfy the conditions of the original simple theory. For silver, Cohen and Heine concluded that the Fermi surface was nearly spherical, so that the conditions of the simple theory applied. For gold they concluded that, at the centres of the octahedral faces, the states inside the zone were purely *s*-like whilst those outside were *p*-like. They thus argued that solutions of zinc, and similar elements would increase the energy gap and make the Fermi surface more distorted, so that contact would occur at a lower electron concentration, and in this way they explained the lower solubilities of elements in gold than in silver and copper.

For copper, the explanation of Cohen and Heine can still apply, but the recent discoveries that the Fermi surface has touched the zone in silver and gold disproves their interpretation of solid solutions in these elements, and the following alternative explanation is suggested.

The complete N(E) curve for the face-centred cubic structure is of the form of fig. 2, when the peaks at A and B correspond to contact of the Fermi surface with the octahedral and cube faces of the zone. For a spherical Fermi surface the peak A corresponds to an electron concentration of 1·36 and if the surface continues to expand whilst retaining a spherical shape on its free surfaces, the peak B corresponds to an electron concentration of 1·88. If, therefore, in the actual structure of copper the peak A has been shifted back from a value of 1·36 to one of less than 1·0, it does not seem unreasonable to suggest that the peak B has been moved back from a value of 1·88 to *ca.* 1·4. After the point B, two sets of zone faces are reducing the number of available energy states and we may, therefore, expect the N(E) curve to fall more steeply after B than after A, and so to intensity the effect proposed by Jones. We suggest, therefore, that the solubility limit in copper alloys corresponds with the fall in the N(E) curve after the second, rather than after the first peak.

Fig. 2

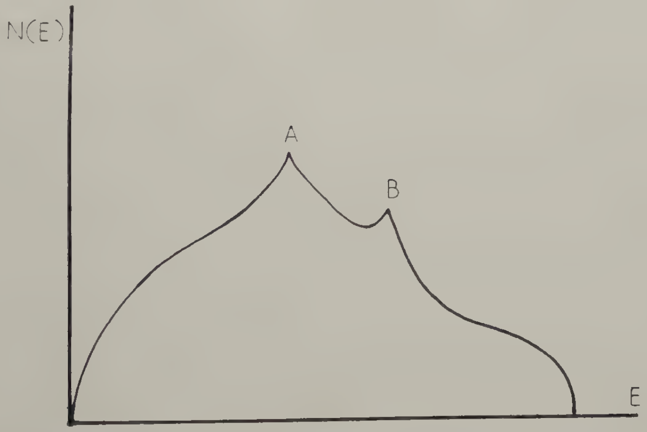

Unfortunately, there is no complete calculation of the band structure of copper from which one could easily verify this suggestion. However, García Moliner (1958) showed that the surface obtained by Pippard could be adequately described by the Slater and Koster (1954) interpolation formula

$$\begin{aligned}\epsilon = C_1(3-\cos\tfrac{1}{2}ak_2\cos\tfrac{1}{2}ak_3-\cos\tfrac{1}{2}ak_3\cos\tfrac{1}{2}ak_1-\cos\tfrac{1}{2}ak_1\cos\tfrac{1}{2}ak_2)\\ +C_2(3-\cos ak_1-\cos ak_2-\cos ak_3)\\ +C_3(3-\cos ak_2\cos ak_3-\cos ak_3\cos ak_1-\cos ak_1\cos ak_2)\\ +C_4(3-\cos 2ak_1-\cos 2ak_2-\cos 2ak_3)\\ +\ldots+\ldots \qquad (1)\end{aligned}$$

with $\epsilon/C_1=3{\cdot}6301$, $C_2/C_1=0{\cdot}0995$ (C_3 and higher coefficients zero).

The member of this family of surfaces which just touches the (200) face of the zone has $\epsilon/C_1=4$. Sampling in 27 directions (representing 794 points by symmetry) we find that this surface contains 1·63 electrons per atom. This is rather higher than the observed ratio at the phase boundary.

The general form of energy contour at the face of a Brillouin zone is such that the Fermi surface will probably be pulled out as it approaches the (200) zone face. This is confirmed by Shoenberg's work which suggests that the Fermi surface of pure copper is pulled out in the (200) directions (as the area of a central cross section in the (200) direction exceeds that in a (111) direction by 2·7%). A surface described by (1) with

$$\epsilon/C_1=3{\cdot}84, \qquad C_2/C_1=0{\cdot}119, \qquad C_3/C_1=0{\cdot}064 \qquad . \quad . \quad (2)$$

contains one electron per atom and has the correct area of contact on the (111) faces and the correct ratio of cross-sectional areas (though these are taken 8% below Shoenberg's areas which exceed the area of a central section of a free electron sphere). The member of the family with ($\epsilon/C_1=4$) which touches the (200) face contains 1·21 electrons per atom. This is rather too small but it is probable that the true Fermi Surface is not as depressed in the (110) directions as (2) suggests. The addition of suitable harmonics to allow for this might well give a surface touching the cube faces at a higher electron concentration. For example

$$\epsilon/C_1=3{\cdot}823, \quad C_2/C_1=0{\cdot}118, \quad C_3/C_1=0{\cdot}045, \quad C_4/C_1=0{\cdot}01$$

fits Shoenberg's surface as well as (2) and the member of the family in contact contains 1·25 electrons per atom. These calculations show that the position of the (200) peak on the N(E) curve is very sensitive to the exact form of the Fermi surface. The calculations are tentative and qualitative, but suggest, that the identification of the α-solubility limit with the fall in the density of states after the (200) peak is at least reasonable.

The $\alpha/\alpha+\beta$ type of equilibrium is found only in alloys of copper and silver. In the gold alloys, the more electro-negative nature of gold results in an increased electrochemical factor, and in some systems (e.g. Au–Cd, Au–Zn) the random body-centred cubic β-phase is replaced by an ordered Cs–Cl type of structure with a maximum freezing point in the equilibrium diagram. In these systems the smaller solubility of Cd and Zn in gold follows from the usual free energy principle of the effect of a stable intermediate phase on the limits of a primary solid solution. Heine (private communication) suggests that, since in the free atom of gold the *s* level is so much lower than the *p* level, it is still possible that the mechanism of Cohen and Heine is responsible for the lower solubility limit in the gold alloys. The solubility limits of the face-centred cubic structure in equilibrium with a close-packed hexagonal structure are not yet understood.

ACKNOWLEDGMENT

One of the authors (D. J. R.) is indebted to the Department of Scientific and Industrial Resarch for a research maintenance grant.

References

Cohen, M. H., and Heine, V., 1958, *Advanc Phys.*, **7,** 395.
García Moliner, F., 1958, *Phil. Mag.*, **3,** 207.
Hume-Rothery, W., Mabbott, G. W., and Channel Evans, K. M., 1934, *Phil. Trans.* A, **233,** 1.
Jones, H. See Mott, N. F., and Jones, H., 1936, *Theory of the Properties of Metals and Alloys* (Oxford : Clarendon Press); 1937, *Proc. phys. Soc. Lond.*, **49,** 250.
Pippard, A. B., 1957, *Phil Trans.* A, **250,** 325.
Shoenberg, D., 1960, *Phil. Mag.*, **5,** 105.
Slater, J. C., and Koster, G. F., 1954, *Phys. Rev.*, **94,** 1498.

The Charge Correlation Function of a Plasma in a Magnetic Field†

By S. F. Edwards
Theoretical Physics Division, University of Manchester and
Theoretical Physics Division, A.E.R.E., Harwell‡

[Received July 18, 1960]

Abstract

A linear integral equation is derived for the correlation function in the presence of a magnetic field, and solved and the errors estimated.

§ 1. Introduction

In a fully ionized plasma whose charge density in $\rho(\mathbf{x}, t)$, a fundamental quantity in the description of the plasma in say thermal equilibrium is the correlation function $\langle \rho(\mathbf{x}, t)\rho(\mathbf{x}', t')\rangle$, where the brackets mean that the quantity is averaged over the thermal equilibrium state. This quantity is a directly observable quantity by probe measurements, and plays a key position in the theory of transport phenomena of states slightly removed from equilibrium since it appears in the kernel of the transport equation. It will be studied in this paper in a simple approximation which will allow the inclusion of an external magnetic field. A linear integral equation for the correlation function will be deduced and solved and the corrections briefly discussed. A more general approach which can lead to an analysis of the complete solution will be discussed in a later paper since it requires a much more elaborate mathematical apparatus. The application to transport theory is also deferred to a subsequent paper.

To simplify the analysis the gas will be considered to consist of only one kind of particle with a neutralizing background. Before considering the whole problem some simplified versions which can be solved exactly will be considered. If $\mathbf{x}_\alpha$ are the coordinates of the electrons, the density is

$$\rho(\mathbf{x}) = \sum_\alpha \delta(\mathbf{x} - \mathbf{x}_\alpha) - N/V \qquad . \quad . \quad . \quad . \quad . \quad (1.1)$$

which has Fourier components

$$\rho_{\mathbf{k}} = \sum_\alpha \exp(i\mathbf{k} \,.\, \mathbf{r}_\alpha). \qquad . \quad . \quad . \quad . \quad . \quad . \quad (1.2)$$

The overall neutrality has the effect of making ρ_0 zero, so that the equation of motion of an electron becomes

$$m\ddot{\mathbf{x}}_\alpha = \frac{4\pi e^2}{V} \sum_{k \neq 0} \frac{\mathbf{k}}{k^2} \exp\left[i\mathbf{k} \,.\, (\mathbf{x}_\alpha - \mathbf{x}_\beta)\right] + \frac{e}{c}\dot{\mathbf{x}}_\alpha \times \mathbf{B}, \qquad . \quad . \quad (1.3)$$

---

† Communicated by the Author.
‡ Vacation Consultant.

where $\mathbf{k}$ runs over the values $(2\pi/R)(n_1, n_2, n_3)$, R being the side of the box, $V=R^3$, and n_1, n_2, n_3 are integers.

The correlation function $C(k,t)$ is defined by

$$C(k,t)=\langle\rho_{\mathbf{k}}(t)\rho_{\mathbf{k}}^*(0)\rangle \qquad . \quad . \quad . \quad . \quad . \quad . \quad (1.4)$$

so that $C(k,t)$ is the Fourier transform with respect to $\mathbf{x}-\mathbf{x}'$ of

$$\langle\rho(\mathbf{x},t)\rho(\mathbf{x}',t')\rangle. \qquad . \quad . \quad . \quad . \quad . \quad . \quad . \quad (1.5)$$

Consider firstly the case of free particles. Then

$$\left.\begin{aligned}\ddot{\mathbf{x}}_\alpha&=0,\\ \mathbf{x}_\alpha(t)&=\mathbf{x}_\alpha+\mathbf{v}_\alpha t.\end{aligned}\right\} \qquad . \quad . \quad . \quad . \quad . \quad . \quad . \quad . \quad (1.6)$$

Averaging against the Maxwell distribution

$$\langle\rho_{\mathbf{k}}(t)\rho_{\mathbf{k}}(0)\rangle$$
$$=\frac{1}{Q}\sum_{\alpha\beta}\int\exp\left[-\sum_\alpha \tfrac{1}{2}mv_\alpha{}^2/\kappa T+i\mathbf{k}\,.\,\mathbf{v}_\alpha t+i\mathbf{k}(\mathbf{x}_\alpha-\mathbf{x}_\beta)\right]\prod d^3v_\alpha d^3x_\alpha \qquad . \quad . \quad . \quad (1.7)$$

where

$$Q=\int\exp\left(-\sum\tfrac{1}{2}\,mv_\alpha{}^2/\kappa T\right)\prod d^3v_\alpha d^3x_\alpha. \qquad . \quad . \quad (1.8)$$

Therefore

$$C(k,t)=N\exp\left[-k^2(\kappa T)t^2/2m\right]. \qquad . \quad . \quad . \quad . \quad (1.9)$$

Now consider the case with Coulomb interactions and long wavelength, i.e. small $\mathbf{k}$. This means that the first term, that of order k^2 in

$$\ddot{\rho}_k=\sum-(\mathbf{k}\,.\,\dot{\mathbf{x}}_\alpha)^2\exp(i\mathbf{k}\,.\,\mathbf{x}_\alpha)+i\sum(\mathbf{k}\,.\,\ddot{\mathbf{x}}_\alpha)\exp(i\mathbf{k}\,.\,\mathbf{x}_\alpha) \qquad (1.10)$$

can be ignored so that

$$\ddot{\rho}_{\mathbf{k}}(t)=\frac{4\pi e^2}{V}\sum_{\mathbf{j}}\sum_{\alpha\beta}\frac{\mathbf{k}\,.\,\mathbf{j}}{\mathbf{j}^2}\exp(i(\mathbf{k}+\mathbf{j})\mathbf{x}_\alpha-i\mathbf{j}\mathbf{x}_\beta). \qquad . \quad . \quad (1.11)$$

When this is averaged in thermal equilibrium only the term $\mathbf{k}+\mathbf{j}=0$ survives, giving N, so that

$$\ddot{\rho}_{\mathbf{k}}(t)+\left(\frac{Ne^2}{Vm}\right)\rho_{\mathbf{k}}=0 \qquad . \quad . \quad . \quad . \quad . \quad . \quad . \quad (1.12)$$

and

$$\langle\rho_{\mathbf{k}}(t)\rho_{\mathbf{k}}^*(0)\rangle=\langle\rho_{\mathbf{k}}(0)\rho_{\mathbf{k}}^*(0)\rangle\cos\omega t \qquad . \quad . \quad . \quad (1.13)$$

where ω is the plasma frequency $(4\pi Ne^2/mV)^{1/2}$.

To evaluate $\langle\rho_{\mathbf{k}}(0)\rho_{\mathbf{k}}^*(0)\rangle$ allowing for the Coulomb interaction requires a solution of the equilibrium properties of the plasma which will be quoted here. In first approximation

$$\langle\rho_{\mathbf{k}}(0)\rho_{\mathbf{k}}^*(0)\rangle=\frac{N}{1+(k^2\lambda^2)^{-2}} \qquad . \quad . \quad . \quad . \quad . \quad . \quad (1.14)$$

where $\lambda=(VkT/4\pi Ne^2)^{1/2}$, the Debye–Huckel length. (Higher approximations to this can be obtained for example by the methods given by Edwards (1959).)

Next consider the effect of the external magnetic field on these two limiting cases. For the free particle the equation of motion is

$$m\dot{\mathbf{x}}_\alpha = (e/c)\dot{\mathbf{x}}_\alpha \times \mathbf{B}. \qquad (1.15)$$

Taking $\mathbf{B}$ in the Z direction and $\Omega = e|\mathbf{B}|/mc$ the solution is

$$x_\alpha(t) = x_\alpha + \Omega^{-1}(u_\alpha \sin\Omega t + v_\alpha(1-\cos\Omega t)), \qquad (1.16)$$

$$y_\alpha(t) = y_\alpha + \Omega^{-1}(v_\alpha \sin\Omega t + u_\alpha(1-\cos\Omega t)), \qquad (1.17)$$

$$z_\alpha(t) = z_\alpha + w_\alpha t. \qquad (1.18)$$

Proceeding as in (1.7)–(1.9), one obtains

$$\begin{aligned}\langle \rho_{\mathbf{k}}(t)\rho_{\mathbf{k}}^*(0)\rangle = N\exp[&-k_z^2 t^2 \kappa T/2m \\ &-(k_x^2+k_y^2)(1-\cos\Omega t)\kappa T/m\Omega^2] \qquad (1.19)\end{aligned}$$

or in invariant form

$$N\exp[-(\mathbf{k}\,.\,\mathbf{B})^2 t^2\kappa T/2mB^2 - (\mathbf{k}\times\mathbf{B})^2(1-\cos\Omega t)\kappa T/\Omega^2B^2m]. \qquad (1.20)$$

For the interacting case, neglecting as before terms in $k^2\kappa T/m$ compared with ω^2 and now also Ω^2, the simplest way to close the equations is to go to fourth order

$$\ddot{\rho}_{\mathbf{k}} = -\omega^2\rho_{\mathbf{k}} + ei\sum \frac{\mathbf{k}\,.\,(\mathbf{v}_\alpha\times\mathbf{B})}{mc}\exp(i\mathbf{k}\,.\,\mathbf{x}_\alpha), \qquad (1.21)$$

$$\begin{aligned}\rho_{\mathbf{k}}^{\mathrm{IV}} &= -\omega^2\ddot{\rho}_{\mathbf{k}} - \frac{Ne^2}{m^2c^2}\sum \mathbf{k}\,.\,[(\mathbf{k}\times\mathbf{B})\times\mathbf{B}]\rho_{\mathbf{k}} \\ &\quad + \sum i\left(\frac{e}{mc}\right)^3 \mathbf{k}\,.\,(((\mathbf{v}_\alpha\times\mathbf{B})\times\mathbf{B})\times\mathbf{B}) \qquad (1.22) \\ &= -\omega^2\ddot{\rho}_{\mathbf{k}} - \frac{ie\Omega^2}{mc}\sum \mathbf{k}\,.\,(\mathbf{v}_\alpha\times\mathbf{B})\exp(i\mathbf{k}\,.\,\mathbf{x}_\alpha) \\ &\quad + \omega^2\Omega^2[(k^2B^2-(\mathbf{k}\,.\,\mathbf{B})^2)/(k^2B^2)]\rho_{\mathbf{k}}; \qquad (1.23)\end{aligned}$$

i.e.

$$\left(\frac{\partial^2}{\partial t^2}+\omega^2\right)\ddot{\rho}_{\mathbf{k}} = -\left(\frac{\partial^2}{\partial t^2}+\omega^2\right)\Omega^2\rho_{\mathbf{k}} + \Omega^2\omega^2\,\frac{k^2B^2-(\mathbf{k}\,.\,\mathbf{B})^2}{k^2B^2}\rho_{\mathbf{k}}; \qquad (1.24)$$

i.e.

$$\left(\frac{\partial^2}{\partial t^2}+\omega^2\right)\left(\frac{\partial^2}{\partial t^2}+\Omega^2\right)\rho_{\mathbf{k}} = \mu\Omega^2\omega^2\rho_{\mathbf{k}}, \qquad (1.25)$$

where

$$\mu = \cos(\sin^{-1}(\mathbf{k}\,.\,\mathbf{B})/kB).$$

This equation corresponds to oscillations of frequency q where

$$(q^2-\omega^2)(q^2-\Omega^2) - \mu\Omega^2\omega^2 = 0\;; \qquad (1.26)$$

i.e.

$$q^2 = \tfrac{1}{2}(\omega^2+\Omega^2 \pm \sqrt{[(\omega^2-\Omega^2)^2+4\omega^2\Omega^2\mu]}). \qquad (1.27)$$

The two simple cases are $\mathbf{k}$ and $\mathbf{B}$ parallel, i.e. $\mu=0$, giving the roots $q^2=\omega^2$ and $q^2=\Omega^2$, and k and B perpendicular giving $q^2=\omega^2+\Omega^2$ or 0. As μ goes from 0 to 1, the solution ω goes to $\sqrt{(\omega^2+\Omega^2)}$ and the solution Ω goes to zero. In general there will be two solutions $\pm\varpi(k)$ and $\pm\phi(k)$ say, and the analogue of

$$\langle\rho_{\mathbf{k}}(t)\rho_{\mathbf{k}}{}^*(0)\rangle=\langle\rho_{\mathbf{k}}(0)\rho_{\mathbf{k}}{}^*(0)\rangle\cos\omega t$$

becomes

$$\langle\rho_{\mathbf{k}}(t)\rho_{\mathbf{k}}{}^*(0)\rangle=\langle\rho_{\mathbf{k}}(0)\rho_{\mathbf{k}}{}^*(0)\rangle\left[\frac{\phi^2-\omega^2}{\phi^2-\varpi^2}\cos\omega t+\frac{\varpi^2-\omega^2}{\varpi^2-\phi^2}\cos\phi t\right]. \quad (1.28)$$

The equilibrium distribution depends upon $\exp(-H/\kappa T)$, and since the kinetic energy is $\sum(\mathbf{p}-e\mathbf{A})^2$, i.e. still $\sum\frac{1}{2}mv^2$, the magnetic field has no effect upon $\langle\rho_{\mathbf{k}}(0)\rho_{\mathbf{k}}{}^*(0)\rangle$ which is the same as in (1.13).

In general the correlation function $C(k,t)$ will have collective and individual particle motion aspects and in the next section integral equations will be derived containing the two extreme cases as limits.

§ 2. THE INTEGRAL EQUATION FOR THE CORRELATION FUNCTION

Consider at first the case when the magnetic field is absent. Then the equation of motion

$$m\ddot{\mathbf{x}}_{\alpha}(t)=e^2\sum_{\alpha\neq\beta}\frac{\mathbf{x}_{\alpha}(t)-\mathbf{x}_{\beta}(t)}{|\mathbf{x}_{\alpha}(t)-\mathbf{x}_{\beta}(t)|^3} \quad . \quad . \quad . \quad . \quad . \quad . \quad (2.1)$$

can be formally integrated into

$$\mathbf{x}_{\alpha}(t)=\mathbf{x}_{\alpha}+\mathbf{v}_{\alpha}t+\frac{e^2}{m}\sum_{\alpha\beta}\int_0^t d\tau\int_0^{\tau}ds\,\frac{\mathbf{x}_{\alpha}(s)-\mathbf{x}_{\beta}(s)}{\mathbf{x}|_{\alpha}(s)-\mathbf{x}_{\beta}(s)|^3}, \quad . \quad . \quad (2.2)$$

$$\mathbf{x}_{\alpha}(t)=\mathbf{x}_{\alpha}+\mathbf{v}_{\alpha}t+\mathbf{a}_{\alpha}(t) \quad \text{say}, \quad . \quad . \quad . \quad . \quad . \quad . \quad . \quad . \quad . \quad . \quad (2.3)$$

where $\mathbf{x}_{\alpha}$, $\mathbf{v}_{\alpha}$ will be used to mean $\mathbf{x}_{\alpha}(0)$, $\mathbf{v}_{\alpha}(0)$. The correlation function $C(k,t)$ is then

$$C(k,t)=\sum_{\alpha,\gamma}\langle\exp[i\mathbf{k}(\mathbf{x}_{\alpha}(t)-\mathbf{x}_{\gamma})]\rangle \quad . \quad . \quad . \quad . \quad (2.4)$$

$$=\sum_{\alpha,\gamma}\langle\exp[i\mathbf{k}(\mathbf{x}_{\alpha}-\mathbf{x}_{\gamma})+i\mathbf{k}\,.\,\mathbf{v}_{\alpha}t+i\mathbf{k}\,.\,\mathbf{a}_{\alpha}(t)]\rangle. \quad . \quad (2.5)$$

Now assume that the motion of any one particle deviates slightly from the rectilinear path, and that only the collective effects of the many slight deviations matter, so that $\exp[i\mathbf{k}\,.\,\mathbf{a}_{\alpha}(t)]$ can be expanded in a series. A more general discussion of this expansion will be given in § 4. This gives

$$\begin{aligned}C(k,t)=&\sum_{\alpha,\gamma}\langle\exp[i\mathbf{k}(\mathbf{x}_{\alpha}-\mathbf{x}_{\gamma})+i\mathbf{k}\,.\,\mathbf{v}_{\alpha}t]\rangle\\&+\frac{4\pi e^2}{V}\sum_{j}\sum_{\substack{\alpha\neq\beta\\ \gamma}}\int_0^t d\tau\int_0^{\tau}ds\,\frac{(\mathbf{k}\,.\,\mathbf{j})}{j^2}\\&\times\exp[i\mathbf{k}(\mathbf{x}_{\alpha}-\mathbf{x}_{\gamma}+\mathbf{v}_{\alpha}t)+i\mathbf{j}(\mathbf{x}_{\alpha}(s)-\mathbf{x}_{\beta}(s))]. \quad . \quad . \quad (2.6)\end{aligned}$$

In the same spirit the $\mathbf{x}_{\alpha}(s)$ can also be expanded giving

$$\begin{aligned}C(k,t)=&\sum_{\alpha\beta}\langle\exp[i\mathbf{k}(\mathbf{x}_{\alpha}-\mathbf{x}_{\gamma})+i\mathbf{k}\,.\,\mathbf{v}_{\alpha}t]\rangle\\&+\frac{4\pi e^2}{V}\sum_{j}\sum_{\substack{\alpha\neq\beta\\ \gamma}}\int_0^t d\tau\int_0^{\tau}ds\,\frac{\mathbf{k}\,.\,\mathbf{j}}{j^2}\\&\times\langle\exp[i(\mathbf{k}+\mathbf{j})\mathbf{x}_{\alpha}+i(\mathbf{k}t+\mathbf{j}s)\mathbf{v}_{\alpha}-i\mathbf{j}\mathbf{x}_{\beta}(s)+i\mathbf{k}\mathbf{x}_{\gamma}]\rangle. \quad (2.7)\end{aligned}$$

Now in equilibrium the average value of $\sum_\alpha \exp[i(\mathbf{k}+\mathbf{j})\mathbf{x}_\alpha]$ is zero unless $\mathbf{k}+\mathbf{j}$ is zero, when it gives N. Assuming that this averaging will not interfere with the averaging of $\exp[-i\mathbf{j}\mathbf{x}_\alpha(s)+i\mathbf{k}\mathbf{x}_\gamma]$ the equation becomes, putting $g(k,t)C(k,0)$ for the first term on the right

$$C(k,t)=C(k,0)\,g(k,t)-\omega^2\int_0^t d\tau\int_0^\tau ds g(k,t-s)C(k,s) \tag{2.8}$$

or integrating by parts:

$$C(k,t)=C(k,0)g(k,t)-\omega^2\int_0^t (t-\tau)g(k,t-\tau)C(k,\tau)\,d\tau. \tag{2.9}$$

This equation is readily solved by the Laplace transform:

If

$$\tilde{C}(k,p)=p\int_0^\infty \exp(-pt)C(k,t)\,dt, \quad . \quad . \quad . \quad . \tag{2.10}$$

$$\tilde{g}(k,p)=p\int_0^\infty \exp(-pt)g(k,t)\,dt$$

$$=\frac{1}{2}\sqrt{\frac{\pi}{\alpha}}\exp(p^2/4\alpha)\operatorname{erf}\left(\frac{p}{\sqrt{(2\alpha)}}\right) \quad . \quad . \tag{2.11}$$

where $\alpha=k^2\kappa T/2m$, and

$$G(k,p)=p\int_0^\infty \exp(-pt)tg(k,t)\,dt$$

$$=-p\frac{\partial}{\partial p}\left\{\frac{\tilde{g}(k,p)}{p}\right\}, \quad . \quad . \quad . \quad . \quad . \quad . \quad . \tag{2.12}$$

then

$$\frac{\tilde{C}(k,p)}{p}=\frac{\tilde{g}(k,p)C(k,0)}{p}-\frac{\omega^2G(k,p)\tilde{C}(k,p)}{p^2}, \tag{2.13}$$

$$\tilde{C}(k,p)=\frac{\tilde{g}(k,p)C(k,0)}{1+\omega^2G(k,p)/p},$$

and

$$C(k,t)=\frac{C(k,0)}{2\pi i}\int_{\epsilon-i\infty}^{\epsilon+i\infty}\frac{\exp(pt)}{p}\,\frac{\tilde{g}(k,p)}{1+\omega^2G(k,p)/p}\,dp. \quad . \quad . \quad . \tag{2.14}$$

This readily reproduces the limiting cases $\omega=0$ trivially, and for $\alpha=k^2\kappa T/2m=0$, $\tilde{g}(k,p)=1$ and $G(k,p)=1/p^2$ so that

$$C(k,t)=\frac{C(k,0)}{2\pi i}\int_{\epsilon-i\infty}^{\epsilon+i\infty}\frac{p\exp(pt)\,dp}{p^2+\omega^2} \quad . \quad . \quad . \quad . \tag{2.15}$$

$$=C(k,0)\cos\omega t \quad . \quad . \quad . \quad . \quad . \quad . \quad . \quad . \quad . \tag{2.16}$$

as in (1.13).

Though the integral (2.14) cannot be evaluated without further approximation, an important use of it is in transport theory where its time integral is required in the kernel of the Boltzmann integral equation. This can be obtained analytically, for let it be called Λ_k:

$$\Lambda_k = \int_0^\infty C(k,t)\,dt. \qquad (2.17)$$

Then

$$\Lambda_k = \left.\frac{\tilde{C}(k,p)}{p}\right|_{p=0} \qquad (2.18)$$

$$= \left.\frac{(\tilde{g}_k(p)/p)C(k,0)}{1+\omega^2 G(k,p)/p}\right]_{p=0} \qquad (2.19)$$

$$= \frac{\frac{1}{2}\sqrt{(\pi/\alpha)}C(k,0)}{1+\omega^2/2\alpha} \qquad (2.20)$$

$$= \frac{\sqrt{\pi}}{2}\,C(k,0)\,\frac{(2m/k^2kT)^{1/2}}{1+\omega^2 m/k^2\kappa T}. \qquad (2.21)$$

But $\omega^2 = 4\pi e^2 N/mV$ and $\lambda^2 = VkT/4\pi e^2 N$, therefore

$$\Lambda_k = \sqrt{\frac{\pi}{2}}\,\frac{C(k,0)}{k}\left(\frac{m}{\kappa T}\right)^{1/2}(1+(k^2\lambda^2)^{-1})^{-1}. \qquad (2.22)$$

The dynamical effect of the Coulomb interaction upon Λ_k is to multiply it by a factor $(1+(k^2\lambda^2)^{-1})^{-1}$, so using the fact that $C(k,0)$ is N times this factor

$$\Lambda_k = \sqrt{\frac{\pi}{2}}\,\frac{1}{k}\left(\frac{m}{\kappa T}\right)^{1/2}(1+(k^2\lambda^2)^{-1})^{-2}. \qquad (2.23)$$

Approximate evaluations of (2.14) can be made near the limits $\omega=0$ and $\alpha=0$. For the latter one can compare the discussion given by Landau (1946), for the problem of plasma oscillations, which, though discussing a slightly different problem and using a different derivation, reduces to very similar analysis to that given above.

Another way to approximate to $C(k,t)$ has been given (Edwards 1958) by fitting the exact Taylor expansion of $C(k,t)$ to the form $\cos\sqrt{(at)}\exp(-bt^2)$, and this checks with a similar approximate evaluation of (2.14).

The correlation function for the current can be deduced immediately for the above in the absence of a magnetic field since the only vector available in the problem is $\mathbf{k}$. They are

$$\langle \mathbf{j}_{\mathbf{k}}(t)\rho_{\mathbf{k}}^*(0)\rangle = \mathbf{k}(k^2)^{-1}\partial C/\partial t, \qquad (2.24)$$

$$\langle j_{k_\alpha}(t)\,j_{k_\beta}(0)\rangle = \frac{k_\alpha k_\beta}{(k^2)^2}\,\frac{\partial^2 C}{\partial t^2}. \qquad (2.25)$$

These results can also of course be obtained by setting up integral equations for them and solving directly.

§ 3. THE CORRELATION FUNCTION IN THE PRESENCE OF AN EXTERNAL FIELD

The presence of a constant external magnetic field $(0, 0, B)$ alters the equations of motion to

$$m\ddot{\mathbf{x}}_\alpha(t) = e^2 \sum \frac{\mathbf{x}_\alpha(t) - \mathbf{x}_\beta(t)}{|\mathbf{x}_\alpha(t) - \mathbf{x}_\beta(t)|^3} + \frac{e}{c}\dot{\mathbf{x}}_\alpha \times \mathbf{B} \quad . \quad . \quad . \quad . \quad (3.1)$$

which has the formal solution

$$\begin{aligned} x_\alpha(t) &= x_\alpha + \Omega^{-1}(u_\alpha \sin \Omega t + v_\alpha(1 - \cos \Omega t)) \\ &\quad + \frac{4\pi e^2}{V} \sum_{\alpha \neq \gamma} \int_0^t ds \int_0^s d\tau \{\cos(\Omega(\tau - s))(x_\alpha(\tau) - x_\gamma(\tau)) \\ &\quad + \sin \Omega(\tau - s)(y_\alpha(\tau) - y_\gamma(\tau))\} |\mathbf{x}_\alpha(\tau) - \mathbf{x}_\gamma(\tau)|^{-3} \, d\tau, \quad . \quad . \quad (3.2) \end{aligned}$$

$$\begin{aligned} y_\alpha(t) &= y_\alpha + \Omega^{-1}(v_\alpha \sin \Omega t - u_\alpha(1 - \cos \Omega t)) \\ &\quad + \frac{4\pi e^2}{V} \sum_{\alpha \neq \gamma} \int_0^t ds \int_0^s d\tau \{\cos[\Omega(s - \tau)](y_\alpha(\tau) - y_\gamma(\tau)) \\ &\quad + \sin[\Omega(\tau - s)][x_\alpha(\tau) - x_\gamma(\tau)]\} |\mathbf{x}_\alpha - \mathbf{x}_\gamma(\tau)|^{-3}, \quad . \quad . \quad . \quad (3.3) \end{aligned}$$

$$z_\alpha(t) = z_\alpha + w_\alpha t + \frac{4\pi e^2}{V} \int_0^t ds \int_0^s d\tau (z_\alpha(\tau) - z_\gamma(\tau)) |\mathbf{x}_\alpha(\tau) - \mathbf{x}_\gamma(\tau)|^{-3}. \quad (3.4)$$

One proceeds exactly as in the last section, (2.5)–(2.9), the final equation being

$$C(k, t) = g(k, t)C(k, 0) - \omega^2 \int_0^t ds \int_0^s d\tau Q(s - \tau) g(k, t - \tau) C(k, t) \quad (3.5)$$

where $g_k(t)$ is the appropriate function in the magnetic field

$$\exp[-(k \,.\, B)^2 t^2 \kappa T / 2mB^2 - (k \times B)^2 (1 - \cos \Omega t) \kappa T / \Omega^2 B^2 m] \quad (3.6)$$

and

$$Q(s - t) = (k^2 B^2)^{-1} [(\mathbf{k} \,.\, \mathbf{B})^2 + (\mathbf{k} \times \mathbf{B})^2 \cos \Omega(s - \tau)]. \quad (3.7)$$

In this form (3.5) clearly reduces to (2.8) when Ω goes to 0.

By integration by parts (3.5) becomes

$$\begin{aligned} C(k, t) = g(k, t)C(k, 0) - \omega^2 \int_0^t \Big\{ (k^2 B^2)^{-1} \Big[(\mathbf{k} \,.\, \mathbf{B})^2 (t - \tau) + (\mathbf{k} \times \mathbf{B})^2 \frac{\sin \Omega(t - \tau)}{\Omega} \Big] \\ \times g(k, t - \tau) C(k, \tau) \, d\tau \Big\}. \quad (3.8) \end{aligned}$$

This equation can now be solved by the Laplace transform, since

$$\begin{aligned} \frac{\tilde{C}(k, p)}{p} = \frac{\tilde{g}(k, p)C(k, 0)}{p} - \frac{\omega^2}{p} (k^2 B^2)^{-1} \Big[(\mathbf{k} \,.\, \mathbf{B})^2 \frac{G(k, p)}{p} \\ + \frac{(\mathbf{k} \times \mathbf{B})^2}{2i\Omega} \Big(\frac{\tilde{g}(k, p - i\Omega)}{p - i\Omega} - \frac{\tilde{g}(k, p + i\Omega)}{p + i\Omega} \Big) \Big] \tilde{C}(k, p) \quad (3.9) \end{aligned}$$

and therefore

$$C(k,t) = \frac{C(k,0)}{2\pi i} \int_{\epsilon - i\infty}^{\epsilon + i\infty} \frac{\exp(pt)}{p}$$

$$\times \frac{\tilde{g}(k,p)}{\left[1 + \frac{\omega^2}{p} (k^2 B^2)^{-1} \left\{ (\mathbf{k}\,.\,\mathbf{B})^2 G(k,p)/p + [(\mathbf{k} \times \mathbf{B})^2/2i\Omega] \mathscr{I} \left(\frac{\tilde{g}(k, p - i\Omega)}{p - i\Omega} \right) \right\} \right]} \quad . \quad . \quad . \quad (3.10)$$

the symbol $\mathscr{I}$ meaning the imaginary part.

As before the time integral of C takes a simple form, but not so simple that it can be evaluated explicitly

$$\Lambda_k = \frac{C(k,0) \int_0^\infty g(k,t)\, dt}{1 + \omega^2 \int_0^\infty Q(t) g(k,t)\, dt} \quad . \quad . \quad . \quad . \quad . \quad (3.11)$$

§ 4. Higher Approximations

To investigate the approximation used above, before analysing the complete problem, consider the next approximation to the integral equation; for simplicity work without the magnetic field though there is no reason in principle why it should not be included. It turns out that to the next order the new terms coming from the expansion of the exponential and from the further expansion of $x_\alpha(t)$ give

$$\frac{e^4}{m^2} \left[\int_0^t d\tau \int_0^\tau d\sigma_1 \int_0^{\sigma_1} d\sigma_3 \int_0^{\sigma_3} d\sigma_2 \left\{ \frac{(\mathbf{k}\,.\,\mathbf{j})/(\mathbf{k}\,.\,\mathbf{l})}{j^2 l^2} \right\} \right.$$
$$\left. + \frac{1}{2} \int_0^t d\tau_1 \int_0^{\tau_1} d\sigma_1 \int_0^t d\tau_2 \int_0^{\tau_2} d\sigma_2 \left\{ \frac{(\mathbf{k}\,.\,\mathbf{j})(\mathbf{j}\,.\,\mathbf{l})}{j^2 l^2} \right\} R(t, \sigma_1, \sigma_2) \right] \quad (4.1)$$

where

$$R(t, \sigma_1, \sigma_2) = \sum_{\alpha\beta\gamma\delta} \langle \exp [i\mathbf{x}_\alpha(\mathbf{k} + \mathbf{j} + \mathbf{l}) + i\mathbf{v}_\alpha(\mathbf{k}t + \mathbf{j}\sigma_1 + \mathbf{l}\sigma_2)$$
$$- \mathbf{j}\,.\,\mathbf{x}_\gamma(\sigma_1) - \mathbf{l}\,.\,\mathbf{x}_\delta(\sigma_2) - i\mathbf{k}\,.\,\mathbf{x}_\beta] \rangle. \quad (4.2)$$

These terms can be estimated from the original integral eqn. (2.8) and are smaller by a power of the density, except in as far as there will be some terms of the expansion in which pairs of the indices α, β, γ, δ are equal. These correspond to the fact that the expansion of the collision of two particles as a power series in e^2 has nothing to do with the density but only with the smallness of e^2 and the analyticity of the scattering cross section in terms of e^2. For the Coulomb case this is strictly speaking a difficulty for the potential is unbounded near the origin, and one has the same kind of difficulty that arises in say the Fokker–Planck equation. This in practice is not very serious and can be avoided crudely by cutting the potential off at small distances, i.e. large **k**, or by using the correct description of two-body scattering after the manner of the recent developments in nuclear structure (see e.g. Watson 1953). A more general discussion of the higher approximations to the correlation function will be given in another paper since they involve more powerful mathematical techniques than are involved here.

ACKNOWLEDGMENTS

The author would like to thank Professor B. H. Flowers and Dr. W. B. Thompson for their discussions of this work and Mr. T. Gaskell for checking the calculations. Part of the work was done whilst the author was Vacation Consultant at A.E.R.E., in the summer of 1958 and the author would like to thank the head of the Theoretical Physics Division for his hospitality.

REFERENCES

EDWARDS, S. F., 1958, *Phil. Mag.*, **3,** 302 ; 1959, *Ibid.*, **4,** 1171.
LANDAU, L. D., 1946, *J. Phys., Moscow.*, **10,** 25.
WATSON, K. M., 1953, *Phys. Rev.*, **89,** 575.

A New Approach to Transport Problems in Fully Ionized Plasmas†

By S. F. Edwards and J. J. Sanderson
Theoretical Physics Department, University of Manchester, and
Theoretical Physics Division, A.E.R.E., Harwell‡

[Received July 11, 1960]

Abstract

Exact formulae for transport coefficients are given in terms of one and two-body equilibrium Green functions in velocity space. Equations are derived for these Green functions which apply under plasma conditions and which automatically include shielding and plasma oscillation effects. The method is illustrated by simple examples.

§ 1. Introduction

The problem of obtaining the transport coefficients of a fully ionized plasma concerns the fact that one cannot describe the physical consequences of the long-range coulomb potential in terms of the two-body encounters of the usual Boltzmann equation of gas dynamics. The many-body effects resulting from the long-range forces alter the static and dynamic properties of the gas, producing the shielding of the forces and the ability of the plasma to sustain plasma oscillations. The object of this paper is to derive a method of calculating transport properties when the long-range nature of the forces is properly taken into account. The method depends essentially on the fact that the equilibrium properties of the plasma are completely given by the Gibbs distribution $\exp(-H/\kappa T)$. If one considers situations not far removed from equilibrium one can derive transport equations based on the static averages derived from the Gibbs function, and on the dynamic correlation functions which are derived from the Gibbs function and the equations of motion. In this way the Debye–Hückel shielding and the effects of plasma oscillations should appear naturally in the transport equations and do not have to be inserted in the *ad hoc* manner adopted for example, when one uses a shielded potential in the Boltzmann or Fokker Planck equations.

Any approach to the transport problem must be approximate in some sense to be useful, and it is important therefore to be able to understand the nature and magnitude of higher approximations, and a considerable part of this paper is involved with this point. The actual formulation of the problem is in terms of the Green functions for the propagation of one and two particles which reproduce mathematically a faithful analogue of the actual physical processes taking place. In this paper the simplest transport coefficient, the electical conductivity, is treated in detail and the equations for the appropriate Green functions derived. The method is illustrated by applying it to the Lorentz gas, detailed calculations of the conductivity and other transport coefficients being deferred to a subsequent paper.

---

† Communicated by the Author.
‡ Vacation Consultants.

§ 2. THE DERIVATION OF EXACT FORMULAE FOR THE TRANSPORT COEFFICIENTS

The simplest transport problem is that of electrical conductivity, in which the distribution function $f(\mathbf{r}_1 \ldots \mathbf{r}_n, \mathbf{u}_1 \ldots \mathbf{u}_n, t)$ may be taken in the form

$$f = f_0 + f_1 \qquad \text{(2.1)}$$

f_0 being the partition function

$$f_0 = \exp\left(-H(\mathbf{r}_1, \ldots, \mathbf{r}_n, \mathbf{u}_1, \ldots, \mathbf{u}_n)/\kappa T + F/\kappa T\right) \qquad \text{(2.2)}$$

and f_1 the change resulting from the presence of the external electric field $\mathscr{E}$ which may be time dependent. Liouville's equation governs f:

$$\frac{\partial f}{\partial t} + \sum_{\alpha} \mathbf{u}_{\alpha} \frac{\partial f}{\partial r_{\alpha}} + \sum_{\alpha \neq \beta} \frac{\mathbf{F}(\mathbf{r}_{\alpha} - \mathbf{r}_{\beta})}{m_{\alpha}} \cdot \frac{\partial f}{\partial \mathbf{u}_{\alpha}} + \sum \frac{e_{\alpha}}{m_{\alpha}} \mathscr{E} \cdot \frac{\partial f}{\partial \mathbf{u}_{\alpha}} = 0. \qquad \text{(2.3)}$$

Since f_0 satisfies this equation but for the term in $\mathscr{E}$, and

$$H = \sum \tfrac{1}{2} m_{\alpha} \mathbf{u}_{\alpha}^{2} - \sum \Phi(\mathbf{r}_{\alpha} - \mathbf{r}_{\beta}), \qquad \text{(2.4)}$$

where Φ is the coulomb potential $e_{\alpha} e_{\beta}/|\mathbf{r}_{\alpha} - \mathbf{r}_{\beta}|$, the equation for f_1, ignoring for the moment the dependence of f_1 upon $\mathscr{E}$, is

$$\left(\frac{\partial}{\partial t} + \sum_{\alpha} \mathbf{u}_{\alpha} \cdot \frac{\partial}{\partial \mathbf{r}_{\alpha}} + \sum_{\alpha \neq \beta} \frac{\mathbf{F}_{\alpha\beta}}{m_{\alpha}} \cdot \frac{\partial}{\partial \mathbf{u}_{\alpha}}\right) f_1 = \sum_{\alpha} e_{\alpha} \mathbf{u}_{\alpha} \cdot \mathscr{E} f_0/\kappa T. \qquad \text{(2.5)}$$

Consider the Green function of the left-hand side defined by

$$\begin{aligned}\left(\frac{\partial}{\partial t} + \sum \mathbf{u}_{\alpha} \cdot \frac{\partial}{\partial \mathbf{r}_{\alpha}} + \sum_{\alpha \neq \beta} \frac{1}{m_{\alpha}} \mathbf{F}_{\alpha\beta} \cdot \frac{\partial}{\partial \mathbf{u}_{\beta}}\right) & G(\mathbf{r}_1, \ldots, \mathbf{r}_n, \mathbf{u}_1, \ldots, \mathbf{u}_n, \mathbf{r}'_1 \ldots, \mathbf{r}_n', \\ & \times \mathbf{u}_1', \ldots, \mathbf{u}_n', t, t',) = \prod_{\alpha} \delta(\mathbf{r}_{\alpha} - \mathbf{r}_{\alpha}')\delta(\mathbf{u}_{\alpha} - \mathbf{u}_{\alpha}')\delta(t - t'). \qquad \text{(2.6)}\end{aligned}$$

This function formally solves (2.5) giving

$$\begin{aligned} f_1(\mathbf{r}_1, \ldots, \mathbf{r}_n, \mathbf{u}_1, \ldots, \mathbf{u}_n, t) = \int \cdots \int & G(\mathbf{r}_1, \ldots, \mathbf{r}_n, \mathbf{u}_1, \ldots, \mathbf{u}_n, \mathbf{r}_1', \ldots \mathbf{r}_n', \\ & \times \mathbf{u}_1', \ldots, \mathbf{u}_n', t, t') \sum_{\alpha} \frac{e_{\alpha}}{\kappa T} \mathbf{u}_{\alpha}' \cdot \mathscr{E} f_0(\mathbf{r}_1', \ldots, \mathbf{r}_n', \mathbf{u}_1', \ldots, \mathbf{u}_n') \\ & \times \prod_{\alpha} d^3 r'_{\alpha} d^3 u'_{\alpha} \, dt'. \qquad \text{(2.7)}\end{aligned}$$

Hence the current

$$\mathbf{j}(\mathbf{r}, t) = \int \cdots \int \sum \mathbf{u}_{\alpha} e_{\alpha} \delta(\mathbf{r} - \mathbf{r}_{\alpha}) \prod_{\beta} d^3 u_{\beta} d^3 r_{\beta} \qquad \text{(2.8)}$$

is, under uniform conditions, with no contribution from f_0,

$$\mathbf{j} = \int^{t} dt' \int \cdots \int \sum e_{\alpha} \mathbf{u}_{\gamma} G \sum \frac{e_{\beta}}{\kappa T} \mathbf{u}_{\beta}' \cdot \mathscr{E} f_0' \prod d^3 u_{\alpha} d^3 r_{\alpha} \prod d^3 r'_{\beta} d^3 u_{\gamma} \qquad \text{(2.9)}$$

where dashed functions refer to functions of the dashed variables. If the ions are considered fixed so that the current is carried by electrons, the current contains two terms:

$$\mathbf{j} = \frac{Ne^2}{\kappa T}\int \cdots \int \mathbf{u}_1 G \mathbf{u}_1' \,.\, \mathscr{E} f_0' \prod d^3r' \prod d^3u \prod d^3u' \prod d^3r \, dt'$$
$$+ \frac{N(N-1)e^2}{\kappa T}\int \cdots \int \mathbf{u}_1 G \mathbf{u}_2' \,.\, \mathscr{E} f_0' \prod d^3r \prod d^3r' \prod d^3v \prod d^3v' dt' \quad (2.10)$$

This formula can be reduced by introducing the Green functions G_1 and G_{12} defined by

$$G_1(\mathbf{u}_1, \mathbf{u}_1', t, t') = \int \cdots \int G(\mathbf{r}_1, \ldots, \mathbf{r}_n, \mathbf{r}_1', \ldots, \mathbf{r}_n', \ldots, \mathbf{u}_1, \ldots, \mathbf{u}_n, \mathbf{u}_1', \mathbf{u}_n', t, t')$$
$$\times \exp\left[(-H' + F + \tfrac{1}{2}mv_1'^2)/(\kappa T)\right] \prod_{\alpha} d^3r_{\alpha} d^3r_{\alpha}' \prod_{\alpha \pm \beta} d^3u_{\beta} d^3u_{\beta}' \quad . \quad . \quad . \quad (2.11)$$

and

$$G_{12}(\mathbf{u}_1, \mathbf{u}_1', \mathbf{u}_2', \mathbf{u}_2', t, t') = \int \cdots \int G(\mathbf{r}_1, \ldots, \mathbf{r}_n, \mathbf{r}_1', \ldots, \mathbf{r}_n', \mathbf{u}_1, \ldots$$
$$\times \mathbf{u}_n, \mathbf{u}_1', \ldots \mathbf{u}_n' \, t, t') \exp\left[(-H' + F + \tfrac{1}{2}m\mathbf{u}_1'^2 + \tfrac{1}{2}m\mathbf{u}_2'^2)/\kappa T\right] \prod_{\alpha} d^3r_{\alpha} d^3r_{\alpha}'$$
$$\times \prod_{\beta \neq 1, 2} d^3u_{\beta} d^3u_{\beta}' \quad . \quad . \quad . \quad (2.12)$$

These Green functions have a clear physical meaning: G_1 is the probability that in equilibrium one finds a particle at a time t' with a velocity $\mathbf{u}'$ and that subsequently the same particle has velocity $\mathbf{u}$ at t. Similarly G_{12} refers to the velocities of two particles. In both functions the spatial coordinates have been integrated out. Consider the electric field switched on at time $t = 0$, and define the conductivity by

$$j_{\alpha}(t) = \sum_{\beta} \sigma_{\alpha\beta}(t) \mathscr{E}_{\beta}, \quad . \quad . \quad . \quad . \quad . \quad . \quad . \quad . \quad (2.13)$$

then using (2.11, 2.12) one obtains

$$\sigma_{\alpha\beta} = \frac{Ne^2}{\kappa T}\left(\frac{m}{2\pi\kappa T}\right)^{3/2} \int_0^t dt' \int u_{1\alpha} G_1 u_{1\beta}' \exp(-m\mathbf{u}_1'^2/2\kappa T) d^3v_1' d^3v_1$$
$$+ \frac{N(N-1)e^2}{\kappa T}\left(\frac{m}{2\pi\kappa T}\right)^3 \int_0^t dt' \int u_{1\alpha} G_{12} u_{23}' \exp\left[(-m\mathbf{u}_1'^2 - m\mathbf{u}_2'^2)/2\kappa T\right]$$
$$\times d^3u_1 d^3u_1' d^3u_2 d^3u_2' \quad . \quad . \quad . \quad . \quad . \quad . \quad . \quad . \quad (2.14)$$

In the same way other transport coefficients can be calculated if one assumes that the system is not far removed from a local equilibrium, so that if there is a local density $n(\mathbf{r})$, a local velocity $\mathbf{V}(\mathbf{r})$ and a local temperature $T(\mathbf{r})$, the starting distribution function will be

$$f_0 = \prod n(\mathbf{r}_i) \exp\left[(-\sum m_k(\mathbf{u}_k - \mathbf{V}(\mathbf{r}_k))^2/2 + \sum_{k,j} \Phi(\mathbf{r}_k - \mathbf{r}_j))/\kappa T(\mathbf{r}_k) + F/\kappa T(\mathbf{r}_k)\right]. \quad . \quad . \quad . \quad (2.15)$$

The temperature is assumed not to vary across the effective range of the force so that it is immaterial whether $T(\mathbf{r}_k)$ or $T(\mathbf{r}_j)$ is used in (2.15).

If this form is substituted into Liouville's equation it will no longer satisfy it and just as before an f_1 will be required depending upon the gradients of n, $\mathbf{V}$, T, and giving rise to fluxes of matter, momentum and energy and hence to the coefficients of viscosity and thermal conductivity. Though it is hoped to return to explicit calculations of this type elsewhere they will be pursued no further here and the rest of the paper will be devoted to deriving G_1 and G_{12} for the electrical conductivity problem.

§ 3. THE EQUATIONS FOR THE AVERAGE PROPAGATION FUNCTIONS

It is convenient to perform the averaging in (2.11) upon the unprimed rather than the primed variables. If S is introduced by the expression

$$S=\exp\left[\left(\sum_{\alpha\neq 1} m_\alpha \mathbf{u}_\alpha{}^2\Big/2+\sum_{\alpha,\beta}\Phi_{\alpha\beta}\right)\Big/\kappa T\right]$$
$$\times G\exp\left[-\left(\sum_{\alpha\neq 1} m_\alpha u_\alpha{}'^2\Big/2+\sum_{\alpha,\beta}{}'\Phi_{\alpha\beta}\right)\Big/\kappa T\right] \quad . \quad . \quad (3.1)$$

which satisfies

$$\left(\frac{\partial}{\partial t}+\sum_{\alpha\pm 1}\mathbf{v}_\alpha\cdot\frac{\partial}{\partial \mathbf{r}_\alpha}+\sum_{\alpha\neq 1}\frac{1}{m_\alpha}\mathbf{F}_{\alpha\beta}\cdot\frac{\partial}{\partial \mathbf{u}_\beta}+\mathbf{u}_1\frac{\partial}{\partial \mathbf{r}_1}+\frac{\mathbf{F}_1}{m_1}\cdot\left(\frac{m_1\mathbf{u}_1}{\kappa T}+\frac{\partial}{\partial \mathbf{u}_1}\right)\right)S$$
$$=\prod\delta(\mathbf{r}_\alpha-\mathbf{r}_\alpha{}')\delta(\mathbf{u}_\alpha-\mathbf{u}_\alpha{}')\delta(t-t'), \quad . \quad . \quad . \quad . \quad (3.2)$$

then the average propagator G_1 is given by

$$G_1=\int\ldots\int\exp\left[-\left(\sum\Phi+\sum_{\alpha\pm 1}\tfrac{1}{2}m_\alpha\mathbf{u}_\alpha{}^2\right)\Big/\kappa T+F/\kappa T\right]S$$
$$\prod_{\alpha\pm 1} d^3r_\alpha d^3r_\alpha{}' d^3u_\alpha d^3u_\alpha{}' d^3r_1,\ d^3r_1{}' \quad . \quad . \quad . \quad . \quad . \quad (3.3)$$

Before considering the general case, which is quite complicated, the averaging process will be illustrated by considering the simpler case in which all particles but particle one are very heavy and can be considered at rest relative to particle one, though distributed in thermal equilibrium. Using Q for S in this case, the equation for Q depends dynamically only upon the variables $\mathbf{r}_1$, $\mathbf{v}_1$:

$$\left(\frac{\partial}{\partial t}+\mathbf{u}_1\cdot\frac{\partial}{\partial \mathbf{r}_1}+\sum_\alpha\frac{\mathbf{F}_{1\alpha}}{m}\cdot\left(\frac{\partial}{\partial \mathbf{u}_1}+\frac{m\mathbf{u}_1}{\kappa T}\right)\right)Q=\delta(\mathbf{r}_1-\mathbf{r}_1{}')\delta(\mathbf{v}_1-\mathbf{u}_1{}')\delta(t-t'). \quad . \quad . \quad . \quad (3.4)$$

The averaging is static, so employing brackets to mean averaging value,

$$\langle Q\rangle=\frac{1}{\mathcal{N}}\int\ldots\int Q(\mathbf{r}_1,\mathbf{r}_1{}',\mathbf{u}_1,\mathbf{u}_1{}',t,t',\mathbf{R}_1,\mathbf{R}_3,\ldots,\mathbf{R}_n)$$
$$\times\exp\left(-\sum_{\alpha,\beta}\Phi(\mathbf{R}_\alpha,\mathbf{R}_\beta)\Big/\kappa T-\sum_\alpha\Phi(\mathbf{R}_\alpha,\mathbf{r}_1)\Big/\kappa T\right)\prod_\alpha d^3R_\alpha \quad . \quad . \quad . \quad (3.5)$$

where

$$\mathcal{N}=\int\ldots\int\exp\left[-\sum_{\alpha,\beta,1}\Phi\Big/\kappa T\right]\prod_\alpha d^3R_\alpha, \quad . \quad . \quad . \quad (3.6)$$

and capital letters $R_1, \dots R_n$ are used for the static particle coordinates. To perform the averaging consider the equation for Q written by iteration in the form

$$\left(\frac{\partial Q}{\partial t} + \mathbf{u}_1 \cdot \frac{\partial Q}{\partial \mathbf{r}_1}\right) = \delta(\mathbf{r}_1 - \mathbf{r}_1{}')\delta(\mathbf{u}_1 - \mathbf{u}_1{}')\delta(t-t') - \sum_\alpha \int \frac{\mathbf{F}_{1\alpha}}{m} \cdot \left(\frac{\partial}{\partial \mathbf{u}_1} + \frac{m\mathbf{u}_1}{\kappa T}\right) Q_0$$
$$+ \sum_\alpha \sum_\beta \int \int \frac{\mathbf{F}_{1\alpha}}{m} \cdot \left(\frac{\partial}{\partial \mathbf{u}_1} + \frac{m\mathbf{u}_1}{\kappa T}\right) Q_0(\mathbf{r}_1, \mathbf{r}_1{}'', \mathbf{u}_1, \mathbf{u}_1{}'', t, t'')$$
$$\times \frac{\mathbf{F}_{1\beta}{}''}{m} \cdot \left(\frac{\partial}{\partial \mathbf{u}_1{}''} + \frac{m\mathbf{v}_1{}''}{\kappa T}\right) Q(\mathbf{r}_1{}'', \mathbf{r}_1{}', \mathbf{u}_1{}'', \mathbf{u}_1{}', t'', t') d^3r_1{}'' d^3u_1{}'' \, dt'' \qquad (3.7)$$

where Q_0 satisfies

$$\left(\frac{\partial}{\partial t} + \mathbf{u}_1 \frac{\partial}{\partial \mathbf{r}_1}\right) Q_0 = \delta(\mathbf{r}_1 - \mathbf{r}'_1)\delta(\mathbf{u}_1 - \mathbf{u}_1{}')\delta(t-t'); \qquad (3.8)$$

i.e.

$$Q_0 = \delta(\mathbf{r}_1 - \mathbf{r}_1{}' - \mathbf{u}_1(t-t'))\delta(\mathbf{u}_1 - \mathbf{u}_1{}')\Theta(t-t') \qquad (3.9)$$

where

$$\begin{aligned} \Theta(t-t') &= 1, \quad t > t', \\ &= 0, \quad t < t'. \end{aligned}$$

It will now be argued that the average of the last term in (3.7) can in a good approximation be replaced by

$$\left\langle \sum \sum \int \frac{\mathbf{F}_{1\alpha}}{m} \cdot \left(\frac{\partial}{\partial \mathbf{u}_1} + \frac{m\mathbf{u}_1}{\kappa T}\right) Q_0 \frac{\mathbf{F}_{1\beta}}{m} \left(\frac{\partial}{\partial \mathbf{u}_1{}''} + \frac{m\mathbf{u}_1{}''}{\kappa T}\right)\right\rangle \langle Q \rangle d^3r_1{}'' d^3u_1{}'' \, dt''. \qquad (3.8)$$

The average of the linear term in (3.7) vanishes, and by referring to (3.5), one can use integration by parts to show that

$$\left\langle \mathbf{u}_1 \cdot \frac{\partial Q}{\partial \mathbf{r}_1}\right\rangle = \left\langle -\sum_\alpha \frac{\mathbf{F}_{1\alpha}}{m} \cdot \frac{\mathbf{u}_1}{\kappa T} Q \right\rangle, \qquad (3.9)$$

which can be averaged approximately by the same methods:

$$\left\langle -\sum_\alpha \frac{\mathbf{F}_{1\alpha}}{m} \cdot \frac{\mathbf{u}_1}{\kappa T} Q \right\rangle \cong \frac{1}{m^2} \int \left\langle - \sum \frac{\mathbf{F}_{1\alpha}}{\kappa T} \cdot \mathbf{u}_1 Q_0 \mathbf{F}_{1\beta} \cdot \left(\frac{\partial}{\partial \mathbf{u}_1{}''} + \frac{m\mathbf{u}_1{}''}{\kappa T}\right)\right\rangle$$
$$\times \langle Q' \rangle d^3u_1{}'' d^3r_1{}'' \, dt''. \qquad (3.10)$$

So the final approximate form of the equation satisfied by $\langle Q \rangle$ is

$$\frac{\partial}{\partial r} \langle Q \rangle - \frac{1}{m^2} \int \left\langle \sum_\alpha \mathbf{F}(\mathbf{r}_1 - \mathbf{R}_\alpha) \cdot \frac{\partial}{\partial \mathbf{u}_1} Q_0(\mathbf{r}_1, \mathbf{r}_1{}'', \mathbf{u}_1, \mathbf{u}_1{}'', t, t'')\right.$$
$$\left. \times \sum_\beta \mathbf{F}(\mathbf{r}_1{}'' - \mathbf{R}_\beta) \cdot \left(\frac{\partial}{\partial \mathbf{u}_1{}''} + \frac{m\mathbf{u}_1{}''}{\kappa T}\right)\right\rangle \langle Q \rangle d^3u_1{}'' d^3r_1{}'' \, dt''$$
$$= \delta(\mathbf{r}_1 - \mathbf{r}_1{}')\delta(\mathbf{u}_1 - \mathbf{u}_1{}')\delta(t-t') \qquad (3.11)$$

That this is a good approximation can only be checked by looking at the corrections. If the exact equation for $\langle Q \rangle$ can be written in the form

$$\frac{\partial}{\partial t} \langle Q \rangle + \int M \langle Q \rangle = \delta(\mathbf{r}_1 - \mathbf{r}_1{}')\delta(\mathbf{u}_1 - \mathbf{u}_1{}')\delta(t-t'), \qquad (3.12)$$

then (3.11) can be regarded as giving the first approximation to M. The next approximation is then

$$\begin{aligned}\Big\langle \sum \mathbf{F} \cdot \frac{\partial}{\partial \mathbf{u}} Q_0 \sum \mathbf{F} \cdot \left(\frac{\partial}{\partial \mathbf{u}''} + \frac{m\mathbf{u}''}{\kappa T}\right) \Theta \left(\sum \mathbf{F} \cdot \left(\frac{\partial}{\partial \mathbf{u}''} + \frac{m\mathbf{u}''}{\kappa T}\right) + \mathbf{u}'' \cdot \frac{\partial}{\partial \mathbf{r}''}\right) Q_0 \\ \times \sum \mathbf{F} \cdot \left(\frac{\partial}{\partial \mathbf{u}'''} + \frac{m\mathbf{u}'''}{\kappa T}\right)\Big\rangle - \Big\langle \sum \mathbf{F} \cdot \frac{\partial}{\partial \mathbf{u}} Q_0 \sum \mathbf{F} \cdot \left(\frac{\partial}{\partial \mathbf{u}''} + \frac{m\mathbf{u}''}{\kappa T}\right)\Big\rangle \\ \times \Theta \Big\langle \sum \mathbf{F} \cdot \frac{\partial}{\partial \mathbf{u}''} Q_0 \sum \mathbf{F} \cdot \left(\frac{\partial}{\partial \mathbf{u}''} + \frac{m\mathbf{u}''}{\kappa T}\right)\Big\rangle, \qquad (3.13)\end{aligned}$$

since the terms involving the correlation of three forces give a small contribution of order of the square of the ratio of the interparticle distance to the Debye length.

The term
$$\mathbf{F} \cdot \left(\frac{\partial}{\partial \mathbf{u}''} + \frac{m\mathbf{u}''}{\kappa T}\right) + \mathbf{u}'' \cdot \frac{\partial}{\partial \mathbf{r}''}$$

is at a time t''', but the average has a material value only if $t''' \sim t$, in fact if $t''' - t$ is less than a collision time, because the two F's are strongly decreasing functions. This being the case one can integrate the term $u'' . \partial/\partial r''$ by parts, just as in (3.9), replacing it by $-\mathbf{F} . m\mathbf{u}''/\kappa T$. Thus (3.13) becomes

$$\begin{aligned}\Big\langle \sum \mathbf{F} \cdot \frac{\partial}{\partial \mathbf{u}} Q_0 \sum \mathbf{F} \cdot \left(\frac{m\mathbf{u}''}{\kappa T} + \frac{\partial}{\partial \mathbf{u}''}\right) \Theta \sum \mathbf{F} \cdot \frac{\partial}{\partial \mathbf{u}''} Q_0 \sum \mathbf{F} \cdot \left(\frac{\partial}{\partial \mathbf{u}'''} + \frac{m\mathbf{u}'''}{\kappa T}\right)\Big\rangle \\ - \Big\langle \sum \mathbf{F} \cdot \frac{\partial}{\partial \mathbf{u}} Q_0 \sum \mathbf{F} \cdot \left(\frac{\partial}{\partial \mathbf{u}''} + \frac{m\mathbf{u}''}{\kappa T}\right)\Big\rangle \Theta \Big\langle \sum \mathbf{F} \cdot \frac{\partial}{\partial \mathbf{u}''} Q_0 \sum \mathbf{F} \cdot \left(\frac{\partial}{\partial \mathbf{u}'''} + \frac{m\mathbf{u}'''}{\kappa T}\right)\Big\rangle. \\ \qquad (3.14)\end{aligned}$$

This term has the same dependence upon the coordinates of the free particle in both parts, and its magnitude therefore depends on the size of multiple averages which are schematically in the form

$$\langle \sum \mathbf{F} \sum \mathbf{F} \sum \mathbf{F} \sum \mathbf{F} \rangle - \langle \sum \mathbf{F} \sum \mathbf{F} \rangle \langle \sum \mathbf{F} \sum \mathbf{F} \rangle. \qquad (3.15)$$

In the same way the next term will depend on a combination of the six, four, and two force averages. The validity of (3.11) depends then on the cancellation to a good approximation of the two terms of (3.15), since it can be shown that either of these terms can give rise to corrections to the transport coefficients comparable with their values derived from (3.11). Writing out the terms of (3.15) in detail they are

$$\sum_{\alpha, \beta} \langle \mathbf{F}(\mathbf{r}_1 - \mathbf{R}_\alpha) \mathbf{F}(\mathbf{r}_1' - \mathbf{R}_\beta) \rangle$$

and

$$\sum_{\alpha, \beta, \gamma, \delta} \langle \mathbf{F}(\mathbf{r}_1 - \mathbf{R}_\alpha) \mathbf{F}(\mathbf{r}_1' - \mathbf{R}_\beta) \mathbf{F}(\mathbf{r}_1'' - \mathbf{R}_\gamma) \mathbf{F}(\mathbf{r}_1''' - \mathbf{R}_\delta) \rangle. \qquad (3.16)$$

It is simpler to consider these quantities Fourier transformed

$$\sum_{\alpha,\beta}\langle \mathbf{F}_i(\mathbf{r}_1-\mathbf{R}_\alpha)\mathbf{F}_l(\mathbf{r}_1{}'-\mathbf{R}_\beta)\rangle$$

$$=-\frac{2e^4}{\pi}\sum_{k,j}k_ij_l\exp(i\mathbf{k}\,.\,\mathbf{r}_1+i\mathbf{j}\,.\,\mathbf{r}_1{}')\sum_{\alpha,\beta}\langle\exp(-i\mathbf{k}\,.\,\mathbf{R}_\alpha-i\mathbf{j}\,.\,\mathbf{R}_\beta)\rangle, \quad . \quad . \quad . \quad (3.17)$$

$$\sum_{\alpha,\beta,\gamma,\delta}\langle \mathbf{F}_i(\mathbf{r}_1-\mathbf{R}_\alpha)\mathbf{F}_l(\mathbf{r}_1{}'-\mathbf{R}_\beta)\mathbf{F}_m(\mathbf{r}_1{}''-\mathbf{R}_\gamma)\mathbf{F}_n(\mathbf{r}_1{}'''-\mathbf{R}_\delta)\rangle$$

$$=\frac{4e^8}{\pi^2}\sum_{\mathbf{k},\mathbf{j},\mathbf{p},\mathbf{q}}k_ij_lp_mq_n\exp[i(\mathbf{k}\,.\,\mathbf{r}_1+\mathbf{j}\,.\,\mathbf{r}_1{}'+\mathbf{p}\,.\,\mathbf{r}_1{}''+\mathbf{q}\,.\,\mathbf{r}_1{}''')]$$

$$\times\sum_{\alpha,\beta,\gamma,\delta}\langle\exp[-i(\mathbf{k}\,.\,\mathbf{R}_\alpha+\mathbf{j}\,.\,\mathbf{R}_\beta+\mathbf{p}\,.\,\mathbf{R}_\gamma+\mathbf{q}\,.\,\mathbf{R}_\delta)]\rangle. \qquad (3.18)$$

The homogeneity of the averaged system requires that

$$\sum_{\alpha,\beta}\langle\exp(-i\mathbf{k}\,.\,\mathbf{R}_\alpha-i\mathbf{j}\,.\,\mathbf{R}_\beta)\rangle=\delta(\mathbf{k}+\mathbf{j})\Big\langle\sum_{\alpha,\beta}\exp(-i\mathbf{k}\,.\,(\mathbf{R}_\alpha-\mathbf{R}_\beta))\Big\rangle$$

$$=\delta(\mathbf{k}+\mathbf{j})C(k^2),\quad \text{say,} \quad . \quad . \quad . \quad (3.19)$$

and

$$\sum_{\alpha,\beta,\gamma,\delta}\langle\exp[-i(\mathbf{k}\,.\,\mathbf{R}_\alpha+\mathbf{j}\,.\,\mathbf{R}_\beta+\mathbf{p}\,.\,\mathbf{R}_\gamma+\mathbf{q}\,.\,\mathbf{R}_\delta)]\rangle$$

$$=\delta(\mathbf{k}+\mathbf{j}+\mathbf{p}+\mathbf{q})d(\mathbf{k},\mathbf{j},\mathbf{p},\mathbf{q}). \quad . \quad . \quad (3.20)$$

A detailed account of the evaluation of the averages will be given in the Appendix; to the accuracy of taking the Debye length λ much greater than the interparticle distance μ one obtains

$$C(k^2)=N/(1+k^{-2}\lambda^{-2}). \quad . \quad . \quad . \quad . \quad (3.21)$$

It is now essential for the cancellation in the expression (3.15) that the four-particle average splits to a good approximation into

$$\delta(\mathbf{k}+\mathbf{j}+\mathbf{p}+\mathbf{q})d(\mathbf{k},\mathbf{j},\mathbf{p},\mathbf{q})$$

$$\cong\delta(\mathbf{k}+\mathbf{j})\delta(\mathbf{p}+\mathbf{q})C(k^2)C(p^2)+\delta(\mathbf{k}+\mathbf{p})\delta(\mathbf{j}+\mathbf{q})C(k^2)C(q^2)$$

$$+\delta(\mathbf{k}+\mathbf{q})\delta(\mathbf{j}+\mathbf{p})C(k^2)C(j^2). \qquad (3.22)$$

That this is indeed the case in a plasma is discussed in the Appendix. The term with $\delta(\mathbf{k}+\mathbf{j})\delta(\mathbf{p}+\mathbf{q})$ produces the desired cancellation, and the two remaining terms can be shown to produce only small corrections to the transport coefficients, of order $(\mu/\lambda)^3$. It is important to realize that this cancellation does not happen in more general systems such as a normal liquid, though it is extensively employed there, being equivalent to the superposition approximation. Indeed a fully ionized plasma is perhaps the only physical system for which the approximation really works. Readers familiar with quantum field theory or many-body theory, will recognize the above discussion as being equivalent to saying that the single particle mass operator may be calculated by perturbation theory i.e. by the first Feynman diagram.

Returning now to the general problem (3.1) one can see how (3.11) will be generalized in physical terms. Equation (3.11) shows how a particle moves on an average in velocity space through an equilibrium distribution of heavy charged particles, the kernel of eqn. (3.11), being derived from the mean second approximation to the motion of the particle, or in quantum mechanical language from the mean second Born approximation. Now in fact the particles of the plasma are moving with their random velocities and with the thermal distribution of plasma oscillations. So one may expect not just the instantaneous correlation function to enter, but the time dependent correlation function. If $\mathbf{R}_\alpha(t)$ is regarded as the coordinate of a particle in the Lagrangian sense, and is taken to be a solution of the equations of motion having the initial conditions averaged over the Gibbs function $\exp(-H/\kappa T)$, one expects

$$C(k,t-t')=\left\langle \sum_{\alpha,\beta} \exp(i\mathbf{k}\,.\,(\mathbf{R}_\alpha(t)-\mathbf{R}_\beta(t')))\right\rangle \quad . \quad . \quad (3.23)$$

to play the part previously taken by $C(k^2)$.

Another way to look at this is to recognize $\sum\limits_\alpha \exp(i\mathbf{k}\,.\,\mathbf{R}_\alpha)$ as the kth fourier component P_k of the density

$$P(\mathbf{r})=\sum_\alpha \delta(\mathbf{r}-\mathbf{R}_\alpha) \quad . \quad . \quad . \quad . \quad . \quad (3.24)$$

in terms of which

$$C(k^2)=\langle P_k P_k{}^*\rangle \quad . \quad . \quad . \quad . \quad . \quad . \quad (3.25)$$

and

$$C(k,t-t')=\langle P_k(t)P_k{}^*(t')\rangle. \quad . \quad . \quad . \quad . \quad (3.26)$$

The electrons move under the influence of forces from protons and electrons, the force acting upon it, depending upon the density of charge. So if P_k is used as above for the density of protons, and ρ_k for electrons, then ρ_k-P_k is the density of negative charge. One would thus expect in the general problem to find the charge correlation function,

$$C(k,t-t')=\langle(\rho_k(t)-P_k(t))(\rho_k{}^*(t')-P_k{}^*(t'))\rangle \quad (3.27)$$

playing the part of $C(k^2)$.

To derive the differential equation for G_1 as defined by (3.1) it is convenient to think of all the particles except particle one in the Lagrangian description, retaining the Liouville description of particle one. The equation for S then becomes, retaining capital $\mathbf{R}_\alpha$ for the Lagrangian coordinate of the αth particle,

$$\left(\frac{\partial}{\partial t}+\mathbf{u}_1\,.\,\frac{\partial}{\partial \mathbf{r}_1}+\sum\frac{1}{m}\mathbf{F}(\mathbf{r}_1-\mathbf{R}_\alpha)\,.\left(\frac{\partial}{\partial \mathbf{u}_1}+\frac{m\mathbf{u}_1}{\kappa T}\right)\right)S(\mathbf{r}_1,\mathbf{r}_1',\mathbf{u}_1,\mathbf{u}_1',\mathbf{R}_\alpha(t),t,t')$$
$$=\delta(t-t')\delta(\mathbf{r}_1-\mathbf{r}_1')\delta(\mathbf{u}_1-\mathbf{u}_1') \quad . \quad . \quad . \quad (3.28)$$

where

$$m_\alpha\ddot{\mathbf{R}}_\alpha=\sum_{\beta\neq\alpha}\mathbf{F}(\mathbf{R}_\alpha(t)-\mathbf{R}_\beta(t))+\mathbf{F}(\mathbf{R}_\alpha(t)-\mathbf{R}_1(t)), \quad . \quad . \quad (3.29)$$

and

$$\mathbf{R}_1(t)=\int \mathbf{r}_1 S(\mathbf{r}_1,\mathbf{r}_1',\mathbf{u}_1,\mathbf{u}_1',\mathbf{R}_\alpha(t),t,t')\,d^3r_1\,d^3u_1. \quad . \quad . \quad (3.30)$$

The boundary conditions upon the $\mathbf{R}_\alpha$'s are

$$\mathbf{R}_\alpha(t')=\mathbf{r}_\alpha' \quad \text{and} \quad \dot{\mathbf{R}}_\alpha(t')=\mathbf{u}_\alpha'. \quad . \quad . \quad . \quad (3.31)$$

This system is of course identical with (3.1, 2). Physically particle one moves in the fluctuating field of all the other particles according to eqn. (3.29). The other particles interact amongst themselves and are influenced by particle one through the coupling of (3.29) with (3.30). Hence in (3.28) the field acting on particle one depends upon its own motion in the past through the dependence of the $\mathbf{R}_\alpha$'s upon $\mathbf{R}_1$ of (3.29). This must be a very small effect, however, only of order $(1/N)$, and will be ignored, so that the system (3.28) and the modified equations

$$m_\alpha \ddot{\mathbf{R}}_\alpha(t) = \sum_\beta \mathbf{F}(\mathbf{R}_\alpha(t) - \mathbf{R}_\beta(t)) \qquad . \quad . \quad . \quad (3.29')$$

will be assumed henceforth. Now one can proceed precisely as before, leading to

$$\frac{\partial G_1}{\partial t} - \sum \sum \int \Big\langle \mathbf{F}(\mathbf{r}_1 - \mathbf{R}_\alpha(t) \, . \, \frac{\partial}{\partial \mathbf{u}_1} Q_0(\mathbf{r}_1, \mathbf{r}_1'', \mathbf{u}_1, \mathbf{u}_1'', t, t'') \sum \mathbf{F}(\mathbf{r}_1'' - \mathbf{R}_\alpha(t''))$$
$$\times \left(\frac{\partial}{\partial \mathbf{u}_1''} + \frac{m \mathbf{u}_1''}{\kappa T} \right) \Big\rangle \, . \, G_1(\mathbf{u}_1'', \mathbf{u}_1', t'', t') \, d^3 u_1'' \, d^3 r_1'' \, dt'' = \delta(\mathbf{u}_1 - \mathbf{u}_1') \delta(t - t').$$
$$. \quad . \quad . \quad (3.32)$$

Using the correlation function $C(k, t)$ defined in (3.27) this can be written

$$\frac{\partial G_1}{\partial t} + \int \sum_{\mathbf{k}} \int \left(\frac{1}{k^2} \right)^2 C(k, t - t'') \mathbf{k} \, . \, \frac{1}{\partial \mathbf{u}_1} Q_0(\mathbf{u}_1, \mathbf{u}_1'', t, t'') \mathbf{k} \, . \left(\frac{\partial}{\partial \mathbf{u}_1''} + \frac{m \mathbf{u}_1''}{\kappa T} \right)$$
$$\times G_1(\mathbf{u}_1'', \mathbf{u}_1', t'', t') \, dt'' \, d^3 u_1'' = \delta(\mathbf{u}_1 - \mathbf{u}_1') \delta(t - t'). \qquad (3.33)$$

The function $C(k, t)$ is a property of equilibrium, and can be calculated to the accuracy of the other approximations of this paper by various means, for example by the method of the preceding paper. If $g(k, t)$ is defined by

$$g(k, t) = \exp(-k^2 t^2 \kappa T / 2m), \qquad . \quad . \quad . \quad . \quad (3.34)$$

then $C(k, t)$ satisfies

$$C(k, t - t') = \tfrac{1}{2}(g(k, t - t') + 1) C(k, 0) + \omega^2 \int_{t'}^{t} g(k, t - s) C(k, s) \, ds, \qquad (3.35)$$

where ω is the plasma frequency given by $\omega^2 = 4\pi N e^2 / V$. This is solved by the Laplace transform giving

$$C(k, t - t') = \frac{C(k, 0)}{2\pi i} \int_{\epsilon - i\infty}^{\epsilon + i\infty} \frac{\exp(pt)}{p} \, \frac{(\tilde{g}(k, p) + 1)}{2(1 + \omega^2 \tilde{G}_k(p)/p)} \, dp \qquad (3.36)$$

where

$$\tilde{g}(k, p) = p \int_0^\infty \exp(-pt) g(k, t) \, dt \qquad . \quad . \quad . \quad . \quad (3.37)$$

and

$$\tilde{G}_{\boldsymbol{k}}(p) = -p \frac{\partial}{\partial p} \left(\frac{\tilde{g}}{p} \right). \qquad . \quad . \quad . \quad . \quad . \quad . \quad . \quad (3.38)$$

Since Q_0 is given by (3.9), the kernel of (3.33) contains

$$\int \exp(i\mathbf{k}\,.\,\mathbf{u}t)C(k,t)\,d^3k.$$

Moreover it can be assumed that G_1 varies very slowly in time compared with a collision time, so that the time integral can be extended to infinity. This gives the kernel directly in terms of the Laplace integral

$$P(\mathbf{k},\mathbf{u})=\left\{\frac{1}{2}\int_0^\infty \exp(i\mathbf{k}\,.\,\mathbf{v}t-k^2t^2\kappa T/2m)\,dt+\pi\delta(\mathbf{k}\,.\,\mathbf{u})/2+i\pi/2\mathbf{k}\,.\,\mathbf{u}\right\}$$
$$\times\left\{1+\omega^2\int_0^\infty t\exp(i\mathbf{k}\,.\,\mathbf{u}t-k^2t^2\kappa T/2m)\,dt\right\}^{-1}. \quad . \quad . \quad (3.39)$$

We find

$$\frac{\partial G_1}{\partial t}+\int\frac{d^3k}{k^4}C(k,0)\mathbf{k}\,.\,\frac{\partial}{\partial\mathbf{u}}P(\mathbf{k},\mathbf{u})\mathbf{k}\,.\left(\frac{\partial}{\partial\mathbf{u}}+\frac{m\mathbf{u}}{\kappa T}\right)G_1(\mathbf{u},\mathbf{u}',t,t')$$
$$=\delta(\mathbf{u}-\mathbf{u}')\delta(t-t'). \quad (3.40)$$

The plasma oscillations are represented by the denominator in (3.39) a fact noted by other authors, e.g. Balescu (1959), Hubbard and Thompson (1960). But consider for the moment only the term $\delta(\mathbf{k}\,.\,\mathbf{u})$.

This is the only surviving term for the case of a Lorentz gas, i.e. a gas of stationary scatterers which was used as the model at the start of this section. It gives

$$\frac{\pi}{2}\int d^3kC(k,0)\mathbf{k}\,.\,\frac{\partial}{\partial\mathbf{u}}\frac{\delta(\mathbf{k}\,.\,\mathbf{u})}{(1+\omega^2m/\kappa Tk^2)}\mathbf{k}\,.\left(\frac{\partial}{\partial\mathbf{u}}+\frac{m\mathbf{u}}{\kappa T}\right) \quad (3.41)$$

for the integral in (3.40). Since

$$C(k,0)=N(1+k^{-2}\lambda^{-2})^{-1} \quad \text{and} \quad \omega^2m/\kappa T=\lambda^{-2},$$

this reduces to

$$\pi^2\int\frac{dk}{(1+k^{-2}\lambda^{-2})}\frac{1}{k}\frac{1}{u^3}\frac{\partial^2}{\partial\Omega^2} \quad . \quad . \quad . \quad . \quad . \quad (3.42)$$

where $\partial^2/\partial\Omega^2$ represents the angular part of the Laplacian in velocity space. This integral converges at small k, whereas in more elementary treatments, such as the Fokker–Planck equation, it diverges at small k and is customarily cut off at $k^2\lambda^2\sim 1$ which agrees with the convergent form above. It is interesting to notice that the factor $(1+k^{-2}\lambda^{-2})^{-1}$ comes from two sources: the static sheilding effect contained in $C(k,0)$ giving one factor $(1+k^{-2}\lambda^{-2})^{-1}$ and the dynamic effects of the motion of the charge through a collision represented by the time integration of $C(k,t)$ giving another. If one uses the elementary theory the shielded potential appears twice in the cross section for scattering and overestimates the effect of static shielding by a factor $(1+k^{-2}\lambda^{-2})^{-1}$. But the elementary theory ignores the dynamic effect, and in the end reaches, rather surprisingly, the same answer (3.42). This agreement however is not present for any of the other terms of (3.39). The integral (3.42) still diverges at large k, which comes from the inadequacy of using perturbation theory for large angle collisions, i.e. close encounters. It is customary to make a cut-off at $k=2/r_0$ where $r_0=e^2(3\kappa T)/2$, so as to give the same behaviour as the Boltzmann equation which handles 'hard' collisions exactly. This cut-off could be removed in the present work using the exact two-body scattering, instead of the Born approximation, but this requires quite complicated analysis which is not matched by any physical interest and so will not be discussed further.

The differential operator $\partial^2/\partial\Omega^2$ depends only upon angles because with all the ions at rest all collisions are elastic and only affect the direction of the velocity of the scattered particle, not its magnitude. The remaining terms in (3.39) due to electron–electron scattering are more complicated. For small v they contribute a term

$$\int d^3k C(k,0)(1+k^{-2}\lambda^{-2})^{-1}\mathbf{k}\,.\,\frac{\partial}{\partial\mathbf{u}}\exp\left[-m(\mathbf{k}\,.\,\mathbf{u})^2/(2k^2\kappa T)\right] \times \mathbf{k}\,.\left(\frac{\partial}{\partial\mathbf{u}}+\frac{m\mathbf{u}}{\kappa T}\right)\frac{1}{2}\sqrt{\left(\frac{\pi(\kappa T)}{k^2 2m}\right)} \qquad (3.43)$$

to the integral in (3.40).

For general u however the expression is complicated and shows resonance structure at $\omega^2\sim(\mathbf{k}\,.\,\mathbf{u})^2$.

For large u one can write the denominator

$$1+\omega^2\int_0^\infty t\exp\left[i\mathbf{k}\,.\,\mathbf{u}t-k^2t^2(\kappa T/m)\right]dt$$
$$\cong 1-\frac{\omega^2}{(\mathbf{k}\,.\,\mathbf{u})^2}+\frac{i\omega^2(\mathbf{k}\,.\,\mathbf{u})m}{2k^2(\kappa T)}\exp\left[-m(\mathbf{k}\,.\,\mathbf{u})^2/(2k^2\kappa T)\right] \quad . \qquad (3.44)$$

which becomes small when $\omega^2\sim(\mathbf{k}.\ \mathbf{u})^2$. To get some idea of the effect of the resonance one can consider its effect concentrated at the points $\omega=\pm\mathbf{k}\,.\,\mathbf{u}$ and approximate that part of (3.39) coming from the resonance by

$$(\pi/16)\int C(k^2,0)\,d^3k\mathbf{k}\,.\,\frac{\partial}{\partial\mathbf{u}}\left[\delta(\omega-\mathbf{k}\,.\,\mathbf{u})+\delta(\omega+\mathbf{k}\,.\,\mathbf{u})\right]\mathbf{k}\,.\left(\frac{\partial}{\partial\mathbf{u}}+\frac{m\mathbf{u}}{\kappa T}\right). \quad . \quad . \quad . \qquad (3.45)$$

For large u this again gives rise to a term like that of the Lorentz gas

$$(\pi^2/4)\int\frac{k^2dk}{(1+k^{-2}\lambda^{-2})}\,\frac{1}{k}\,\frac{1}{u^3}\,\frac{\partial^2}{\partial\Omega^2}. \quad . \quad . \quad . \quad . \qquad (3.46)$$

Crude as this approximation is it shows that nothing spectacular arises from the plasma resonance, and within the near-equilibrium analysis of this paper does not block the runaway nature of the conduction problem which is implicit in the u^3 velocity dependence of (3.46) as will be discussed further below. The final equation for G_1

$$\left(\frac{\partial}{\partial t}+A(\mathbf{u}_1)\right)G_1(\mathbf{u}_1,\mathbf{u}_1',t,t')=\delta(\mathbf{u}_1-\mathbf{u}_1')\delta(t-t') \quad . \quad . \quad (3.47)$$

where

$$A(\mathbf{u})=-\frac{2Ne^4}{\pi m^2}\int\frac{d^3k}{k^2(k^2+\lambda^{-2})}\,\mathbf{k}\,.\,\frac{\partial}{\partial\mathbf{u}}\,\alpha(\mathbf{k},\mathbf{u})\mathbf{k}\,.\left(\frac{\partial}{\partial\mathbf{u}}+\frac{m\mathbf{u}}{\kappa T}\right), \quad (3.48)$$

$$\left.\begin{aligned}
\alpha(\mathbf{k},\mathbf{u})=&\left\{\frac{\pi}{2}\delta(\mathbf{k}\,.\,\mathbf{u})\left[1+\frac{m\omega^2}{\kappa Tk^2}(1-\beta(\mathbf{k},\mathbf{u}))\right]\right.\\
&\left.+\sqrt{\left(\frac{\pi m}{8\kappa Tk^2}\right)}\left(1+\frac{2m\omega^2}{\kappa Tk^2}\right)\exp\left[-\frac{m(\mathbf{k}\,.\,\mathbf{u})^2}{2\kappa Tk^2}\right]\right\}\\
&\times\left\{\left[1+\frac{m\omega^2}{\kappa Tk^2}(1-\beta(\mathbf{k},\mathbf{u}))\right]^2\right.\\
&\left.+\frac{\pi m^3\omega^4(\mathbf{k}\,.\,\mathbf{u})^2}{2k^6(\kappa T)^3}\exp\left[-\frac{m(\mathbf{k}\,.\,\mathbf{u})^2}{\kappa Tk^2}\right]\right\}^{-1},\\
\text{and}\qquad&\\
\beta(\mathbf{k},\mathbf{u})=&(\mathbf{k}\,.\,\mathbf{u})\sqrt{\left(\frac{2m}{\kappa Tk^2}\right)}\int_0^{(\mathbf{k}.\,\mathbf{u})(m/2\kappa Tk^2)^{1/2}}dx\\
&\qquad\qquad\times\exp\left[x^2-\frac{m(\mathbf{k}\,.\,\mathbf{u})^2}{2\kappa Tk^2}\right].
\end{aligned}\right\} \quad (3.49)$$

In the same way the equation for G_{12} becomes

$$\left(\partial t+A(\mathbf{u}_1)+A(\mathbf{u}_2)+B(\mathbf{u}_1,\mathbf{u}_2)+B(\mathbf{u}_2,\mathbf{u}_1)\right)G_{12}(\mathbf{u}_1,\mathbf{u}_1',\mathbf{u}_2,\mathbf{u}_2',t,t')$$

$$=\delta(\mathbf{u}_1-\mathbf{u}_1')\delta(\mathbf{u}_2-\mathbf{u}_2')\delta(t-t') \quad . \quad . \quad . \quad (3.50)$$

where

$$B(\mathbf{u}_i,\mathbf{u}_j)=\frac{2e^4}{\pi m^2}\int\frac{d^3k}{k^2(k^2+\lambda^{-2})}\,\mathbf{k}\,.\,\frac{\partial}{\partial\mathbf{u}_i}\alpha(\mathbf{k},\mathbf{u}_i-\mathbf{u}_j)\mathbf{k}\,.\left(\frac{\partial}{\partial\mathbf{u}_j}+\frac{m\mathbf{u}_j}{\kappa T}\right). \quad (3.51)$$

It is intended to give detailed calculations based upon these equations in a subsequent paper, but they will be illustrated in the next section by evaluating the case of the Lorentz gas.

§ 4. THE LORENTZ GAS

In the case of the Lorentz gas, the cross terms B in (3.50) are absent, and this equation has the solution

$$G_{12}=G_1G_2. \quad . \quad . \quad . \quad . \quad . \quad . \quad . \quad . \quad (4.1)$$

Hence the conductivity comes solely from the first term in (2.14) because

$$\int\mathbf{u}_1G_1G_2\mathbf{u}_2'\exp(-H/\kappa T)\,d^3u_1\,d^3u_2\,d^3u_1'\,d^3u_2'=0. \quad . \quad . \quad (4.2)$$

The equation for G_1 is

$$\left(\frac{\partial}{\partial t}+\frac{\alpha_0}{u^3}\frac{\partial^2}{\partial\Omega^2}\right)G_1(\mathbf{u},\mathbf{u}',t,t')=\delta(\mathbf{u}-\mathbf{u}')\delta(t-t') \qquad (4.3)$$

where

$$\alpha_0=-\frac{2\pi Ne^4}{m^2}\int_0^{2/r_0}\frac{k\,dk}{(k^2+\lambda^{-2})}, \qquad (4.4)$$

$$=-\frac{2\pi Ne^4}{m^2}\log(2\lambda/r_0+1), \qquad (4.5)$$

$$\cong-(2\pi Ne^4/m^2)\log(2\lambda/r_0). \qquad (4.6)$$

Since there are no dynamic effects in the strict Lorentz gas, only one factor $(1+k^{-2}\lambda^{-2})^{-1}$ appears, but this suffices to make things finite. Since the differential operator in (4.3) does not involve $|\mathbf{u}|$ one can write

$$G_1=G_1'\delta(|\mathbf{u}|-|\mathbf{u}'|) \qquad (4.7)$$

and as

$$\delta(\mathbf{u}-\mathbf{u}')=\frac{1}{v^2}\delta(\cos\theta-\cos\theta')\delta(\phi-\phi')\delta(|\mathbf{u}|-|\mathbf{u}'|) \qquad (4.8)$$

the equation for G_1', becomes

$$\left(\frac{\partial}{\partial t}+\frac{\alpha_0}{u^3}\frac{\partial^2}{\partial\Omega^2}\right)G_1'=\frac{1}{u^2}\delta(\cos\theta-\cos\theta')\delta(\phi-\phi'). \qquad (4.9)$$

This is solved in terms of spherical harmonics $Y_{lm}(\theta,\phi)$ which are eigenfunctions of the differential operator $\partial^2/\partial\Omega^2$:

$$G_1'=\frac{1}{u^2}\sum\exp[-\alpha_0(t-t')l(l+1)/u^3]Y_{lm}(\theta,\phi)Y_{lm}{}^*(\theta',\phi')\Theta(t-t'). \qquad (4.10)$$

Hence $\sigma_{\mu\nu}$ which is clearly isotropic

$$\sigma_{\mu\nu}=\sigma\delta_{\mu\nu}$$

is given, when the electric field is switched on at $t=0$, by

$$\sigma=\frac{Ne^2}{\kappa T}\left(\frac{m}{2\pi\kappa T}\right)^{3/2}\int_0^t\cos\theta\cos\theta'\sum\frac{1}{u^2}Y_{lm}Y_{lm}{}^*u^2$$
$$\times\exp[-\alpha_0(t-t')l(l+1)/u^3-mu^2/2\kappa T]\,.\,u^2\,d^3u. \qquad (4.11)$$

The only values of l, m contributing are $l=1$, $m=0$, and as t tends to infinity σ tends to

$$\sigma=\frac{2Ne^2}{3\kappa T}\left(\frac{m}{2\pi\kappa T}\right)^{3/2}\int_0^\infty\int_0^\infty\exp(-2\alpha_0t/u^3)\,dt\,2\pi u^4\,du\exp(-mu^2/2\kappa T)$$
$$=\frac{2Ne^2\pi}{3\alpha_0\kappa T}\left(\frac{m}{2\pi\kappa T}\right)^{3/2}\int_0^\infty u^7\exp(-mu^2/2\kappa T)\,du \qquad (4.12)$$
$$=2(2\kappa T/\pi)^{3/2}(e^2m^{1/2}\log(2\lambda/r_0))^{-1}, \qquad (4.13)$$

which is the customary solution.

In terms of the distribution function

$$\begin{aligned} f &= f_0 + f_1 \\ &= f_0 + \frac{Ne}{\kappa T}\left(\frac{m}{2\pi\kappa T}\right)^{3/2} \int^{t} \sum_{lm} Y_{lm} Y_{lm}^{*} \exp\left(-\alpha_0 l(l+1)(t-t')/u^3\right) \\ &\quad \times u^{-2}\delta(|\mathbf{u}|-|\mathbf{u}'|)\mathscr{E}\,.\,\mathbf{u}' \exp\left(-mu^2/2\kappa T\right) d^3v \\ &= f_0 + (Ne(\mathscr{E}\,.\,\mathbf{u})u^3/(2\alpha_0\kappa T))f_0, \qquad (4.14) \end{aligned}$$

when $t-t'$ tends to infinity.

It is interesting to note that the knowledge of G_1 allows one to see how f settles down to the value (4.14) when the electric field is switched on at the time $t=0$. This point of view can be used if one wishes to consider the runaway problem, for in this formulation a continually increasing current is represented by a conductivity which increases with time. The dependence of f_1 upon $\mathscr{E}$ was ignored from (2·5) upwards, if it is restored the equation for G_1 for the Lorentz gas becomes

$$\left(\frac{\partial}{\partial t} + \frac{\alpha_0}{u^3}\frac{\partial^2}{\partial \Omega^2} + e\mathscr{E}\,.\,\frac{\partial}{\partial \mathbf{u}}\right) G_1 = \delta(\mathbf{u}-\mathbf{u}')\delta(t-t'). \qquad (4.15)$$

It is now clear that for large enough u the term in $\mathscr{E}$ dominates and such electrons are accelerated indefinitely giving a correspondingly increasing σ. It is also the case that if G_1 were expanded in a series in $\mathscr{E}$ and the conductivity evaluated term by term, each term is finite, but the series diverges as t tends to infinity. As has been noted above the plasma resonance in the realistic problem does not affect this conclusion within the accuracy of this paper.

The Lorentz gas model also illustrates the modification due to a constant magnetic field, which gives rise to an external force $e(\mathbf{u}\times\mathbf{B})/c$ (and to a modification of $C(k,t)$ in the general case (3.40) which is negligible provided that the Debye length is less than the Larmor radius) so that

$$\left(\frac{\partial}{\partial t} + \frac{e}{mc}(\mathbf{u}\times\mathbf{B})\,.\,\frac{\partial}{\partial \mathbf{u}} + \frac{\alpha_0}{u^3}\frac{\partial^2}{\partial \Omega^2}\right) G_1 = \delta(\mathbf{u}-\mathbf{u}')\delta(t-t'), \qquad (4.16)$$

Choosing B in the Z direction this becomes

$$\left(\frac{\partial}{\partial t} + \frac{eB}{mc}\frac{\partial}{\partial \phi} + \frac{\alpha_0}{u^3}\frac{\partial^2}{\partial \Omega^2}\right) G_1 = \delta(\mathbf{u}-\mathbf{u}')\delta(t-t'), \qquad (4.17)$$

which has the solution

$$G_1 = \delta(|\mathbf{u}|-|\mathbf{u}'|)u^{-2} \sum_{lm} Y_{lm} Y_{lm}^{*} \exp\left[\left(-\alpha_0 l(l+1)/u^3 + ienB/mc\right)(t-t')\right] \times \Theta(t-t'). \qquad (4.18)$$

The calculation of σ proceeds as before; σ_{zz} is unchanged, but σ_{xx} and σ_{yy} involving $l=1$, $n=\pm 1$, become

$$\sigma_{xx}=\sigma_{yy}=\int_0^\infty u^2\,du\,u^2\exp(-2\alpha_0 t'/u^3)\cos(eBt'/cm)\exp(-mu^2/2\kappa T)\,dt'$$
$$=\int_0^\infty\left(\frac{2\alpha_0}{u^3}\right)\frac{u^{10}\exp(-mu^2/2\kappa T)}{1+(u^6e^2B^2)/(4\alpha_0{}^2c^2m^2)}\,du. \quad . \quad . \quad . \quad . \quad . \quad . \quad (4.19)$$

This method of handling the magnetic field is important when the Larmor radius and mean free path are comparable so that the transport coefficients cannot be expanded in terms of either ratio. For example, it is hoped to discuss in a future paper the off-diagonal elements of the pressure tensor which vary like B^{-1} in strong fields and are difficult to obtain by conventional methods.

§ 5. CONCLUSION

This paper has attempted to set up a formalism for transport processes in a plasma in which the equations used are direct representations of the physical processes involved. Thus eqn. (2.10) states that the conductivity can be related to the rate at which a single particle travelling through a plasma loses momentum and how the momentum lost by such a particle is in part transferred to other particles in such a way that it still contributes to the current flowing. The Green function G_1 represents the probability that a particle with velocity $\mathbf{u}'$ at t' will have $\mathbf{u}$ at t and similarly for a pair of particles in G_{12}, and can be handled simply because of the immense simplification brought about by the predominance of weak collisions in a plasma. This is probably the only case in nature in which this condition really applies and here only within use of a cut-off at very large momenta. Perhaps the greatest simplification in matters of principle is however to consider only situations which are near equilibrium, because the use of the partition function as the first approximation transfers all questions of randomness to questions concerning the equilibrium state which are of course all answered by the use of the partition function. The assumption of molecular chaos or stosszahlansatz never has to be invoked, since such questions are referred back to the equilibrium state, whose status is well understood.

The final eqns. (3.47) and (3.50) are still of course very complicated but it is hoped to give a quantitatively reliable evaluation of the transport coefficients from these in a subsequent paper.

APPENDIX

It is required to evaluate the static four-body correlation function of the charge density in thermal equilibrium and to show that the four-body correlation function is represented by the combination of products of two-body correlation functions. If the Fourier components of the charge density are denoted by σ_k

$$\sigma_k = \sum_{\text{electrons}} \exp(i\mathbf{k}\,.\,\mathbf{x}_\alpha) - \sum_{\text{protons}} \exp(i\mathbf{k}\,.\,\mathbf{x}_\alpha), \qquad . \quad . \quad . \quad \text{(A 1)}$$

then one wishes to evaluate

$$\langle \sigma_k \sigma_j \rangle \quad \text{and} \quad \langle \sigma_k \sigma_j \sigma_l \sigma_m \rangle$$

with the weight factor

$$\exp(-H/\kappa T) = \exp[-(4\pi e^2/v) \sum (\sigma_k \sigma_k^* - 2N)/k^2 \kappa T]. \qquad \text{(A 2)}$$

The σ_k's themselves are not good coordinates as they are an infinite set where there are N electrons and N protons, but it is possible to introduce a set of coordinates ϕ_k which are completely independent and allow the correlation functions to be written in closed form as integrals over the ϕ_k's. The details of this procedure are given in an early paper (Edwards 1959) and here only the results of a straightforward extension will be given. If $\phi(\mathbf{r}) = \sum \exp(i\mathbf{k}\,.\,\mathbf{r})\phi_k$ then using for convenience the physically equivalent grand canonical distribution rather than the canonical ensemble above, one gets

$$\langle \sigma_k \sigma_j \rangle = \mathcal{N} \int \dots \int \left[\frac{\delta}{\delta\phi_k} \frac{\delta}{\delta\phi_j} \exp\left\{ Z \int \cos\left[\frac{e}{\kappa T} (\phi(\mathbf{r}) - \phi(\mathbf{s})) \right] d^3r\, d^3s \right\} \right]$$
$$\times \exp\left[(-1/8\pi\kappa T) \int (\nabla\phi)^2\, d^3r \right] \prod \delta\phi_k, \qquad . \quad . \quad . \quad \text{(A 3)}$$

$$\mathcal{N}^{-1} = \int \dots \int \exp\left[(-1/8\pi\kappa T) \int (\nabla\phi)^2\, d^3r \right] \prod \delta\phi_k \qquad \text{(A 4)}$$

and

$$\langle \sigma_k \sigma_j \sigma_l \sigma_m \rangle = \mathcal{N} \int \dots \int \left[\frac{\delta}{\delta\phi_k} \frac{\delta}{\delta\phi_j} \frac{\delta}{\delta\phi_l} \frac{\delta}{\delta\phi_m} \right.$$
$$\left. \times \exp\left\{ (Z) \int \cos[e(\phi(\mathbf{r}) - \phi(\mathbf{s}))/\kappa T]\, d^3r\, d^3s \right\} \right]$$
$$\times \exp\left[(-1/8\pi\kappa T) \int (\nabla\phi)^2\, d^3r \right] \prod \delta\phi_k \qquad . \quad . \quad \text{(A 5)}$$

where $Z = (2\pi\kappa T/m)^3 \exp(\nu/\kappa T)$, ν being the chemical potential.

In the first approximation of writing

$$Z \int \cos(e\phi(\mathbf{r})/\kappa T)\, d^3r = ZV(1 - e^2/V(\kappa T)^2) \sum \phi_k \phi_{-k}$$
$$= ZV - \phi_k \phi_{-k}/\kappa T \lambda^2 \qquad . \quad . \quad . \quad . \quad \text{(A 6)}$$

so that the exponent contains

$$\exp\left[- \sum_k (k^2/\kappa T) \phi_k (1 + k^{-2}\lambda^{-2}) \phi_{-k} \right]$$

these formulae lead to

$$\langle \sigma_k \sigma_j \rangle = N\delta(\mathbf{k} + \mathbf{j})/(1 + k^{-2}\lambda^{-2}). \qquad . \quad . \quad . \quad . \quad \text{(A 7)}$$

To obtain higher approximations one has to consider the coulomb potential cut-off at some small radius to avoid an essential singularity inherent in the Gibbs distribution, but apart from such terms the corrections to (A 7) can be shown to be of order $(\mu/\lambda)^3$. If one now proceeds to $\langle\sigma_k\sigma_j\sigma_l\sigma_m\rangle$ there are terms coming from $\alpha=\beta=\gamma=\delta$ in

$$\langle\exp[i(\mathbf{k}\,.\,\mathbf{R}_\alpha+\mathbf{j}\,.\,\mathbf{R}_\beta+\mathbf{l}\,.\,\mathbf{R}_\gamma+\mathbf{m}\,.\,\mathbf{R}_\delta)]\rangle \quad . \quad . \quad . \qquad (A\,8)$$

which are static analogues of the failure of the Born approximation discussed after (3.42), but the remaining terms are again to order $(\mu/\lambda)^3$:

$$\langle\sigma_k\sigma_j\sigma_l\sigma_m\rangle=\langle\sigma_k\sigma_j\rangle\langle\sigma_l\sigma_m\rangle+\langle\sigma_k\sigma_l\rangle\langle\sigma_j\sigma_m\rangle+\langle\sigma_k\sigma_m\rangle\langle\sigma_j\sigma_l\rangle. \qquad (A\,9)$$

For a detailed discussion of the handling of the short-range part of the potential and the evaluation of the ϕ_k integration the reader is referred to the reference above.

ACKNOWLEDGMENTS

Part of this work was done when the authors were vacation consultants at the Theoretical Physics Division, A.E.R.E., Harwell, in the summer of 1959, and they would like to thank Dr. W. M. Lomer, the head of the division, for his hospitality and other members, particularly Dr. W. B. Thompson for many helpful conversations. They would also like to thank Professor Flowers for his comments on the paper. One of the authors (J. J. S.) acknowledges a D.S.I.R. studentship held during this work.

REFERENCES

BALESCU, R., 1959, *Physica*, **25**, 325.
EDWARDS, S. F., 1959, *Phil. Mag.*, **4**, 1171; 1961, *Ibid.*, **6**, 61.
HUBBARD, J., and THOMPSON, W., 1960 (to be published.)
ROSTOKER, N., and ROSENBLUTH, M. N., 1960, *Proceedings Upsala Conference on Gas Discharges* (Amsterdam: North Holland Publishing Co.) (to be published).

The Study of High-energy γ-rays Produced by Cosmic Radiation at 40 000 feet†

Part I. Experimental Disposition, and Determination of Energy and Nature of Electromagnetic Cascades

By J. G. Duthie, C. M. Fisher, P. H. Fowler,
A. Kaddoura‡, D. H. Perkins and K. Pinkau

H. H. Wills Physical Laboratory, University of Bristol

[Received June 28, 1960]

Abstract

Two composite stacks of alternate sheets of nuclear emulsion have been used to investigate electromagnetic cascades in the cosmic radiation. The stacks were exposed in BOAC Comet aircraft for a total of 1400 hours at about 38 000 ft. Approximately 600 cascades were observed, and a sample of these was classified as arising either from γ-rays incident from the atmosphere or as a result of nuclear interactions in the stack. The zenith-angle distribution of the cascades has been used to determine the attenuation length of the radiation producing the cascades. The number of electron tracks in the cascades has been determined by a photometric method, and the relation between the photometric density and the cascade energy has been established for the two types of cascade.

§ 1. Introduction

During the past few years, many papers§ have appeared describing the results of studies of energetic nuclear interactions or 'jets', produced in emulsion by particles in the cosmic radiation with energies in the range from 1000 to 100 000 bev. Most of the experiments were carried out with small stacks of nuclear emulsion, exposed for periods of only a few hours at balloon altitudes. The number of recorded events was therefore small, and it was difficult to establish or maintain any rigorous criteria for their detection; the results were correspondingly uncertain.

The great advantage of work with stacks of pure emulsion is that the tracks of individual particles can be followed for great distances, and their secondary effects observed in detail. Important advantages can be gained, however, if this feature is sacrificed by employing large stacks built up of emulsion and layers of heavy elements. Many of the nuclear interactions then escape observation, but it is possible to make a much more powerful attack on the detailed features of the electromagnetic cascades which result from the nuclear interactions. Briefly, the advantages thus gained are threefold:

---

† Communicated by the Authors.

‡ On leave from University of Damascus, U.A.R.

§ For review article see, for example, Perkins (1960).

First, in an appropriate assembly, the radiation length can be made so short that cascades of comparatively low-energy (a few hundred BeV) appear as concentrated bundles of tracks, visible to the unaided eye. Secondly, such electromagnetic cascades grow, reach their maximum intensity, and are attenuated, within the assembly; the precision with which their energy can be determined is thereby increased. Thirdly, the depth of the stack can readily be made large compared with the conventional value of the nuclear 'interaction length'—about 150 g/cm^2, so that some features of development of the individual *nuclear* cascades can be investigated.

To exploit the above advantages, two very large assemblies of lead and emulsion were exposed to the cosmic radiation in BOAC Comet 2E airliners for total period of about 1400 hours at an altitude above 30 000 feet during the period November 1957 to March 1958. Because of the length and intensity of these exposures, they allowed a statistically significant analysis to be made of some features of the interactions of particles with energies up to about 10^{15} ev.

In the present series of papers, we present an account of the methods employed together with some of the results of an analysis of the events. This is followed by a discussion of the origin of the cascades and of their distribution in zenith angle, of the method of determining their energies, and of the energy spectrum of the cascades. The work relates both to cascades due to single gamma rays or electrons incident upon the stack, and to those associated with nuclear interactions occurring within the stack.

§ 2. Experimental Disposition

Both assemblies, referred to hereafter as Comet 1 and Comet 2 stacks, were made up of vertical sheets of lead and emulsion. The proportions of lead and emulsion were varied, however, so as to give three horizontal layers of different mean density; see fig. 1. The top 7·5 cm, designated section 1, consisted of pure emlusion made up of alternate sheets 400 μ and 600 μ thick. The next 12·5 cm, section 2, was composed of sheets of emulsion 600 μ thick alternating with 400 μ sheets of lead. The bottom layer of 10 cm, section 3, was made up of 600 μ emulsions alternating with 2400 μ lead sheets. The sheets of lead were all wrapped in a thin layer of terylene, 6 μ thick, which prevented electro-chemical action between the metal and the emulsion.

In the three sections, the effective values of the 'radiation-lengths' were 2·9 cm, 1·0 cm, and 0·6 cm, respectively†. Using a value of 32 cm, for the mean 'nuclear interaction length' in pure emulsion, the corresponding values for sections 2 and 3 are 23 cm, and 18 cm, respectively. It follows that for particles at vertical incidence, each stack presented a depth of 32 'radiation-lengths' and 1·4 conventional 'nuclear interaction lengths'.

---

† In this paper, values of radiation length have been calculated from the formula given by Rossi (1952, p. 54) which assumes the validity of the Born approximation.

This particular design of the stacks, incorporating several centimetres of pure emulsion at the top, was originally chosen to allow the observation of high-energy nuclear interactions in pure emulsion, and to ensure a rapid development, in the lead-emulsion layers, of any electromagnetic cascades resulting from them. It was also thought desirable to be able to observe the points of conversion into electron pairs of any high-energy γ-rays incident from outside the stack, and to investigate the change in the cross section for *bremsstrahlung* predicted by Migdal (1956, 1957) and others (see Fowler *et al.* 1959).

Fig. 1

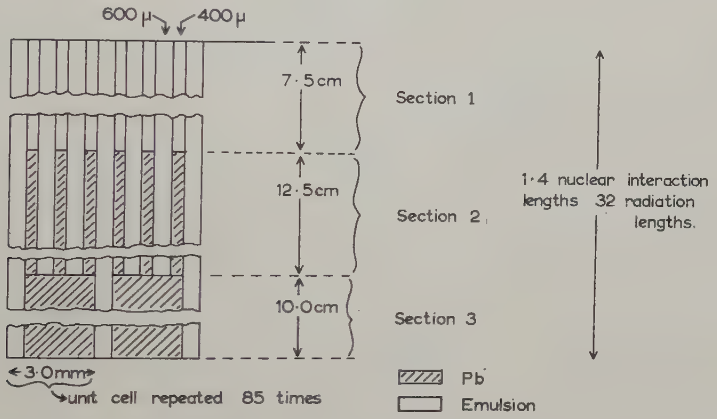

Cross section of Comet stack, showing disposition of lead and emulsion sheets. Taking the three sections individually, the values of radiation length and nuclear interaction length are respectively: section 1, 3·0 cm and 32 cm; section 2, 1 cm and 23 cm; section 3, 0·6 cm and 18 cm.

The Comet 1 stack had a sensitive volume of 20 litres, with approximate dimensions 25 cm wide, 26 cm thick and 30 cm deep. The dimensions of the Comet 2 stack differed only slightly from those of Comet 1; it was 30 cm wide, 24 cm thick and 30 cm deep. Both stacks were thermally insulated and packed in wooden crates. No cooling arrangement was installed for the first stack; the second was kept below 4°c with the aid of solid carbon dioxide.

In the Comet 1 stack, all the emulsion was of type Ilford G5 with normal gelatine content. In the Comet 2 stack, the 400 μ (even-numbered) emulsions of section 1 were × 2 gelatine, either G5 or K5. Section 2 of this stack was in two halves, the first incorporating G5 emulsion only, whilst in the second, every third emulsion was of type G5, the others being of K5. In section 3, all emulsions were of type G5. The reason for employing emulsions with different values of the gelatine content was to give the possibility of investigating nuclear interactions in light and heavy elements.

Emulsions of type K5 were used because they were thought to provide better conditions for investigating ‘jets’, since their smaller grain-size gave improved optical resolution. Unlike the G5 emulsion, K5 was found to be particularly sensitive to surface marking from the terylene employed to separate the emulsion and lead sheets; as a result the K5 emulsions could not be used for photometric measurements.

The most interesting results obtained in the experiments were those concerning the energy spectrum of the cascades produced both by incident γ-rays, and those arising from nuclear interactions occurring in the stacks. For such studies, a more uniform distribution of lead and emulsion, and the use of ordinary G5 emulsion throughout, would have been preferable.

The Comet 1 stack was exposed above 30 000 feet for 840 hours, and the Comet 2 stack for 580 hours. From the typical flight curves shown in fig. 2, it may be seen that the effective altitude of exposure was 11 500 metres corresponding to a depth of 220 g/cm^2 within the atmosphere. Most of the total time of the exposures was obtained whilst the aircraft was flying between London and Beirut.

Fig. 2

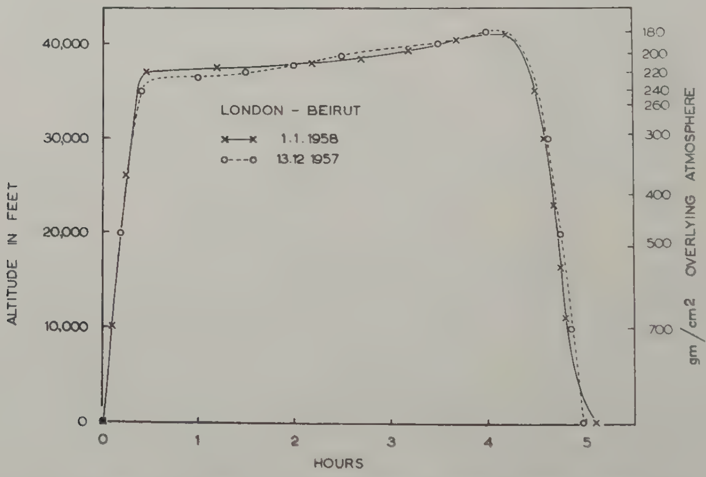

Height–time curves for two of the Comet flights from London to Beirut. The return flights were typically half an hour longer. About 300 such flights were made for the total exposure of 1400 hours above 30 000 feet.

§ 3. Scanning

Cascades occurring in the stacks were detected by viewing the emulsion sheets by unaided eye against a suitable illuminated screen. The cascades then appear as lines, which are, in most cases, readily distinguishable from scratches and other background marks. All lines thus detected were examined under the microscope to confirm that they were in fact formed by cascades. In this way, about 200 events were found in the first, and 400 in the second Comet stack. The first stack, although of slightly smaller volume, was given the longer time of exposure, and more cascades should have been recorded in it. The apparent discrepancy is due to the lower grain density in this stack, which was not cooled during exposure, and to a greater degree of surface marking. This increased the energy threshold for detecting a cascade by about 30%. The 'plateau-value' of the grain density for relativistic particles of charge $|e|$ is 8·5 grains per 50 μ in the first Comet stack, compared with 11 per 50 μ in the G5 emulsions of the second. The developed grains in the first stack, however, have an area about 10% greater than that in the second.

The efficiency with which cascades are detected depends on their blackness with respect to the background, and on their angles of dip with respect to the emulsion plane. Cascades of high energy may be detected with very high probability, even when they are very steep. Low-energy cascades are more readily visible when they are flat. The biases involved in the scanning will be discussed in more detail in a later paragraph (§ 1, Part II). By way of illustration, fig. 3 C† shows a contact print (natural size) of an emulsion containing seven cascades of various densities, and having various angles of dip with respect to the plane of the emulsion.

After finding a cascade, it was traced back through a series of plates towards its origin, using the illuminated screen. When it became too faint to be distinguished by the unaided eye, it was followed under the microscope to its origin on to its point of entry into the stack. Those cascades produced in nuclear interactions in the stack, or in matter in its immediate vicinity, were classified as 'nuclear events'. Those produced by individual γ-rays or electrons which entered the stack with no associated nuclear-active components were classified as 'electromagnetic' events.

§ 4. ORIGINS OF THE EVENTS

In a total of approximately 600 events detected in the two stacks by scanning, 300 events were followed back to their origins. This sample included all events with a cascade energy estimated to be greater than 3000 BEV (see §§ 7 and 8), together with those of lower energy which occurred in conditions of favourable geometry and which were used in determining the energy spectrum of the cascades.

4.1. *Classification*

The origins of the cascades were classified as:

(i) '*Electromagnetic*' *events*

The cascade was followed back to either:

(*a*) A single electron pair, originating in the emulsion, or occasionally in the lead of sections 2 or 3, with no neighbouring associated tracks.

(*b*) The track of a single electron, entering the stack from the outside. The identification as an electron depended upon the observed rapid development of the cascade without evidence for nuclear interaction.

---

† Figures 3 and 9 are shown as plates.

(*c*) A number of photons and/or electrons, with no measurable angular divergences, which entered the stack within $\sim 100\,\mu$ of one another.

In almost all cases, events of type (*a*) are due to single γ-rays incident on the stack from the outside, originating directly from a nuclear interaction in the atmosphere; many of them will arise, for example, through the creation of π^0-mesons. In events of type (*b*) and (*c*) the γ-rays will commonly have materialized in the atmosphere before reaching the stack. The effects of multiple scattering and deflection due to the earth's magnetic field, over distances of ~ 1 km, which is equal to one radiation length (r.l.) at this altitude, can account for the lateral spread of the particles in events of type (*c*).

In events of all three types, the maximum density of tracks in the cascade, as measured photometrically (§ 6), occurs at about 7 r.l. from the point of entry into the stack.

(ii) *Nuclear events*

In these events, the cascade was followed back to either:

(*a*) A nuclear interaction in one of the emulsion layers.

(*b*) A nuclear interaction in one of the lead sheets interposed between emulsions. Such an event is characterized by a measurable convergence of the shower tracks and electron pairs in the first emulsion in which they are recorded. In all cases, it was required that the convergence measurements should show that the origin was inside the adjacent lead sheet.

(*c*) A nuclear interaction in the 'dural' end-plates clamping the stack, in the wooden containing box, or in the aircraft fuselage. In such events, a close bundle of γ-rays and shower particles entered the stack, and their measured convergences indicated the position of the origin. The nuclear origin was confirmed by secondary nuclear interactions in all except one of the events of this class, and the events were easily distinguished from those in (i) *c*, which arise from *bremsstrahlung* and pair-production in the atmosphere.

(iii) '*Families of cascades*'

Occasionally, 'families' are observed, consisting of a large number of cascades, having no measurable divergence and laterally separated by distances of the order of a few centimetres. Most of the cascades in a family are 'electromagnetic' in origin, but a few are 'nuclear' events. Figure 3 (A and B) shows contact prints of some of the members of a large family (total 28) in the Comet 1 stack. Events of this type are attributed to very high-energy nuclear collisions in the overlying atmosphere, typically 1 km above the stack, the individual γ-rays having a divergence of the order of 10^{-5} radians. They represent large air showers in the very early stages of development. The detailed features of such events will be discussed in a later paper.

The relative numbers of events of the different types are indicated in the following table:

Origins of all cascades of energy $\geqslant 3000$ BEV in both stacks (total 75)

	Number observed
(i) Electromagnetic events	
(*a*) Pure γ's	26
(*b*) Close bundles of photons and/or electrons	11
(ii) Nuclear events	
(*a*) In emulsion	11
(*b*) In lead	22
(*c*) In packing	5

4.2. *Primaries of Nuclear Events*

In addition to tracing back all cascades of high energy, those of lower energy and of favourable geometry, were also followed, and gave an additional 15 events of nuclear origin in the emulsion. Among all the 27 nuclear events in emulsion, 18 were due to singly-charged primaries, 8 to neutral primaries, and one to an α-particle. This restricted sample of events does not provide any indication of a variation in the ratio of charged to uncharged primaries with changes in the energy of the associated cascade. Thus, if the sample is divided into two groups, it is found that for a cascade energy $1500 < E < 3000$ BEV, there are ten charged and five neutral primaries; for $E > 3000$ BEV, eight charged and three neutral primary particles. The large excess of charged over neutral particles cannot be attributed to a residual excess of protons over neutrons in the nucleonic component in the atmosphere. As will be shown below, the attenuation length of the nucleonic component is $\sim 110\,\mathrm{g/cm^2}$, whereas the interaction length can be taken as $\sim 70\,\mathrm{g/cm^2}$. The calculated ratio of the numbers of true primary protons to the total number of nucleons at a depth of 220 g/cm^2, is then only about 18%. It follows that if the observations are interpreted in terms of pions and nucleons only, the observed excess of charged primaries is consistent with the view that 20% of all primaries are charged pions; the statistical uncertainty in the number of pions is however of the order of 100%.

§ 5. ZENITH-ANGLE DISTRIBUTION OF CASCADES

Both stacks were flown with the emulsion sheets in a vertical plane, at an effective atmospheric depth of about 220 g/cm^2. The zenith-angle distribution of cascades therefore gives a measure of the attenuation of the radiation producing them. Assume that the attenuation in the number of cascades of a given class varies exponentially with the mass of overlying atmosphere. Denoting the attenuation length by λ, the vertical atmospheric depth by h, and the zenith angle by θ, it follows that the number of cascades per unit solid angle at θ is given by

$$\frac{dN}{d\Omega} = \frac{dN(0)}{d\Omega} \cdot \exp\left[-h(\sec\theta - 1)/\lambda\right].$$

The distribution with zenith angle of the number of the cascades has been calculated from the above relation for various values of h/λ. From this formula, the distribution in the projected zenith angle, θ_{p}, in the emulsion plane, for different intervals in the angle of dip, δ, relative to the emulsion plane can be computed. This procedure is necessary as the probability of detection for the weaker cascades falls below unity for the larger angles of dip. Over a small range in the values of sec δ, the projected angular distribution will be independent of δ; variations in detection efficiency with δ will then not affect the distribution in θ_{p}. Although the detection efficiency for the low-energy cascades is low, there is no reason to suppose that this efficiency will depend on the projected angle θ_{p}. It follows that for values of $\delta < 30°$, the projected angular distribution for the events can be closely approximated by the expression

$$\frac{dN}{d\theta_{\mathrm{p}}} \propto \exp\left[-1{\cdot}05h\left(\sec\theta_{\mathrm{p}} - 1\right)/\lambda\right]$$

where 1·05 is the effective value of sec δ averaged over the events considered.

Fig. 4

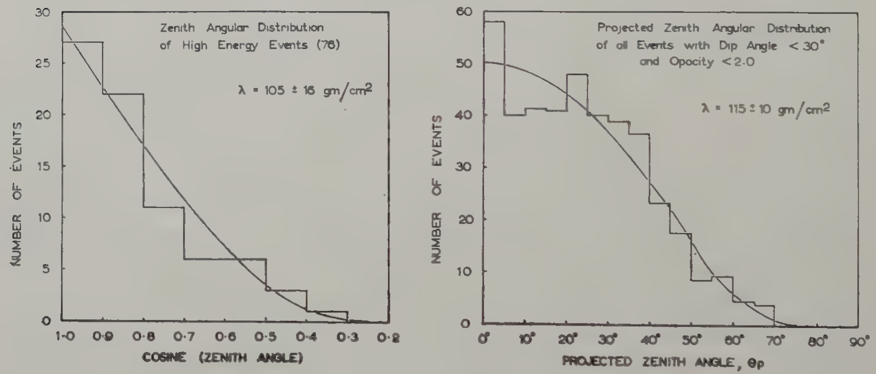

Distribution of cascades as a function of zenith angle.

(*a*) True zenith-angle distribution for energetic events where scanning losses were negligible.

(*b*) Distribution of the zenith angle of the cascades, projected into the plane of the emulsions, for the more numerous cascades of lower energy ($E < 3000$ BEV). Only cascades with angles of dip below 30° are included. Although the scanning efficiency for the events varies appreciably with dip angle, there is no reason to expect any dependence on projected angle.

The two distributions are consistent with an exponential absorption in the atmosphere of the radiation producing the cascades, with an absorption length $\lambda = 110$ g cm^2. The figures for λ given in the two graphs represent the best fits for each distribution. It is of course assumed that the attitude of the aircraft was horizontal and constant during the high-altitude part of the flight.

In fig. 4 (*a*), the true angular distribution of the 75 events of highest energy ($E > 3000$ Bev) is plotted, as a function of cos θ. We are confident that in these events, the scanning efficiency was unity up to the highest angle of dip. A 'maximum likelihood' analysis for different assumed values of λ gives a best fit for $\lambda = 105 \pm 16\,\text{g/cm}^2$; the computed curve for this value of λ is indicated.

In fig. 4 (*b*), the projected angular distribution is plotted for events of low cascade energy ($1000\,\text{Bev} < E < 3000\,\text{Bev}$), and of dip angle $\delta < 30°$. A 'maximum likelihood' analysis gives $\lambda = 115 \pm 10\,\text{g/cm}^2$.

It follows from the above results that the attenuation in the number of cascades, over the interval 220 g/cm^2 to about 400 g/cm^2 of atmosphere, is exponential, with an attenuation length of approximately 110 g/cm^2. This value of λ appears to apply over the whole range in the values of the cascade energy here considered, and to be valid for both 'nuclear' and 'electromagnetic' events. The primary energies involved in the case of these cascades are in the range 10^4 to 10^6 Bev.

The above value of λ is in good agreement; (i) with the measurements of Kaplon *et al.* (1953) on the ratio of the numbers of cascades produced by nucleons of primary energy $\geqslant 1000$ Bev at balloon and mountain altitudes; they obtained $\lambda = 130 \pm 15\,\text{g/cm}^2$; (ii) with the variation in the rate of extensive air showers between sea-level and mountain altitudes, and with barometric pressure or zenith angle at sea-level. The values thus obtained group around 110–120 g/cm^2 (for a review see Greisen 1956). There is indeed a remarkable consistency in the value of λ obtained by different methods, over the very wide range in primary energy from 10^3–10^7 Bev.

§ 6. THE PHOTOMETRIC MEASUREMENT OF CASCADE DENSITY

6.1. *Optical System*

In order to measure the energy of a cascade, the numbers of tracks must be determined at some given distance from the origin. When the density of tracks is very high, they cannot be individually distinguished and counted. In such circumstances, however, their number may be estimated by photometric measurements, which determine the opacity due to the assembly of tracks. The densitometer employed consisted of an (RCA 931) photomultiplier tube attached to a modified Cooke M 4000 microscope. A CRO displays the signal from the photomultiplier. The optical system is shown in fig. 5. The axes of all slits in the system are aligned to the y-motion of the microscope stage, as also is the cascade under consideration. An image of the lower slit is focused into the plane of the emulsion by means of a × 22 oil-immersion objective (N.A. 0·65), used as a condenser. A × 22 oil-immersion objective (of the same type as used for the condenser) is then adjusted to project the image of the lower slit onto the plane of the upper slit. This projected image is made to sweep across the upper slit by means of a rotating glass cuboid, driven by a small two-phase a.c. motor running at 1000 r.p.m. Two opposite faces of the cuboid were blackened so that at each revolution the image traversed the upper slit twice.

The image of the lower slit in the plane of the emulsion had a width of about 15 μ, and a length of 200 μ. The upper slit was adjusted to accept light coming from a region in the object plane, 10 μ in width.

As can be seen from fig. 6, the grains contributing to the attenuation of light as registered by the photomultiplier are contained in the region ABCDEF. The figure here relates to the unprocessed emulsion, and the angle $\theta_{\max}$ is given by the formula

$$\sin\theta_{\max} = \frac{\text{N.A.}}{\mu s}$$

where N.A. is the numerical aperture of both condenser and objective (0·65); μ is the refractive index of the processed emulsion (1·5); and s is the shrinkage factor (the ratio of thickness of unprocessed to processed emulsion, approximately equal to 2). Thus $\theta_{\max} = 13°$, represents the greatest angle of inclination of light rays to the normal to the emulsion plane, given by the condenser and accepted by the objective.

Fig. 5

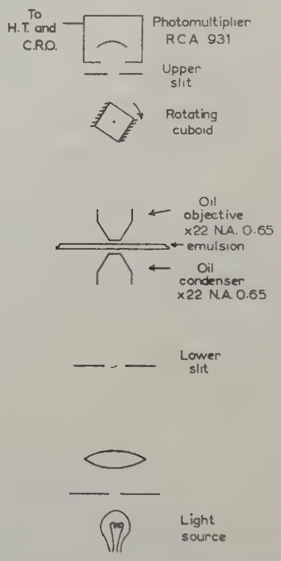

Diagrammatic representation of the optical system employed for photometric determination of cascade density. This system is an adaptation of that developed by Ney (1955) for measurements on the tracks of α-particles and heavier nuclei in the primary cosmic radiation.

Suppose now that the axis of a cascade—cylindrically symmetrical in the unprocessed emulsion—lies in the centre of the slit BE—the slit itself is normal to the plane of this diagram. A ray GH, normal to the emulsion plane, at distance x laterally from the centre of the slit, is attenuated according to the number of grains per square micron in the emulsion plane, integrated over the emulsion thickness (600 μ). A ray JK, at an angle θ to the normal, will be attenuated according to the integrated number of grains per square micron at a distance $x \cos \theta$ from the axis, over a thickness equal to 600 sec θ microns.

We have so far considered light rays lying in the plane of the diagram in fig. 6. Consider now the more general case of a ray making an angle θ to the normal to the emulsion, but with azimuthal angle ϕ with respect to the plane of the diagram. Then one has to project the ray into this plane. The value of the angle ψ, which this projected ray makes to the vertical is always less than θ. Since the values of $\cos \theta$, or $\cos \psi$ lie between 1·0 and 0·975 for all permitted light rays, it follows, for our purpose, that it is sufficient to consider all light rays as being normally incident on the emulsion. Thus, the arrangement employed measures the number of grains per square micron projected normal to the emulsion plane; in effect, we have to consider the attenuation in a parallel beam of light, 10 μ wide, produced by the tracks in the cascade.

Fig. 6

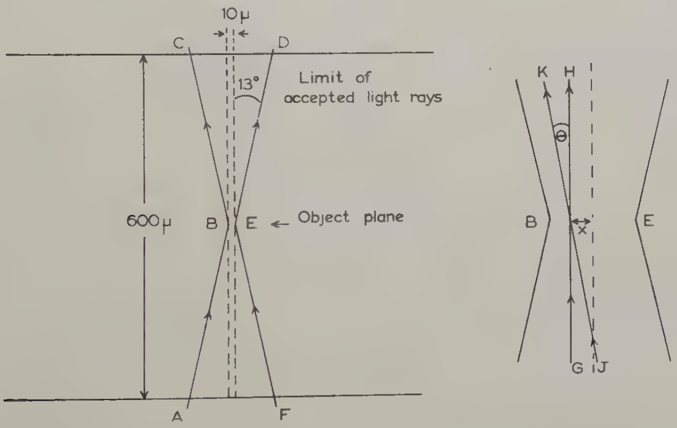

An enlarged view of the distribution in light rays traversing the emulsion layer. The thickness has been taken as that of the unprocessed emulsion. A cascade with axis perpendicular to the plane of the diagram will have a track distribution possessing circular symmetry about its axis. The significance of individual rays is explained in the text.

6.2. *Relation between the Cascade Density and the Number of Tracks*

Let A be the cross-sectional area of a grain, and assume that a track consists of n grains per unit path length. Let $f(x, y)$ represent the number of tracks per unit area in a plane normal to the cascade axis; we shall assume at present that this axis lies in the emulsion plane. The coordinates of a particular track relative to the cascade axis are designated x and y; x is the coordinate in the plane of the emulsion. Then one has the following relation for the attenuation of the light intensity I, I_0 being the incident intensity

$$\left(\frac{dI}{dy}\right) = -I\,A\,n\,f(x,y) \quad . \quad . \quad . \quad . \quad . \quad . \quad . \quad . \quad (1)$$

or

$$I(x) = I_0 \exp\left(-A\,n\,\tau(x)\right), \quad \text{where} \quad \tau(x) = \int_{-300\mu}^{+300\mu} f(x,y)dy. \qquad (2)$$

Here, $\tau(x)$ is the integrated track density per micron, at a projected distance x. To obtain the total intensity, J, incident on the photomultiplier tube, one finally has to integrate over the slit width, i.e.

$$J = J_0 \int_{-5\,\mu}^{+5\,\mu} \exp\left(-An\,\tau(x)\right).\,(dx/10), \quad \text{where} \quad J_0 = I_0\,.\,10\,\mu. \qquad (3)$$

If one assumes, as a first approximation, that the projected track density $\tau(x)$ does not vary over the slit width, then one obtains the important relation

$$J = J_0 \exp\left(-A\,n\,\tau\right), \quad \text{or} \quad \ln\left(J_0/J\right) = A\,n\,\tau. \quad . \quad . \quad . \quad . \quad (4)$$

Here, the values of A and n are constants throughout the stack of emulsions, if the development is uniform. J_0 can be determined from a 'background' reading, and τ is the projected number of tracks per micron in the slit. The quantity $\ln(J_0/J)$ will be called the cascade density, D. If variations of τ over the slit are taken into account, it can be shown (see below) that, to a high degree of accuracy:

$$D = \ln\left(J_0/J\right) = A\,n\bar{\tau}$$

where $\bar{\tau}$ is the value of τ averaged over the slit width.

6.3. *Effect of Angle of Dip of a Cascade*

There are three ways in which the angle of dip, δ, of a cascade, relative to the plane of the emulsion, affects the estimation of track density:

(*a*) The projected grain-density is proportional to $\sec\delta$.

(*b*) The integral in eqn. (2) is carried to the limits $\pm 300 \cos\delta$ microns.

(*c*) Since the slit image in the emulsion is $200\,\mu$ in length, it is focused only on that part of the cascade in the centre of the field of view.

The effect of (*a*) is to increase the projected grain density, and hence absorption, produced by a given number of tracks in the cascade, whereas (*b*) and (*c*) reduce it. From the form of the radial distribution—see Pinkau (1957)—it is found that the overall effect is to increase D by a factor of $(0{\cdot}1 + 0{\cdot}9 \sec\delta)$. This factor is therefore only slightly smaller than the effect of (*a*) alone.

6.4. *Effects of Multiple Scattering of Light and Saturation of Grain-size and Density*

In the derivation of the above formulae, two assumptions have been made: (i) That the multiple scattering of light back into the 'allowed cone' of the optical system may be neglected, and (ii) That the area of the developed grains, A, and the grain density, n, of a track due to a particle of minimum ionisation are constants for all values of τ.

(i) The magnitude of the effect of scattering has been investigated by increasing the numerical aperture *of the objective*, to 1·0, the aperture of the condenser remaining unchanged, so that $\theta_{\max}$ becomes $\sim 20°$; this increases the solid angle accepted by the objective by a factor of $\sim 2{\cdot}4$. Even for very dense cascades ($D \sim 3$ as measured with the original objective), the change in D amounted to less than 7%. Thus we are confident that, except possibly for the three most dense cascades considered in this experiment, multiple scattering of light is unimportant with the optical system employed.

(ii) There are two possible reasons why the second assumption (A and n constant) might be invalidated. First, if the particle density is extremely high, the number of developed grains may no longer be proportional to the number of electrons, for there is a significant probability of a particular halide crystal being activated by more than one electron. Calculation shows that such saturation effects are completely negligible in G5 emulsion for the particle densities considered in this investigation. In emulsions with fewer and larger halide crystals (e.g. X-ray emulsions) such effects might become important.

A second source of error may arise from a failure to develop sufficiently all the activated grains in the core of dense cascades. Experiments carried out with intense beams of X-rays and β-rays, show that, with the normal development procedure we employ, the blackening produced in prolonged exposures is no longer proportional to exposure time. This is due to the fact that the amount of developer available in the emulsion is insufficient to develop fully the activated grains. Such effects will be important when the lateral spread of the beam of tracks extends over a distance of several hundred microns; if however the width of the pencil of tracks is small compared with the emulsion thickness, developer can diffuse inwards from all round the axis and replenish the shortage in the region of the pencil. Such replenishment, for example, takes place in the development of the tracks of heavy primary nuclei. For an extended beam of tracks, however, the effect of 'developer-starvation' results mainly in a reduction in the degree of physical development, and a corresponding decrease in the size of the developed grains.

The results obtained with X-ray and β-ray exposures indicate however that the effect is unimportant for the cascades under discussion. As a check on the effect in the actual cascades, a visual count was made of the projected grain density (in grains per square micron) at various positions in several cascades, together with the results of photometric measurements in $\ln J$. The regions of the cascades employed in this measurement were such that the projected grain density did not vary significantly over the slit width. Applying formula (4) for two readings, ρ_1, J_1 and ρ_2, J_2 respectively:

$$A(\rho_2-\rho_1)=\ln J_1/J_2 \qquad \qquad (5)$$

The results of the measurements are displayed in fig. 7. It may be seen that the experimental relation between $(\rho_2-\rho_1)$ and $\ln J_1/J_2$ is linear, the straight line passing through the origin; thus eqn. (4) is confirmed. The slope of the line yields a value for the effective cross-sectional area of a grain, $A=0{\cdot}32\,\mu^2$ (for the Comet 2 stack). The contribution by grains on δ-ray tracks must, of course, be included in the estimate of n, the number of grains/100 μ per cascade track. These extra grains amount to ~10% of the total. This estimate is obtained readily from measurements in other emulsions of the form of tracks of relativistic nuclei with $Z\sim26$ (Powell *et al.* 1959) and applies to contribution from δ-rays with ranges $1\,\mu<R<300\,\mu$. Longer-range δ-rays contribute very little, as they leave the emulsion, and grains on shorter δ-rays will be counted as part of the grain density of an individual track.

Fig. 7

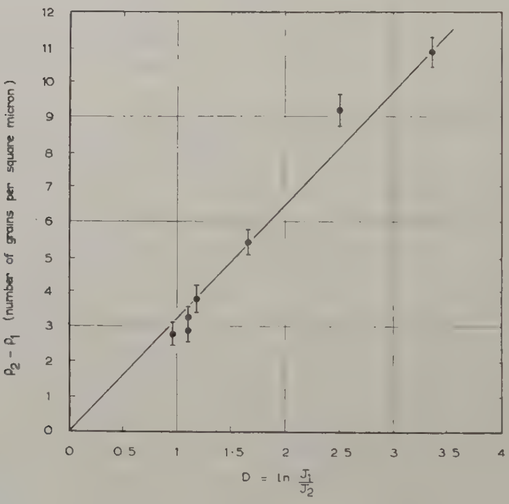

Comparison between the observed number of developed grains due to a cascade and the photometric density in the same position in the Comet 2 stack. ρ is defined as the projected *number* of developed grains per square micron through the emulsion thickness. J is the output signal from the photomultiplier tube. The projected *area* covered by developed grains throughout the emulsion thickness, per unit area, will be proportional to the logarithm of the transmission since double scattering of light can be shown to be unimportant. ρ_1, J_1 and ρ_2, J_2 refer to two positions relative to the cascade axis. The observed linear relation between $(\rho_2-\rho_1)$ and $\ln(J_1/J_2)$ shows that the mean area, A, of a developed grain is independent of the grain density n. The slope of the line corresponds to a value of $A=0{\cdot}32\,\mu^2$ (see eqn. (5)). In the grain counting, grains associated with low-energy electron tracks (mainly δ-rays) account for 10% of the total number of grains, but grains in heavily ionizing tracks were not included.

The value of A above is in accord with direct measurements of the apparent grain size from the gap-length distribution in tracks produced by particles with ionization about four times the minimum value.

A further check was made by determining the central density of a number of high-energy cascades (3000 to 6000 BEV), both at 7 r.l. distance from the origin, where the density is near its maximum, and at 10 r.l., where the number of electrons per square micron in the core of the cascade is reduced by about a factor of 5. The average difference between the values of the cascade energies based on the two different sets of measurements was only 3%.

Thus we conclude that systematic errors introduced, either by multiple scattering of light, or by variations in number and size of developed grains in the cascade tracks, as a function of cascade density, are unimportant, over the entire range of densities encountered in this experiment. The validity of the simple formula (4) is thus verified and it can be applied with confidence.

6.5. *Statistical Errors in Determination of Density D*

It is found in practice that an individual reading, J, on the oscilloscope, of the transmission of light at any point in the emulsion is subject to an r.m.s. deviation of the order of $\pm 8\%$. These variations are due, firstly, to fluctuations in the number and grain density of background tracks, and their inclination to the slit; and secondly, to variations in the degree of surface marking. An individual estimate of D is obtained by taking one reading, J, on the cascade, and two background readings, J_0, one on each side of the cascade. Thus, the r.m.s. error in $D = \ln J_0/J$ is approximately 0·10. This figure applies to the Comet 2 stack. In the Comet 1 stack, the surface markings on the emulsions were more troublesome, and the error in D was typically twice as great. As a result, only events with values of $D_{\max} > 0{\cdot}7$ were accepted for the energy-spectrum in stack 1.

For normal values of dip, $\sim 20°$, several independent readings of D can be taken in each emulsion; if the cascade is steep however—$\delta = 45°$ for example—only one reading is possible, but the cascade will pass through more emulsions near the region of maximum density, and the statistical error in the determination of $D_{\max}$ is almost unaltered.

§ 7. RELATION BETWEEN DENSITY AND ENERGY FOR CASCADES INITIATED BY γ-RAYS

7.1. *Relation between Maximum Density and Energy*

Having obtained a relationship between D and the projected track density, τ, the latter quantity must be related to the cascade energy. It is convenient first to consider cascades produced by single γ-rays. From the curves of Pinkau (1957), which are in good agreement with more recent theoretical calculations by Nishimura and Kamata (1958), one can conclude that the electron density $f(x, y)$ in the 'target diagram' of a cascade must be a function of the form

$$f(x, y) = E_0^2 g(r \times E_0) \qquad \qquad (6)$$

where $g(r \times E_0)$ is a function of the product E_0 and r only. Here, E_0 is the cascade energy, and $r=(x^2+y^2)^{1/2}$. Such a formula follows at once if most of the particles responsible for the optical density of the central region of the cascade are of high energy, so that 'Approximation A' is valid.

From eqn. (2), the relation between $\tau(0)=\tau(x=0)$ and E_0 can now be obtained:

$$\tau_0=\int_{-300\mu}^{+300\mu} f(0, y)\, dy=2\int_0^{300\mu} E_0^2 g(r\times E_0)\,.\,dr$$
$$=2E_0\int_0^{Z_0} g(z)\, dz$$

where $z=r\times E_0$ and $z_0=E_0\times 300\,\mu$.

If the upper limit to the integral may, to a sufficient degree of approximation, be taken as infinity (i.e. if the contribution for $r>300\,\mu$ can be neglected), then τ_0 will be strictly proportional to E_0 (again only under Approximation A). In practice, only a small proportion of the tracks are excluded on account of the finite emulsion thickness, so that τ_0 is found to increase only slightly more rapidly than the primary energy E_0.

A second effect is concerned with the finite slit width employed ($10\,\mu$). As already explained, eqn. (4) assumes the track density τ to be constant over the slit. If this is not so, then the light transmitted is a measure of the average value of $\exp(-An\tau)$ taken over the slit—eqn. (3). This quantity is nearly equal to $\exp(-An\bar{\tau})$ where $\bar{\tau}$ is the average value of τ taken over the slit. This approximation holds to a high degree of accuracy (better than 5%), provided the ratio of the intensities of light transmitted at the edges and at the centre of the slit is less than four. Such extreme variations of projected track density over short distances will only be found in cascades of extremely high energy and in their early stages of development. Where the effect begins to operate ($E_0>4000$ Bev at $t=5$ r.l.), the value of D as measured photometrically with a slit $10\,\mu$ wide, results in a slight underestimation of $\bar{\tau}$, and this tends to offset the overestimation resulting from the finite emulsion thickness described above. Empirically indeed, it is found that the relation between the central density, D_7, of the cascade at $t=7$ r.l., where it is close to its maximum, and E_0 is practically linear. Briefly, $E_0=4000(D_7)^{0\cdot94}$ Bev over the range 6000 Bev $>E_0>$ 2000 Bev, for section 2 of the stack where the radiation length is 1 cm. If, instead of D_7, one takes the maximum central density, $D_{\max}$, one finds $E_0=4000D_{\max}$ Bev, no appreciable departure from linearity being expected.

The general relation between cascade energy and $D_{\max}$ is:

$$E_0=\frac{31\,000X}{An}D_{\max} \quad \text{Bev},$$

where X is the radiation length measured in centimetres, and An represents the total area of grains in square microns per cascade electron track per hundred microns, and includes contributions from δ-rays. $D_{\max}$ refers to the maximum density as determined with a slit of width equal to

10 microns. If we substitute $X = 1$ cm and $An = 7{\cdot}7$ square microns per $100\,\mu$ per minimum track, we obtain the previous relation applicable to section 2 of the Comet 2 stack. In order to determine accurately the energy of an individual cascade, we find that the most convenient method is in fact to determine the maximum central density, $D_{\max}$, since this value is the one associated with the smallest statistical errors of measurement.

7.2. *Energy Calibration from Examples of Neutral Pion Decay*

So far, a relation between E_0 and $D_{\max}$ (the maximum central density) has been established on a theoretical basis. The method must now be calibrated. For low energies, Pinkau (1956) has determined values for E_0 by performing scattering measurements on the tracks of the cascade electrons. Since his results showed agreement with the theory of Nishimura and Kamata (1958), it is clear that the curves in fig. 8 must be in agreement with the points obtained from his cascades 'A' and 'D'. In fact, this result would be sufficient to calibrate the curves of fig. 7 over the entire range. This becomes clear if one remembers that essentially only two assumptions are involved in order to extend the distribution of cascade theory from low to high energies, provided Approximation *A* is valid in both regions. These are (i) that the cross sections for pair production and radiation remain homogeneous; and (ii) that multiple Coulomb scattering varies inversely as the particle energy. Effects such as the suppression of low-energy bremsstrahlung by high-energy electrons are completely negligible in these energy regions, as far as the development of the cascade at appreciable depths is concerned.

A completely independent check on the determination of the cascade energies is provided by measuring the angular divergence of the two γ-rays resulting from the decay of a single neutral pion, and determining the density of the subsequent cascades. The angle of divergence, χ, of the two γ-rays is related to the energy of the parent neutral pion by the equation

$$E_{\pi^0} = \frac{135}{\chi}(\epsilon^{1/2} + \epsilon^{-1/2})\,\text{Mev} \quad . \quad . \quad . \quad . \quad . \quad . \quad (10)$$

where ϵ is the ratio of the energies of the two γ-rays. In this formula, ϵ need only be known approximately (for a value of $\epsilon = 16$, the value of χ is only twice that for equipartition). In the material available to us there are three nuclear events, designated α8, P20 and 192α, in which only one or two neutral pions were emitted. It has been possible in these cases to give rather close limits to the total energy in γ-rays, from the observed angular divergence of the photons. Consider, for example, the event 192α in the Comet 2 stack. In this case, a nuclear interaction in the 'dural' end-plate gave rise to a single energetic neutral pion, but no observable shower particles. The two γ-rays by chance converted in pure emulsion (section 1) within 1 mm of each other, after passing through 7 cm of emulsion. Their separation was then $\sim 5\,\mu$. The angular divergence

Fig. 8

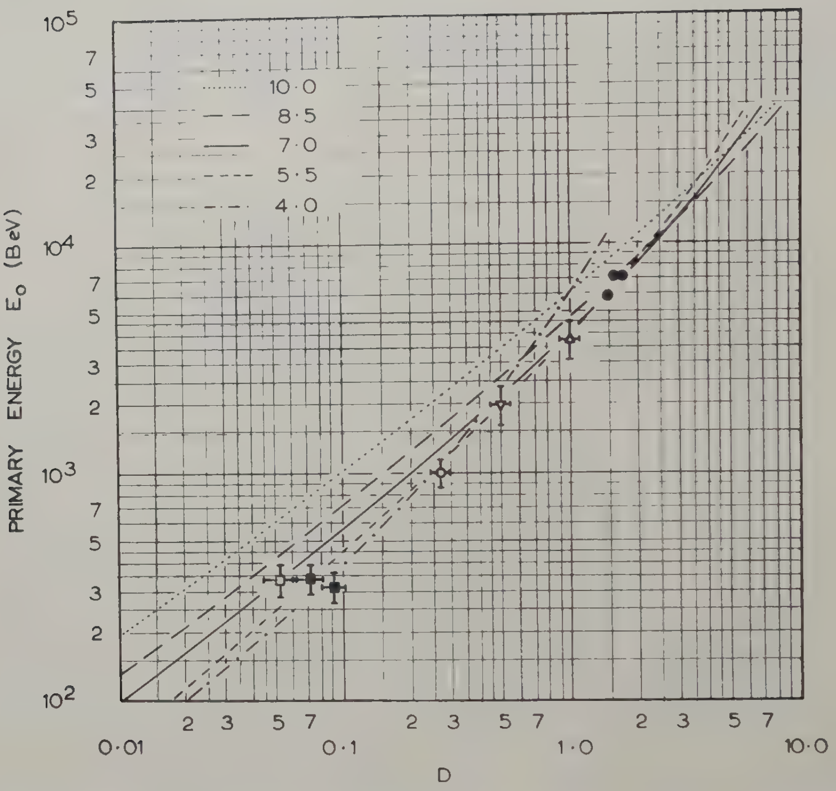

Relation between the primary energy E_0 of a cascade initiated by a γ-ray, and the central photometric density D. D is equal to $\ln (J_0/J)$, where J is the amplitude of the photomultiplier signal with the cascade axis focused in the centre of the image of the defining slit (fig. 5), and J_0 is the signal for a point in the emulsion remote from the cascade. The curves indicate the expected variation of D with E_0, calculated from the data of Pinkau (1957), at various depths from the point of conversion of the parent γ-ray (4, 5·5, 7·0, 8·5 and 10·0 r.l.). The lower envelope of the curves gives the relation between E and $D_{\max}$, and it can be seen that this envelope is very nearly a straight line; $E_0 = 4000 D_{\max}$ Bev. The relation between D and E_0 shown here refers to section 2 of the Comet 2 stack, where the radiation length was 1 cm, and the mean area of developed grains on a minimum track was $An = 7{\cdot}7$ square microns per hundred microns of track length.

For differing conditions of development, the values of D, for a given energy, will be proportional to An. For given values of An and D, the true value of E_0 is proportional to the radiation length. For example, in section 3 of the Comet 2 stack, where An is identical with that in section 2, but where the radiation length is 0·6 cm, a cascade of maximum density 1·0 would be produced by a γ-ray of energy $0{\cdot}6 \times 4000$ Bev.

The experimental points shown in the graph are as follows:

(i) The three lowest points are taken from the cascades ' A ' and between the two axes could be determined and was found to be $(7 \pm 1) . 10^{-5}$ rad. From the appearance of the subsequent cascade, it would appear that ϵ was close to unity; thus the energy estimated for the parent neutral pion (3800 ± 600 BeV) will be independent of small errors in ϵ. Photographs of this event are shown in fig. 9. At 7 cm distance from the point of conversion of the γ-rays (7 r.l. in section 2), the calculated separation of the cores is $\sim 10\,\mu$. This separation is quite insignificant compared with the lateral spread of each cascade at this position; hence the cascade density will be indistinguishable from that obtaining if the axes of the cascades had been exactly collinear. Since the density D is proportional to the energy, it follows that D will be the same as that produced by one cascade due to a single γ-ray of the same total energy (3800 BeV). This calibration point is plotted in fig. 7, together with events P20 and α8 which occurred in stacks of pure emulsion, and to which corrections were applied to allow for the different grain density, grain size and radiation length in the different medium.

The four points at highest energy in fig. 8 refer to events where the radial track distribution was determined directly by visual counting on the cascades at depths of 3–4 r.l. and the energy estimated from Pinkau's curves.

§ 8. ENERGY DETERMINATION FOR CASCADES ASSOCIATED WITH NUCLEAR INTERACTIONS

8.1. *Differences between Nuclear and Electromagnetic Cascades*

Let us now consider cascades produced as a result of nuclear interactions in the stack assembly. These cascades differ from those produced by single γ-rays, in that: (i) several γ-rays, distributed in energy, are involved; (ii) the axes of the individual cascades are laterally separated, according to the relative transverse momentum of the γ-rays (typically 200 MeV/c); (iii) secondary interactions may occur which reinforce the cascade from the original interaction.

Both effects (i) and (ii) increase the lateral spread of a 'nuclear' cascade over that of an 'electromagnetic' cascade of the same total energy, if this

---

'D' of Pinkau (1956) where the energy was estimated from scattering measurements on cascade electrons. The stack employed was of pure emulsion, and the energies have been reduced as indicated above.

□ measured at 7 r.l. ■ measured at 5·5 r.l.

(ii) The next three points refer to cases where the energy could be estimated from the divergence of the γ-rays in π^0-decay.

△ ; Event 192α, Comet 2 stack (see fig. 9), measured at 7 r.l.

▽ and ○ ; Events P20 (two π^0's) and α8 (one π^0) respectively, in pure emulsion stacks, at 6 r.l.

(iii) In the three highest sample points shown without errors, the energy was estimated by determining the total numbers of tracks inside 300 μ and comparing this with the energy estimate based on the central density D. The measurements were performed at 7 r.l. on three cascades in the Comet 2 stack (compare fig. 10).

spread is measured at the same depth t (measured from the nuclear interaction in the one case, and the stack edge in the other). To a first approximation, the effect of a source spectrum of γ-rays on the lateral spread will automatically be allowed for if the maximum density is determined. This maximum will occur about 1 r.l. earlier however, than that of an electromagnetic cascade produced by a single γ-ray of the same total energy. This result follows since the spectrum of secondary photons and electrons about 1 r.l. from the point of conversion of a single primary γ-ray, is similar in form to the spectrum of γ-rays produced at the origin of a nuclear interaction. In both cases about 30% of the total energy is carried by the most energetic γ-ray or electron, and the energy content of the low energy radiation is small. These results are obtained from the study of nuclear interactions occurring in the emulsion stack, and from the study of 'families' of parallel γ-rays originating in nuclear interactions in the overlying atmosphere. The experimental evidence will be described in detail in a later paper.

As a specific example, let us consider a cascade of total energy 4000 Bev. The most energetic γ-ray will typically have energy 1000–1500 Bev. γ-rays of energy 100 Bev or less will account for less than 20% of the total energy, and, at 6 r.l., their axes will deviate laterally by about 100 μ from that of the most energetic γ-ray. Because of this source of lateral spread, the projected central density of the cascade will be reduced from the value obtaining when all the γ-rays are collinear. (We at present neglect the effect of secondary nuclear collisions.) However, the total number of electron tracks within a fairly large radius of the main axis will be unaltered. Since the emulsions are of 600 μ thickness, it is convenient to measure the integrated track flux through a square of side 600 μ, centred on the main cascade axis. (This flux will for all practical purposes be the same as that through a circle of radius 350 μ centred on the axis.) Inside this radius, it can be assumed that the integral number of tracks will be equal to within a few per cent to that in a cascade produced by a single γ-ray of the same total energy at the same effective depth. As explained above, this will correspond to a γ-ray converting approximately 1 r.l. before the star origin.

8.2. *Integrated Lateral Distribution of Nuclear and Electromagnetic Cascades*

In order to determine the energy in the soft component associated with nuclear events, we have measured the mean cascade density over a lateral distance of 300 μ on each side of the main axis. Using the values of A and n above (§ 6.4), this yields the total number N_0, of electron tracks within 350 μ radius of the axis. N_0 was determined typically at a depth $t = 7$ r.l. from the star origin. From the curves of integral number of tracks as a function of $(E \times r)$ (Pinkau 1957), the value of the energy E of the equivalent single γ-ray was then determined for $r = 350\,\mu$ and $t = 8$ r.l. (measured from the point of conversion of this equivalent γ-ray). We shall call this energy $E_{7/300}$, to denote the value obtained from the number of tracks within a 300 μ box, at 7 r.l. from the star origin. $E_{7/0}$ denotes the energy determined from the central density at 7 r.l. from the star, which is the same as that for a γ-ray of this energy at 8 r.l. from the point of conversion. If secondary interactions could be neglected, the value of E_{300} thus derived should be largely independent of the choice of t.

The histograms of fig. 10 show the distribution in the ratio

$$R=\frac{E_{7/300}}{E_{7/0}}$$

for cascades initiated by interactions in the stack and by single γ-rays from outside. For cascades due to single γ-rays, the mean value of R is consistent with unity, as it should be. The r.m.s. spread in individual values of R is $\sigma \sim 0{\cdot}3$; this spread is to be accounted for in terms of fluctuations in cascade development, and errors of measurement. The majority of the nuclear events ($\sim 90\%$) have values of R similar to those for single γ-rays; the distribution is however skewed to high R values, and $\sim 10\%$ of the nuclear events give R values greater than unity by more than twice the standard deviation, σ, of the γ-rays.

Fig. 10

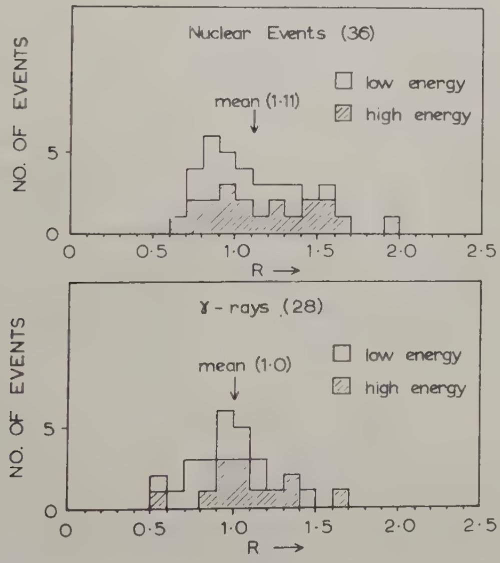

R is the ratio of the cascade energy in individual events as estimated from the total number of tracks within 350 μ of the cascade axis, to that determined from the central density. The distribution of R is shown for a sample of 36 'nuclear events' and 28 'electromagnetic events'.

These larger values of R in the nuclear events must be attributed to the effects of abnormal divergence of the individual γ-rays at the point of production. Detailed inspection of these events clearly reveals the occurrence of abnormally large values of transverse momenta. There appears to be no significant variation of the mean value of R with energy, over the small energy range investigated, and its absolute value is only slightly greater than unity ($R = 1{\cdot}11 \pm 0{\cdot}05$). This result means that the expected increase in R above unity, due to the effect of relative transverse momenta between individual γ-rays, is approximately compensated by the increase of the central density resulting from the effects of secondary nuclear disintegrations, and that the effect on the energy estimate due to the source spectrum of the γ-rays is correctly allowed for by considering the equivalent γ-ray to have converted 1 r.l. prior to the nuclear disintegration†.

In order to determine the spectrum of the total energy in the soft component liberated in nuclear interactions, we have employed the maximum central density of the cascade, $D_{\max}$, this value having the greatest statistical weight. The energy derived from $D_{\max}$, treating the cascade as initiated by a γ-ray—i.e. $E_{\max} = 4000\ D_{\max}$ BeV—will in general be greater than either of the other estimates $E_{7/300}$ or $E_{7/0}$ just considered, since the observed maximum of nuclear cascades occurs on average about 9 r.l. from the origin. This shift is of course due to the effects of secondary nuclear interactions. From the longitudinal development (see § 3, Part II) of high-energy nuclear cascades it is found that the $E_{\max}$ is $1{\cdot}10 \pm 0{\cdot}05$ times the value $E_{7/0}$. This factor exactly cancels the factor R in the foregoing analysis. Thus one obtains the result that $E_{\max}$ is equal to $E_{7/300}$ to within a few per cent, and is therefore, on average, a good estimate of the total energy liberated in the soft component in the *original* nuclear interaction. As emphasized above, this estimate will be incorrect in a few individual cases; where the value of R is abnormally large, the energy $E_{\max}$ will be an underestimate; and where the effects of secondary interactions are severe, $E_{\max}$ will clearly be an overestimate.

ACKNOWLEDGMENTS

This experiment was made possible only by the very generous facilities offered to us by the British Overseas Airways Corporation, for prolonged exposures at high altitudes in the course of proving flights by their Comet 2E aircraft. We have very great pleasure in thanking Captain T. B. Stoney, D.S.C., Flight Manager Comets; Captain R. E. Millichap, D.F.C., Deputy Flight Manager Comets; Mr. F. E. Hart, Base Engineer; Mr. Thomas Campbell, Base Foreman, and their staffs.

We wish to acknowledge the assistance of Mrs. Mary Webb, Mrs. Nevette Hillier, and Mrs. Najat Kaddoura in scanning the plates; Mrs. I. Pobjoy

---

† In the original presentation of this material (Perkins, I.U.P.A.P. Conference on Cosmic Rays, Moscow, July 1959), no experimental values of R were available, and the quantity R was calculated from the superposition of cascades due to γ-rays with the appropriate energy spectrum ($\sim E^{-1\cdot 0}\,dE$) and relative transverse momenta (~ 200 MeV/c). The calculated values of R decreased with increasing cascade energy, and resulted in a cascade energy spectrum somewhat steeper than that presented in this paper.

for drawing the diagrams; and Mr. W. Harbor for the photographs. We wish to thank Dr. J. Losty for help in the initial stages of the work.

This research was supported in part by a grant from the Department of Scientific and Industrial Research. J. Duthie and C. M. Fisher acknowledge this body also for maintenance grants. A. Kaddoura wishes to thank UNESCO for the award of a scholarship.

REFERENCES

FOWLER, P. H., PERKINS, D. H., and PINKAU, K., 1959, *Phil. Mag.*, **4,** 1030.
GREISEN, K., 1956, *Progr. Cosmic Ray Phys.*, Vol. 3 (Amsterdam: North Holland Publishing Co.).
KAPLON, M. F., KLOSE, J. Z., RITSON, D. M., and WALKER, W. D., 1953, *Phys. Rev.*, **91,** 1573.
MIGDAL, A. B., 1956, *Phys. Rev.*, **103,** 1811; 1957, *J. exp. theor. Phys.*, **32,** 633.
NEY, E. P., 1955, Proceedings 5th International Cosmic Ray Congress, Mexico.
NISHIMURA, J., and KAMATA, K., 1958, *Progr. theor. Phys.*, **6,** 93.
PERKINS, D. H., 1960, *Progr. Cosmic Ray Phys.*, Vol. 5 (Amsterdam: North Holland Publishing Co.).
PINKAU, K., 1956, *Nuovo Cim.*, **3,** 1285; 1957, *Phil. Mag.*, **2,** 1389.
POWELL, C. F., FOWLER, P. H., and PERKINS, D. H., 1959, *The Study of Elementary Particles by the Photographic Method* (Pergamon Press), p. 591.
ROSSI, B., 1952, *High Energy Particles* (New York: Prentice Hall).

The Study of High-energy γ-rays Produced by Cosmic Radiation at 40 000 feet†

Part II. The Energy Spectrum of Cascades and its Interpretation

By J. G. Duthie, C. M. Fisher, P. H. Fowler, A. Kaddoura‡,
D. H. Perkins, K. Pinkau and W. Wolter§
H. H. Wills Physical Laboratory, University of Bristol

[Received June 28, 1960]

Abstract

The results of the measurement of the density of electromagnetic cascades described in Part I are discussed. For events initiated by single γ-rays from the atmosphere it is found that the integral spectrum of cascade energy may be represented by a power law with exponent $-3{\cdot}0 \pm 0{\cdot}20$ for the range 1200–8000 Bev. The corresponding exponent for cascades associated with local nuclear interactions is $-2{\cdot}9 \pm 0{\cdot}2$ in the same energy range. The γ-ray spectrum may be used to calculate the pion spectrum in the atmosphere and this is compared with that deduced from measurements on μ-mesons at sea-level or underground. Reasons for the resulting discrepancies are discussed. The flux of cascades associated with local nuclear events when compared with the nuclear flux deduced from measurements on extensive air showers yields values for the fractional energy, K_π, radiated as pions in collisions of nucleons in the energy range 10 000–100 000 Bev. It is found that K_π decreases strongly with increasing primary energy. An upper limit to K_π has also been deduced from observations on the longitudinal development of these cascades.

---

§ 1. Introduction

The study of high-energy nuclear interactions has often proceeded through the detailed investigation of individual events. A more indirect approach can, perhaps, yield some valuable complementary information. An example of this second approach is the study of the μ-meson energy spectrum at sea-level. This energy spectrum can be interpreted in terms of that of the parent π-mesons which have been created in the high atmosphere. Barrett *et al.* (1952), Pine *et al.* (1959), and Ashton *et al.* (1960) have investigated this problem over an extensive energy range.

The study of high-energy γ-rays in the atmosphere is an alternative method of establishing the energy spectrum of π-mesons. The rapid absorption of γ-rays in the atmosphere limits the scope of experiments at sea-level and consequently long exposures at aircraft or higher altitudes are desirable. The emulsion-lead sandwich assembly described in Part I is a very good detector of γ-rays in the energy region above 1500 Bev. Furthermore the study of electromagnetic cascades associated with high-energy nuclear interactions, when combined with the primary nucleon spectrum, allows one to decide the fraction of the primary energy radiated in the form of π-mesons.

---

† Communicated by the Authors.

‡ On leave from the University of Damascus, U.A.R.

§ On leave from the Institute of Nuclear Research, Cracow, Poland.

§ 2. Energy Spectrum of Cascades

Applying the formula $E=4000D_{\max}$ Bev derived in Part I to both the electromagnetic and nuclear events, the integral energy spectrum of cascades has been determined.

Fig. 1

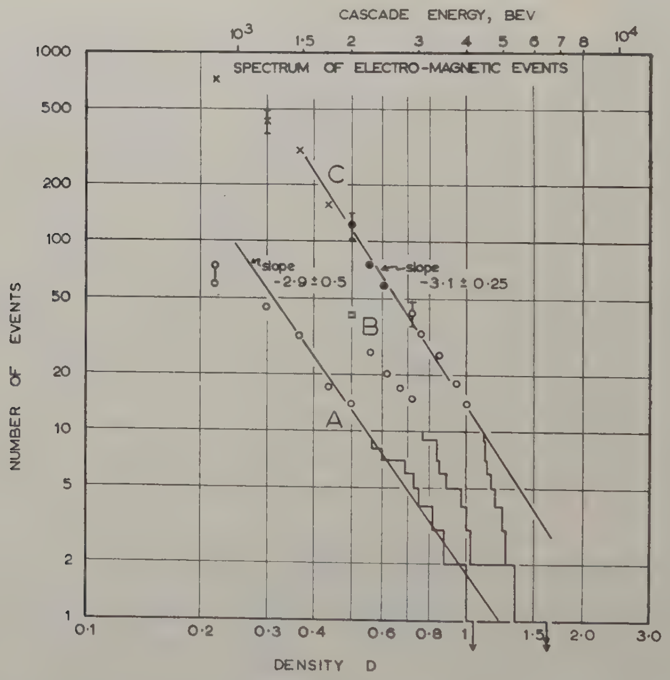

Integral spectrum of maximum central density D of cascades produced by electromagnetic events. For explanation of the distributions A, B and C, see text. The cascade energy E_0 is related to D by the relation $E_0=4000D$ Bev. The absolute flux of cascades in number/cm^2/ster/sec. can be obtained by multiplying the number of events shown in curve C. by $1{\cdot}0\times10^{-10}$.

2.1. *Electromagnetic Events*

In determining the densities, and thence the 'energy-spectrum', of the cascades, it is important to ensure that the effects of scanning loss for the cascades of low energy are made as small as possible. For this purpose, the events have been divided into three categories:

(i) As mentioned previously, we are confident that all events for which $D_{\max} > 0{\cdot}7$ have been detected in both stacks. This group of events will be referred to as selection C. The 'integral' distribution of the 42 events of this class is shown by the open circles, and as steps in the distribution C, of fig. 1.

(ii) For somewhat smaller values of D, the events in the Comet 2 stack are subject to severe scanning losses, and the measurements of D, for reasons given in Part I, are not considered reliable. For the Comet 2 stack, however, an analysis of the distribution of the measured angles of dip and of projected angle of the events found indicates that the scanning efficiency was high for angles of dip $< 30°$, and for values of $D_{\max} > 0{\cdot}5$. It was therefore appropriate to make a second selection of events from the Comet 2 stack for which $D_{\max} > 0{\cdot}5$, $\delta < 30°$. 42 events fell in this selection B, and their distribution is included in fig. 1 B.

(iii) To extend the spectrum to lower densities, only the events found in the most favourable conditions of observation in the Comet 2 stack (G5 section) are considered, i.e. those in layer 2, see fig. 2 (Part I) for which $2° < \delta < 11°$; together with those in layer 3, where the radiation length is shorter, for which $10° < \delta < 30°$. Among about 100 events thus chosen, 60 have measured values of $D > 0{\cdot}23$. These are plotted as distribution A of fig. 1. Conditions for detection are most favourable in layer 3. If events in this layer only are considered, the estimated number of events with $D > 0{\cdot}23$ occurring in *both* layers is 75, a result which suggests that about 15 in layer 2 have been missed. We believe that the selection A is not seriously affected by scanning loss for values of $D > 0{\cdot}3$.

The above procedures result in the collecting rate (cm^2. ster. sec) for the various selections being different. For selection C the whole collecting area of both stacks was used, and there was no restriction for the angle of dip. In selection B, only the second stack was used, and this stack represented 43% of the total collecting rate, when due allowance is made for the size of the stacks and the durations of their exposures. The further restriction $\delta < 30°$, that was imposed, results in an additional factor of 0·73 in the collecting rate, which is computed on the basis of the value of h/λ determined experimentally from the observed distribution of projected angles. It follows that selection B corresponds to only 31% of the total collecting rate of both stacks. In a similar manner, selection A is found to correspond to 10% of the whole. These factors for the rate of collection of events in the different classes are approximately in the ratios 10 : 3 : 1, in agreement with the numbers of events greater than a common energy that are observed.

The best estimate of the fluxes over the whole range of energies can now be obtained by scaling selections A and B by the appropriate factors. In the range $0{\cdot}50 < D < 0{\cdot}72$, selection B is used and added to the integral number in selection C at $D=0{\cdot}72$; this gives the results represented by the solid circles in distribution C. Similarly, for $D<0{\cdot}5$, selection A is added, and the results are represented by the crosses in distribution C.

The resulting integral spectrum, whether expressed in terms of density, D, or energy, corresponds to a power spectrum, $N(E)=KE^n$, with an index $n=-3{\cdot}1\pm0{\cdot}25$, for $D>0{\cdot}3$, corresponding to $E>1200$ Bev. This 'slope' is very steep compared with the generally accepted index for the primary cosmic-ray spectrum (of the order of $-1{\cdot}8$). It does not depend at all critically on the conversion factors employed above; for it may be seen that all three distributions in fig. 1 can be fitted by a line of this slope. It may be remarked that the two points of lowest energy fall below this line; at least a part of this fall must be ascribed to scanning losses, which become progressively more important in approaching lower energies. Selection C flattens off below $D=0{\cdot}7$, and selection B below $D=0{\cdot}5$; a comparison with selection A indicates that the fall-off in these two cases was due to scanning losses.

For the spectrum C, fig. 1, the absolute vertical flux of γ-rays/cm^2/ster/sec may be obtained by multiplying the number of events shown in the figure by a factor $1{\cdot}0\times10^{-10}$; further details are given in § 3.

It should be emphasized that the large value of the index n for the integral-spectrum here reported refers only to the energy interval from about 1500 Bev. At some lower value of the energy, the spectrum must 'flatten off', since it is well known that for secondary particles in the energy region of a few Bev, the energy distribution of pions expressed as a power spectrum, has an index similar to that of the primary radiation producing them.

Independent measurements of the γ-ray spectrum, using emulsions, were also reported by the Japanese group at the 1959 Moscow Conference (Nishimura 1959). In experiments at mountain altitudes, they observed an integral spectrum of individual γ-rays with an index $-2{\cdot}8$ in the energy range 500–1500 Bev. On the other hand, at balloon altitudes, they observed an integral γ-ray spectrum, for energies below 500 Bev, with an index of $-1{\cdot}8$. Neither of these results can be directly compared with those presented in this paper, for the altitudes of observation were quite different.

2.2. *Nuclear Cascades*

An analysis similar to that described above has been applied to the cascades associated with nuclear events. The spectra are shown in fig. 2, the selection criteria being identical with those for the γ-rays. Spectrum C is based on 39 events with $D>0{\cdot}72$. Above this limit, the spectrum is markedly 'flatter' than that of the electro-magnetic events, with an index $n=-1{\cdot}9\pm0{\cdot}4$. Spectrum B is based on 37 events in the Comet 2 stack only, and spectrum A on 97 events, of which 70 have measured values of $D>0{\cdot}23$. For $D>0{\cdot}3$, spectrum A has an index of $-3{\cdot}0\pm0{\cdot}5$, in contrast with the slope (spectrum C) at higher energy. Again, the lowest energy point in spectrum A has two values, the upper one denoting the number calculated using only layer 3 of the stack (as in fig. 1). In the case of the nuclear events, the normalization factors for the three selections differ slightly from those for the electro-magnetic events. This is due to the fact that the nuclear events originate nearly uniformly throughout the volume of the stack, whereas the electro-magnetic cascades are initiated near its surfaces.

Fig. 2

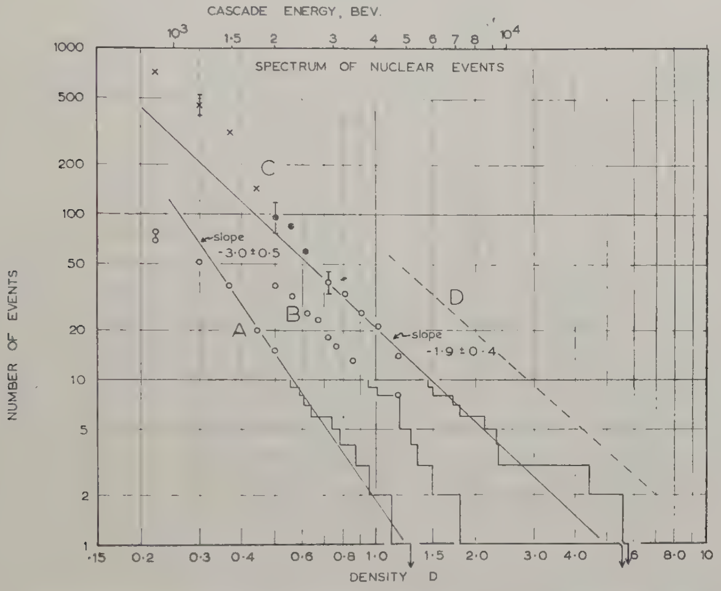

Integral spectrum of maximum central density D of cascades produced by nuclear events. For explanation of the distributions A, B and C, see text. The cascade energy E_0 is related to D by the relation $E_0 = 4000D$ Bev. The line D is the estimated flux of nucleons which would interact in the stack; the energy of these nucleons, as read off from the cascade energy scale, is to be multiplied by a factor 10. Thus, we expect 20 nucleons with energy exceeding 80 000 Bev to have interacted in the stacks.

The absolute flux of cascades in number/cm²/ster/sec, can be obtained by multiplying the number of events shown in curve C, by $1{\cdot}0 \times 10^{-10}$.

The ratio of the calculated factors for distributions C and B is independent of the assumed value of the interaction length, whereas the observed number of events in distribution A depends on the magnitude of the shielding provided by layers 1 and 2 of the stack assembly. Assuming the ‘geometrical’ value for the nuclear interaction length, the normalization factors for the distributions C, B and A are estimated to be in the ratio 9 : 3 : 1, in excellent agreement with the numbers of events actually observed. It is therefore again reasonable to construct a composite spectrum shown in spectrum C, as was done for the electro-magnetic events. This composite spectrum rather strongly suggests a 'flattening' in the slope of the spectrum with increasing energy. The best fit to the experimental results for the interval $0{\cdot}3 < D < 2{\cdot}0$ corresponds to an index $n = -2{\cdot}9 \pm 0{\cdot}2$.

A summary of the slopes of the spectra for electro-magnetic and nuclear events in different energy intervals is given in table 1.

Table 1

	Cascade energy range (Bev)	E.M. events	Nuclear events
Selection C	$\geqslant 3000$	$-3{\cdot}7 \pm 0{\cdot}6$	$-1{\cdot}9 \pm 0{\cdot}4$
Selection A	$\geqslant 1200$	$-2{\cdot}9 \pm 0{\cdot}5$	$-3{\cdot}0 \pm 0{\cdot}5$
Composite spectrum	1200–8000	$-3{\cdot}0 \pm 0{\cdot}2$	$-2{\cdot}9 \pm 0{\cdot}2$

§ 3. DISCUSSION OF THE ENERGY SPECTRA

3.1. *Introduction*

The principal results of the present measurements on the energy spectra of the cascades may be summarized as follows: (i) the integral energy spectrum of cascades initiated by individual γ-rays incident from the atmosphere is of the form $E^{-\beta}$, where $\beta \simeq 3{\cdot}0$; (ii) the spectrum of the cascades associated with nuclear interactions is of the same form for cascade energies between 1200 and 8000 Bev, but at higher energies the distribution appears to be appreciably flatter; (iii) the proportion of all the cascades which are associated with nuclear interactions inside the stack is about 50%, except at the highest energies, where events with associated local nuclear interactions predominate.

If we assume that the γ-rays are produced in the decay of π^0-mesons with a differential energy spectrum of the form

$$dN_{\pi^0} = aE^{-(\beta+1)}\,dE,$$

it may readily be shown that the resultant γ-rays have a spectrum

$$dN_\gamma = \frac{2a}{(\beta+1)}E^{-(\beta+1)}\,dE\,;$$

thus the spectrum of γ-rays is similar to that of their parent π^0-mesons, but they are diminished in intensity by a factor of $2/(\beta+1)$.

By similar arguments, the energy spectrum of individual electrons arising from conversion of these γ-rays, and of γ-rays arising from *bremsstrahlung*, may also be shown to follow a power law of the same 'slope'. The spectrum of 'electro-magnetic' events entering the stack from outside, will therefore reflect the energy spectrum of *individual* π^0-mesons produced in nuclear interactions in the air above the stack.

In contrast, the energy of the cascade resulting from a nuclear event, as determined photometrically, is a measure of the *total* energy released into the 'soft component' by the interaction.

As the two spectra are very similar between 1200 and 8000 Bev, we conclude that there is little change in the ratio of the total energy appearing as electro-magnetic radiation as a result of a nuclear interaction to the energy carried by the π^0–meson of highest energy.

3.2. *The Significance of the Spectrum of Individual γ-rays*

3.2.1. *Comparison of photon and muon fluxes*

From the observed γ-ray spectrum, it is possible to calculate the pion spectrum in the atmosphere, under the assumption that all the γ-rays originate as the decay products of neutral pions; if there are other sources of γ-rays, we shall obtain an upper limit to the pion flux. This flux may than be compared with that calculated from observations of the muon flux at sea-level and underground.

Suppose $A\exp(-x/\lambda_p)$ represents the source distribution of charged pions above a certain energy, E, at vertical incidence, where x is the depth in the atmosphere (g/cm^2), and λ_p the attenuation length of the pion-producing component. The total number of pions throughout the atmosphere is then $A[1-\exp(-H/\lambda_p)]$, where the total depth of the atmosphere corresponds to $H = 1000\,\text{g/cm}^2$. The source distribution of γ-rays of energy exceeding E, at depth x, will then be $A/(\beta+1)\exp(-x/\lambda_p)$, where β is the index of the integral pion spectrum, under the assumption that the number of neutral pions is half the number of charged pions. The number of such γ-rays (and/or electrons), vertically incident on a stack at depth h, is then

$$\frac{A\lambda_\gamma}{(\beta+1)(\lambda_p-\lambda_\gamma)}\,[\exp(-h/\lambda_p)-\exp(-h/\lambda_\gamma)]$$

where λ_γ is the attenuation length of the γ-rays. It follows that the (vertical) pion flux can be obtained from the observed (vertical) γ-ray flux by multiplying by a factor

$$Q=\frac{(\lambda_p-\lambda_\gamma)}{\lambda_\gamma}(\beta+1)\,\frac{(1-\exp(-H/\lambda_p))}{[\exp(-h/\lambda_p)-\exp(-h/\lambda_\gamma)]}.$$

For $\lambda_p = 110\,\text{g/cm}^2$, $\lambda_\gamma = 60\,\text{g/cm}^2$, $\beta = 3$, $h = 220\,\text{g}$, one obtains $Q = 30$. The corresponding pion spectrum is shown by the line B in fig. 3.

This spectrum may be compared with the pion spectra deduced from observation on muons at sea-level or underground. In such a comparison it may be assumed tentatively, that pions are the principal sources of both γ-rays and muons. Magnetic spectrometer measurements of the muon energy spectrum at sea-level have been made by both the Cornell and Durham groups (Pine *et al.* 1959, Ashton *et al.* 1960). The results extend at present up to an energy of several hundred Bev. The pion spectrum can be derived from them by calculating the energy loss of the muons in the atmosphere, and the probability that the parent pions decay before interacting. Both groups of results yield a pion integral spectrum of the form: $N(E) = 9{\cdot}5\times10^{-2}E^{-1{\cdot}64}$/cm^2/ster/sec, where E is in Bev, for

$E < 400$ Bev. This spectrum, extrapolated to the energies considered in the present experiment, is indicated by the line C 1 in fig. 3. Within the energy range 1200–4500 Bev, the two independent estimates of the absolute number of pions agree to within a factor of about 2.

The Cornell underground measurements (Barrett *et al.* 1952) of the range spectrum of muons yield a pion spectrum, above 400 Bev, somewhat steeper (integral index $-2{\cdot}0$) than that deduced from the spectrometer results. Normalizing the two spectra at 400 Bev, the line C 2 in fig. 3 shows the integral pion spectrum deduced from these underground measurements.

Fig. 3

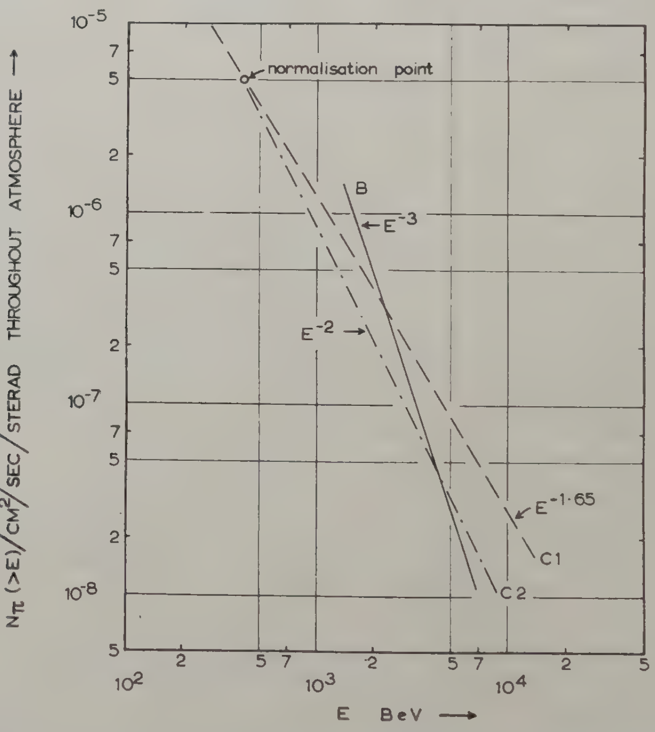

The energy spectrum of all charged pions produced throughout the atmosphere, as calculated by three different methods.

Curve C1 is the extrapolation of the pion spectrum deduced from the muon energy spectrum at sea-level, as determined with magnetic spectrometers (Ashton *et al.* 1960, Pine *et al.* 1959). The muon spectrum has been measured reliably up to ~400 Bev, and up to this energy, the pion spectrum has an index of $-1{\cdot}64$.

Curve C2 shows the slope of the pion spectrum calculated from the muon range spectrum underground (Barrett *et al.* 1952). The absolute flux has been normalized to that from the spectrometer measurements at 400 Bev.

Curve B is that deduced from the γ-ray spectrum observed in the present experiment.

Although the pion fluxes deduced from the muon measurements on the one hand, and the γ-ray cascades on the other, agree in order of magnitude, the discrepancy in absolute number, a factor 2 at 1500 Bev, cannot easily be accounted for in terms of errors of measurements. Much more serious however, is the difference in the 'slopes' of the pion spectra. The present experiment suggests $n = -3{\cdot}0$ for E between 1200 and 8000 Bev, whereas the muon results suggest a value of n between $-1{\cdot}65$ and $-2{\cdot}0$.

The pion spectrum deduced from the γ-rays, B in fig. 3, has been calculated assuming the index β of the power law to be constant. If in fact there is a change in slope of the γ-ray spectrum, below 1500 Bev, for example, then the conversion factor Q will be reduced over part of the spectrum. It should be noted that the attentuation length λ_γ, of the electron–photon component, depends slightly on the slope of the spectrum; thus as $\beta \rightarrow \infty$, $\lambda_\gamma \rightarrow 48$ g/cm^2, the conversion length (see, for example, Rossi 1952). The effect of a moderate reduction in the index of the photon spectrum near our lower limit (1500 Bev) will therefore result in an appreciable reduction in the estimate of the pion flux at this energy (see table 2).

Table 2

β	λ_γ (g/cm^2)	Q
$-3{\cdot}0$	57	32·6
$-2{\cdot}5$	62	25·4
$-2{\cdot}0$	72	18·0

It does not seem possible, however, to account for the whole of the difference in the two estimates of the pion flux in terms of errors of measurements, or small variations in the index β of the spectrum. It should be pointed out that the estimate of the pion production throughout the atmosphere as inferred from observations on the μ-mesons is largely determined by the rate of pion production at atmospheric depths less than 40 g/cm^2, and depends on the assumed value of the nuclear interaction length of the pions, λ_π. In the present experiment, however, the main contribution to the photon flux arises from nuclear interactions at a depth of about 160 g/cm^2. There will, therefore, be serious discrepancies between the two estimates of pion flux if the source distribution of pions departs appreciably from the exponential one assumed ($\lambda_{\mathrm{p}} = 110$ g/cm^2); or if either this source distribution, or λ_π, vary with energy.

3.2.2. *Effects of other sources of photons and muons*

Hitherto, we have assumed that the photons and muons arise only through the decay of pions. It is evident, however, that, in the high-energy region heavier particles, such as K$^\pm$-mesons, on account of their greater rest-mass and shorter lifetime, may constitute an important source of muons. In addition, most of any $\mathrm{K_0}^1$ particles, because of their very short lifetime (10^{-10} sec), decay before interacting, and of these one-third provide γ-rays through the decay mode $\mathrm{K_0}^1 \rightarrow 2\pi^0$. An approximate formula for the probability that a particle will decay before interacting, assuming an interaction length of 70 g/cm^2, and an exponential source distribution corresponding to an attenuation length of 110 g/cm^2 (a value which is not critical), is

$$f \simeq [1+8\times 10^4(p\tau/mc)]^{-1},$$

where τ is the mean lifetime in seconds, and p is the momentum.

Table 3 shows the relevant decay processes of mesons and hyperons. In many cases the μ-meson or γ-ray is produced as the result of a succession of two, sometimes three, decay processes. The column headed 'Weighting factor' gives the number of particles decaying in the appropriate mode; it takes account of the branching ratio in cases where alternate decay modes occur; and it gives the relative production rates for the parent particles assuming charge-independence to hold at production. Column 3 gives the probability that the decay chain will be completed in the atmosphere.

Values of $e_{\max}=E_{\max}/E$ and $e_{\min}=E_{\min}/E$, the maximum and minimum values for the ratio of the energy of a secondary particle to that of its parent, are given in columns 4 and 5; they apply to the first decay in cases where a chain of decay is involved.

For a particular decay mode, the ratio, R, of the flux of secondaries above a given energy to the flux of the parent particles above the same energy which decayed according to the particular mode, is given by the relation

$$R=\frac{n}{\beta+1}\,\frac{(e_{\max})^{\beta+1}-(e_{\min})^{\beta+1}}{e_{\max}-e_{\min}}$$

where n is the number of secondaries of the appropriate type produced in each decay.

In cases where the μ-meson or γ-ray is produced as a result of a decay chain, the ratio of the flux of μ-mesons or γ-rays, to the flux of particles initiating the decay chain which decayed in the manner indicated, will be given by the product of appropriate values of R. This ratio is given in an approximate form in column 6.

The final column shows the corresponding contributions made by the various decay chains to the flux of μ-mesons and γ-rays for the particular value, $\beta=2$. These results, taking account of the various weighting factors and decay probabilities, are the product of columns 2, 3 and 6, except in the case of the decay of Λ^0-hyperons. There, production resulting from the decay of Σ^0 and Ξ hyperons is taken account of in the last column only.

Other decay modes, such as $K^{\pm}\rightarrow\pi^{\pm}+\pi^0\rightarrow\mu^{\pm}+2\gamma$, contribute very little to the flux of γ-rays or μ-mesons. This follows because the decay probability $f_k\times f_\pi$ for the production of μ-mesons compares unfavourably with the other processes at high energy; and as a source of γ-rays a value of f_k for the decay probability has to be compared with 1 for the decay of $K_0{}^1$ and π^0.

At high energies ($\gtrsim 1000$ Bev), $f_k/f_\pi \simeq 7$. Thence, for $\beta = 2$, using the values shown in table 3, column 7, it follows that the ratio of the number of muons above a given energy arising from K-decay to the number arising from π-decay is $2{\cdot}7\ (N_k{}^{\pm}/N_\pi{}^{\pm})$. This figure stands in sharp contrast with the figure for the ratio of the number of γ-rays arising from the decay of K and π-mesons respectively, viz. $0{\cdot}21\ N_k{}^{\pm}/N_\pi{}^{\pm}$; neither coefficient is very sensitive to the value of β. It therefore follows that the contribution of K-particles to the muon flux is at least ten times more important than its contribution to the photon flux.

It is also interesting to consider the possible effects of any hyperons. The relevant factors are included in table 3. It may be seen that, assuming charge-independence to be valid, the relative numbers of muons and γ-rays above a given energy derived from this source is close to $2f_\pi$; almost the same ratio as if directly produced pions were the only source. Any difference in the spectra of muons and photons cannot therefore be ascribed to hyperon production. Hyperon production would be an important factor if, for example, in a high-energy interaction, the highest energy baryon were equally likely to be a hyperon or a nucleon, and if its energy were comparable with that of the primary. In these circumstances, the energy transformed into γ-rays by decay in the atmosphere would be of the order of 5% of the primary energy, a value comparable with that of the most energetic photon resulting from direct pion production (see § 3.4).

It is interesting to note that the decay of hyperons results in a strong negative excess of the muons, the negative to positive ratio being 4:1. Accompanying these hyperons, however, there will, of course, be K^0 and K^+ particles of strangeness +1; the net charge excess of the muons from both hyperon and K-particle decays will depend critically on the partition of energy between these particles at production. It may be remarked that the positive excess of muons (at all energies) is customarily explained as due to the preponderance of protons in the primary cosmic-ray beam. In fact, if strange-particle production is an important process in high-energy collisions, the interpretation of the observed positive/negative ratio for the muons will be greatly complicated.

Finally, direct nuclear production of γ-rays may occur at high energies, through the process of 'inner bremsstrahlung'—this radiation being associated with acceleration and creation of the many charged secondary particles in the nuclear encounter. At present, it is not possible to assess experimentally the importance of this contribution; general theoretical considerations suggest, however, that the contribution to the total γ-ray flux would be very small.

3.3. *The Cascade Spectrum from Nuclear Interactions in the Stack*

The interpretation of the 'nuclear cascades' is complicated by the fact that cascades are apparently produced by both nucleons and pions, in comparable numbers, and possibly by other particles. This result, it will be remembered, follows from the observed relative numbers of neutral and charged primaries of the 'jets' recorded in pure emulsion.

3.3.1. *Proportion of pion primaries*

It is of importance to try to estimate the proportion of pion primaries from the observed γ-ray flux. Assuming all the γ-rays to originate in π^0-decay, and $N_{\pi^\pm} = 2N_{\pi^0}$, the ratio of numbers of charged pions and photons above a given energy, vertically incident on the stack from the atmosphere, is

$$R = \frac{(\beta+1)[1-\exp(-x(\lambda_{\mathrm{P}}-\lambda_\pi)/\lambda_{\mathrm{P}}\lambda_\pi) \,.\, (\lambda_{\mathrm{P}}-\lambda_\gamma) \,.\, \lambda_\pi]}{1-\exp(-x(\lambda_{\mathrm{P}}-\lambda_\gamma)/\lambda_{\mathrm{P}}\lambda_\gamma) \,.\, (\lambda_{\mathrm{P}}-\lambda_\pi) \,.\, \lambda_\gamma}$$

where, as before, β is the exponent of the integral pion spectrum, and λ_{P} is the attenuation-length of the pion source; λ_γ is the attenuation length for γ-rays above a certain energy, and is tabulated in table 3. λ_π is to be identified with the interaction-length of pions, since pion production by pions is accounted for in the source distribution. Thus, taking $\lambda_{\mathrm{P}} = 110\,\mathrm{g/cm^2}$, $\lambda_\pi = 70\,\mathrm{g/cm^2}$, and $\lambda_\gamma = 57\,\mathrm{g/cm^2}$, and an effective value of $x = 260\,\mathrm{g/cm^2}$, one obtains $R = 5$. This value is rather insensitive to the choice of parameters employed.

Virtually all the energetic photons incident on the stack are detected, whereas, assuming the interaction mean free path to be geometrical, only $\sim 50\%$ of the pions will interact at points such as to give a detectable cascade. Further, only a fraction, F, of the pion energy is transformed into γ-rays. The relative numbers of cascades due to pions and γ-rays respectively is then $(R/2)(F)^\beta$. Upper and lower limits to F can be set as follows: The upper limit of $(F)^\beta$ will be $\frac{1}{3}$; that is, in $\frac{1}{3}$ of the events, practically the entire energy will be transformed into γ-rays if charge-exchange is an important process. A lower limit is $F = \frac{1}{3}$. However, even if one-third of the energy is radiated on the average, the quantity $\sqrt[3]{(\overline{F^3})}$ will certainly exceed $\frac{1}{3}$, on account of fluctuations. Hence, the ratio of numbers of cascades produced by pions and γ-rays should lie between 0·1 and 0·9. Thus, we cannot expect the number of cascades produced by interactions of pions releasing a given energy into the electromagnetic cascade, to be more numerous than the number of such cascades initiated by γ-rays or electrons. In fact, the observed neutral to charged ratio of the primaries interacting in emulsion (§ 4, Part I) is consistent with an effective value of F of 0·5.

3.2.2. *The change in the index of the spectrum; inelasticity of the collisions*

One of the salient features of the energy-spectrum is the great preponderance of local nuclear origins for the cascades of highest energy. Thus, all six cascades of energy > 8000 Bev were associated with nuclear events in the stack. This observation leads to the conclusion that the nuclear disintegrations responsible for these cascades of highest energy

Table 3

Decay mode	Weighting factor	Decay probability	$\frac{E_{\max}}{E}$	$\frac{E_{\min}}{E}$	Spectrum factor	Contribution to flux for $\beta=2$
$\pi^{\pm}\to\mu^{\pm}+\nu$	$N_{\pi}\pm$	f_{π}	1	0·57	$\frac{1\cdot9}{\beta+1}$	$0\cdot63 f_{\pi}N_{\pi}{}^{\pm}$
$K^{\pm}\to\mu^{\pm}+\nu$	$\sim\frac{2}{3}N_{K}\pm$	$f_{K}\sim7f_{\pi}$	1	0·05	$\frac{1\cdot05}{\beta+1}$	$1\cdot61 f_{\pi}N_{K}\pm$
$K_1{}^0\to2\pi\to2\mu$	$\frac{1}{3}N_{K}\pm$	f_{π}	0·92	0·08	$\frac{3\cdot8}{(\beta+1)^2}$	$0\cdot13 f_{\pi}N_{K}\pm$
$\pi^0\to2\gamma$	$\frac{1}{2}N_{\pi}\pm$	1	1	0	$\frac{2}{\beta+1}$	$0\cdot33 N_{\pi}{}^{\pm}$
$K_1{}^0\to2\pi^0\to4\gamma$	$\frac{1}{6}N_{K}\pm$	1	0·92	0·08	$\frac{3\cdot8}{(\beta+1)^2}$	$0\cdot070 N_{K}\pm$
$\Lambda^0\to\pi^-+p$ $\searrow\mu^-$	$\frac{2}{3}N_{\Lambda^0}$	f_{π}	0·24	0·06	$2\cdot5\,\frac{(0\cdot24)^{\beta}}{(\beta+1)^2}$	$0\cdot011 f_{\pi}[N_{\Lambda^0}+0\cdot88N_{\Sigma^0}+1\cdot47N_{\Xi^0}]$
$\Sigma^+\to\pi^++n$ $\searrow\mu^+$	$\frac{1}{2}N_{\Sigma^0}$	f_{π}	0·35	0·04	$2\cdot1\,\frac{(0\cdot35)^{\beta}}{(\beta+1)^2}$	$0\cdot015 f_{\pi}N_{\Sigma^0}$
$\Sigma^-\to\pi^-+n$ $\searrow\mu^-$	N_{Σ^0}	f_{π}	0·36	0·04	$2\cdot1\,\frac{(0\cdot36)^{\beta}}{(\beta+1)^2}$	$0\cdot031 f_{\pi}N_{\Sigma^0}$
$\Xi^-\to\pi^-+\Lambda^0$ $\searrow\mu^-$	N_{Ξ^0}	f_{π}	0·25	0·04	$2\cdot4\,\frac{(0\cdot25)^{\beta}}{(\beta+1)^2}$	$0\cdot016 f_{\pi}N_{\Xi^0}$
$\Lambda^0\to\pi^0+n$ $\searrow2\gamma$	$\frac{1}{3}N_{\Lambda^0}$	1	0·24	0·06	$2\cdot6\,\frac{(0\cdot24)^{\beta}}{(\beta+1)^2}$	$0\cdot0056[N_{\Lambda^0}+0\cdot88N_{\Sigma^0}+1\cdot47N_{\Xi^0}]$
$\Sigma^0\to\gamma+\Lambda^0$	N_{Σ^0}	1	0·12	0	$\frac{(0\cdot12)^{\beta}}{\beta+1}$	$0\cdot0048 N_{\Sigma^0}$
$\Sigma^+\to\pi^0+p$ $\searrow2\gamma$	$\frac{1}{2}N_{\Sigma^0}$	1	0·35	0·04	$2\cdot3\,\frac{(0\cdot35)^{\beta}}{(\beta+1)^2}$	$0\cdot015 N_{\Sigma^0}$
$\Xi^0\to\pi^0+\Lambda^0$ $\searrow2\gamma$	N_{Ξ^0}	1	0·26	0·04	$2\cdot4\,\frac{(0\cdot26)^{\beta}}{(\beta+1)^2}$	$0\cdot018 N_{\Xi^0}$

were not produced by pions, but were, very probably, produced by nucleons. The integral energy-spectrum in this high-energy region has an index $n = -1{\cdot}9 \pm 0{\cdot}4$, a value consistent with the assumed index of the primary cosmic-ray spectrum. Using the flux values for primary protons given by the MIT group (Clark *et al.* 1957), and assuming that the nucleons are attenutated in the atmosphere with a coefficient of 110 g/cm^2, the fraction of the energy transformed into the soft component in these nuclear interactions can be estimated. Considering the 21 nuclear events in which more than 4000 BeV was transformed into γ-rays, we find from fig. 2 curve D, that there are 21 nucleons of $E > 80\,000$ BeV expected to interact and give visible cascades in the stacks. It follows therefore that typically it requires nucleons with energy $\sim 80\,000$ BeV to produce cascades with energy ~ 4000 BeV, i.e. that the proportion of energy, K_γ, transformed into γ-rays is $\sim 5\%$. Further, the total energy transformed to all pions, neutral and charged, and taking fluctuations into account, is only $\sim 10\%$ of that of the primary particle. At lower energies, the slope of the energy spectrum changes appreciably, becoming steeper. This must in part at any rate be attributed to the effects of interactions due to pions. Empirically, the spectrum can be expressed as:

$$N = 8D^{-3{\cdot}2} + 14D^{-1{\cdot}6},$$

and the two terms may, tentatively, be attributed to the contributions from pions and other particles respectively. Such a distribution for interactions due to pions would follow if, as seems highly probable, the fraction of the primary pion energy transformed into the soft component is independent of primary energy. It then follows from the above formula that for $D > 0{\cdot}30$ ($E > 1200$ BeV) $\sim 30\%$ of all nuclear interactions should be ascribed to pions. The fraction of neutral primaries predicted by the formula is not however in good agreement with that directly observed (§ 4.2, Part I). For $3000 > E > 1200$ BeV, neutral primaries should be only 9% of the total; yet among 15 primaries observed, five were neutral†. For $E > 3000$ BeV, 25% of the primaries should be neutral: in fact three primaries out of a total of 11 were uncharged.

Because of these apparent inconsistencies between the neutral/charged ratio actually observed at the lower energies, and that predicted by the foregoing equation, it seems improbable that the change in slope of the spectrum can be explained entirely in terms of the contribution of pion primaries.

§ 4. LONGITUDINAL DEVELOPMENT

In any dense medium, where decay of mesons into muons is improbable, it is clear that practically the whole of the primary energy will eventually be transformed into the soft component via successive generations of the *nuclear* cascade. On the other hand discussion in the last section led to the conclusion that, on the average, only a small fraction of the primary energy was transformed into γ-radiation in each individual nuclear interaction.

---

† In a similar study in the same energy range, the presence of about 30% neutral particles among the primaries of nuclear events has again been confirmed.

Similar low values of 'inelasticity' in nuclear collisions have also been suggested by the results of experiments in which the energy of a primary particle making a nuclear collision in emulsion was estimated from a kinematical analysis of individual interactions (see, for example, Perkins 1960). If the 'inelasticity' in such collisions is indeed low, the longitudinal development of the ensuing nucleonic and electromagnetic cascade should show evidence of it.

Fig. 4

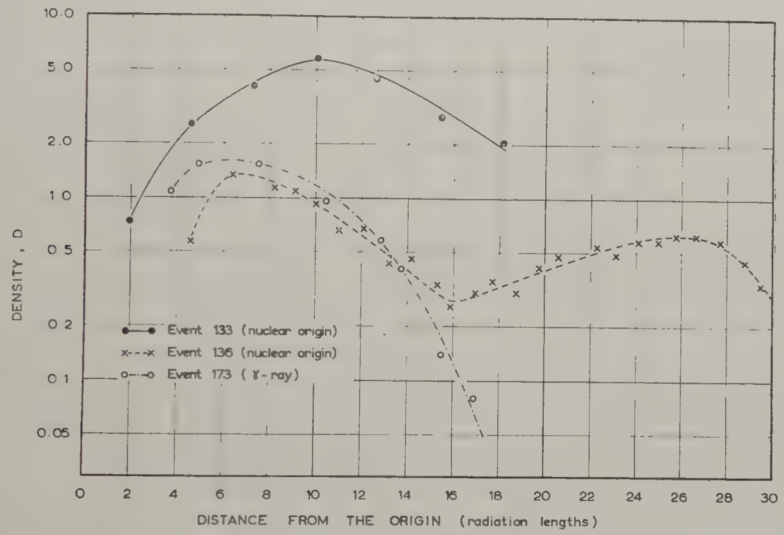

Three examples of the variation of the central density D of cascades with depth from the origin. Event 136 shows a striking rejuvenation due to one or more secondary interactions.

To investigate such an effect in our present 'stacks', we considered only the cascades of highest energy, for those of lower energy quickly pass below the threshold of reliable measurement. That indeed a high-energy secondary particle, capable of rejuvenating the cascade, is sometimes present is shown by the observation of 'double-humped' cascades. An example of such a development is shown in fig. 4. The limited depth of the stacks employed made it necessary to limit the study of the cascade development to 24 r.l. from the origin, or through a distance corresponding to one nuclear interaction length in the medium employed (essentially, 75% by weight Pb, 25% emulsion). In these conditions, any secondary particle of great energy emerging from an interaction should have interacted within the emulsion in about 60% of the events studied.

The longitudinal development of 21 nuclear cascades of high energy, and with suitable geometry, was investigated. Figure 5 shows the average behaviour of the central projected density of tracks per micron and this may be compared with the longitudinal development of cascades initiated by γ-rays of a similar energy. On the average, as stressed in § 8, Part I, for nuclear cascades the maximum of the central projected density is delayed by several radiation lengths, as compared with the results for single γ-rays, and its subsequent decline is, on the average, much less rapid. The ratio of the integral under the curve—see fig. 5—for nuclear events to the corresponding quantity for γ-rays gives a measure of the ratio of energy transformed into γ-rays in the nuclear cascade, to that liberated in the first interaction. More closely it in fact approximates to the ratio of the energy transformed into the soft component in about the first 3 r.l. to that liberated

Fig. 5

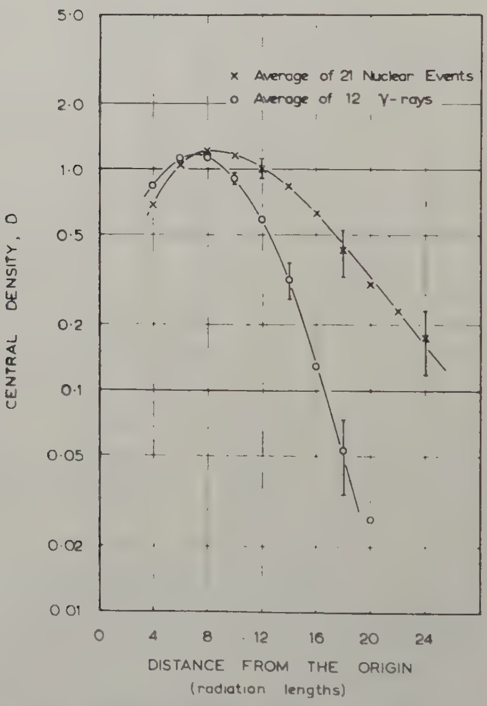

The graphs show the average behaviour of cascades produced by 12 single γ-rays, and 21 nuclear interactions respectively. All events above a certain threshold energy and of suitable stack geometry have been included. The much more rapid attenuation of the cascades initiated by individual γ-rays is clearly demonstrated. The errors shown are deduced from the internal deviations from the average of the individual events. In summing the contributions from the different events, the mean of the observed densities at 4, 6 and 8 r.l. has been normalized to unity, so that undue weight is not given to the events of greatest energy. Similar results have been obtained by Grigorov *et al.* (1959), who employed ionization chambers in an assembly mainly composed of iron, exposed at sea-level.

in between about 3 and 20 r.l. (the energy liberated after 20 r.l. will not have passed through enough matter for its cascade to have developed).

The above approximation should be fairly accurate if all secondaries can be assumed to be collinear. Clearly, the effects of divergence will result in some underestimate of the total energy transformed into γ-rays. The integral under curve 1 (fig. 5) is approximately double that under curve 2, so we conclude that the extra energy radiated in these secondary nuclear interactions is, on the average, approximately equal to or greater than that liberated in the primary nuclear interaction. If one takes a value of $\frac{1}{3}$ for the fractional energy transformed into γ-rays in the secondary events (probably correct for pion secondaries, but clearly an over-estimate for nucleon secondaries), the nucleonic cascade will be attenuated exponentially with a characteristic length equal to 3 interaction lengths. Thus, taking $\lambda_{\mathrm{int}}=160\,\mathrm{g/cm^2}$ in the composite medium of the stack, one finds that, in order to liberate an additional energy in the soft component between 3 and 20 r.l., equal to E_γ, the amount liberated in the first interaction, the total energy carried by the secondary particles must be at least $6E_\gamma$. The energy carried by the charged pions would be expected to be on average approximately equal to that in neutral pions from the first interaction (E_γ), and not twice as great, on account of fluctuations, so on its own could not provide the degree of rejuvenation that is observed. This behaviour is consistent with an inelasticity, in the first interaction, $\mathrm{K}_\gamma \sim 20\%$. This value for K_γ is certain to be an overestimate, however, for if the primary interaction by a nucleon is inefficient at producing γ-rays, it would seem very likely that the high energy secondary nucleons or hyperons were also inefficient. In order to get an estimate of this effect a much deeper stack is required. Furthermore, some of the primary interactions will themselves have been produced by pions, and in these no large secondary contributions are to be expected. Thus, the value of K_γ appropriate to *nucleon* primaries is certainly less than 20%.

In the simplified analysis considered so far, no account has been taken of the angle of divergence of the individual particles. This clearly reduces the central density of the cascade—and is most important at large distances. Any formal analysis awaits more detailed knowledge of the transverse momenta possessed by the secondaries carrying the highest energy. Experiments are now being made with a stack exposed more recently, of similar size to the Comet 1 and Comet 2 stack, but of much higher mean density ($12\,\mathrm{g/cm^2}$), and this should provide better conditions for investigating the longitudinal development of nuclear cascades.

§ 5. CONCLUSIONS

It is not possible from the present data to give an unambiguous interpretation of the results relating to the flux and energy spectrum of the cascades. However, it seems that the following main conclusions can be drawn.

(i) The integral pion spectrum at 220 g/cm^2 depth in the atmosphere, between the energy limits 1500–4000 BeV, follows a power law. The index is $-3{\cdot}1 \pm 0{\cdot}3$. The discrepancy between this value and that obtained from the muon measurements $(-2{\cdot}0)$—appropriate however to pions or other particles produced near the top of the atmosphere—remains to be explained.

(ii) The integral energy spectrum of cascades produced by nuclear interactions (mainly in lead) has an index $-1{\cdot}9 \pm 0{\cdot}4$ for cascade energies from 4000–30 000 BeV. The primaries of these events are very probably nucleons. The fractional energy radiated into the soft component in these interactions appears to be $K_\gamma \sim 5\%$. At lower cascade energies (1500–4000 BeV), the spectrum is much steeper, with an index equal to that for the γ-rays. It seems clear that this change in slope cannot be ascribed to pion primaries.

(iii) The observed longitudinal development of nuclear cascades is consistent with the conclusion that in the interactions of nucleons producing cascades of energy ~ 4000 BeV, only a very small fraction of the primary energy is transformed into γ-rays in the first interaction.

Clearly, much more experimental data will be required before a more detailed analysis of such results is possible. In particular, it will be most important to extend the γ-ray spectrum to both lower and higher energies, and to investigate the longitudinal development of nuclear cascades—especially those initiated by nucleons—at greater depths from the origin.

ACKNOWLEDGMENTS

This experiment was made possible only by the very generous facilities offered to us by the British Overseas Airways Corporation, for prolonged exposures at high altitudes in the course of proving flights by their Comet 2E aircraft. We have very great pleasure in thanking Captain T. B. Stoney, D.S.C., Flight Manager Comets; Captain R. E. Millichap, D.F.C., Deputy Flight Manager Comets; Mr. F. E. Hart, Base Engineer; Mr. Thomas Campbell, Base Foreman, and their staffs.

We also wish to acknowledge the assistance of Mrs. Mary Webb, Mrs. Nevette Hillier, and Mrs. Najat Kaddoura in scanning the plates; Mrs. I. Pobjoy for drawing the diagrams; and Mr. W. Harbor for the photographs. We wish to thank Dr. J. Losty for help in the initial stages of the work.

This research was supported in part by a grant from the Department of Scientific and Industrial Research. J. Duthie and C. M. Fisher acknowledge this body also for maintenance grants. A. Kaddoura wishes to thank UNESCO, and W. Wolter the International Atomic Energy Agency, for the award of scholarships.

REFERENCES

ASHTON, F., BROOKE, G., GARDENER, M., HAYMAN, P. J., JONES, D. G., KISDNASAMY, S., LLOYD, J. L., TAYLOR, F. E., WEST, R. H., and WOLFENDALE, A. W., 1960, *Nature, Lond.*, **185,** 364.

BARRETT P. BOLLINGER, L., COCCONI, G., EISENBERG, Y., and GREISEN, K., 1952, *Rev. mod. Phys.*, **24,** 133.

CLARK, G., EARL J. KRAUSHAAR, E., LINSLEY, J., ROSSI, B., and SCHERB, F., 1957, *Nature, Lond.*, **180,** 406.

GRIGOROV, N. L., MURZIN, V. S., and RAPOPORT, I. D., 1959, *J. exp. theor. Phys.*, **36,** 1068.

NISHIMURA, J., 1959, Proc. I.U.P.A.P. Conf. Cosmic Rays, Moscow, July.

PERKINS, D. H., 1960, *Progr. Cosmic Ray Phys.*, Vol. 5 (Amsterdam : North Holland Publishing Co.).

PINE, J., DAVISSON, R. J., and GREISEN, K., 1959, *Nuovo Cim.*, **14,** 1181.

ROSSI, B., 1952, *High Energy Particles* (New York : Prentice Hall).

The Interface between a Metal and an Electrolytic Solution†

By R. J. Watts-Tobin
Cavendish Laboratory, Cambridge

[Received July 22, 1960]

Abstract

Measurements of the capacity of the electrical double layer at the interface between a polarizable mercury electrode and an aqueous solution of a strong electrolyte are interpreted theoretically. Attention is concentrated on the layer of charges at the actual phase boundary, whose behaviour has not been satisfactorily explained before.

It is suggested that for anodic polarization an increasing number of mercury atoms is situated at adsorbed sites on an otherwise flat surface. These carry a charge, and lead to a rise in the measured capacity as the polarization becomes anodic. It is thus shown why the capacity as a function of polarization has a form for fluoride electrolytes, where there is no specific adsorption of the anion, so similar to that for other electrolytes, where there is.

The behaviour of the water molecules in contact with the mercury is considered in some detail, and compared with the behaviour of bulk water and of a monolayer of water adsorbed to a mercury surface. It is shown that the hump, which appears in most capacity curves slightly to the anodic side of the electrocapillary maximum, may be due to the high polarizability of the water layer between the metal and the outer Helmholtz plane, when the field there is small. It is not necessary to assume as Grahame does that there is any appreciable chemical or image force polarizing the surface molecules, or that the water takes up a rigid ice-like structure for low fields.

The suggestion that the rise in the capacity for cathodic polarization is due to compression of the double layer by electrostatic forces is also considered, with the implication of this idea on the mechanism of overvoltage in the discharge of cations onto mercury.

§ 1. Introduction

Measurements of the capacity of the interface between mercury and aqueous solutions of strong electrolytes, using a dropping mercury electrode, have recently been made with considerable precision: those of the late Professor D. C. Grahame are of special importance. They have demonstrated that the electrical double layer at the interface falls into two parts: a diffuse layer of ions analogous to the long-range screening charge of an ion in the solution, and an inner layer, between the metal surface and the plane of closest approach of hydrated ions to it, called the outer Helmholtz plane (Grahame 1947). This is sketched in fig. 1. The capacity of the inner layer is roughly in series with that of the diffuse layer, and it is much smaller except in very dilute solutions so that it dominates the measured capacity.

The forms of experimental capacity curves for strong electrolytes, for example due to Grahame (1947, 1951, 1954, 1957 a), are rather similar and after the capacity of the diffuse layer has been removed by the method used by Grahame (1947), they have the form shown in fig. 2. Here σ is the surface charge on the mercury and C is the differential capacity $\partial\sigma/\partial\phi$, where ϕ is the potential of the mercury relative to a standard electrode in the solution.

---

† Communicated by the Author.

Fig. 1

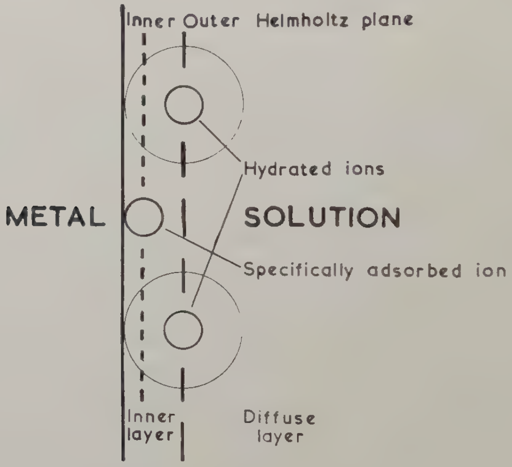

Fig. 2

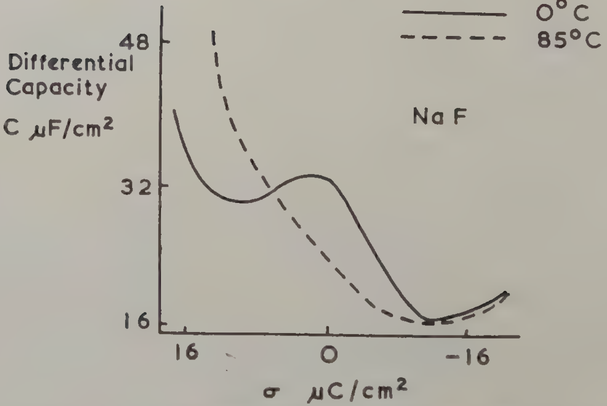

Calculated values of C^{i0}, the differential capacity of the inner part of the electrical double layer, between mercury and aqueous solutions of sodium fluoride at several temperatures. Calculations made from data obtained with 0·8 N solutions.

Most anions can be 'specifically' adsorbed to the mercury and are then partially dehydrated. They have their centres on the inner Helmholtz plane in fig. 1. Their concentration in the plane is proportional to their concentration in the solution, and since they are charged, σ and C depend on the concentration. However, C is found to be practically independent of concentration if the anion is fluoride (Grahame 1954), so fluoride ions cannot be specifically adsorbed. Sodium fluoride is therefore a simple electrolyte to study.

§ 2. THE ELECTRIC FIELD IN THE METAL

The electric field at the interface penetrates into the metal. Rice (1928) applied the Thomas–Fermi approximation to this problem, and showed that for mercury, with two free electrons per atom moving in a medium of mercuric ions, the depth of penetration is about $\frac{1}{2}$ Å. This medium has a low dielectric constant (Pauling 1927) as is pointed out by Rice, so that the layer in the metal would be expected to have a capacity of at most $16\,\mu\text{F}/\text{cm}^2$, even if the solution behaved like a perfect conductor. However, the measured capacity in moderately concentrated aqueous solutions of strong electrolytes is never less than this, and it depends strongly on the temperature. Temperature-dependence cannot be due to the electrons, so the layer contributing to the capacity must extend into the solution. It is shown in the appendix that if the positions of all the charges in the layer are known, the potential drop across it is the same as if they were smeared out in planes parallel to the layer, which can therefore be regarded as a number of condensers connected in series. However the field on an individual charge is by no means the same as if the other charges were smeared out, so the equilibrium distribution of charges depends on the potential across the whole layer, not just the drop in the metal. It is for this reason that the penetration of the field into the metal does not imply that the capacity of the whole layer is always less than $16\,\mu\text{F}/\text{cm}^2$. This is considered further by Mott and Watts-Tobin (1961).

§ 3. ADSORPTION OF IONS

The capacity rises sharply when the polarization is anodic and it depends strongly on temperature there. Measurements with 0·916 molar sodium fluoride (Grahame 1954) show that the sharp rise occurs as the potential approaches the exchange potential for a normal calomel electrode. This suggests that it is associated with the electrochemical reaction which would occur on the mercury at even more anodic potentials. The capacity curves for sodium fluoride are remarkably similar to those for electrolytes whose anions are specifically adsorbed, for example that for sodium nitrate (Grahame 1957 a). The adsorption to the interface of positively charged ions from the mercury, or of negatively charged ones from the solution, would explain this, and we shall consider these possibilities.

Gerischer (1958) has observed the current during sudden changes of polarization in electrode reactions. It provides evidence that on otherwise flat surfaces of solid metals in contact with electrolytic solutions containing their own ions, some of the metal atoms are adsorbed as 'ad-atoms' in a partially charged state. We therefore suggest that mercury atoms are pulled out of its surface by the electric field to form ad-atoms. Gerischer and Krause (1958) have shown that the exchange current of the charge transfer between a mercury electrode and a solution containing mercurous ions is almost unaffected by freezing the mercury. From the fact that this current is almost as great on solid mercury as on liquid mercury they deduce the existence of ad-atoms on the solid, for if they did not exist charge transfer could presumably occur only at kink-sites and the rate would be much less. But the fact that the currents are almost the same suggests that ad-atoms may be present on the liquid as well. Otherwise there would be a considerable change in the number of atoms which can participate in the charge transfer when the surface is melted, unless the solid mercury surface is practically covered with ad-atoms at the melting point. This is unlikely, because the exchange current on mercury (Gerischer and Krause 1958) is less than that on silver (Gerischer and Tischer 1957), and there is only about one ad-atom per hundred atomic sites on silver.

The idea of a liquid metal surface with ad-atoms of the same metal on it seems to be new, but it is possible thermodynamically: if there are few ad-atoms their entropy will be that of a two-dimensional gas, and it follows from the Sackur–Tetrode formula that the entropy per ad-atom increases indefinitely as the degree of coverage tends to zero. This is also true if the ad-atoms are immobile on the surface. If this entropy is S, and that per atom in the liquid is S_0 which is a constant, then at constant temperature T and pressure we may expect ad-atoms to be adsorbed until $T(S-S_0)$ is reduced to the value of the heat of adsorption from the liquid. If there is no actual energy barrier to cross in pulling an ad-atom out of a liquid surface, there will be a rapid fluctuation of atoms in the surface in various stages of this process. However, their average contribution to the potential can be described by means of definite ad-atoms.

The distance from the metal of the inner Helmholtz plane in which the ad-atoms is not known, nor is their charge. Only the product of these, the dipole moment of the ad-atom and the charge induced on the metal by it, affects the potential drop from the metal to the solution. This is also true for anions adsorbed from the solution, although it is more convenient to consider the dipole moment of the ions and the charge induced by it on the outer Helmholtz plane. There is no reason why the distance of such ions from the metal should be the same as the distance of ad-atoms from the metal. If both ad-atoms and adsorbed anions are formed, they will cluster round each other to form complexes[†].

Suppose the dipole moment of a complex is μ_1, positive in the direction from the metal to the solution, the potential drop from the metal to the solution is ϕ, and the thickness of the double layer, namely the distance from the conducting surface of the metal to the outer Helmholtz plane, is d. Then if the distance between the complexes is large compared with d, the electric field in the neighbourhood of one of them, excluding its own field, will be approximately constant across the layer, so it will be ϕ/d. This was first pointed out by Ershler (1946). The number of complexes per unit area of the surface will therefore be

---

[†] This was pointed out to me by Dr. Gerischer.

$$n_1 = N\left(\frac{c_1}{c_0}\right)^m \exp\frac{\mu_1\phi/d - W_0}{kT}.$$

In this equation N is the number of adsorption sites per unit area of the metal surface, and W_0 the heat of adsorption of a complex in the absence of an electric field, but including the image-force attraction. W_0 is supposed to be measured when the concentration of anions in the solution is c_0, their concentration in this experiment being c_1, and m is the number of anions in a complex. The complexes give a contribution to ϕ of magnitude

$$-4\pi n_1\mu_1/K_0 \qquad \text{. . . . . (1)}$$

where K_0 is the dielectric constant of the layer.

§ 4. THE WATER IN THE INTERFACE

4.1. *Dielectric Theory*

Slightly to the anodic side of the electrocapillary maximum, where the mercury is uncharged, there is a hump in most graphs of C against potential or charge. We propose to show that this may be due to an increase in the effective dielectric constant of the layer, marking the point where the average dipole moment of the water in the layer changes sign. Of course, for this to be noticeable as a hump it must be possible to polarize the layer so strongly that an appreciable proportion of the water dipoles is orientated by the field. The average field E necessary to orientate a water molecule with dipole moment μ is $E \sim kT/\mu$. At 300°K, E is $6{\cdot}6 \times 10^6$ volts/cm. In capacity measurements the potential can be changed by more than a volt and it acts over a distance of only a few angstroms, so this field is reached.

Such fields are much stronger than any which can be applied to bulk specimens of water. The water molecules in the interface will also behave differently from those in bulk owing to their proximity to the mercury, and to the fact that the electric field is applied not through the whole solution but by the double layer of ions near the mercury and the balancing charge on it. All the same, it is worth considering the theory of the dielectric constant of water in bulk to see how it must be modified in the interface.

This theory was given by Kirkwood (1939) and applies generally to associated polar liquids. For a substance whose dielectric constant K is as high as that of water his formula takes the form

$$K = K_0 + 4\pi\frac{N}{V}\frac{3}{2}\frac{\boldsymbol{\mu}\cdot\boldsymbol{\mu}^*}{3kT}. \qquad \text{. . . . . . . (2)}$$

In this formula, there are N molecules in a volume V, each having a dipole moment $\boldsymbol{\mu}$ in the absence of an applied field. $\boldsymbol{\mu}$ is not quite the same as the moment of a molecule *in vacuo*, owing to its polarization by the 'reaction field' when it is in the liquid; however, the difference is small. $\boldsymbol{\mu}^*$ is the dipole moment of a large sphere of the liquid surrounded by the same liquid, when one of its molecules is fixed with a dipole moment $\boldsymbol{\mu}$. The interaction energy of the liquid in the sphere with the field $\mathbf{C}$ in the cavity is $-\boldsymbol{\mu}^* \cdot \mathbf{C}$. If the sphere is large enough to treat its surroundings as a continuum of dielectric constant K, and the cavity is filled with a continuum of dielectric constant K_0 (representing the polarizability of the liquid when the dipoles in it are fixed in definite directions), then

$$\mathbf{C} = 3K\mathbf{E}/(2K + K_0) \simeq 3\mathbf{E}/2,$$

where $\mathbf{E}$ is the field in the surrounding liquid. The factor 3 in the denominator of (2) arises from averaging the directions of $\boldsymbol{\mu}$.

The high dielectric constant of water is due to the fact that $|\boldsymbol{\mu}^*|$ is considerably larger than $|\boldsymbol{\mu}|$. The dipole moments of neighbouring water molecules are correlated by their hydrogen bonds, and if this correlation extends only to nearest neighbours, $\boldsymbol{\mu}^* = 7\boldsymbol{\mu}/3$. The theory only applies when the electric field is too weak to produce dielectric saturation. To calculate the saturation of the polarization in stronger fields is much harder, as the field in the cavity is no longer $3K\mathbf{E}/(2K + K_0)$, and the averaging of the magnitude and direction of $\boldsymbol{\mu}^*$ are no longer independent. Only the first term or so in an expansion of the dielectric constant in even powers of $\mathbf{E}$ can reasonably be calculated (Buckingham 1956), but they contain all the information which can be measured with fields that can in practice be applied to bulk specimens of liquid.

4.2. *Structure*

Pauling (1939) gives the energy of the hydrogen bond in water as 4·5 kcal/mole. It is pointed out by Lennard-Jones and Pople (1951) that this is so much greater than RT, that at any instant of time the hydrogen-bonding in it is practically complete. The strength of the electrostatic field E necessary to break an appreciable number of hydrogen bonds is given by $NE\mu \sim 4{\cdot}5$ kcal where N is Avogadro's number, so $E \sim 5 \times 10^7$ volts/cm. The maximum fields applied across a mercury-solution interface are almost certainly less than this, though perhaps not much. It is therefore a reasonable first approximation to suppose that the hydrogen bonds between water molecules there are all intact, except for the water molecules actually in contact with the mercury, and those in the primary hydration shells of ions. Since the dipole moment of the water molecule can be resolved into components along the hydrogen bonds, it follows that the only water molecules whose moments contribute to the capacity lies between the outer Helmholtz plane and the mercury surface. This is shown in fig. 3, in which the arrows represent dipole moments.

Quite apart from the structure of the water, if the water molecules on the solution side of the outer Helmholtz plane have any average dipole moment, the ions, which are free to move there, will arrange themselves so as to screen out the field, in a reasonably concentrated solution, and the dipole moment in this region will not be observed. However, the fact that the structure of the water is maintained may help to explain why the capacity of the diffuse layer outside the outer Helmholtz plane can be calculated accurately with the assumption that the water has its normal dielectric constant (Grahame 1954).

Fig. 3

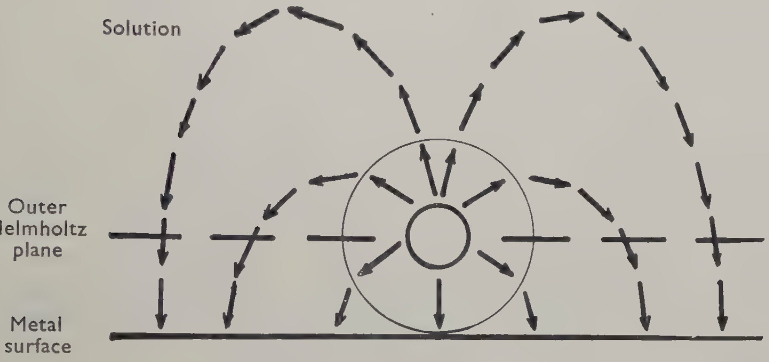

The rate at which the water molecules turn over is of the order of magnitude of the reciprocal of the dielectric relaxation time. This is much faster than the rate at which the ions diffuse, so that in calculating the equilibrium configuration of the water we shall assume the ions to be frozen into fixed positions.

The water molecules whose dipole moments contribute to the capacity, between the outer Helmholtz plane and the metal, are probably in contact with the metal. For the barrier to movement of an ion towards the metal is presumably the high energy needed to remove its primary hydration shells, so the distance between the outer Helmholtz plane and the metal is probably only the diameter of a water molecule plus half that of an ion, and the distance of penetration of the field into the metal. Indeed the outer Helmholtz plane may even pass through the first layer of water molecules, and if this happens, their contribution to the capacity will be reduced.

Kemball (1947) has shown that the heat of adsorption of water molecules from the vapour on to a mercury surface is 17·6 kcal/mole. This is so much higher then the energy of a hydrogen bond between two water molecules, that it seems likely that the water molecules in contact with the mercury in an inter-face are in much the same state as if they were adsorbed in a close-packed mono-layer on mercury, and are only slightly affected by the presence of the rest of the water. This is supported by the fact that the interfacial tension of a mercury-water interface (427 dynes/cm) is almost the same as the surface tension of mercury with a monolayer of water on it (438 dynes/cm).

4.3. *Electrostatics*

To calculate the contribution of these water molecules to the capacity we need to know at what angle their dipole moments are held by the mercury, whether they have a preferential orientation corresponding to the 'natural field' on the metal surface discussed by Grahame (1957 a), and to what extent their orientations are correlated with those of other water molecules (giving a value of μ^* for them)†. None of these questions can be answered with any certainty, but we can attempt to answer them on the following lines.

If the surface of the mercury were an ideal electrical conductor a water molecule would be attracted by its electrical image in it, and would therefore form a bond with the mercury very similar to that with another water molecule. The surface is not an ideal conductor, but a measure of its deviation from one is given by the ratio of the screening distance of an electric field in the metal to the distance of the charges we are interested in from it. In the case of a water molecule this ratio is less than one for most of the charge, so that to treat the mercury as a conductor is reasonable.

The non-zero screening distance of the field in the metal means that image charges are further away than they should be, and image forces correspondingly weaker. Therefore if the interaction of a water molecule with the mercury is akin to hydrogen-bond formation, we expect that three of its bond-forming directions are attached to it, to account for the heat of adsorption. This would leave one bonding direction free to link with another water molecule. In the case of water adsorbed on mercury, Kemball shows that the entropy of adsorption suggests the assumption that the water molecules are associated in pairs. Our picture accounts for this in terms of bonds, though it is difficult to vizualize geometrically.

The attachment of three bond-forming directions to the mercury may be aided by the atomic structure of the mercury surface, assumed close-packed. In such a configuration the dipole moment of the molecule makes an angle $\cos^{-1}(1/\sqrt{3})$ with the normal to the surface, since the bond-forming directions of the molecule are directed to the vertices of an approximately regular tetrahedron. Just two configurations of the water molecule can be realised in this way. The components of its dipole moment along the normal to the interface are equal and opposite in them, and they are drawn in fig. 4.

The water molecules will have a preferred sense of orientation on the mercury surface, if they bond to a mercury atom with a lower energy through a proton (+) bond than through a lone-pair (−) bond, or vice versa. If we regard the metal as a conductor, and the bond as due to electrostatic forces between rigid charged structures, we can determine this electrostatically, in a very similar manner to that used by Buckingham (1957) to explain the difference in hydration energies of positive and negative ions of similar sizes.

---

† I am grateful to Dr. A. D. Buckingham for discussion of these questions.

Fig. 4

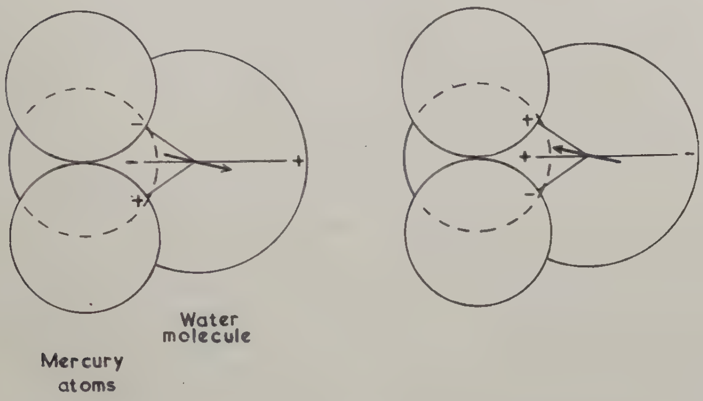

We define the dipole and quadrupole moments of a system containing charges e (not necessarily all equal) at positions $\mathbf{r}=(x_1, x_2, x_3)$ to be

$$\boldsymbol{\mu}=\sum e\mathbf{r}$$

and

$$\theta_{\alpha\beta}=\sum e x_\alpha x_\beta$$

respectively, where the summation is over the charges. We consider two systems of charges, each electrically neutral as a whole, having dipole and quadrupole moments $\boldsymbol{\mu}$, $\boldsymbol{\mu}'$ and $\theta_{\alpha\beta}$, $\theta_{\alpha\beta}'$. The unit vector from the origin of the undashed system to the origin of the dashed system is $\boldsymbol{\lambda}=(\lambda_1, \lambda_2, \lambda_3)$, and the distance between them is R. This is supposed to be large compared with the spread of either system about its origin. The interaction energy between the two systems is

$$\begin{aligned} W= & -\mu_\alpha \mu_\beta'(3\lambda_\alpha \lambda_\beta-\delta_{\alpha\beta})/KR^3 \\ & -(\mu_\alpha \theta_{\beta\gamma}'-\mu_\alpha' \theta_{\beta\gamma})(3\lambda_\alpha \delta_{\beta\gamma}+3\lambda_\beta \delta_{\gamma\alpha}+3\lambda_\gamma \delta_{\alpha\beta}-15\lambda_\alpha \lambda_\beta \lambda_\gamma)/2KR^4 \\ & +0(1/R^5), \qquad \ldots \ldots \ldots \ldots \quad (3) \end{aligned}$$

if the charges are in a medium whose dielectric constant is K. If the dashed system is the electrical image of the undashed one in a plane conductor, the energy of the image-force is *half* W: this can be seen either by considering moving the system into position from an infinite distance from the conductor, or from the fact that W is the part of the field energy due to interaction between every pair of charges, one in each system. If the conductor is replaced by the image charges, the contributions to the field energy are clearly symmetrical about the plane of the conductor, but the field only really exists on one side of it.

$\boldsymbol{\lambda}$ is now the unit normal to the plane of the conductor, and for every charge e at $\mathbf{r}$ in the undashed system, there is a charge $-e$ at $\mathbf{r}-2(\boldsymbol{\lambda}\,.\,\mathbf{r})\boldsymbol{\lambda}$ in the dashed system, relative to the image of the origin of the undashed system. Therefore

$$\boldsymbol{\mu}' = -\boldsymbol{\mu} + 2(\boldsymbol{\lambda}\,.\,\boldsymbol{\mu})\boldsymbol{\lambda}$$

and

$$\theta_{\alpha\beta}' = -\theta_{\alpha\beta} + 2\theta_{\gamma\beta}\lambda_\gamma\lambda_\alpha + 2\theta_{\alpha\gamma}\lambda_\gamma\lambda_\beta - 4\theta_{\gamma\delta}\lambda_\gamma\lambda_\delta\lambda_\alpha\lambda_\beta.$$

Substituting these expressions in (3) we obtain

$$\begin{aligned}\tfrac{1}{2}W = &-[\boldsymbol{\mu}^2 + (\boldsymbol{\lambda}\,.\,\boldsymbol{\mu})^2]/2KR^3\\ &-3[\boldsymbol{\lambda}\,.\,\boldsymbol{\mu}(\theta_{\alpha\beta}\lambda_\alpha\lambda_\beta - \theta_{\alpha\alpha}) + 2\theta_{\alpha\beta}\lambda_\alpha\mu_\beta]/2KR^4\\ &+0(1/R^5).\end{aligned}$$

If the system of charges is a water molecule, its dipole moment is along one principal axis of its quadrupole tensor. We take this as the x_3-axis, and the x_1- and x_2-axes along the other two principal directions of the quadrupole tensor, with the x_1-axis parallel to the line joining the protons. Writing

$$\boldsymbol{\mu} = (0,\ 0,\ \mu),$$

$$[\theta_{\alpha\beta}] = \mathrm{diag}\,(\theta_1,\ \theta_2,\ \theta_3),$$

and

$$\lambda_3 = \cos\theta,$$

we obtain

$$\begin{aligned}\tfrac{1}{2}W = &-\mu^2(1+\cos^2\theta)/2KR^3\\ &-3\mu\cos\theta[(\theta_3-\theta_1)(1-\lambda_1{}^2) + (\theta_3-\theta_2)(1-\lambda_2{}^2)]/2KR^4\\ &+0(1/R^5). \qquad (4)\end{aligned}$$

An accurate theory would also take into account the polarization of the molecule by its image.

Given accurate values of the components of the quadrupole tensor, we could use (4) to calculate the equilibrium orientation of the molecule. However here we shall assume it has one of the orientations shown in fig. 4, with three bonds in the direction of the metal (or more exactly, one away from it), and use (4) to calculate the relative energies and hence in thermal equilibrium the probabilities of the two orientations. In the discussion of both these points it should be borne in mind that the series for the interaction energy does not converge rapidly when the charges are as near the conductor as those we are considering, compared with their average spread. However, the next term in the energy comprising the dipole–octupole and quadrupole–quadrupole interaction, is complicated, and it is of the same order as the van der Waals forces, so to get a better approximation they would have to be brought in as well.

With the axes used in (4), the components of $\boldsymbol{\lambda}$ are $(\pm\sqrt{\frac{2}{3}}, 0, -\sqrt{\frac{1}{3}})$ when a proton (+) in the water molecule points away from the metal, and $(0, \pm\sqrt{\frac{2}{3}}, \sqrt{\frac{1}{3}}$ when a lone-pair orbital (−) does. The components of the dipole moment along the outward normal to the metal are $+\mu/\sqrt{3}$ and $-\mu/\sqrt{3}$ respectively. It follows from (4) that the difference between the interaction energies in the two positions is $G = 2\mu[2\theta_3 - \theta_1 - \theta_2]/\sqrt{3}KR^4$, the position with the dipole pointing towards the metal having the lower energy if the quantity in square brackets is positive. The first term in (4), the dipole–dipole energy, is $-2\mu^2/3KR^3$ in both positions.

The value of R is uncertain, but it can hardly be less than 3 Å. The dipole–dipole energy multiplied by K is then at most 1·2 kcal/mole. Buckingham derives an empirical value of $2\theta_3 - \theta_1 - \theta_2$ for water, namely $3{\cdot}9 \times 10^{-26}$ e.s.u. Theoretical estimates (Duncan and Pople 1953) are an order of magnitude smaller. Buckingham's value gives KG as at most 1·5 kcal/mole. These values are so small compared with the energy of a hydrogen bond, let alone the heat of adsorption of water on to mercury, that we are almost compelled to suppose that $K = 1$ in this interaction, and we shall do so. The smallness of the dipole–dipole interaction shows that our assumption, that in equilibrium the water dipole is not along the normal to the metal surface, is not an absurd one.

The dielectric constant of normal water is so high, that in calculating the equilibrium configuration of the water molecules in the double layer, we can consider the potential difference across it to be applied between two planes, in the metal and in the water. Outside them the material can be treated as a conductor to a high degree of approximation. Kirkwood (1939) makes a similar approximation in supposing that the field in his spherical cavity is $3\mathbf{E}/2$ instead of $3K\mathbf{E}/(2K + K_0)$.

We must now refer to fig. 3 again. If each of the water molecules in contact with the mercury has three bonding directions occupied, the remaining one is bonded to another water molecule. The component of its dipole moment in this direction is repeated along a bonding direction in the next molecule, and so on until the chain of dipoles ends on an ion, or on the surface of the metal again. For the purpose of calculating its interaction with the field, however, this chain can be considered to run from the plane of the conducting surface of the metal to the plane beyond which the water is normal, provided the ions are not too close together. If a typical normal to these planes cuts n water molecules between them, the dipole moment of this chain will have a component $\mu^* = \pm n\mu/\sqrt{3}$ along the normal to these planes. The potential drop between them is ϕ, the potential drop from the metal to the solution, since the material outside them is supposed to be conducting. The distance between them is approximately equal to nd, so the electric field E is ϕ/nd, and the interaction energy of the chain of dipole with the field is $-E\mu^* = \mp \mu\phi/\sqrt{3}d$. It is useful that this is independent of n, since it would be very difficult to estimate the minimum distance between the planes. However, the independence is not really surprising: since the criterion of a suitable plane on the solution side is that the water should be normal beyond it, any plane further into the solution should do equally well, as long as the distance between the planes remains small compared with the distance between the ions in the outer Helmholtz plane.

§ 5. A CALCULATION OF THE CAPACITY

We can now make a theoretical estimate of the capacity, taking into account the water dipoles and the adsorption of ions. We shall find that with a reasonable choice of some parameters, they explain the hump in the middle of capacity curves, and the rise on the anodic side, respectively, and we shall try to interpret the necessary values of the parameters.

If there are N free water molecules per unit area of the interface, of which L have a component of their dipole moment from the metal to the solution, and M the other way, then the energies of the chains of dipoles associated with these molecules are

$$A = C' - \mu\phi/\sqrt{3}d$$

and

$$B = D' + \mu\phi/\sqrt{3}d$$

respectively: C' and D' are the adsorption energies of the water molecule in contact with the metal and are equal to half the relevant values of W. Provided the layer across which the chains of dipoles run is not thick, the chains will be approximately independent of one another, so that $L/M = \exp\{-(A-B)/kT\}$. Therefore the contribution of the water molecules to ϕ is

$$\begin{aligned} -4\pi(L-M)\mu/\sqrt{3}K_0 &= (4\pi N\mu/\sqrt{3}K_0)\tanh\{(A-B)/2kT\} \\ &= -(4\pi N\mu/\sqrt{3}K_0)\tanh\{\mu(\phi-V)/\sqrt{3}dkT\} \end{aligned}$$

where

$$V = \sqrt{3}d(C'-D')/2\mu = \sqrt{3}dG/2\mu. \qquad (5)$$

If there is a surface charge σ on the mercury balancing a charge $-\sigma$ on the outer Helmholtz plane, it contributes $4\pi\sigma d/K_0$ to ϕ. Adding the contributions (1) from the adsorbed complexes, and the contribution from the water dipoles, we obtain

$$\begin{aligned} \phi = {} & 4\pi\sigma d/K_0 \\ & -(4\pi N\mu_1 c^m/K_0 c_0{}^m)\exp\{\mu_1(\phi-V_0)/dkT\} \\ & -(4\pi N\mu/\sqrt{3}K_0)\tanh\{\mu(\phi-V)/\sqrt{3}dkT\}. \end{aligned} \qquad (6)$$

In this equation we have put

$$W_0 d/\mu_1 = V_0, \qquad (7)$$

and we have assumed that the number of adsorption sites per unit area for the complexes is the same as N, the number of water molecules. It follows that

$$\begin{aligned} \sigma = {} & K_0\phi/4\pi d \\ & +(N\mu_1 c_1{}^m/c_0{}^m d)\exp\{\mu_1(\phi-V_0)/dkT\} \\ & +(N\mu/\sqrt{3}d)\tanh\{\mu(\phi-V)/\sqrt{3}dkT\}. \end{aligned} \qquad (8)$$

The differential capacity C of the layer is $\partial\sigma/\partial\phi$, namely

$$\begin{aligned} C = {} & K_0/4\pi d \\ & + (N\mu_1^2 c_1^m/c_0^m d^2 kT)\exp\{\mu_1(\phi - V_0)/dkT\} \\ & + (N\mu^2/3d^2kT)\,\mathrm{sech}^2\{\mu(\phi - V)/\sqrt{3}dkT\}. \qquad (9) \end{aligned}$$

In this expression, the first term is the ordinary capacity per unit area of a parallel-plate condenser, the next is due to the adsorption of complexes, and the last is due to the water. The exponential in the term due to adsorption rises extremely rapidly when ϕ is greater than V_0. We shall calculate a capacity curve for mercury in sodium fluoride in water from (9). The values of the unknown parameters in (9) will be adjusted to fit the experimental curve given in fig. 2.

The following values have been taken in the calculation, and the resulting capacity curves at 0°c and at 85°c are shown in fig. 5.

$N = 10^{15}$ molecules/cm^1, $\mu = 1{\cdot}84 \times 10^{-18}$ e.s.u.; $V = 0$;
$V_0 = 0{\cdot}7$ volt; $\mu_1 = 3{\cdot}31 \times 10^{-18}$ e.s.u.; $d = 3{\cdot}45$ Å; $K_0 = 2$.

The first two values are standard. Auty and Cole (1952) have found that the dielectric constant of ice tends to the value 3·1 as the frequency of an incident alternating field is increased above 50 kc/sec. This seems to be the value corresponding to libration and distortion of the water molecules fixed in definite orientations (Onsager and Dupuis 1960) and is appropriate here. However, part of the thickness of the condenser in the interface is the depth of penetration of the field into the metal, where the dielectric constant is probably lower, so we have taken $K_0 = 2$. It follows from the calculation in the Appendix that to take an average value of K_0 for the whole layer is not strictly correct. d is adjusted to fit fig. 2: its value is reasonable.

V can be calculated from (5), if we know the quadrupole moment of water. The value of 1·5 kcal/mole for G gives V as 0·51 volt. If this were correct, the hump due to water molecules would be about half a volt to the anodic side of the electrocapillary maximum, in the absence of specific adsorption of ions. However, Buckingham's value of the quadrupole moment is doubtful, and is probably too high (Everett 1957). It is noticeable that the hump on most experimental capacity curves is about 0·1 volt to the anodic side of the electrocapillary maximum. If our interpretation of the hump is correct, this could be used to find an empirical value of the quadrupole moment of water, which would be of the same order of magnitude as Duncan and Pople's. Their value would give V as 0·06 volt. In the calculation V has been taken as zero for simplicity.

If we assume that mercury ad-atoms are formed, and that the exponential term in (9) is due to them, μ_1/d could be measured by a technique due to Gerischer (1958). This consists in estimating the variation in the number of ad-atoms in equilibrium on the surface, when the concentration of metal ions in the solution is changed. Applied to silver, this method yields a value of 0·19 of a proton charge e for μ_1/d, which we may call γe

to conform with Gerischer. It would be interesting to apply this technique to mercury: presumably the formation of an ad-atom is a step in detaching a mercurous ion from its surface, but since these ions are associated in pairs in solution they are not really comparable with silver ions. For the calculation, we have taken $\gamma=0{\cdot}2$, giving the value of μ_1, and adjusted V_0 to fit fig. 2. This fitting can be performed with quite a range of values of γ, so we should not attach much significance to the value of V_0, especially as Gerischer's method of estimating γ is very rough.

Fig. 5

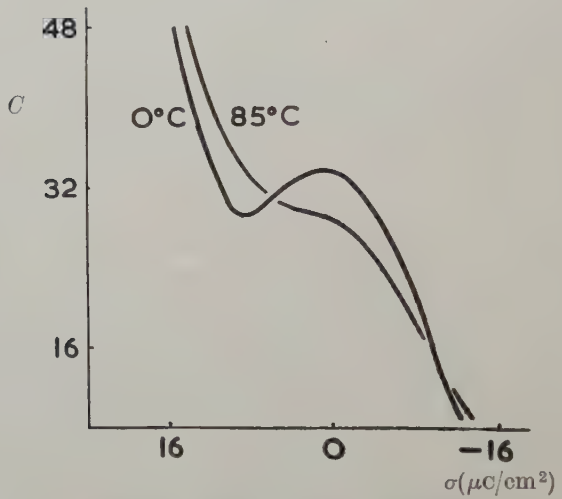

W_0, the heat of formation of an ad-atom, can also be measured, as it is the difference between the heat of dissolution of the metal and the heat of dissolution of an ad-atom. The latter can be found from the dependence of the number of ad-atoms on temperature (Gerischer 1958). However, its connection with V_0 depends on γ (eqn. (7)). Very roughly we should expect the heat of formation of an ad-atom on a mercury surface in contact with its vapour to be half the latent heat of vapourization of mercury. The heat of formation of an ad-atom at a mercury-solution interface should be lower, owing to the interaction of its dipole moment with the charges in the solution. Our value of V_0 gives $W_0=0{\cdot}14$ ev, and this may be compared with the latent heat of evaporation of mercury, which is about 0·6 ev. It is therefore quite reasonable to suppose that the exponential term in the capacity is due to ad-atoms.

An alternative possibility, in a fluoride solution, is that it is due to the adsorption of hydroxyl ions†. The test of this is to measure capacities in solutions of different pH. The contribution of hydroxyl ions to C may be written from (9),

$$(N\mu_1^2/d^2kT)\exp\{\mu_1(\phi-V_1)/dkT\}$$

---

† This suggestion is due to Dr. J. Wanklyn.

where

$$V_1 = V_0 + (mdkT/\mu_1)\ln(\mu_2, c_2).$$

We must remember that μ_1 is the dipole moment of an adsorbed hydroxyl ion and its induced charge on the outer Helmholtz plane. If we assume that in forming a hydroxyl ion from a water molecule in contact with the metal, a proton moves through about half the double layer, then $\mu_1/d = \frac{1}{2}e$ (or less if the charge on the hydroxyl ion is partly neutralised by its bond with the metal). kT is about 1/40 ev, so that an increase of one unit in pH should shift the part of the capacity curve due to hydroxyl ions by at least 0·12 volt to the cathodic side, even if $m = 1$. Grahame (1947) has measured capacities in normal solutions of sodium hydroxide and perchloric acid. His values of C are plotted against potential measured relative to the electrocapillary maximum, whose potential on our scale varies with pH if the hydroxyl ion is adsorbed. However, the hump on the curves gives a fixed reference point if it is due to the water. A comparison of these curves with that for sodium fluoride shows that the rise on the anodic branch of Grahame's curves does shift to the cathodic side with increasing pH, but only about a third as much as if it were simply due to the adsorption of hydroxyl ions. The very considerable shift in the curve for sodium hydroxide suggests that there the rise is due to adsorption of hydroxyl ions. The rise in the other cases is more likely to be due to the formation of ad-atoms of mercury, or to the formation of complexes on the surface between mercury atoms and hydroxyl ions. A careful series of capacity measurements in fluoride solutions having different values of pH would be very valuable. Acid solutions would have to be contained in material unattacked by hydrofluoric acid.

§ 6. DISCUSSION

The calculated values of C shown in fig. 5 are in fair agreement with the experimental ones for sodium fluoride (Grahame 1957 a) shown in fig. 2, except on the far cathodic side. The calculated temperature-dependence is not large enough on the anodic side, and the fact that the hump on the experimental curves is always at a small positive value of the surface charge, suggests that water molecules tend to have their dipole moments pointing towards rather than away from the mercury.

Adsorbed anions give a very similar contribution to C to that of ad-atoms, so we may also compare fig. 5 with many other capacity curves for electrolytes whose anions are specifically adsorbed, for example sodium nitrate (Grahame 1957 a). The similarity between the curves is remarkable, and is very strong evidence that an adsorption process also occurs in sodium fluoride solutions. We suggest that capacity measurements with mercury amalgams or other liquid metals should be made to alter the adsorption energy of ad-atoms, in order to check the hypothesis that they contribute to the capacity. If anions are very easily adsorbed the capacity due to their adsorption may rise rapidly when the polarization is only slightly anodic and this may mask the capacity due to the water molecules turning over. This may be the reason for the absence of humps in curves for sodium hydroxide, carbonate and iodide (Grahame 1947).

When humps appear in experimental capacity curves for aqueous solutions they generally have much the same height. This supports the hypothesis that it is the water which causes them. An important test of it is to measure capacity curves in other solvents, or in fused salts. Grahame (1955) and Minc and Jastrzebska (1960) measured capacity curves for sodium and potassium fluorides dissolved in methyl and ethyl alcohol, and these do not show humps. This may be because the alcohol molecules have a strong preferential orientation on mercury, so that they do not turn over in the usable range of polarization, or because the freezing points of the alcohols are lower and the measurements in them should be compared with those at higher temperatures in water†. Measurements of the capacity in methyl and ethyl alcohols over a range of temperatures should decide between these explanations.

An interesting feature of some capacity curves in water is that specifically adsorbed anions sometimes seem to intensify the hump rather than masking it: for example the curve for potassium nitrate may be compared with those for sodium fluoride (Grahame 1957 a). A possible explanation of this is that the outer Helmholtz plane is further from the metal in a nitrate solution and therefore the layer of water contributing to the capacity is thicker‡. The nitrate ion is so strongly adsorbed when the polarization is anodic that on the average there are many more cations than anions in the outer Helmholtz plane, or rather in the diffuse layer (Grahame and Soderberg 1954). However, the cations will be clustered round the specifically adsorbed anions: this is shown in fig. 6. The ions facing the rest of the metal surface will mainly be anions. If they are nitrate ions they will be further from the metal than fluoride ions, owing to their larger size and to the greater number of water molecules in their primary hydration shells. The water molecules contributing to the capacity will be in the thicker part of the layer, away from the adsorbed ions.

6.1. *Compression of the Double Layer*

So far we have not considered the fact that all experimental capacity curves rise on the cathodic side. It has been suggested by Macdonald (1954) that this is due to a compression of the layer in the strong electric field. This is supported by the fact that Grahame's curves for methyl alcohol solutions rise roughly symmetrically on both sides, and more sharply than those for water solutions on the cathodic side. The layer is presumably more compressible in methyl alcohol solutions than in water, as Macdonald points out.

---

† This suggestion is due to Dr. J. N. Agar.

‡ Our assumption that just one layer contributes is approximate, and the contribution is really proportional to the thickness of the layer.

We can obtain a rough estimate of the elastic force, necessary to produce the capacity rise observed on cathodically polarized mercury in an aqueous sodium fluoride solution, as follows. We suppose that only the first term in (9) is important there. This is not a very good approximation with the values of the constants we have used, as it can be seen from fig. 5 that the capacity due to the water, the third term in (9), is still decreasing throughout the range of measurements on the cathodic side. The thickness of the layer is $d-eE/\kappa$, where κ is the force necessary to produce a decrease of one unit in the thickness of the layer, and

Fig. 6

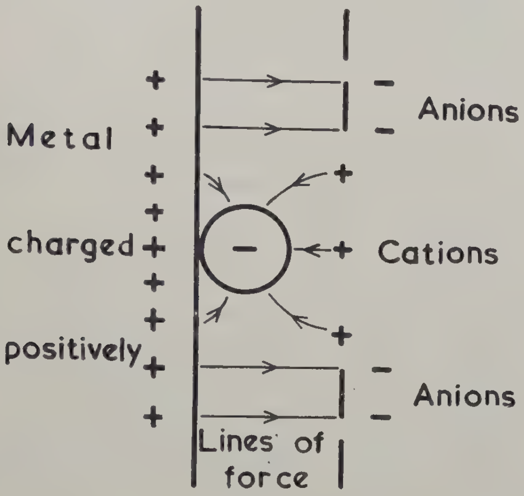

$$\phi = 4\pi\sigma(d-eE/\kappa)/K_0 + \text{constant},$$

from which it follows that

$$C = K_0/4\pi(d-8\pi e\sigma/K_0\kappa).$$

If the second term in this denominator is small, that is, the layer is not much compressed,

$$dC/d\sigma = 8\pi eC/K_0\kappa d.$$

Using the graph reproduced as fig. 2, $dC/d\sigma$ is about $\frac{1}{3}$ volt^{-1} when C is 20 μF/cm². With the previous values of K_0 and d we obtain

$$\kappa \simeq 2e\,\mathrm{V}/\text{Å}^2.$$

The interest of this is that it gives a clue to the height of the free energy barrier which an ion which is specifically adsorbed, or deposited on the metal, has to cross to become free of part of its hydration shell. Of course alkali metal ions, which are the ones whose displacement we are estimating, are not specifically adsorbed, though in principle they have a low energy state on the metal side of the interface, when they form an amalgam with the mercury. If we imagine that there is such a state, and that the ions in it are at a distance l from the outer Helmholtz plane, then when they are in equilibrium with the hydrated ions there, the free energy of an ion in an intermediate state at a distance z from the other Helmholtz plane will be something like

$$F=\tfrac{1}{2}A[1-\cos(2\pi z/l)]=A\sin^2(\pi z/l),$$

where A is the height of the energy barrier between the two states. But we know that for small values of z,

$$F=\tfrac{1}{2}\kappa z^2,$$

so that

$$A=\kappa l^2/2\pi^2.$$

The value of l is uncertain, though for a specifically adsorbed ion in the inner Helmholtz plane it is given by

$$l=d-d'.$$

Here d' is the distance of the inner Helmholtz plane from the conducting surface of the metal. Since a hydrated ion is probably surrounded by a close-packed shell of water molecules, we may expect that l is roughly the diameter of a water molecule. Taking this as 2·76 Å, the energy barrier height is about 0·8 ev. It is difficult to say whether this is a reasonable value. Vermilyea (1956) shows that an activation energy of this amount in the electrolytic deposition of a metal would make the reaction have a fairly high overvoltage (which he attributes to a different mechanism), but the value of the over-voltage is very sensitive indeed to small changes in the activation energy.

The compression of the double layer at high field strength should certainly be studied further, on account of the light it can throw on electro-deposition. If it occurs it has the further consequences that the thickness of the water layer contributing to the capacity varies, and that d in our theory of the capacity is a function of ϕ. To take this into account would complicate the calculation without much improving its accuracy.

ACKNOWLEDGMENTS

I should like to thank Professor N. F. Mott, F.R.S., for suggesting this problem, and for his constant help and advice. I should also like to thank Dr. P. H. Cutler for many discussions, and the Central Electricity Authority for a research grant; acknowledgment is also made to the American Chemical Society for reproduction of fig. 2.

APPENDIX

AVERAGE POTENTIALS

We set up an orthogonal Cartesian coordinate system with coordinates x, y, z, with the (x, y) plane parallel to the double layer, and we consider a disc-shaped right cylinder in the double layer whose generators pass through a circle C in the (x, y) plane. Its interior we call S, of area A, and the disc is bounded by planes $z=u$ and $z=v$, which are cut by the generators in circles whose interiors are U, V respectively. These are the projections of S on to the planes. The construction is drawn in fig. 7.

Fig. 7

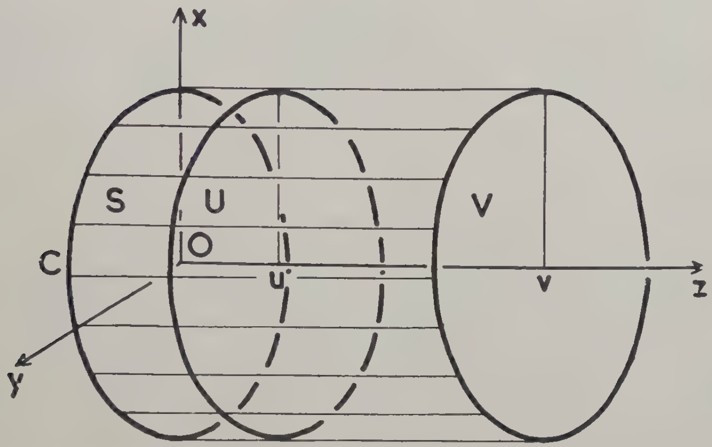

If the electrostatic potential is ϕ, and the field and displacement are $\mathbf{E}$ and $\mathbf{D}$ respectively, generated by a volume charge density ρ and a polarization $\mathbf{P}$, then

$$\mathbf{D}=\mathbf{E}+4\pi\mathbf{P}=-\operatorname{grad}\phi+4\pi\mathbf{P}. \qquad \text{(A1)}$$

Applying Gauss's theorem to the disc whose interior is I and unit outward normal n, we obtain

$$\iint_U \mathbf{D}\cdot\mathbf{n}\,dS+\iint_V \mathbf{D}\cdot\mathbf{n}\,dS=4\pi\iiint_I \rho\,d\tau, \qquad \text{(A 2)}$$

provided that the radius of C is so much larger than the thickness of the disc $(v-u)$ that we can neglect the flux through its curved surface compared with that through the flat ones. Substituting for $\mathbf{D}$ from (A 1) into (A 2) gives

$$\iint_S\left[\left(\frac{\partial\phi}{\partial z}\right)_{(x,\,y,\,u)}-4\pi P_z(x,\,y,\,u)-\left(\frac{\partial\phi}{\partial z}\right)_{(x,\,y,\,v)}+4\pi P_z(x,\,y,\,v)\right]dx\,dy$$

$$=4\pi\int_u^v dw\iint_S \rho(x,\,y,\,w)\,dx\,dy \qquad \text{(A 3)}$$

where P_z is the z-component of $\mathbf{P}$. Denoting averages over the projections of S on to planes parallel to the (x, y) plane by bars, for example

$$\bar{\phi}(z)=\frac{1}{A}\iint_S \phi(x,\,y,\,z)\,dx\,dy,$$

and denoting derivatives with respect to z by dashes, (A 3) becomes

$$\bar{\phi}'(u)-4\pi\bar{P}_z(u)-\bar{\phi}'(v)+4\pi\bar{P}_z(v)$$

$$=4\pi\int_u^v \bar{\rho}(w)\,dw \qquad \text{(A 4)}$$

We now take the plane $z=u$ to the left of all the charges in the layer. Subject to this condition the integral on the right of (A 4) is independent of u, and $\bar{\rho}_z(u)=0$. It follows that $\bar{\phi}'(u)$ is independent of u, so it is a constant, and if the layer is electrically neutral as a whole, and no field is imposed on it externally, it must vanish. Of course we must keep u so that

$$|v-u| \ll \sqrt{A}.$$

to apply this equation. On integrating it with respect to v from u to z and rearranging it, we obtain

$$\bar{\phi}(u)-\bar{\phi}(z)=-4\pi\int_u^z \bar{P}_z(v)dv+4\pi\int_u^z dv\int_u^v \bar{\rho}(w)dw$$

$$=4\pi\int_u^z [-\bar{P}_z(v)+(z-v)\bar{\rho}(v)]\,dv.$$

This is exactly the same potential drop as if the charge were smeared out in planes parallel to the double layer, for then the part between the planes $z=v$, $z=v+dv$ could be regarded as a combination of an electrical double layer of moment $P_z(v)dv$, and a surface charge of density $\bar{\rho}(v)dv$ at a distance $(z-v)$ from the field point. In particular, if part of the polarization of the medium to the right of $z=u$ is due to a perfect dielectric of constant K_0, then

$$\mathbf{P}=-(K_0-1)\operatorname{grad}\phi/4\pi+\mathbf{P}_1 \quad \text{(say)}$$

and

$$\bar{\phi}(u)-\bar{\phi}(z)=\frac{4\pi}{K_0}\int_u^z [-\bar{p}_{1,z}(v)+(z-v)\bar{\rho}(v)]\,dv.$$

Equation (6) is of this form; the potential drop ϕ in it is between two conductors, so averaging ϕ parallel to the double layer makes no difference. A special case of this theorem was proved differently by Grahame (1958).

REFERENCES

AUTY, R. P., and COLE, R. H., 1952, *J. chem. Phys.*, **20,** **1309.**

BUCKINGHAM, A. D., 1956, *J. chem. Phys.*, **25,** 428; 1957, *Disc. Faraday Soc.*, **24,** 151.

DUNCAN, A. B. F., and POPLE, J. A., 1953, *Trans. Faraday Soc.*, **49,** 217.

ERSHLER, B. V., 1946, *J. phys. Chem., Moscou*, **20,** 679.

EVERETT, D. H., 1957, *Disc. Faraday Soc.*, **24,** 229.

GERISCHER, H., 1958, *Z. Electrochem.*, **62,** 256.

GERISCHER, H., and KRAUSE, M., 1958, *Z. phys. Chem.*, N.F., **14,** 184.

GERISCHER, H., and TISCHER, R. P., 1957, *Z. Electrochem.*, **61,** 1159.

GRAHAME, D. C., 1947, *Chem. Rev.*, **41,** 447; 1951, *CITCE Extrait des Comptes Rendus de la IIIe Réunion* (Milan: Carlo Manfredi, 1952): 1954, *J. Amer. chem. Soc.*, **76,** 4819; 1955, *Z. Elektrochem.*, **59,** 740; 1957 a, *J. Amer. chem. Soc.*, **79,** 2093; 1957 b, Technical Report to the Office of Naval Research, No. 5. Second series. Research Contract N–onr–2309(01): 1958, *Z. Elektrochem.*, **62,** 264.

GRAHAME, D. C., and SODERBERG, B. A., 1954, *J. chem. Phys.*, **22,** 449.

KEMBALL, C., 1947, *Proc. roy. Soc.* A, **90,** 117.
KIRKWOOD, J. G., 1939, *J. chem. Phys.*, **7,** 911.
LENNARD-JONES, SIR JOHN, and POPLE, J. A., 1951, *Proc. roy. Soc.* A, **205,** 155.
MACDONALD, J. R., 1954, *J. chem. Phys.*, **22,** 1857.
MINC, S., and JASTRZEBSKA, J., 1960, *J. electrochem. Soc.*, **107,** 135.
MOTT, N. F., and WATTS-TOBIN, R. J., 1961, *Electrochimica Acta* (to be published).
ONSAGER, L., and DUPUIS, M., 1961, Contribution No. 1601 from the Sterling Chemical Laboratory, Yale University.
PAULING, L., 1927, *Proc. roy. Soc.* A, **114,** 181: 1939, *The Nature of the Chemical Bond* (Cornell University Press), p. 313.
RICE, O. K., 1928, *Phys. Rev.*, **31,** 1051.
VERMILYEA, D. A., 1956, *J. chem. Phys.*, **25,** 1254.

CORRESPONDENCE

Magnetic Properties of Chromium between 0° and 350°C

By E. W. Collings†, F. T. Hedgcock and A. Siddiqi‡
Department of Physics, University of Ottawa,
Ottawa, Canada

[Received August 29, 1960]

The maximum in the susceptibility of chromium observed by Bates and Baqi (1936) was attributed by McGuire and Kriessman (1952) to the presence of the antiferromagnetic oxide Cr_2O_3 in their samples. Fine *et al.* (1951) and Söchtig (1940) reported no abnormality in the susceptibility of chromium at 40°C. Recently Lingelback (1958) observed a maximum in the susceptibility of high purity Australian chromium near 37°C in a sample where the content of Cr_2O_3 must have been extremely low. Neutron diffraction investigations of the possible antiferromagnetic transition (see Edwards 1959) have led to confusing results in that the diffraction pattern seems extremely sensitive to particle size and purity. However recent specific heat measurements by Morrison *et al.* (1960) indicate that there is an antiferromagnetic transition occurring in chromium at 38·5°C. The purpose of the present note is to report measurements on the magnetic susceptibility of chromium made on samples of various particle size and purity and electron spin resonance measurements in a sample of high purity chromium.

Figure 1 shows the susceptibility of chromium as a function of temperature for the various samples studied. The description of the samples and room temperature susceptibility value is included as a footnote in the figure. The susceptibility of all of the samples was measured as a function of field to a maximum field of 8000 oersted. All of the samples showed a field dependent susceptibility and the ferromagnetic correction $C\sigma_s$ obtained from H^{-1} plots is also included in fig. 1. As expected the higher purity samples showed a smaller ferromagnetic correction; the correction for all samples obtaining a maximum value in the region of the susceptibility maximum. All of the samples show a maximum in the magnetic susceptibility at a temperature of $39 \pm 0{\cdot}5$°C. It seems fairly conclusive therefore that the maximum in the susceptibility of chromium is independent of the physical nature and purity of the sample in the range of samples studied. In particular the apparent influence of nitrogen content on some properties of chromium (see Edwards 1959) does not influence the size or position of the susceptibility maximum at 39°C.

---

† National Research Council Post-doctoral fellow.
‡ Physics Department Post-doctoral Assistant.

The absolute susceptibilities listed in fig. 1 are in reasonable agreement with the value of $3{\cdot}17 \times 10^{-6} \times 10^{-6}$ e.m.u./g reported by Lingelback (1958). The high-temperature slope of the susceptibility versus temperature curve is in agreement with Lingelback; however the slope on the low-temperature side of the susceptibility maximum has the opposite sign but is in agreement with the earlier observations of Bates and Baqi (1936).

Fig. 1

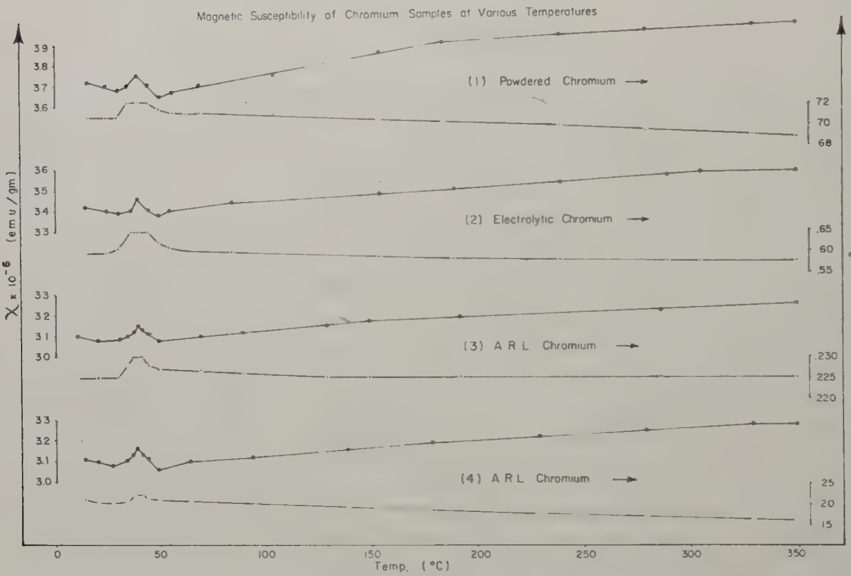

Magnetic susceptibility of chromium and the ferromagnetic correction $C\sigma_s$ plotted as a function of temperature

Sample	$\chi_{R_0 . T_0} \times 10_2$ $\pm 0{\cdot}01$ (e.m.u./g.)	N_2 (weight %)	O_2 (weight %)
(1)	3·70	0·007	0·02
(2)	3·41	0·0230	Estimated 0·5
(3)	3·08	0·0004	Estimated 0·01
(4)	3·10	No analysis made but reported higher purity than sample 3	

Chromium sesquioxide is known to be antiferromagnetic with a Neèl temperature of 38·5°c. Therefore one cannot ignore the possibility that all of the chromium samples contained sufficient oxygen to form a fixed concentration of Cr_2O_3 even though the analysis of the samples would indicate too low an oxygen content to form sufficient Cr_2O_3 to explain the observed size of the susceptibility bump. The amount of Cr_2O_3 needed was estimated from the susceptibility data of Trounson *et al.* (1950) to be 4 weight per cent. The electron spin resonance signal from Cr_2O_3 has the characteristic behaviour of an antiferromagnetic resonance in that it abruptly diminishes in amplitude near the Neèl temperature (Trounson *et al.* 1950). An attempt was made to detect a Cr_2O_3 signal in a thin strip of freshly etched high purity A.R.L. chromium. Although some absorption took place it was of sufficiently low level that it would have to be classified as noise (curve A in fig. 2). When 46 micrograms Cr_2O_3 were placed in the cavity along with the metallic chromium (the chromium strip was retained in order to keep the cavity Q and hence sensitivity constant) a distinct increase in resonance absorption was observed above 33°c (curve B in fig. 2). Allowing for the skin effect in the chromium metal the relative weights of Cr_2O_3 and metallic chromium 'seen' by the r.f. field was 4%. A visual estimate of the sensitivity derived from the results in fig. 2 shows that certainly the transition in less than 1% Cr_2O_3 in metallic chromium would have been detectable in the background level of the pure metal (curve A). It is therefore apparent that there is not sufficient Cr_2O_3 present in the purest chromium to give the susceptibility maximum at 39°c and the resonance results support the previous conclusion based on the susceptibility results alone that there is an antiferromagnetic transition taking place in chromium itself at $39 \pm 0{\cdot}5$°c.

Fig. 2

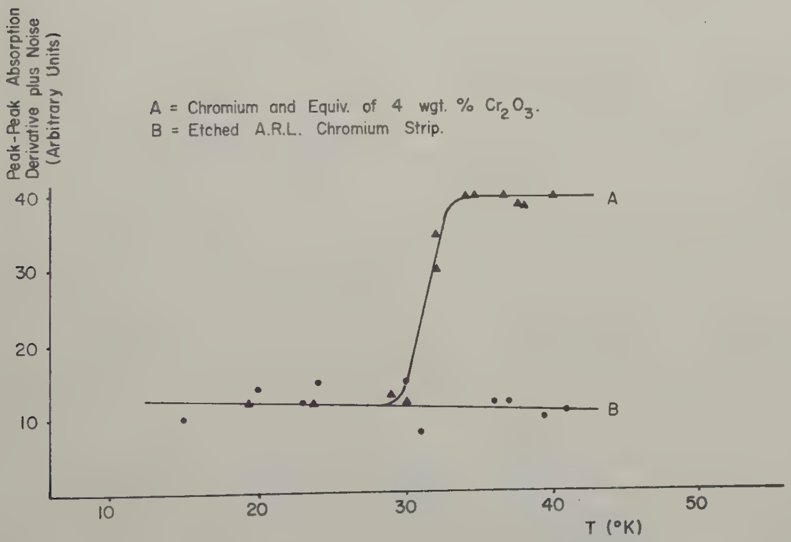

Temperature dependence of peak–peak absorption derivative plus noise for chromium samples.

ACKNOWLEDGMENTS

The authors would like to thank Dr. H. L. Wain of the Australian Aeronautical Research Laboratories for supplying the high-purity

chromium and carrying out analyses on the various samples. It is a pleasure to acknowledge the stimulating correspondence with Dr. G. K. White of the National Standards Laboratory of Australia who originally suggested the problem to one of us (F. T. Hedgcock).

References

Bates, L. F., and Baqi, A., 1936, *Proc. phys. Soc., Lond.*, **48,** 781.
Edwards, A. R., *et al.*, 1959, *Met. Revs.*, **4,** 403.
Fine, M. E., *et al.* 1951, *F. Metals New York*, **191,** 56.
Lingelback, R., 1958, *Z. phys. Chem.*, **14,** 1.
McGuire, T. R., and Kriessman, C. J., 1952, *Phys. Rev.*, **85,** 452.
Morrison, J., *et al.* 1960, *Phil. Mag.*, **5,** 180.
Söchtig, H., 1940, *Ann. Phys., Lpz.*, **38,** 97.
Trounson, F. P., Bleil, D. F., Wangsness, R. K., and Maxwell, L, R., 1950, *Phys. Rev.*, **79,** 542.

The Mechanism of Surface Effects in Crystal Plasticity

By J. J. Gilman†
General Electric Research Laboratory, Schenectady, N.Y.

[Received August 22, 1960]

The stress–strain curves of many plastic monocrystals are sensitive to conditions at the crystal surfaces. Thin surface films of solid materials often harden crystals (the Roscoe Effect, Metzger and Read 1958), and surface-active liquids tend to cause softening (the Rehbinder Effect, Likhtman *et al.* 1958). The effects appear schematically as in fig. 1.

Fig. 1

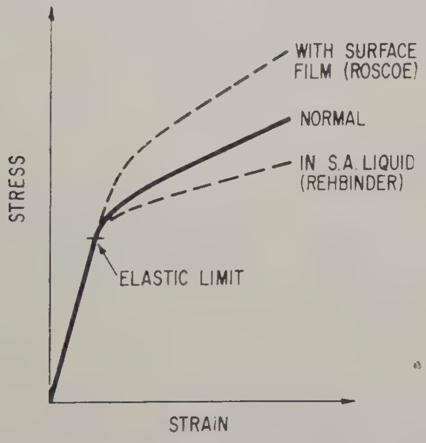

Schematic effects of surface conditions on the stress–strain curves of plastic crystals.

This figure illustrates a prime feature of the effects which is not explained convincingly by previous interpretations. This feature is the fact that the effects do not appear full-blown for small plastic strains ; instead, rather substantial strains ($> 10^{-4}$) are required before they acquire their full magnitude. This means that the effects are not primarily yielding phenomena, but depend on conditions that develop sometime after yielding has occurred. Therefore, a mechanism that simply involves the blocking of dislocations by a surface film does not interpret the observations satisfactorily. Something more subtle is required, and I believe that insight gained in recent experiments with LiF crystals (Johnston and Gilman 1960) suggests a suitable mechanism. Moreover the mechanism is amenable to direct experimental study using etching methods to observe the effects of surface environment on the rate of surface cross-glide.

---

† Now at Brown University, Providence, R.I., U.S.A.

The interpretation that is proposed is illustrated in fig. 2. At (*a*) in the figure, a screw dislocation, AB, lies on a glide plane that is inclined to the surface at an angle, θ. The dislocation's Burgers vector, **b**, is indicated and the dislocation tends to move in the direction AC. However, the dislocation line can shorten its length by moving off the primary glide plane CDEF as shown at (*b*) in fig. 1. This 'cross-gliding' motion is opposed by the fact that a surface step is created by it ; and, in an anisotropic crystal, by the fact that the motion may have to occur on a plane other than a primary glide plane. Such cross-glide motions have been observed in LiF crystals by Johnston and Gilman (1960). Since the cross-gliding is opposed by the surface energy of the step that is left behind, the distance over which gliding occurs will increase with decreasing surface energy and conversely. A surface film that is harder than a crystal, on the other hand, will mechanically resist the formation of the step and thus restrict the motion of the screw dislocation.

Fig. 2

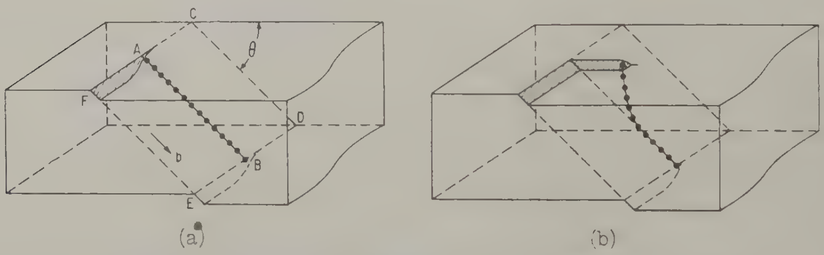

Cross-gliding of a screw dislocation near the surface of a crystal : (*a*) initial configuration ; (*b*) after some cross-gliding.

Cross-gliding of screw dislocations at the surface of a crystal has an important effect on the overall plastic behaviour because it leads to dislocation multiplication (Johnston and Gilman 1960). This in turn leads to strain-hardening because the greater the dislocation density in a crystal, the harder it becomes. Since this surface mechanism does not involve the initial motions of dislocations on their primary glide planes, it has the required characteristic of not influencing the initial yield stress. but only influencing the progress of a stress–strain curve.

A feature of the proposed mechanism that makes it especially attractive as a surface mechanism is that the force that is resisted by the surface step is presented by a dislocation line with relatively low line-energy. This occurs because the shear stresses around a screw dislocation that intersects a surface are relaxed at the surface so the dislocation line has no elastic strain energy ; it has only the much smaller energy of its core. The core energy of a dislocation line is comparable in magnitude with the energy of a surface step, so it is reasonable to expect changes in the surface energy to affect the position of the end of the dislocation line. On the other hand, if one tries to account for surface effects in terms of the blocking of edge dislocations that are trying to emerge from a surface, then the surface energy must oppose a dislocation that has elastic as well as core energy. In this case it seems unlikely that small changes of the surface energy would have much effect.

The fact that an optimum strain-rate is observed for surface effects can be accounted for because the cross-gliding has been found to occur at a certain moderate rate. This will be too small to cause a surface effect at high rates of plastic deformation. At deformation rates that are lower than the optimum, the distance of cross-gliding will be so large that little strain-hardening will occur.

Glide plane orientation effects, irregular glide bands on crystals deformed in a surface-active medium, and enhanced distortions in the surface layers of crystals deformed with surface films present are all observations that seem consistent with the proposed mechanism. Moreover the mechanism is amenable to direct experimental study using etching methods to observe the effects of surface environment on the rate of surface cross-glide.

REFERENCES

JOHNSTON, W. G., and GILMAN, J. J., 1960, *J. appl. Phys.*, **31,** 632.

LIKHTMAN, V. I., REHBINDER, P. A., and KARPENKO, G. V., 1958, *Effect of a Surface Active Medium on the Deformation of Metals* (London : H.M.S.O.).

METZGER, M., and READ, T. A., 1958, *Trans. Amer. Inst. min. (metall.) Engrs,* **212,** 236.

Delayed Alpha Particles from ^{16}N

By R. E. Segel, J. W. Olness and E. L. Sprenkel
Aeronautical Research Laboratory, Dayton, Ohio, U.S.A.

[Received October 15, 1960]

It is energetically feasible for the ^{16}N β-decay to populate three known α-unstable states in ^{16}O: the 2^- state at 8·88 Mev, the 1^- state at 9·58 Mev, and the 2^+ state at 9·84 Mev (Ajzenberg-Selove and Lauritsen 1959). We have measured the alpha particle spectrum resulting from the decay of ^{16}N in order to obtain information pertaining to the decay through these states.

^{16}N was prepared by bombarding nitrogen gas, enriched† to 96% ^{15}N, with 2 Mev deuterons from the Aeronautical Research Laboratory van de Graaff generator. The radioactive gas from the target was allowed to diffuse into a small cell which was viewed by a solid state detector of p-type silicon with a shallow phosphorus diffusion surface layer. The running procedure was to bombard for 15 sec, de-energize the accelerator, and then record for 15 sec. This procedure was repeated several hundred times.

The silicon detector was calibrated with the aid of radioactive α-sources and a mercury pulser. The 'dead' surface layer of the counter, which was measured to be about 0·5 microns, was determined by observing the shift in pulse height when the angle of incidence of alpha particles was changed. In order to reduce the electron counting efficiency the detector was operated at a low bias (~ 1 v).

A pulse height spectrum is shown in the figure. The energy scale is given for alpha particles incident on the face of the detector; corrections for the 'dead' layer have been taken into account. The energy loss in the gas was negligibly small, averaging about 30 kev. It can be seen from the figure that only one alpha particle group was seen: a broad group centred at about 1·72 Mev. We identify this group with the broad state centred at 9·58 Mev (Ajzenberg-Selove and Lauritsen 1959).

The centre of the observed alpha particle spectrum lies about 100 kev below the energy corresponding to the centre of the state as determined by alpha particle scattering on ^{12}C (Hill 1953). A distortion of the spectrum from the normal (i.e. Breit-Wigner) shape can be expected because of the energy dependence of the β-transition rate (roughly proportional to $E_\beta{}^5$ where E_β is the β end-point energy) and, in addition, the shape of the state can be expected to deviate from normal because of the coulomb barrier present to the out-going alpha particles. These two effects tend to work in opposite directions with the β-decay favouring high energy electrons and therefore low energy alpha particles, while the coulomb barrier energy dependence implies a shortened lifetime for high energy alpha particles and therefore a broadening of the state on the high side. At the energies relevant here, the β-factor is the stronger and therefore the alpha spectrum is shifted towards lower energy.

---

† The authors are indebted to Dr. J. A. Jacobs of the State University of Iowa for the loan of the ^{15}N gas.

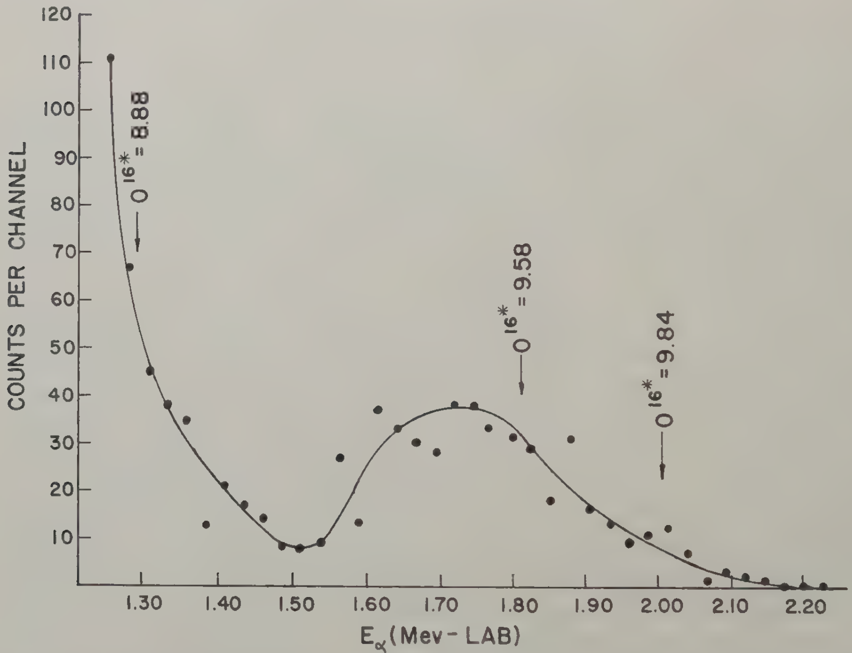

Pulse height spectrum from solid state ionization chamber alpha detector viewing decaying ^{16}N nuclei. The arrows represent the pulse heights corresponding to the centres of the various alpha unstable states in ^{16}O The solid line merely represents an eye smoothing of the data.

The observed spectrum was also subject to instrumental distortion, the primary effect being a smearing of the true spectrum due to alpha particles traversing the counter dead layer at various angles. Because of this instrumental distortion, it was not possible to make an accurate analysis of the spectral shape. However, even without allowing for the energy resolution of the detecting system, we find the peak narrower than would be predicted for the state having the width $\Gamma = 650$ kev (c.m.) as given by Hill (1953). The data presented here implies $\Gamma_\alpha = 450 \pm 100$ kev. This discrepancy is not surprising in view of the difficulty in extracting a width in a reaction in which the transition rates can be expected to vary widely over the width of the state.

From the intensity of the alpha group we find $\log ft = 7{\cdot}2 \pm 0{\cdot}2$ with the β end-point energy taken as corresponding to the centre of the observed alpha particle distribution. We note that the spin of the ^{16}N ground state is known to be 2^- (Ajzenberg-Selove and Lauritsen 1959) and therefore the β-transition to the 1^- 9·58 MeV ^{16}O state is allowed. The observed β-transition rate is therefore a few hundred times lower than what would be normally expected for an allowed transition. Elliot and Flowers (1957) indicate that the 9·58 MeV state should be due to a three nucleon excitation and it is gratifying to note that the β-decay to this state is indeed highly inhibited, thus supporting the Elliott and Flowers description of ^{16}O.

The 8·88 MeV 2^- state is known to be populated by about 1% of the ^{16}N decays (Alburger *et al.* 1959). Break-up into $^{12}C + \alpha$ is parity forbidden and therefore a search for alpha particles from this state is a test of the validity of parity conservation in nuclear interactions. As is shown in the figure, the pulse height region corresponding to alpha particles from the 8·88 MeV state contains pulses from the electron background. However, as the state is sharp and heavily populated (some 2×10^6 decays from this state were viewed) a meaningful upper limit for the alpha width of this state could be deduced. It was determined that as many as about 300 alpha particles emanating from the 8·88 MeV state would have been detected. Hence, we find $\Gamma_\alpha/\Gamma_\gamma < 1{\cdot}3 \times 10^{-4}$.

The gamma width of the 8·88 MeV state has been calculated by Elliot and Flowers (1957) to be about 3×10^{-3} ev, from which we imply $\Gamma_\alpha < 3{\cdot}9 \times 10^{-7}$ ev. The expected Γ_α in the absence of a parity inhibition can be estimated by calculating the single particle width (allowing for the coulomb barrier) and taking the expected Γ_α as 1/20 the single particle width in accordance with the survey of Wilkinson (1957). This estimate predicts a parity allowed $\Gamma_\alpha = 3 \times 10^3$ ev and, therefore, using the notation of Lee and Yang (1956) we find $\mathscr{F}^2 \lesssim 1{\cdot}3 \times 10^{-10}$, emphasizing that this upper limit can be taken only as a rather crude estimate.

The 2^+ assignment to the 9·84 MeV ^{16}O state implies a first forbidden β-transition. No alpha group was seen corresponding to this state: the 'bump' in the spectrum in the figure at about the right energy for this group is not statistically significant. The upper limit to the transition rate to the 9·84 state was found to be $\log ft > 7{\cdot}4$. This value is consistent with the 2^+ assignment to the 9·84 MeV state.

REFERENCES

AJZENBERG-SELOVE, F., and LAURITSEN, T., 1959, *Nucl. Phys.*, **11,** 1.

ALBURGER, D. E., GALLMANN, A., and WILKINSON, D. H., 1959, *Phys. Rev.*, **116,** 939.

ELLIOT, J. P., and FLOWERS, B. H., 1957, *Proc. roy. Soc.* A, **242,** 57.

HILL, R. W., 1953, *Phys. Rev.*, **90,** 845.

LEE, T. D., and YANG, C. N., 1956, *Phys. Rev.*, **104,** 254.

WILKINSON, D. H., 1959, *Proc. Rehovoth Conference on Nuclear Structure* (North-Holland Pub. Co.).

Remark on the Seebeck Coefficient of Polar Semiconductors†

By J. Appel
John Jay Hopkins Laboratory for Pure and Applied Science,
General Atomic, Division of General Dynamics Corporation, San Diego,
California

[Received September 23, 1960]

For a non-degenerate extrinsic semiconductor, the Seebeck coefficient is given by the Pisarenko formula (Joffé 1958)

$$\alpha = \pm \frac{k_B}{e}(b - \zeta/k_B T). \qquad (1)$$

The $-$ and $+$ signs correspond to electron and hole conduction, respectively ($-e$ = electron charge). The number b depends somewhat on the electronic band structure and on the pertinent scattering mechanism; usually b is small compared to $\zeta/k_B T = \log(N_c/n)$, where for an isotropic n-type conductor with a parabolic band $N_c = 2(2\pi m_{\text{eff}} k_B T/h^2)^{3/2}$, and n and m_{eff} are the concentration and the scalar effective mass of the negative charge carriers, respectively. The validity region of eqn. (1) is discussed elsewhere (Lautz 1953).

The Seebeck coefficient depends on the effective mass m_{eff} via ζ. Here we want to consider the dependence of α on that m_{eff} which is associated to the appropriate charge carriers in polar crystals, called polarons (Pekar 1954), provided the polaron eigenvalues can be described by an effective mass concept. Then m_{eff} can be quite different from the bare, free electron mass m, and also from the rigid lattice mass m^*. The polaron effective mass $m_{\text{eff}} = m^{**}$ is defined by the low-lying energy eigenvalues of the polaron eigenstates. In order to calculate these eigenstates there exist two essentially different approaches.

For the approach, resulting in what is called the *large polaron* picture, the paper of Fröhlich *et al.* (1950) is characteristic. The theory is based on a model in which an excess electron interacts with a dielectric continuum, instead of a crystal lattice. In restricting to the ground state of the system, electron plus the dielectric continuum which is represented by plane polarization waves, the polaron eigenstates are determined by virtual emission and reabsorption of quantized longitudinal polarization waves (polarization phonons). Thus, the eigenstates of slow polarons at very low temperatures are calculated by assuming that the dimension of a polaron is large compared to the lattice constant. The effective mass m^{**} of a large polaron consisting of an electron plus its associated cloud of virtual polarization phonons is, of course, temperature independent. The briefly described large polaron picture, based on the continuum model, does not apply in the case of a strong interaction between excess electron and lattice, such that the dimension of a polaron is comparable to a lattice constant.

---

† Part of this project research is sponsored by the Advance Research Projects Agency under Bureau of Ships contract NObs-77144.

A different kind of approach, resulting in what is called the *small polaron* picture, has been worked out by Sewell (1958) and Holstein (1959). In the small polaron picture it is taken into account that at $T > 0$ the electron plus its associated lattice displacement polarizations correspond to an electron with a cloud of virtual *and* real phonons. The method of Sewell is essentially that of a Bloch tight-binding approximation, but taking the electron-lattice interaction into account when calculationg polaron eigenstates. Therefore, the overlap integrals which play a central role in the tight-binding approximation (Bloch 1928), depend on electron *and* phonon quantum numbers. By taking an appropriate thermal average over the eigenvalues, finally the low lying energy eigenvalues of the small polarons can be defined in terms of a temperature-dependent effective mass m^{**}. It may be expected that, in a certain temperature interval around the Debye temperature which corresponds to the frequency of the polarization phonons, the small polaron effective mass is given by the simple formula

$$m^{**} = m^{*} \exp\left(\frac{T}{T_0}\right). \qquad (2)$$

Here m^{*} is the rigid lattice mass and T_0 is a parameter represented by a rather complicated expression which is given in Sewell's paper.

From eqns. (1) and (2) it follows that the Seebeck coefficient of a polar crystal to which the small polaron picture applies is given by

$$\alpha = -\frac{k_B}{e}\left(b + \frac{3T}{2T_0} + \log\left[\frac{2(2\pi m^{*} k_B T)^{3/2}}{h^3 n}\right]\right) \qquad (3)$$

with the above-mentioned restriction on the temperature interval. Thus, the Seebeck coefficient can depend linearly on temperature, provided the polaron concentration n is constant.

Now, according to the results of experimental investigations at General Atomic (Kurnick, private communication); the following are characteristic for Ce–S semiconductors:

1. A strong, almost linear rise of the Seebeck coefficient with temperature between 300 and 1000°K.
2. A slow, non-exponential decrease of the electrical conductivity with increasing temperature in samples with S : Ce ratios 1·3–1·4.
3. An almost undetectable, but finite, Hall voltage.

If one assumes that Ce–S semiconductors are characterized by a strong polar bonding between the lattice particles, a possible explanation of the measured temperature dependence of the Seebeck coefficient is given by eqn. (3). Then, the linear rise of α may be consistent with a slight temperature dependence of the electrical conductivity, provided $n = \text{const.}$ and provided the polaron mobility—a delicate subject—is independent of

m^{**} and is determined by the interaction of polarons with acoustical phonons. It turns out, from a sketch of the polaron mobility by Fröhlich and Sewell (1959), that for the interaction of small polarons with acoustical phonons via two phonon scattering processes, the mobility might be independent of m^{**} (and of the order of $1\,\mathrm{cm}^2\,\mathrm{v}^{-1}\,\mathrm{sec}^{-1}$).

ACKNOWLEDGMENTS

It is a pleasure to thank M. Cutler, W. B. Teutsch, and S. W. Kurnick for helpful discussions, the last also for the Ce–S data, and W. Kohn, University of California, for interesting conversations on the different polaron pictures. The kind encouragement of P. H. Miller, Jr. is gratefully acknowledged.

REFERENCES

BLOCH, F., 1928, *Z. Phys.*, **61,** 209.
FRÖHLICH, H., PELZER, H., and ZIENAU, S., 1950, *Phil. Mag.*, **41,** 221.
FRÖHLICH, H., and SEWELL, G. L., 1959, *Proc. phys. Soc. Lond.*, **74,** 463.
HAKEN, H., 1955, *Halbleiterprobleme II*, edited by W. Schottky (Braunschweig : Vieweg-Verlag).
HOLSTEIN, T., 1959, *Annals of Physics, U.S.A.*, **8,** 325 and 343.
JOFFÉ, A. F., 1958, *Physik der Halbleiter* (Berlin : Akademie-Verlag), p. 293.
LAUTZ, G., 1953, *Z. Naturf.* A, **6,** 361.
PEKAR, S. I., 1954, *Fortschr. Phys.*, **1,** 368.
SEWELL, G. L., 1958, *Phil. Mag.*, **36,** 1361.

Beta-decay of ^{16}N : Conservation of Spin and Parity in ^{16}O†

By D. E. Alburger, R. E. Pixley, D. H. Wilkinson‡
Brookhaven National Laboratory, Upton, New York, U.S.A.

and P. Donovan
Brookhaven National Laboratory and Bell Telephone Laboratories,
Murray Hill, New Jersey, U.S.A.

[Received October 15, 1960]

The degree to which parity is conserved in the strong interactions is an open question. The early experiments (Tanner 1957, Wilkinson 1958 a, Segel *et al.* 1958) made it unlikely that $\mathscr{F}^2$, the intensity of the component of irregular parity in a typical nuclear wave function, can be greater than about 10^{-7}. Subsequent work (see, e.g. Blin-Stoyle 1960) has suggested $\mathscr{F}^2 < 10^{-8}$. We report here an experiment designed to sharpen this limit.

The ground state of ^{16}N is 2^-. It is known to decay with a half-life of 7·4 sec and a total energy release of 10·40 Mev through several states of ^{16}O (Ajzenberg-Selove and Lauritsen 1959); that at 8·88 Mev is 2^- and enjoys a beta branch of 1·1% (Wilkinson *et al.* 1956). This state is energetically unstable by 1·73 Mev to decay into the ground state of ^{12}C plus an alpha particle but such decay is rigorously forbidden if spin and parity are good quantum numbers. In the present work we seek this decay.

We irradiated a thick target of Ti^{15}N with a beam of deuterons of 1·1 Mev which impinged at a grazing angle of 30°. The consequent ^{16}N decay was examined by a solid state counter close to the target and at 90° to the bombarding beam (which was interrupted during the counting period). Owing to the grazing incidence of the bombarding beam and the steeply energy dependent cross section for the reaction ^{15}N(d, p)^{16}N the induced ^{16}N activity is rather superficial and the source is not thick to the possible alpha-particles from the decay of the 8·88 Mev state.

The left-hand side of the figure shows a typical pulse-height spectrum from the solid-state counter. The exponential rise at low channel numbers is due to the great numbers of energetic beta-particles that stream through the counter. The solid line on the left-hand side of the figure is not drawn through the points but is taken directly from another run in which the solid-state counter was covered with a 1 mil. Al foil, sufficiently thick to stop alpha-particles from the decay of any state of ^{16}O accessible to the beta-decay of ^{16}N but not thick enough appreciably to affect the beta particles responsible for the small pulses. It is clear by the departure of the points from the line at high channel numbers that alpha-particles are indeed emitted following the beta decay of ^{16}N. That the alpha-particles are associated with ^{16}N-decay was demonstrated by a rough half-life measurement on the counts at high channel numbers: this gave $7{\cdot}6 \pm 1{\cdot}0$ sec.

---

† Work performed under the auspices of the United States Atomic Energy Commission.

‡ Permanent address: Clarendon Laboratory, Oxford, England.

These alpha particles come from the decay of the broad 1^- state in ^{16}O of nominal excitation 9·58 Mev which is accessible to an allowed beta transition from ^{16}N. The right-hand side of the figure shows the difference between the experimental points (grouped in threes) and the solid line of the left-hand side. The solid line of the right-hand side is the alpha-particle spectrum computed for the break-up of the 9·58 Mev level following its population through beta-decay. This computation allows for the considerable width of the level (Hill 1953) for the beta-decay phase-space factors and for the various effects of target thickness. The energy calibration of the solid state counter was effected with the aid of an

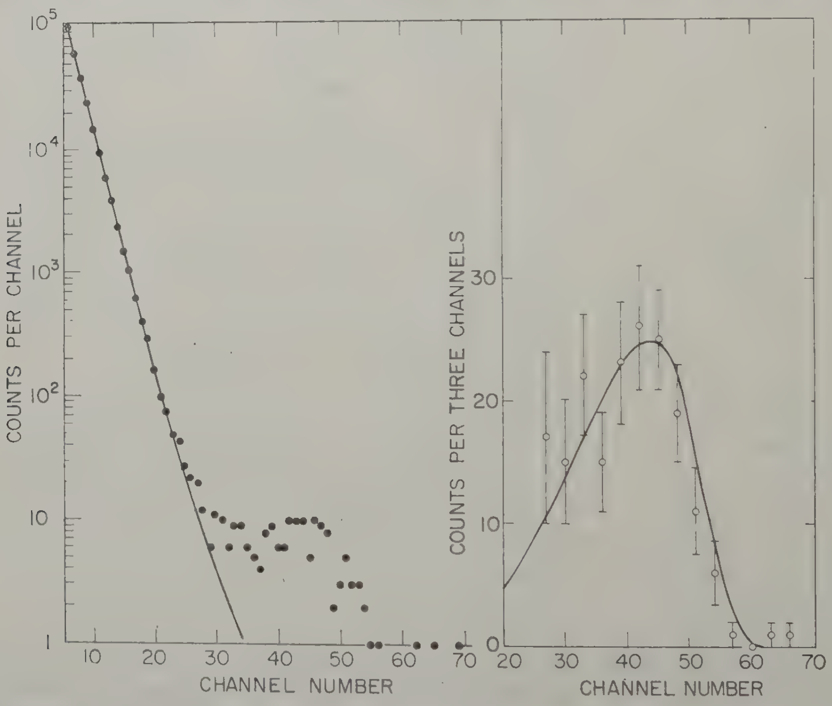

Decay of ^{16}N as seen with a solid-state counter. The left-hand half of the figure shows as the experimental points the pulse distribution in the unshielded counter and as the full line the distribution in the counter when shielded with a 1 mil. Al foil. The right-hand half of the figure shows the difference between the points and the line of the left-hand half; the solid curve is the alpha-particle distribution computed for the decay of the broad 1^- state in ^{16}O of nominal energy 9·58 Mev. Alpha particles from the decay of a sharp level at 9·58 Mev in ^{16}O would reach to channel 54; those from the level at 9·84 Mev to channel 61; those from the level at 8·88 Mev to channel 36.

alpha-particle source and no adjustment in abscissa is made in comparing experimental and theoretical distributions. The ^{16}N source strength was monitored using a 5 in. × 4 in. NaI(Tl) crystal and as a result we can quote the branching ratio $3{\cdot}0 \times 10^{-6}$ for transitions to the broad 9·58 Mev state. This corresponds to $\log ft = 7{\cdot}0$. (Using as beta-decay energy the value appropriate to the maximum of the computed and observed alpha-particle spectrum, viz. an effective level energy of about 9·45 Mev rather than 9·58 Mev; the lower energy is favoured by the greater energy released in the beta-decay.) The uncertainty in the branching ratio is about 50%. This $\log ft$ value is interestingly high for an allowed transition. We may recollect however that this 1^- state is not generated as belonging to $1p^{-1}(2s, 1d)$ by the independent particle model in intermediate coupling (Elliott and Flowers 1957) which gives an excellent account of most of the other odd parity $T = 0$ states below 12 Mev or so. It is presumably a state of three-quantum excitation and so the transition is theoretically forbidden although allowed by spin and parity; the large $\log ft$ value is therefore a confirmation of the expectation of the model. (Note that the jj-coupling model of $A = 16$ (Unna and Talmi 1958) describes ^{16}N as $1p_{1/2}{}^{-1}1d_{5/2}$ and the 9·58 Mev state of ^{16}O as $1p_{1/2}{}^{-1}2s_{1/2}$: it therefore seeks to understand the large $\log ft$ value as due to l-forbiddenness.)

The absence of alpha particles from the break-up of the 2^+ state of ^{16}O at 9·84 Mev implies $\log ft > 7{\cdot}3$ for the first forbidden transition to this state.

If the 2^- state at 8·88 Mev broke up by alpha-particle emission it would affect the four points of lowest energy on the right hand side of the figure. The absence of any significant excess in this region above the solid line representing the alpha-particles from the 9·58 Mev state corresponds to $\Gamma_\alpha/\Gamma_\gamma \lesssim 2{\cdot}4 \times 10^{-5}$ for the 8·88 Mev level (this figure represents one standard deviation within which the ratio is zero).

We must now estimate the lifetime of the 8·88 Mev state. The IPM calculation successfully predicts its position. For the preferred values of the parameters of the model it also predicts satisfactorily not only the branching ratios of the transitions from this state to the 7·12, 6·14 Mev and ground states (experiment: 0·15 : 1 : 0·09; theory: 0·06 : 1 : 0·05), but also the M1 : E2 mixing ratio in the case where it has been estimated namely the transition to the 6·14 Mev level. It also predicts accurately the properties of the low-lying states of ^{16}N (Wilkinson 1957, Freeman and Hanna 1957) and the speed of the beta-decay to the 8·88 Mev level (experimental $\log ft = 4{\cdot}4$; theoretical $\log ft = 4{\cdot}2$). We may therefore have some confidence in its prediction of the absolute width of the 8·88 Mev level which is 2×10^{-3} ev.

An indication of the plausibility of this lifetime comes from the isotopic spin forbidden E1 transition between the 8·88 Mev and 6·91 Mev (2^+) states that is not treated by the IPM. If we apply the usual recipe (Wilkinson 1956) to estimate the speed of an allowed E1 transition of this energy (0·032 of a Weisskopf unit on a radius constant of $1{\cdot}5 \times 10^{-13}$ cm) we find

0·18 ev. We can now combine the theoretical IPM speed with the experimental branching ratios of the 8·88 MeV level to deduce a width for the E1 transition of $1{\cdot}1\times10^{-4}$ ev and so an effective isotopic spin impurity of $\alpha_0^2(1)\approx6\times10^{-4}$. This in turn, using the recommended procedure, (Wilkinson 1958 b) gives the value of the Coulomb matrix element of $H^c=\alpha_0(1)\times\Delta_{01}=0{\cdot}025\times3{\cdot}9\approx0{\cdot}10$ MeV which is eminently reasonable.

Combining our experimental limit on $\Gamma_\alpha/\Gamma_\gamma$ with this figure for Γ_γ we conclude $\Gamma_\alpha\lesssim4{\cdot}8\times10^{-8}$ ev. In order to give a value for $\mathscr{F}^2$ we must now fix on a typical value for Γ_α for a transition allowed by spin and parity. We are well placed to do this since in ^{16}O the reduced alpha-particle widths are known for nine levels of $T=0$ (Lane 1960). The logarithmic mean of these reduced widths is 0·24 single particle units (the arithmetic mean is 0·64). If this value of 0·24 is used to predict a typical allowed value of Γ_α for a state at 8·88 MeV ($l=2$) we find $6{\cdot}7\times10^3$ ev (using an interaction radius of $1{\cdot}4\times(A_1^{1/3}+A_2^{1/3})\times10^{-13}$ cm). This then suggests

$$\mathscr{F}^2\lesssim4{\cdot}8\times10^{-8}/6{\cdot}7\times10^3=7\times10^{-12}.$$

We may similarly determine a limit for spin conservation if we assume that the spin-non-conserving interaction introduces a small element of 1^- into the 2^- state. The allowed value of Γ_α is now ($l=1$) $2{\cdot}0\times10^4$ ev and so the limit on the intensity of the admixed $J=1$ wave-function is 2×10^{-12}.

Although we must voice the usual cautions associated with such estimates as these we are probably safe in saying $\mathscr{F}^2<10^{-10}$ with the limit on spin conservation somewhat sharper.

This experiment is susceptible of considerable refinements that are now being put in train.

REFERENCES

AJZENBERG-SELOVE, F., and LAURITSEN, T., 1959, *Nucl. Phys.*, **11,** 1.
BLIN-STOYLE, R. J., 1960, *Phys. Rev.* (in the press).
ELLIOTT, J. P., and FLOWERS, B. H., 1957, *Proc. roy. Soc.*, **242,** 57.
FREEMAN, J., and HANNA, R. C., 1957, *Nucl. Phys.*, **4,** 599.
HILL, R. W., 1953, *Phys. Rev.*, **90,** 845.
LANE, A. M., 1960, *Rev. mod. Phys.*, **32,** 519.
SEGEL, R. E., KANE, J. V., and WILKINSON, D. H., 1958, *Phil. Mag.*, **3,** 204.
TANNER, N. W., 1957, *Phys. Rev.*, **107,** 1203.
UNNA, I., and TALMI, I., 1958, *Phys. Rev.*, **112,** 452.
WILKINSON, D. H., 1956, *Phil. Mag.*, **1,** 127; 1957, *Phys. Rev.*, **105,** 686; 1958 a, *Ibid.*, **109,** 1603, 1610, 1614; 1958 b, *Proceedings of the Rehovoth Conference on Nuclear Structure* (Amsterdam: North-Holland), p. 175.
WILKINSON, D. H., TOPPEL, B. J., and ALBURGER, D. E., 1956, *Phys. Rev.*, **101,** 673.

REVIEWS OF BOOKS

Quantum Theory of Atomic Structure, Vol. 1. By JOHN C. SLATER. (New York: McGraw-Hill, 1960.) [Pp. 502.] Price £4 5*s*. 6*d*.

ANOTHER volume from Professor Slater's fluent pen is always welcome. Indeed, we have the promise of more good things to come, for this is just the first of a series, adding up to a treatise on the grand scale, covering the application of quantum mechanics to the non-nuclear properties of matter. The first 200 pages set the stage with a more or less conventional account of basic quantum theory; the remainder of this volume deals with the structure of atoms (except for spin–orbit and hyperfine interactions), up to the latest calculations by the M.I.T. team on the multiplet structure of the Iron group. The exposition is, as always, lucid in the extreme; students will be grateful for the clear and simple explanation of difficult topics, and the profound good sense of the comments on the physical interpretation of the mathematical results. In fact, for a work on such a scale, the treatment may be a little informal in places; we sometimes lack a precise statement of the general theorems and principles so that we may know exactly where we stand. Perhaps he has really tried to put in too much. There are other books, or lecture courses, where one would have already learned trivia such as wavepropagation in strings, or where one could try to master highbrow mathematical techniques such as the Calculus of Variations. Much better, for example, merely to refer to Kemble's treatment of the principle of Least Action than to try to explain it in a two-page appendix. Even Professor Slater cannot make a subtle mathematical theory as simple as *that*. But perhaps this is only a comment on the education of the American graduate students at whom this work is chiefly aimed. J. M. Z.

Nuclear Spectroscopy. Edited by F AJZENBERG-SELOVE. (Academic Press, 1960.) [Pp. 1147.] Two volumes. Price $16 each.

THIS excellent two volume work is a readable and comprehensive introduction to experimental nuclear spectroscopy. It consists of a series of articles by some thirty authors, distinguished for this contributions to the subject and sets out to meet the needs both of graduate students entering the experimental field and of others working in related areas who wish to familiarize themselves with present ideas on nuclear spectroscopy. The first volume contains the experimental parts of the subject and is largely devoted to articles on the spectroscopy of charged particles, gamma rays and neutrons. In these attention is focused on up-to-date instruments and techniques and the whole work is liberally illustrated with typical results obtained with them. The second volume contains material of more theoretical nature and is divided into a section on the analysis of experimental data and a section on nuclear models. The former collects together articles which describe the reduction of experimentally measured quantities to quantities which can be directly related to theory. The latter section contains the theory in the form of articles on the shell model the collective model and the complex potential model of the nucleus.

The broad treatment of the whole subject and the general lucidity of presentation, are likely to make this book a good starting point for graduate students for some years to come. It will also appeal to experimental physicists working in this field because of its stimulating and refreshing tone. It is well produced, referenced and indexed and can be strongly recommended to those interested in low energy nuclear physics. M. A. G.

Progress in Nuclear Energy: Technology, Engineering and Safety, Vol. 2. P.N.E. series. Edited by R. Hurst, R. N. Lyon and C. M. Nicholls. (Pergamon Press, 1960.) [Pp. xvl+800.] Price £5 5*s*. 0*d*.

This book is one of a series based on the Proceedings of the Second International Conference on the Peaceful Uses of Atomic Energy, and it contains thirty-four papers by various authors on technological aspects of nuclear reactors, in particular on reactor chemistry, reactor materials, engineering experience and practice, engineering studies, and engineering aspects of reactor safety. As its title might suggest, it is something of a hotch-potch of miscellaneous themes and lacks the unity that is to be found in other volumes devoted to a single topic. Despite the editors' efforts to deal with this basic problem, and despite their skilful ordering of the articles, it does not read as a single book but as a collection of separate reviews and research papers which cover such widely different topics as, for example, ion exchange properties of hydrous oxides, the design of irradiation experiments, and hydrodynamic problems of reactor containment. The chemical aspects of the behaviour of materials in reactors are dealt with in detail, although magnesium is a surprising omission. The physical aspects are dealt with rather scantily and there is nothing on Wigner effects in graphite despite the fact that the chemistry of the graphite —CO_2 system is allowed 70 pages. There are several articles on liquid metal fuels which might have fitted better into the companion volumes on Metallurgy and Fuels. The most systematically developed themes in the volume are those dealing with methods of cooling and with the safety of reactors. The mass of technical data presented vividly illustrates the well-known view that a thousand man-years of scientific and engineering effort are required to develop a single new types of power-producing reactor.

A. H. C.

Advances in Applied Mechanics, Vol. IV. Edited by H. L. Dryden, Th. v. Kármán and G. Kuerti. (London and New York: Academic Press 1960.) [Pp. 294.] Price $9.00.

This is the latest of a series of volumes containing review articles on recent work in continuum mechanics and allied fields. It maintains the generally high standard set by its predecessors, and all that need be said about it is to list the titles and authors of the five articles contained in it. They are :

The theory of unsteady laminar boundary layers, by K. Stewartson;
Boundary-layer theory with dissociation and ionization, by G. Ludwig and M. Heil;
The propagation of shock waves along ducts of varying cross section and by W. Chester;
Similarity and equivalence in compressible flow, by K. Oswatitsch;
Kármán vortex streets, by R. Wille.

G. K.

[*The Editors do not hold themselves responsible for the views expressed by their correspondents.*]

Fig. 2

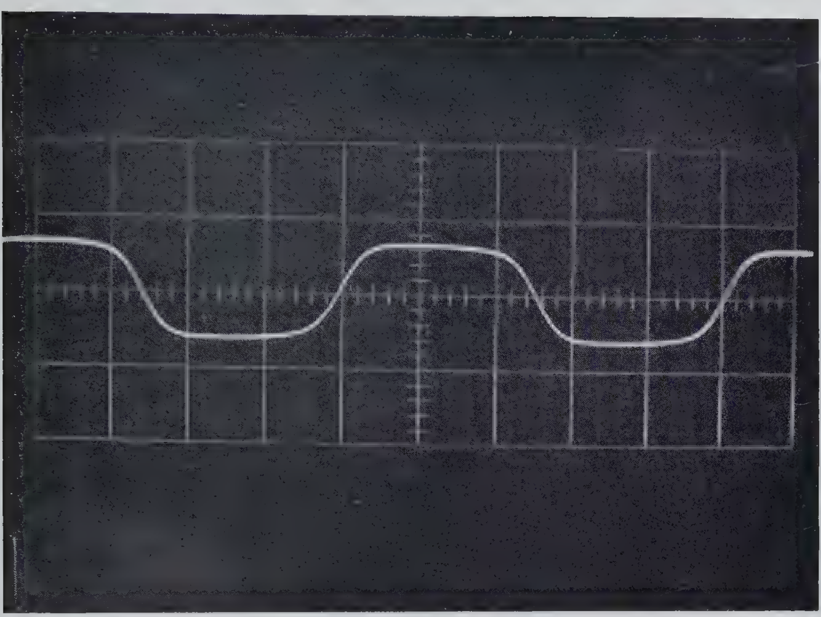

Oscilloscope trace of response of sodium chloride to cyclic bending (100 c/s). One division corresponds to 1 mv.

Fig. 3

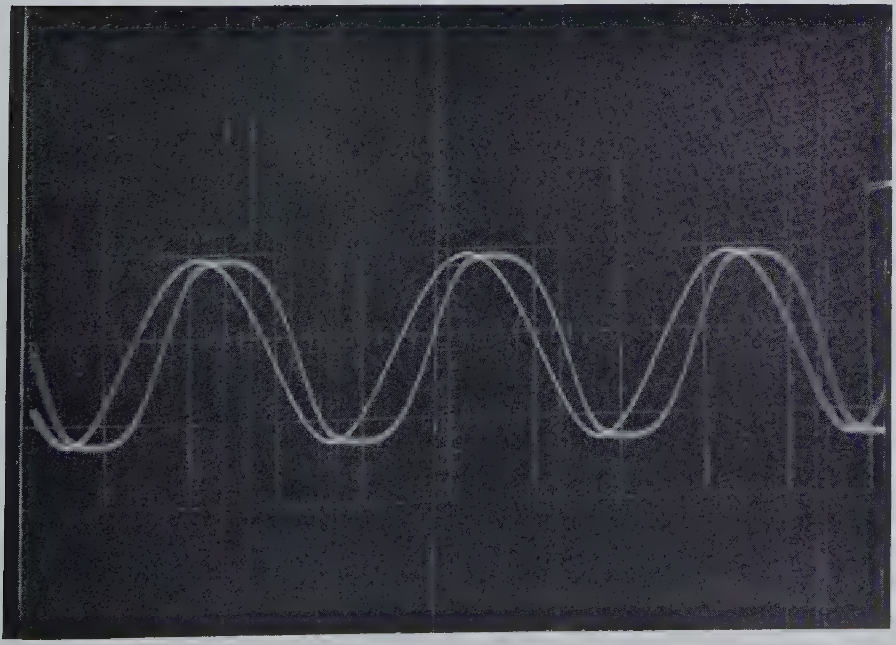

Dual trace oscillogram comparing the signal from the specimen with that from the vibrating capacitor.

Fig. 7

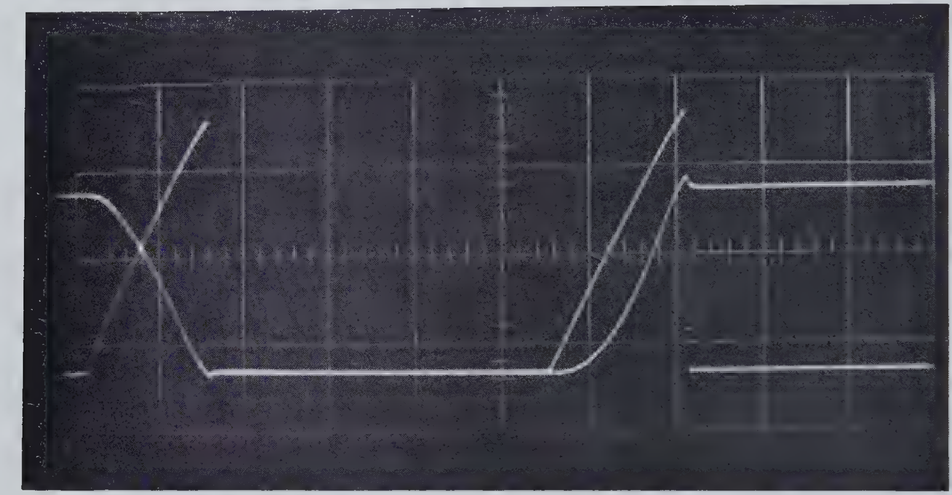

A photo of the sawtooth current pulses and the obtained electrical effect. The polarity of the second pulse is reversed to that of the first pulse.

Fig. 10

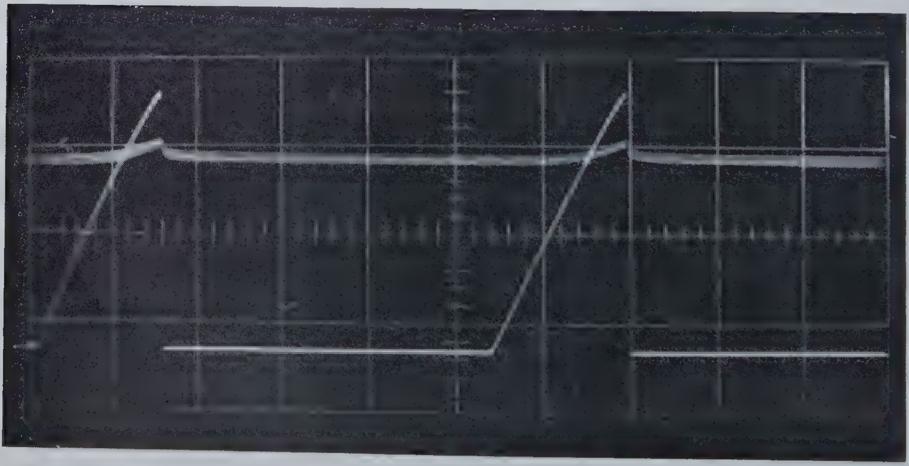

Photo of the signal obtained by imposing on the specimen a series of pulses of the same polarity.

Fig. 2

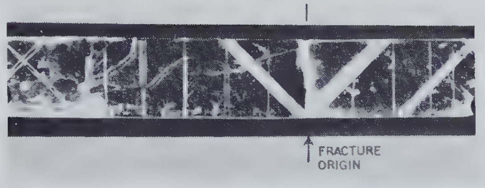

Photomacrograph showing the distribution of slip after fracture in crystal of fig. 1 (*a*). Slip bands revealed by etching and oblique illumination. (×5.)

Fig. 3

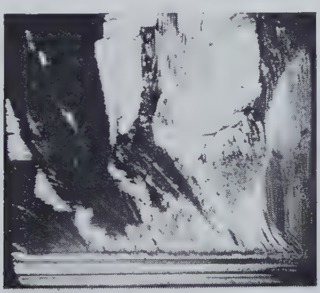

Fracture surface for crystal of fig. 2 illustrating the characteristic (110) [001] step or 'line' source. Note that a number of steps are produced each corresponding with the structure of the slip band on the left of fig. 2. (×20.)

Fig. 4

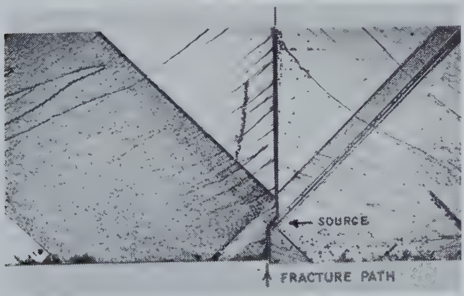

Composite photomicrograph showing the location of the (110) [001] slit fracture source of crystal (*b*), fig. 1, with respect to the slip bands. (×125.)

Fig. 5

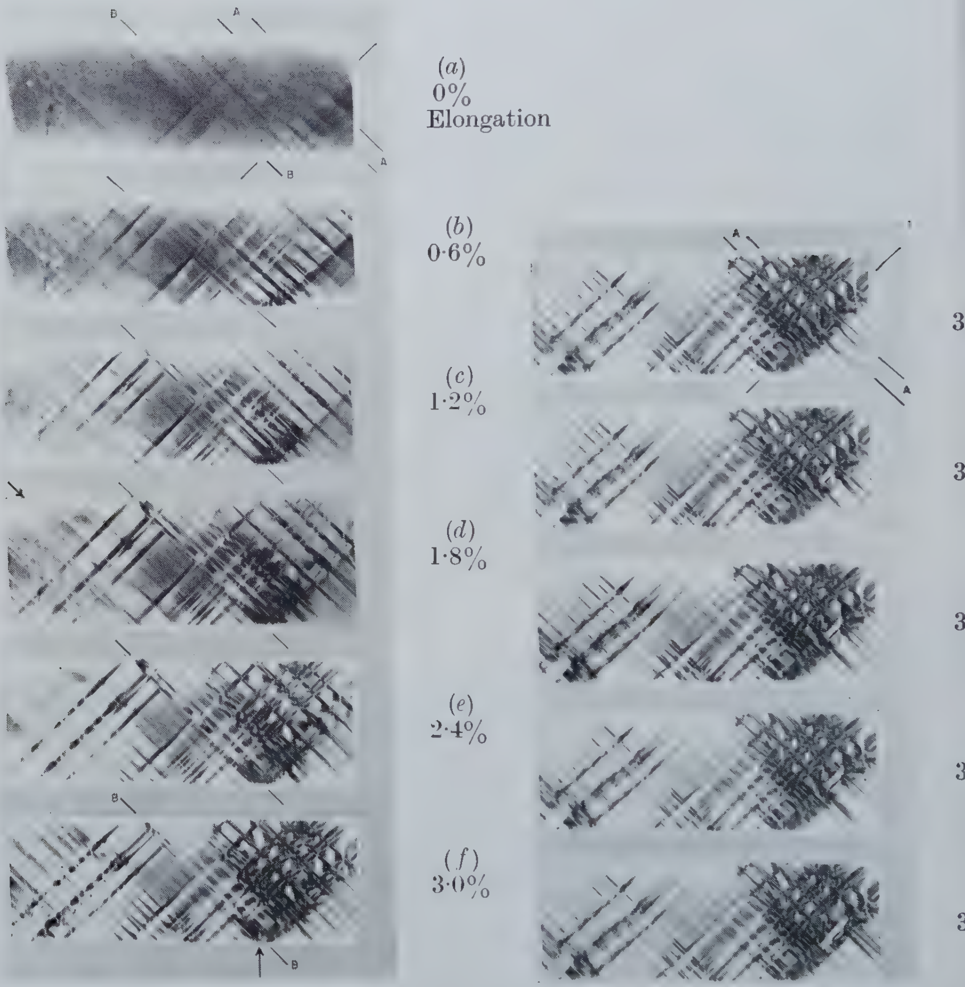

(*a*)
0%
Elongation

(*b*)
0·6%

(*c*)
1·2%

(*d*)
1·8%

(*e*)
2·4%

(*f*)
3·0%

Selected frames from a motion picture showing the development of slip and the formation of cleavage cracks at slip band intersections in magnesium oxide.

The crack located between the slip bands A was responsible for fracture. Frames (*g*) and (*h*), (*j*) and (*k*) were consecutive, i.e., 1/16 sec apart. Polarized illumination. (×5.)

Fig. 6

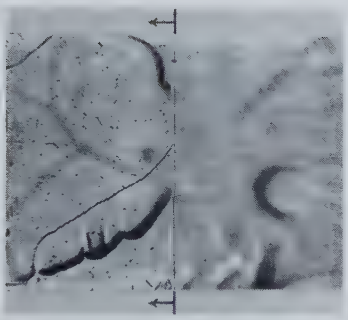

Fig. 9

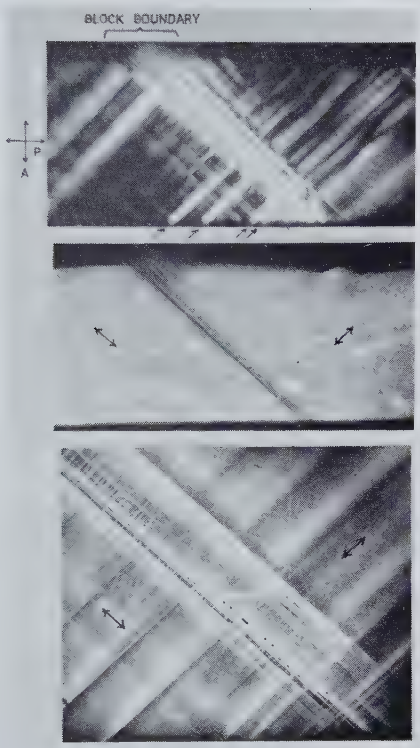

Fig. 6

Etch pits in an expanding band of single slip in magnesium oxide. The direction of growth is from right to left. Note the extremely sharp demarcation between slipped and unslipped material. (×12.)

Fig. 9

Two ‘ blocks ’ of slip in a sprinkled magnesium oxide crystal deformed in tension.

(*a*) Polarized transmitted illumination. P-plane of polarizer, A-plane of analyser. (×12.)

(*b*) Normal transmitted illumination. Etched surface. (×12.)

(*c*) Normal reflected illumination. Enlargement of block boundary in (*b*) to show position of cracks. (×25.)

Arrows in (*b*) and (*c*) indicate directions for *dense* slip in each block. Check by looking along photograph (*c*).

Note: The stress birefringence and etch pit patterns are most marked at block boundary and for isolated slip bands penetrating across block boundary *not* the regions of dense single slip.

Fig. 10

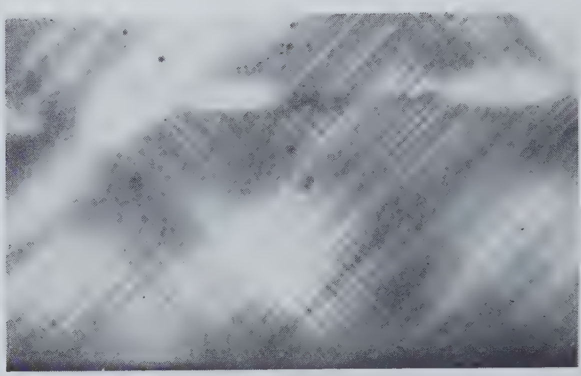

Dense intersecting slip in the tension region of a sprinkled crystal deformed by bending. The bending axis is perpendicular to the plane of the paper. (×19.)

Fig. 12

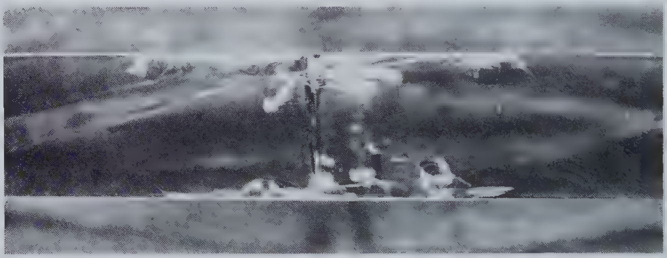

Tension surface of a sprinkled crystal fractured by bending. Tension direction horizontal. The two halves have been butted back together for the picture. Note the shattering along the edges of the specimen and the longitudinal cracks. (×4.)

Fig. 13

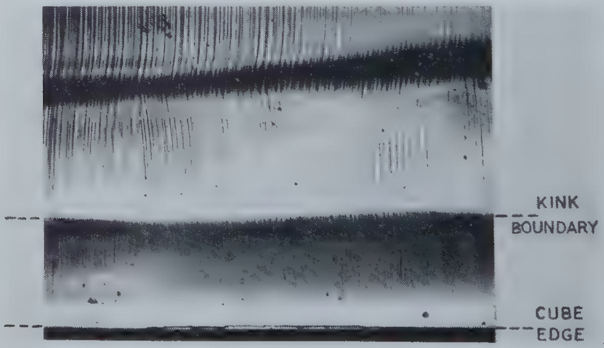

Anticlastic kinking along the edge of the tension surface in crystal of fig. 12. Tension direction horizontal. Fine slip on {110} planes making 45° with cube edge can be seen within kinked region only. Oblique illumination. (×56.)

Fig. 14

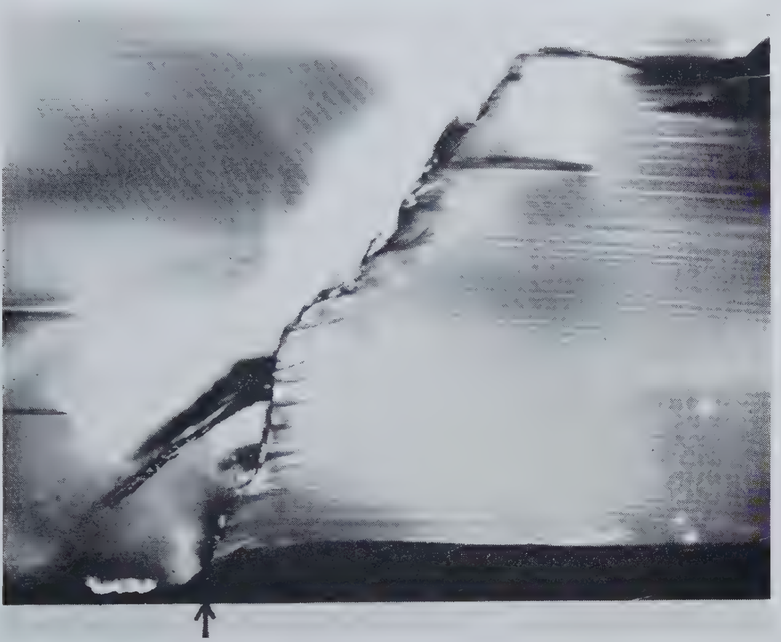

Longitudinal crack in tension surface of a sprinkled magnesium oxide crystal fractured by bending. Tension direction vertical. (×250.)

Fig. 15

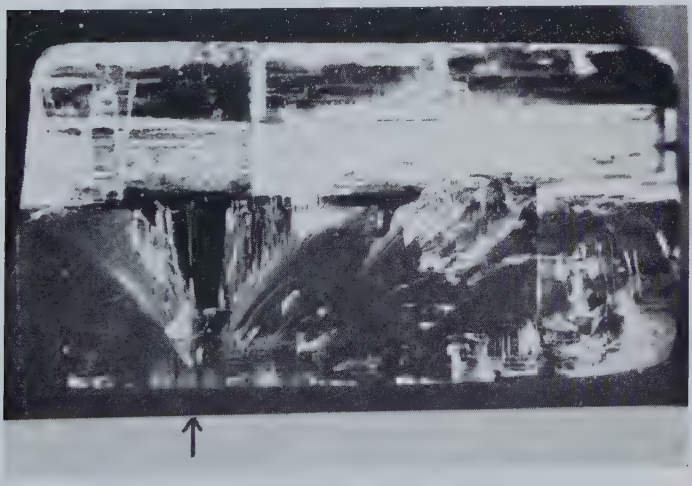

Fracture surface of crystal in fig. 14. Fracture source corresponds with the step indicated by arrow in fig. 14. (×20.)

Fig. 1

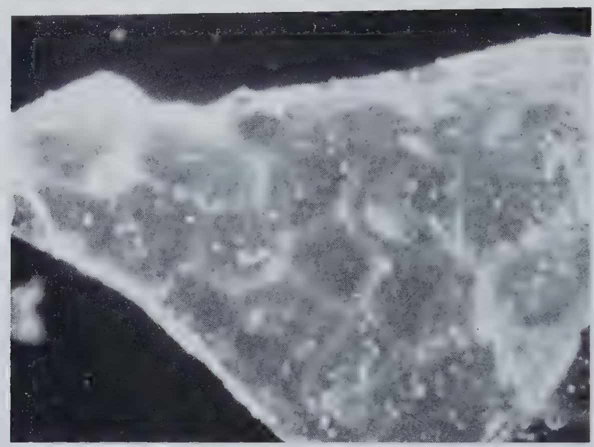

Luminescent fragment of KBr: Sn. Mag. ×13.

Fig. 2

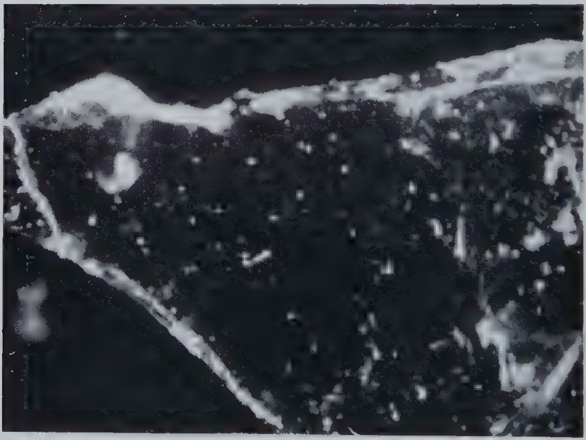

Same field of view as fig. 1, but with the ultra-violet light from the mercury lamp filtered out. Mag. ×13.

Fig. 3

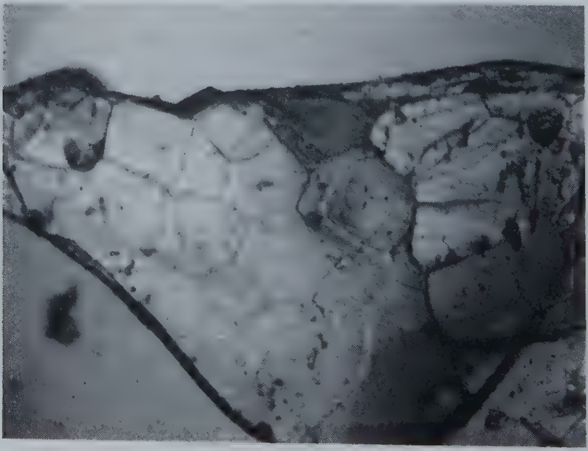

Transmission photograph showing the surface structure. Mag. ×13.

Fig. 4

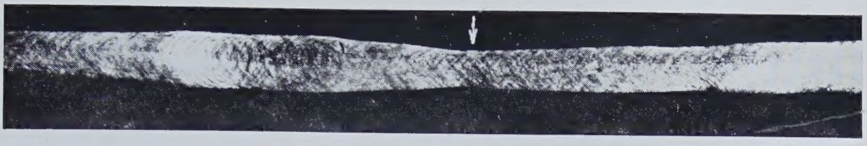

⟨100⟩ crystal deformed at 400°c. Arrow indicates region where deformation took place on different {111} planes in different regions of the crystal (no necking). Approximately ×2½.

Fig. 5

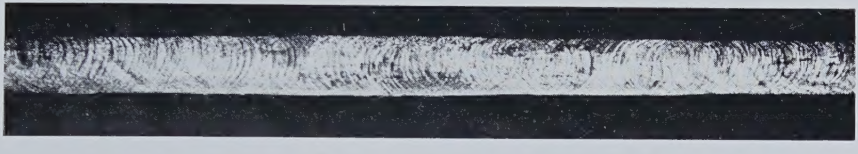

⟨110⟩ crystal deformed at 400°c. Approximately ×2½.

Fig. 6

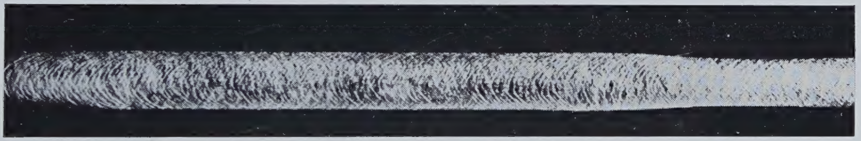

⟨111⟩ crystal deformed at 400°c. Approximately ×2½.

Fig. 7

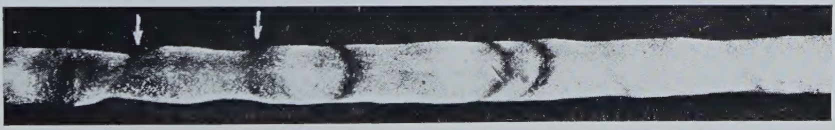

⟨100⟩ crystal deformed at 600°c. Note rounded edges of slip bands. Arrows show region where deformation occurred on different {111} planes. Approximately ×2½.

Fig. 8

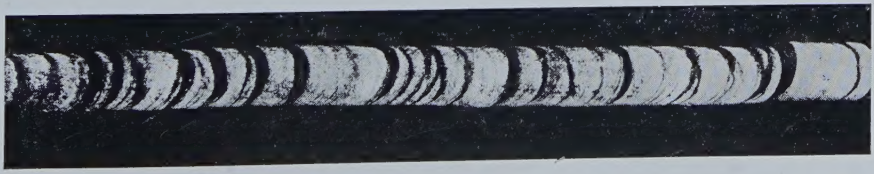

⟨110⟩ crystal deformed at 600°c. Note sharp-edged slip bands. Approximately ×2½.

Fig. 9

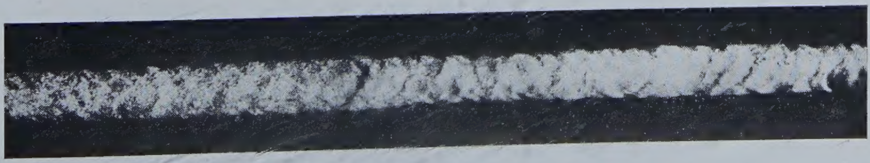

⟨111⟩ crystal deformed at 600°c. Approximately ×2½.

Fig. 3

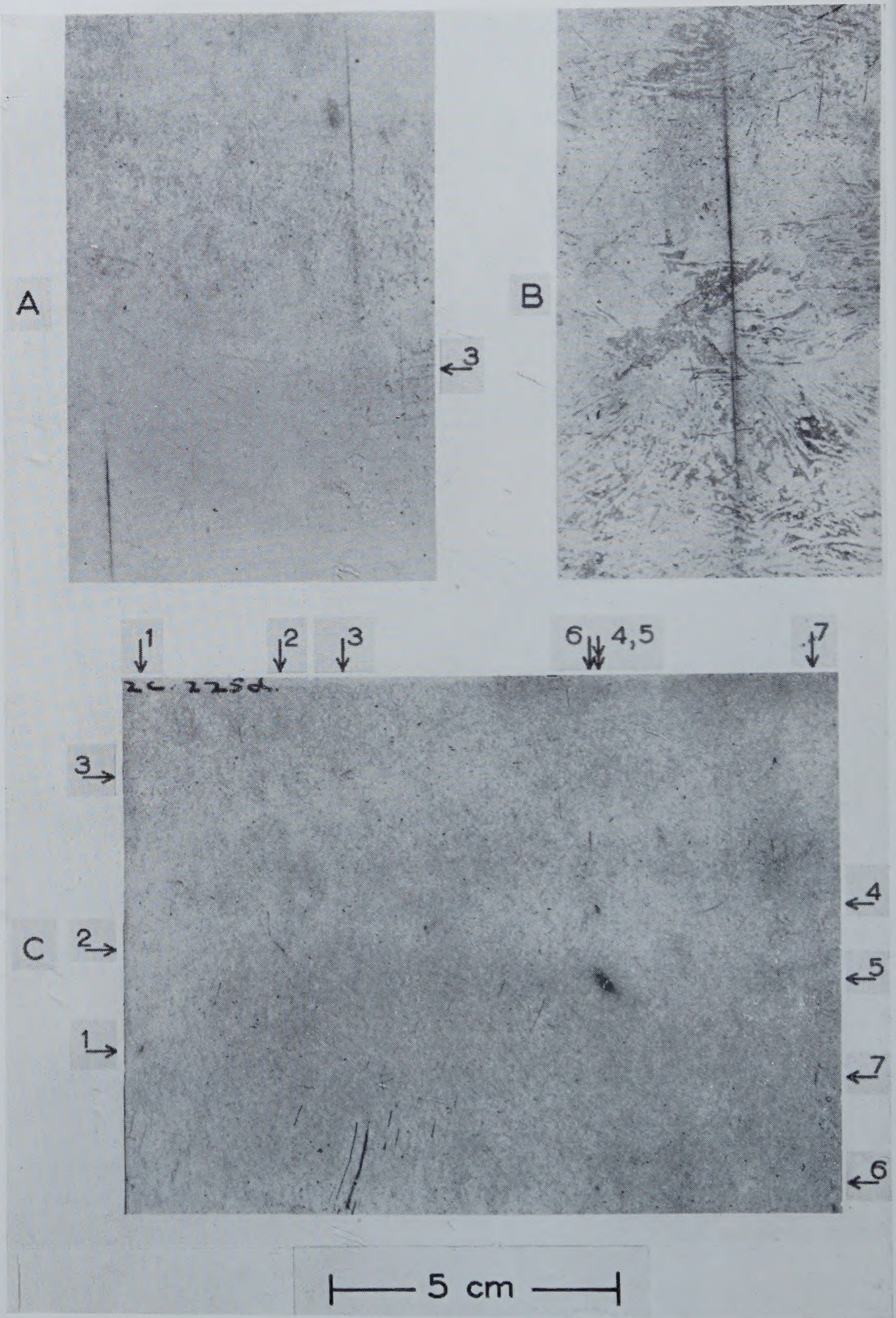

Contact prints of individual emulsion sheets, showing cascades visible to the unaided eye. The cascades shown in (A) and (B) are members of a ‘family’ of about 30 cascades, distributed through the Comet 1 stack; the individual cascade axes are parallel to each other, and most were produced by γ-rays resulting from a nuclear interaction of primary energy $\sim 10^6$ BeV occurring in the air about 1 km above the aircraft. In (C), 7 cascades (all unrelated) can be distinguished in a single emulsion. Their positions are indicated by the intersections of the arrows.

Fig. 9

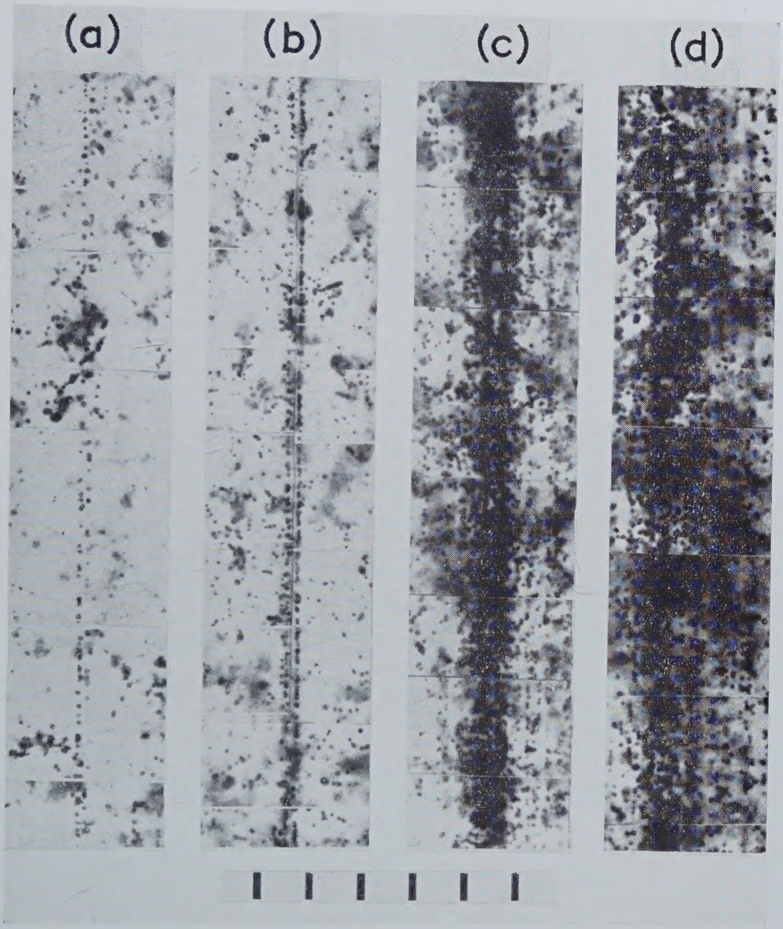

Photomicrographs of event 192α. A single energetic neutral pion (of energy ~ 3800 BeV) was generated in a nuclear interaction in the dural end-plates clamping the stack. Both γ-rays from the π^0-decay convert after traversing ~ 7 cm of emulsion, and the tracks of the two electron pairs are shown in (*a*), with a lateral separation in the emulsion plane of $\sim 1{\cdot}8\,\mu$. In (*b*), 1 r.l. beyond (*a*), the original pairs are now accompanied by other electrons. (*c*) shows the appearance of the cores 4 r.l. beyond (*a*), where their separation is $\sim 2{\cdot}7\,\mu$. In (*d*), 6 r.l. from (*a*), the two cores are no longer distinguishable.